Spin Crossover Systems with highly versatile magnetic bistability using 1,3,4-Thiadiazole Ligands

Dissertation

Zur Erlangung des akademischen Grades

„Doktor der Naturwissenschaften – Dr. rer. Nat.“

im Promotionsfach Chemie

Vorgelegt von

Jonathan Kiehl

Geboren am 08.06.1992 in Aschaffenburg

Die vorliegende Arbeit wurde in der Zeit vom 01.12.2018 bis 01.12 2021 am Institut für Anorganische Chemie der Johannes Gutenberg-Universität Mainz unter Betreuung von ██████████ angefertigt.

Ich, Jonathan Kiehl, Matrikelnummer ██████, versichere, dass ich diese Arbeit selbstständig verfasst und keine anderen als die angegebenen schriftlichen und elektronischen Quellen sowie andere Hilfsmittel benutzt habe. Alle Ausführungen, die anderen Schriften sinngemäß oder wörtlich entnommen wurden, habe ich kenntlich gemacht.

_____   _____

(Ort, Datum)   (Unterschrift)

Dekan:

Erstgutachterin:

Zweitgutachterin:

Prüfer:

Tag der mündlichen Prüfung:

D77

Kurzzusammenfassung

Das Spin-Crossover (SCO) Phänomen beschreibt den Übergang von 3d-Organometall Koordinationsverbindungen zwischen zwei verschiedenen Spin-Zuständen, dem High-Spin- (HS) und dem Low-Spin-Zustand (LS). Dieser kann durch externe Stimuli wir beispielsweise Temperatur, elektromagnetische Strahlung oder Druck beeinflusst werden. Stark kooperative Systeme mit abrupten oder sogar hysteretischen Spinübergängen werden als molekulare Schalter, Speicher oder Sensoren gehandelt. Die Kombination des SCO-Phänomens mit anderen physikalischen Eigenschaften, die für solche Anwendungen interessant sind, wie beispielsweise elektrische Leitfähigkeit, Lumineszenz oder andere magnetische Eigenschaften, führt zu Systemen, die durch ihre SCO Eigenschaften leicht beeinflusst werden können. Systeme mit breiter magnetischer Hysterese eignen sich aufgrund ihrer großen magnetischen Bistabilität besonders gut für die Anwendung und Kombination mit anderen physikalischen Eigenschaften. Jedoch hängt hysteretisches Verhalten stark von den intra- und intermolekularen Wechselwirkungen der spintragenden Übergangsmetallzentren ab. In der Regel wird solch hohe Kooperativität im Festkörper durch intermolekulare Wechselwirkungen wie klassische und nicht-klassische Wasserstoffbrückenbindungen wie auch π-π-Wechselwirkungen von aromatischen Gruppen der Liganden erzeugt. Da das detaillierte Verständnis des Zusammenspiels von Kooperativität und dem Auftreten magnetischer Hysterese für künftige Anwendungen von großem Interesse ist, hat sich die vorliegende Arbeit mit den Auswirkungen von intermolekularen π-π-Wechselwirkungen konzentriert. Es wurden Fe^{II}-SCO-Komplexe untersucht, welche auf nicht-symmetrischen zweizähnigen Liganden mit 1,3,4-Thiadiazol-Koordinationsmotiv basieren. In Anlehnung an eine im Jahr 2010 von *Klingele et al.* Publizierte Arbeit wurden vier neue Liganden synthetisiert, die sich durch die Größe ihres π-Systemes unterscheiden. Anschließend wurden mit den synthetisierten Liganden unterschiedliche einkernige Fe^{II}-Komplexe hergestellt und mittels temperaturabhängiger Messungen der magnetischen Suszeptibilität, Einkristall-Röntgenstrukturanalyse und Mössbauer-Spektroskopie untersucht.

Insgesamt konnten zwölf neue Fe^{II}-Komplexe synthetisiert und charakterisiert werden. Die Verbindungen weisen unterschiedliche SCO-Eigenschaften auf, abhängig der eingesetzten Liganden und ihrer aromatischen nichtkoordinierenden Seitenketten, den koordinierenden Gegenionen und der Kristallpackung im Festkörper. Die in dieser Arbeit vorgestellten Komplexe sind hervorragende Beispiele für die unterschiedlichen komplexen intermolekularen Effekte, die die resultierenden magnetischen Eigenschaften drastisch beeinflussen, und zeigen das große Potenzial von 1,3,4-Thiadiazol-Liganden zur Bildung von SCO-Verbindungen.

Abstract

The spin crossover (SCO) phenomenon describes the transition of 3d-organometalllic coordination compounds between two different spin states, namely the high-spin state (HS) and the low-spin state (LS), which is triggered by external stimuli such as temperature, electromagnetic radiation, or pressure. Highly cooperative systems with abrupt or even hysteretic transitions are traded as a crucial element for molecular switches, memories, or sensors. The combination of the SCO with other physical properties relevant for such applications, such as electrical conductivity, luminescence, or other magnetic properties, leads to systems that are easily tuneable by their spin switching properties. Systems with broad magnetic hysteresis around room temperature are particularly suitable for application and combination with different features due to their high magnetic bistability. This behaviour depends strongly on the intra- and intermolecular interactions of the spin-bearing transition metal ions. Usually, cooperativity is achieved in the solid state, where intermolecular interactions such as classical and non-classical hydrogen bonding or π-π-stacking of aromatic groups of the ligands can lead to long-range ordering. Usually, cooperativity is achieved in the solid state, where intermolecular interactions such as classical and non-classical hydrogen bonding or π-π-stacking of aromatic groups of the ligands can lead to long-range ordering. Since a detailed understanding of the interplay between cooperativity and hysteresis loop is of great interest for future applications, the present work has focused on the role of π-π interactions. Therefore, Fe^{II} SCO-complexes have been investigated, based on a non-symmetric bidentate ligand exhibiting a 1,3,4-thiadiazole coordination motif. Inspired from a publication of *Klingele et al.* in the year 2010, four new ligands were synthesised that differ in their ability to form π-π-interactions due to different sizes of their π-systems. The ligands were used to generate mononuclear Fe^{II} complexes potentially exhibiting SCO properties. The magnetic and structural properties of these compounds were investigated by temperature-dependent measurements of the magnetic susceptibility, single-crystal X-ray structural analysis, and Mössbauer spectroscopy.

In total, twelve new Fe^{II} SCO-complexes were synthesised and characterised. The compounds have varying properties depending on the ligands and their aromatic non-coordinating side chains, the coordinating counterions and the crystal packing in the solid state. The complexes presented in this work are excellent examples of the multiple and complex intermolecular effects that drastically affect the resulting magnetic properties and show the great potential of 1,3,4-thiadiazole ligands to form SCO compounds.

Abrevations and Units

Å	Angström
abs.	absolute
Av., ave	average
APCI	Atmospheric-pressure chemical ionization
B	Racah parameter
°C	Grad Celsius
c	centi
cm^{-1}	wavenumber
χ	magnetic susceptibility
calc.	calculated
conc.	Concentrated
C_p	heat capacity
D	dimensional
d	Dublett
DCM	dichloromethane
DMF	N,N'-dimethylformamide
DMSO	dimethylsulfoxid
Δ	difference
eq.	equivalent
Δ_O	octahedral ligand field splitting
δ	isomer shift
Δc	critical ligand field strength
ΔE_{HL}	energy difference between the high spin and the low spin ground state
ΔE_Q	quadrupole splitting
Δr_{HL}	difference between the equilibrium iron-donor atom distance of the high spin and the low spin state
Δ_T	octahedral ligand field splitting
DSC	differential scanning calorimetry
E	energy
el	electronic
E_p	mean spin pairing energy
Σ	octahedral distortion parameter
EPR	electron paramagnetic resonance
eq.	Equivalents
et al.	et alii (and coworkers)
EtOH	ethanol
f	vibrational force constant
FT	fourier transformation
G	free Gibbs energy

g, g	gyromagnetic factor, gramm
γHS	mole fraction of the high spin state
h	hour(s)
H	enthalpy
HS	High-Spin
hν	light irradiation
Hz	Hertz / cm^{-1}
IR	infrared
J, J	coupling constant, Joule
K	Kelvin
k	kilo
k_B	Boltzmann constant: $1.380649*10^{-23}$ JK^{-1}
L, L	total orbit momentum, ligand, liter
L^{dptd}	2,5-di-(2-pyridyl)-1,3,4-thiadiazole
L^1	2-naphthy-5-pyridyl-1,2,4-thiadiazole
L^2	2-phenyl-5-(pyridin-2-yl)-1,3,4-thiadiazole
L^3	2-(anthracen-2-yl)-5-(pyridin-2-yl)-1,3,4-thiadiazole
L^4	2-(6-methoxynaphthalen-2-yl)-5-(pyridin-2-yl)-1,3,4-thiadiazole
λ	wavelength
LIESST	light induced excited spin state trapping
LS	low spin
M	metal, mega, mass peak
m, m	mass, meter, mili, multiplet
MeCN	acetonitrile
MeOH	methanol
Min	minute(s)
MLCT	metal to ligand charge transfer
MS	mass spectrometry
μ, µ	dipole moment, micro
μ_B	Bohr magneton: $9.27401007823*10^{-24}$ JT^{-1}
μ_{eff}	effective magnetic moment
μ_{SR}	muon spin relaxation
m/z	mass/charge ratio
n	nano
NA	Avogadro constant: $6.022*10^{23}$ mol^{-1}
NIL	non-innocent ligand
NIR	near infrared
NMR	nuclear magnetic resonance
NSR	nuclear resonance scattering
ν	frequency
Oe	Oersted

p	pressure
PAS	positron annihilation spectroscopy
phen	1,10-phenanthroline
φ_i	cis-angles inside an octahedron
ppm	parts per million
py	pyridine
quant.	Quantitative
r	distance
R	gas constant: 8.3144598 $JK^{-1}mol^{-1}$
r.t.	room temperature
ρ	density
s, s	electron spin, second, singlet
SCO	spin crossover
SMM	single molecule magnet
SQUID	superconducting quantum interference device
T, T	temperature, tesla
t	tons, triplet
TDA	1,3,4-thiadiazole
THF	tetrahydrofurane
TIESST	thermally induced excited spin state trapping
TLC	thin layer chromatography
TOF	time of flight
UV	ultraviolet
V	volume
vib	vibrational
Vis	visible
XAS	X-ray absorption spectroscopy
X-ray	electromagnetic radiation with a wavelength ranging from 0.01-10 nm and a corresponding energy of 0.1 – 100 keV
Z	cell formula units
z	charge

„per aspera ad astra"
(„durch das Raue zu den Sternen")
- **Seneca**-

Für all die Liebsten die meinen Weg kreuzten und diesen mit mir Seite an Seite bestreiten

Content

1. Introduction

In the field of modern materials science research focuses on the design of new functional molecules with controllable properties. The constant miniaturization of modern processes is crucial in this context. In the process of digitalisation, society must process and store ever larger amounts of data. For this reason, the scientific community is very keen to develop innovative molecular compounds with the ability to combine switching and other physical properties.[1,2] This goal is illustrated in the following diagram (Figure 1), in which the number of publications on such materials per year is depicted from 1990 until today. There has been a marked increase in interest in this field of research, as well as in the number of successful and interesting projects.
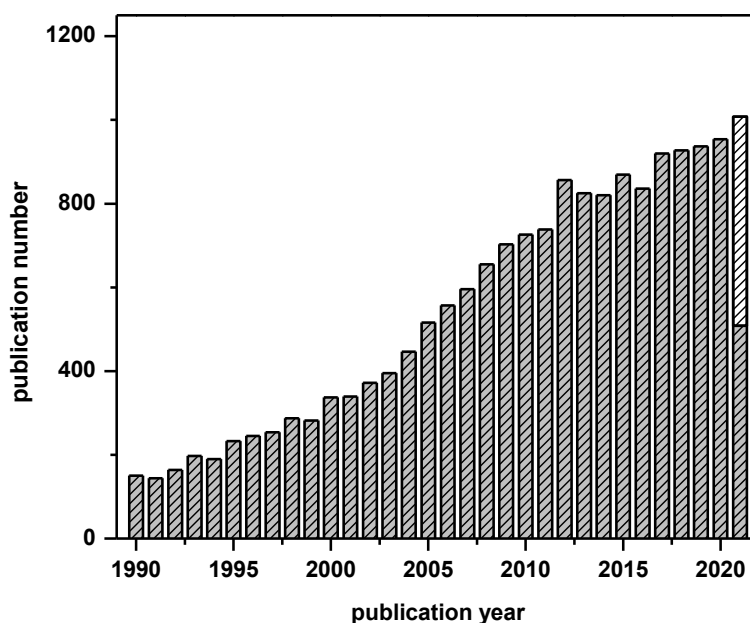
Figure 1: increasing numbers of publications published each year between 1990 and 2021 (light grey pattern). The white pattern represents the estimated prediction for the end of the year 2021. The data are extracted fromSci-finder, search term: spin crossover, molecular switches, molecular magnetism and bistability).

Several articles, books and book chapters on the miniaturization of magnetic materials with functional properties see/show a potential field of application for these materials in data storage,[1–3] sensors,[2,4,5] and even contrast agents.[6–8] Molecular switches and Spin Crossover (SCO) compounds have been in the foreground over the last decades and seem to be particularly good candidates for the realization of multifunctional materials.

Molecular Switches

The creation of materials consisting of molecules with extraordinary capabilities is a major challenge for the chemical society, but equally interesting it offers a new range of applications. The importance of this type of research is reflected by the Nobel Prize in chemistry of the Year 2016, awarded to *Sauvage*, *Stoddart* and *Feringa* "for the design and synthesis of molecular machines".[9] The most diverse molecular machines,[10,11] pumps,[12] rotors[13] or cars[14] were manufactured with a great deal of finesse and experience.

An important component within the molecular machines are molecular switches, which are molecules capable of switching between two different states.[15] External stimuli such as pressure, temperature, magnetic fields, pH values or contact with different chemicals lead to a change of states. Bistable molecular systems are of great interest in scientific research as they are in the spotlight for future application.[16] However, the most promising and powerful external stimuli is light, which can be applied with high spatial and time resolution. Furthermore, light is non-invasive and its wavelength and intensity are easily fine-tuned. Photochromic compounds such as azobenzenes, spiropyranes, diarylethers and others are particularly suitable for a light-driven change of state.[17,18] One prominent example is the so called "record player molecule" and was designed by *Herges et al.* in the year 2011 (Figure 2).[19]
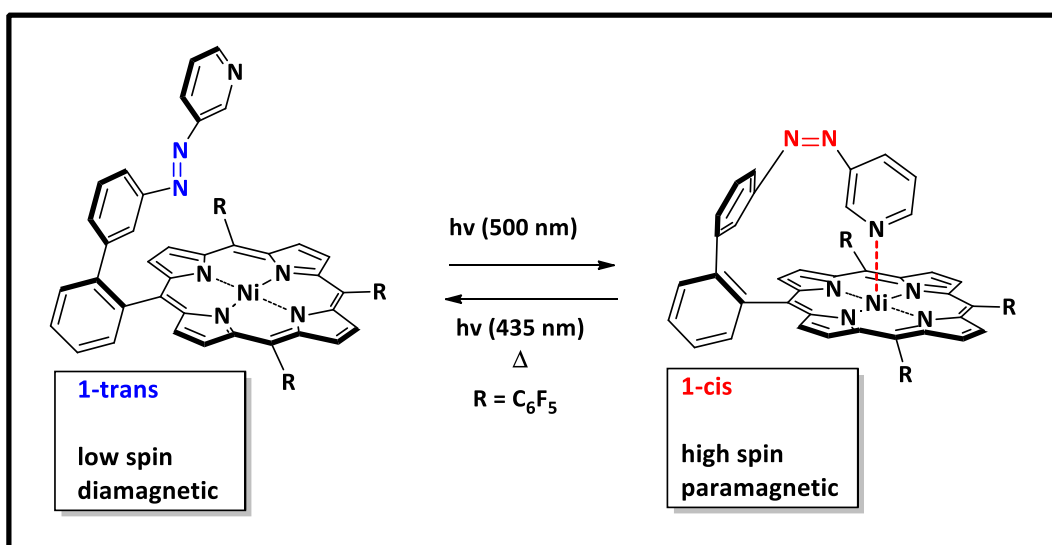
Figure 2: Nickel(II)-tetrakis(pentafluorophenyl)porphyrin functionalized with an azopyridine in the trans (left) and cis (right) form, designed by Herges et al.. The figure was reproduced from literature.[19]

The Ni-(II)-tetrakis(pentafluorophenyl)porphyrin complex was functionalized with an azopyridine, which undergoes a cis/trans isomerisation during light irradiation. However, the special feature in this case is that the central nickel atom in the porphyrin ring changes its coordination environment and thus its magnetic spin state at the same time due to the photoisomerisation. In the trans form, the nickel(II) ion exists in the diamagnetic (S=0) low spin state, whereas the cis form is characterised by its paramagnetic (S=1) high spin state. The terminology of this special spin change is called "light-driven coordination-induced spin state switching" (LD-CISSS). The remarkable aspect is that this is possible

under aerobic environmental conditions in solution without noticeable fatigue of the compound even after more than 100.000 cycles.[20–23]

The fact that the findings from 2011 were only the keystone for this type of molecular switches and their potential future application is shown recently by *Herges at al*. Potential applications in biological environments or in vivo were targeted, which requires high switching efficiency in water and switching wavelengths in the far-red or near-infrared range. This is called "operating in the bio-optical window".[24] This publication demonstrates that both goals could be achieved by replacing the porphyrin core either by chlorin (dihydroporphyrin) or bacteriochlorin (tetrahydro- porphyrin) and by substitution with solubilising substituents.

Porphyrin   Chlorin   Bacteriochlorin
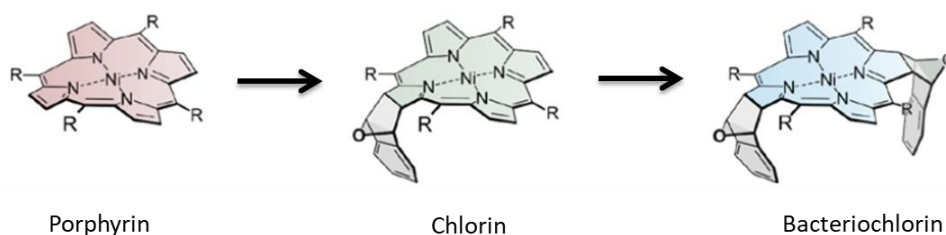
Figure 3: Evolution of the metal carrying core of Porphyrin to chlorin to bacteriochlorin. For the sake of clarity, the azopyrine unit that can be cis/trans isomerised by light is not illustrated. The picture was reproduced from literature.[24]

The light-driven spin state change occurs exactly as in the parental porphyrin complex through cis/trans isomerisation of the axially bound azopyridine unit. However, the wavelength of the cis/trans isomerisation of the side arm was successfully shifted bathochromically from 435 nm (porphyrin) to 620 nm (chlorin) to 720 nm (bacteriochlorin). Although the detailed mechanism of the long-wave photoisomerization of azobenzenes still needs to be investigated, it was possible to create a water-soluble, optically switchable system that is also stable in solution for at least two weeks and has potential applications in medicine.[24]

It has been made clear up to this point how much importance science attaches to multifunctional switchable materials. For that reason, this work deals with the synthesis and investigation of new spin crossover materials with unique switching capabilities. The design of the SCO compounds focusses on the existence of magnetic functionality and the combination with other physical properties. In this dissertation, success and shortcomings are reported and discussed. This leads to a concluding outlook which may drive the discussed projects forward, while also highlighting problems that still need to be solved. The following chapter provides a brief introduction to the theoretical principles of the spin crossover phenomenon.

<u>2.</u> Scientific Background

2.1. Ligand field theory and the Spin crossover phenomenon

The chemical and physical properties of the transition metal atoms are strongly influenced by the occupation of the d-orbitals. Most transition metal ions do not have fully occupied d-orbitals. Repulsive electrostatic interactions between d-electrons and ligands lead to a cancelling of the degeneracy of the d-orbitals of the transition metal ion. In the octahedral ligand field anti-bonding orbitals with e_g^* - (d_z^2 and $d_{x^2-y^2}$) and non-bonding orbitals with t_{2g} symmetry (d_{xy}, d_{yz} and d_{xz}) are obtained. The atomic orbitals d_z^2 and $d_{x^2-y^2}$ point directly in the direction of the ligands and are thus energetically raised by the increased electrostatic interaction.[25] Contrary, the atomic orbitals d_{xy}, d_{yz} and d_{xz} are located exactly between the respective coordinate axes and are thus lowered in its energies. The energy difference of the ligand field splitting is known as Δ_O or 10 Dq. [25–27] If symmetry operations are applied to the orbitals xy, xz and yz, they behave like the irreducible representation t_{2g} of the symmetry adapted linear combinations of the orbitals (SALCs), which is why this set of orbitals is described with the term symbol t_{2g}. The letters A, B, E, T of the irreducible representation indicate the degeneracy, where doubly degenerated orbitals denoted by e and triply degenerated orbitals denoted by t. Orbitals are described with lower case letters, where inversion centres are designated as the so called parity and are written with the index g for "gerade" or u for "ungerade". [25,26,28,29] The parity of an orbital is "gerade" (g) if the amplitude of the wave function remains the same during an inversion at the symmetry centre of the molecule, and "ungerade" (u) if the amplitude flips sign in that process. Heteroatomic diatomic molecules do not have an inversion centre, therefore a classification of the orbitals according to their parity is not possible. The index 1 or 2 describes whether if there is a C_2-axis perpendicular to the main rotation axis C_n or a σ_d-plane. If the signs are kept for the corresponding operations (rotation and mirroring) the symbol gets the index 1. If the sign flips, index 2 is used.[28,29] The value of the ligand field splitting is dependent of the donor and acceptor properties of the ligand, the oxidation state of the metal centre ion and the geometric arrangement of the ligands. Typical values for Δ_O are 7000 – 40.000 cm^{-1}.[30] Orbitals of e_g symmetry are raised 0.6 Δ_O in energy, whereas orbitals of t_{2g} symmetry are lowered 0.4 Δ_O in energy.[31]

In the tetrahedral ligand-field the situation is different. Here the xy -, xz -, and yz – orbitals have a higher electronic interaction with the ligands and are therefore higher in energy. The d_z^2 – and $d_{x^2-y^2}$ - orbitals are energetically lowered in return. Compared to the octahedron, there is an inverse splitting of the orbitals. Because there is no centre of inversion in a tetrahedron the sets of orbitals are just named with t_2 and e. The ligand field splitting of the orbitals, with constant charge of the metal centre and equal metal-ligand distances in a tetrahedral coordination environment, is $\Delta_T \approx \frac{4}{9} \Delta_O$ and thus smaller than that of an octahedron.[25,26,28]

In general, transition metal ions with an electronic configuration of 3d^n with n = 4-7 (Cr^{II},Mn^{III},Mn^{II},Fe^{II},Fe^{III},Co^{II}, Co^{III}) are present in the low spin state (LS) or high spin state (HS),

depending on the ligand field strength and the spin pairing energy P. The spin pairing energy P describes the energy that is required to place two electrons in an orbital with inverted spin. If the spin pairing energy P of the d electrons is significantly smaller than the ligand field strength Δ_O ($\Delta_O \gg P$), the energetically lower t_{2g} orbitals are occupied first. The ground state of the central atom is the one with the smallest possible total spin. This is called a low-spin configuration. If, on the other hand, the spin pairing energy is significantly larger than the ligand field strength ($\Delta_O \ll P$), the occupation of the orbitals occurs according to Hund's second rule, resulting in the occupation of the orbitals to be populated in such a way that there is a maximum total spin. This is generally referred to as a high-spin compound. The term spin crossover (SCO) or spin transition is used when the electronic ground state of the selected system changes as a result of external stimuli (pressure p, temperature T, light $h\nu$), while the number of electrons remains constant. This is possible in the case where ligand field strength Δ_O and spin pairing energy P are approximately equal, and thus the energetic transition between HS and LS is in the range of thermal energy $k_b T$.[2,32] Iron(II) as the central metal ion holds a special role in between the SCO – compound class, since the largest change of the magnetic moment, the strongest colour change (Fe^{II}-HS (colourless) $\leftrightarrow$ Fe^{II}-LS (purple)) and also the strongest metal to ligand bond length change Δr can be observed. The electronic ground state alternates in each case between a diamagnetic (S = 0) and a paramagnetic (S = 2) configuration (*Figure 4*). [2,27,32–34] For these reasons, the present work focuses on complexes with iron(II) ions as the central atom, knowing full well that the complexes could also be formed with other central atoms.
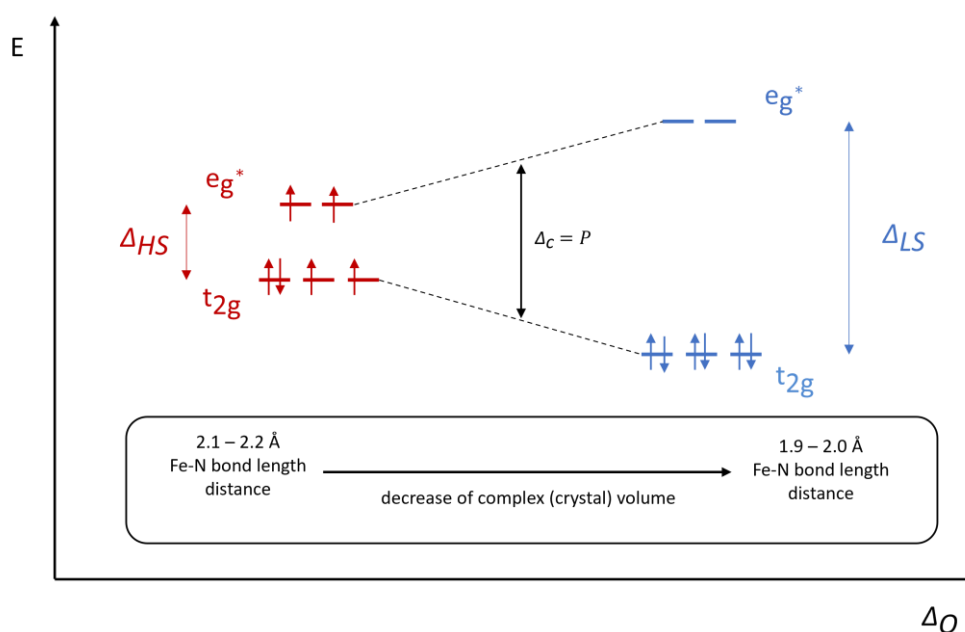
Figure 4: Schematic diagram of a d^6 ion in an ideal octahedral coordination sphere. Left (red): Paramagnetic HS state with the maximum spin (S = 2) ($^5T_2$), when the spin pairing energy P is larger than the ligand field strength Δ_{HS}. Right (blue): Diamagnetic LS state with the minimum spin (S = O) ($^1A_1$), when the spin pairing energy P is smaller than the ligand field strength Δ_{LS}. Δ_c describes the critical ligand field strength. [33,34]

In the context of ligand field theory, a one-electron approximation (uncoupled electrons) is assumed. This approximation is not sufficient for systems with multiple electrons, where the electron - electron repulsion of a free transition metal ion must be considered. A suitable extension of the ligand field

theory is the *Russell-Saunders* coupling scheme. Accordingly, different states result to this interaction described by the term symbolism ^{2S+1}L, where 2S+1 refers to the spin multiplicity and *L* for the orbital momentum. The effect of the ligand field strength on the different spin states, i.e., the energetic distance of the t_{2g} and e_g^* orbitals, is further illustrated by the corresponding *Tanabe – Sugano* diagram of a d^6 – configuration. The energy of the electronic ground and excited terms are plotted against the ligand field strength. Both values are normalized by the Racah - parameter *B*.[33,35,36]
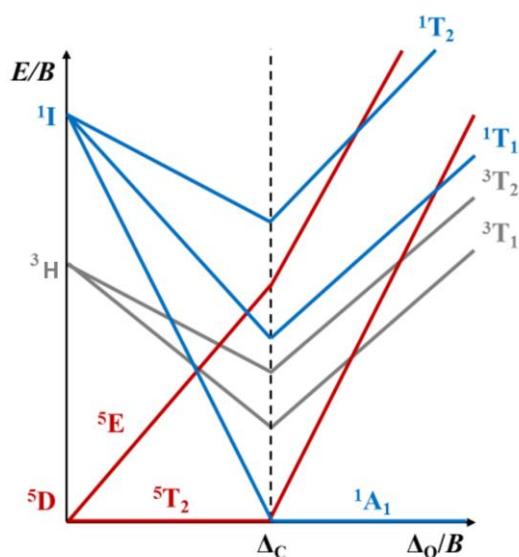
Figure 5: Simplified representation of a Tanabe-Sugano diagram for a $\boldsymbol{d^6}$ ion in an octahedral coordination sphere. Red: Crystal field terms of the HS state. Blue: Crystal field terms of the LS state. [34,37]

The free iron-(II) – ion has an ^5D electronic ground state with the largest possible spin multiplicity. In the weak octahedral field, the ground state splits into the crystal field components $^5T_2$ and ^5E, with $^5T_2$ representing the electronic ground state. At a critical ligand field strength Δ_c, a transition can occur from the HS - $^5T_2$ to the LS $^1A_1$ - ground state which originates from the ^1I term of the free ion, and vice versa (Figure 5). This happens at the equilibrium point of the ligand field splitting Δ_O and the spin pairing energy *P*. At a ligand field splitting larger than Δ_c, the electronic ground state becomes the $^1A_1$ - term of the LS – state. SCO compounds therefore always range close to the critical ligand field splitting Δ_c, which is why external stimuli can lead to a spin transition.[2,29,30,34,37] Typical values for the ligand field are $\Delta LS > 21\ 500\ cm^{-1}$ for low spin compounds and $\Delta HS < 11\ 000\ cm^{-1}$ for complexes in HS configuration.[33,34] To get a better understanding about the critical ligand field strength Δ_c and the spin transition, considering the *Tanabe-Sugano* diagram is not satisfactory as it only takes in to account the energetic differences between the ground and electronic ground states. The approximation to the critical transition point Δ_c depends on several factors, such as the bond distances *r* of a not charged ligand to the metal centre ion. The distance is related to the dipole moment μ as follows:[33,38]

$$10\,Dq \sim \frac{\mu}{r^6}$$ 1

10 Dq (*r*) can be estimated for any metal to ligand distance as long as the ligand field strength 10 Dq (r) is experimentally determined for the complex ground state at a given equilibrium metal to ligand distance. [33]

$$10\,Dq(r) = 10\,Dq\,(r_0)\,\left(\frac{r_0}{r}\right)^6$$ 2

Due to the significant change in the bond length distance of about 10 %, these can be related to the spin state present in each compound. Typical values for the distances of metal to nitrogen-ligands are 2.16 Å und 2.20 Å for the HS – state and 1.96 Å und 2.00 Å for the LS - state.[33,34,37] The widening of the metal to ligand bond lengths of HS complexes can be explained with the population of anti – bonding e_g^* orbitals, which leads to a decrease of the bond order. Contrary, the bond order is increased by a spin transition from HS – to LS – state due to the depopulation of the e_g^* orbitals.

2.2. Thermally induced SCO

Furthermore, both spin states can be visualized by the respective harmonic potentials (Figure 6). The energy is plotted on the y-axis, whereas the metal to ligand distances are plotted as nucleus coordinates on the x-axis. Because of the already mentioned increase in bond order, due to depopulation of the anti – bonding e_g^* - orbitals, the LS potential is shifted to smaller bond lengths. This is possible via an electronic ground state change ($^5T_2 \leftrightarrow\,^1A_1$). The higher bond order leads to a stronger bond, which in turn leads to a narrowing of the potential parabola by increasing the force constant of the metal to ligand atom bond. Contrary to this, a spin transition into the HS state leads to a widening of the potential parabola due to a smaller force constant. The vertical shift ΔE_{HL} depends on the ligand involved and its induced ligand field strength. If the energy difference of the vertical shift of both potentials is in the range of the kinetic energy $k_b T$, a transition can take place which is spoken of as a thermally induced spin crossover. According to this, the LS state would be the electronic ground state at low temperatures, whereby higher vibrational states are occupied by an increase in temperature until the crossing point of both potentials (Δ_c) is reached. The crossing point of the two potential wells corresponds to the critical ligand field strength in the *Tanabe-Sugano* diagram. According to the Franck - Condon principle, a change of spin state and the associated ground state can take place.[25,33,37] In the correct physical sense, however, this crossover point can never be the ground state of the system. Therefore, for SCO systems, the values for ΔLS and ΔHS are only close, but never equal to Δ_c.[3,27,33,34]
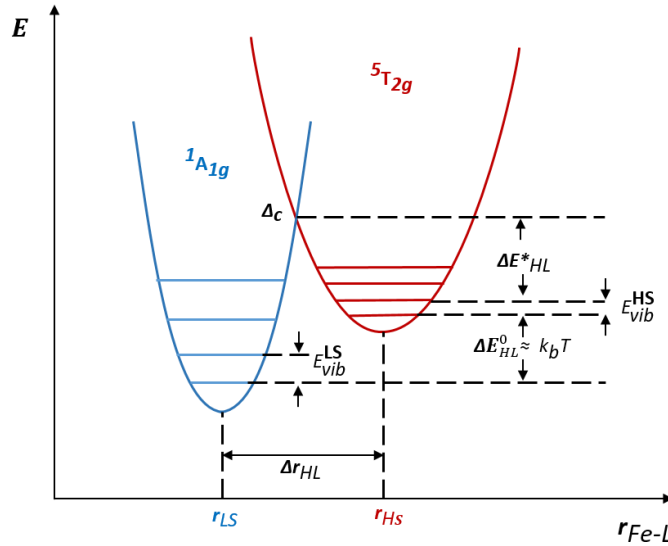
Figure 6: Schematic representation of the harmonic potential wells for the of an iron (II)- donor atom symmetrical stretching vibration mode (Fe − L) for the HS- $^5T_2$ (red) − and LS - $^1A_1$ (blue) state of a SCO compound according to Gütlich et al.[33] ΔE_{HL}^0 represent the zero-point energy difference and ΔE_{HL}^* the activation energy.

ΔE_{HL}^0 is the zero − point energy difference between the two states determined by the difference of E_{HS}^0-E_{LS}^0, whereas the activation energy ΔE_{HL}^* represents the energy difference of the critical crossing point Δ_c and E_{HS}^0. The energy of the vibrational levels E_{vib}^i (with i = HS or LS) is given by:

$$E_{vib}^i = h \left(n + \tfrac{1}{2}\right) \tfrac{1}{2\pi} \sqrt{\frac{f_i}{M}}$$

3

with the reduced mass M and the vibrational force constant f_i ($f_{LS} > f_{HS}$). This results in higher vibrational energies for HS − states.

Formula 5 describes the change of ligand field strength as a function of the metal to ligand distances. Accordingly, it decreases from 10 Dq^{LS} to 10 Dq^{HS} by a factor of 1.74.

$$\frac{10\ Dq^{LS}}{10\ Dq^{HS}} = \left(\frac{r_{HS}}{r_{HS}}\right)^6 \approx 1,74$$

4

The free energy *ΔG* according to *Gibbs-Helmholz* (equation 6) is dependent on the enthalpy *ΔH* and entropy *ΔS*, which are also closely connected to the temperature. Due to the temperature dependence of a spin transition, the transition is therefore also strongly entropy driven. For very low temperatures, the Gibbs free energy *ΔG* is directly dependent on the enthalpy *ΔH*, which is why entropy plays an increasingly important role with increasing temperature.

$$\Delta G = \Delta H - T\Delta S$$

5

The contribution to the change of the entropy ΔS for the population of the HS state derives from vibrational and electronic contributions:

$$\Delta S = \Delta S_{el} - \Delta S_{vib}$$

6

Orbit and spin contribute to S, whereby the former is mostly quenched and can thus be neglected.[33] Thus, a thermally induced spin crossover can be considered as an entropy controlled process. 30% of the total measured entropy gain comes from the change in spin multiplicity (M_s=2S+1), which is shown in equation 7:

$$\Delta S_{mag} = R \ln \left(\frac{M_s \ (HS)}{M_s \ (LS)}\right)$$

7

The remaining 70% of the entropy change is divided equally between stretching and deformation oscillations, which results from the change in the metal-ligand distances described above.[39]

The previous chapters provided an overview of the fundamental principles of thermal-induced SCO. From these theoretical backgrounds, it could be expected that a SCO must always occur in an abrupt manner, since the SCO only occurs between two electronic states and the molecule is either only in the LS or HS state. However, experience shows that this is rarely the situation. If there is more than one spin switching centre, the spin transition may be significantly different from that described due to cooperative interactions in the solid. In addition to the intramolecular changes due to the spin switch, such as change in bond length, distortion of the coordination plane and thus closely related volume change, intermolecular interactions also drastically affect the spin transition (ST) curves. Using the obtained temperature dependent $\chi_m(T)$ values and the expected magnetic susceptibilities of the pure spin states χ_{HS} and χ_{LS} the fraction of the HS ($\gamma_{HS}(T)$)-and LS ($\gamma_{LS}(T) = 1 - \gamma_{HS}(T)$) molecules can be calculated:

$$\chi(T) = \gamma_{HS}(T) \ \chi_{HS} + (1 - \gamma_{HS}(T))\chi_{LS}$$

8

The transition curves can provide a lot of information like for example about the transition temperature $T_{1/2}$, at which half of the molecules are in the HS state and the degree of cooperative interactions. [3,33,34] Cooperativity will be explained in more detail in section 2.6.
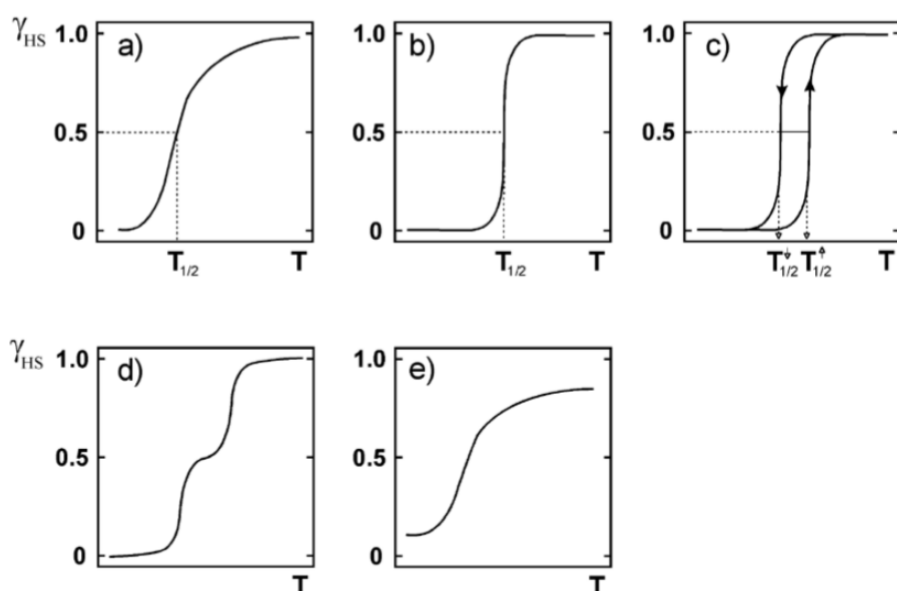
Figure 7: Schematic representation of the possible Spin crossover transition curves of a gradual ST (a), abrupt ST (b), ST with hysteresis (c), two-step ST (d) and incomplete ST (e). The molecular high spin fraction γ_{HS} is plotted in each graph against the temperature T.[34]

In the case of low cooperativity, i.e., spin centres being mostly independent of each other, a gradual SCO process occurs (Figure 7a), causing the spin transition to extend over a wide temperature range. This mainly takes place in solution, which results from a Bolzmann distribution of the vibronic states. The interaction is weak.[34] Strong cooperativity leads to an abrupt transition curve that ranges over only a few Kelvin (Figure 7b). Hydrogen bonds via noncoordinating anions or solvent molecules, π-π interactions via aromatic ligand systems and the linkage of polynuclear SCO compounds enhance the communication of the individual centres. If there is a particularly high degree of cooperative networking, hysteretic behaviour is often observed (Figure 7c). A hysteresis curve represents two different possible states of the system at the same temperature, thus inducing a memory effect. The two-step ST plays an important role in the field of di-nuclear SCO complexes (Figure 7d). The two SCO-active centres can switch independently, resulting in three possible spin states ([LS-LS], [HS-LS] and [LS-LS]).[40,41] There are also examples of two-step spin transitions in mononuclear complexes. However, the situation here is not quite as transparent as in the case of two-nuclear systems. Mostly there is a phase change from one space group to another one. In the Intermediate state, two molecules of the said complex are present in the unit cell of a particular space group, which can then be addressed differently in respect of temperature.[42] Furthermore, it is possible to generate a superposition of two different spin states (LS ↔ HS) of the same molecule in the same unit cell, which is responsible for the two-step SCO.[43] Of course, there are even more examples of multi-step spin crossover, which refer to supramolecular systems such as [2X2]-grid complexes.[44] The hysteretic (c) and the multi-step transition are the most favoured one as they capture potential bistability for the use in molecular switches. If a small amount of residual γ_{HS} is observed even at low temperatures, the γ_{HS} (T) curve does not fully decrease toward zero. This reflects an incomplete spin crossover, which can be caused by lattice defects, misalignments or even impurities in the sample.[34]

2.3. Pressure induced SCO

Contrary to the entropy – controlled thermal spin crossover, pressure as external perturbation will have an influence on the two HS and LS harmonic potential wells relative to each other. The phenomenon is known since the early 1960s.[45] Increasing pressure (mechanical or chemical) destabilizes the HS state, because of its longer bond distances, and thus larger volume. The consequence for the system at equilibrium is the shift of the transition temperature $T_{1/2}$ to higher values, due to a vertical displacement of the potential well to higher energies.[37,46–51] Thus the LS state is favoured and can be understood by the enthalpy change ΔH of the following equation:

$$\Delta H = \Delta E_{el} + \Delta E_{vib} + p\Delta V + V \Delta p \qquad\qquad 9$$

Furthermore, pressure can also have a direct impact on cooperative effects of neighbouring complex molecules in the crystal lattice by increasing intermolecular contacts,[47] or even supress the spin crossover properties by the formation of a stable high pressure phase.[49]

2.3.1. High Pressure generation using a Diamond Anvil Cell

In physics, pressure is the result of a force F operating perpendicularly on a surface A. Very high pressures are therefore generated as the force impacts on a more and more decreasing surface area. To accomplish this task in laboratories the diamond anvil cell (DAC) was developed in the middle of the 20th century and has been continuously refined until today. Due to their hardness, diamonds are particularly suitable for the use as pressure stamps, the so-called culets (50-800 μm). According to the above statement, the smallest culets therefore allow the greatest achievable pressures up to several 100s of GPa.[52–54] The diamonds are also transparent for large parts of the electromagnetic spectrum. This enables diverse in-situ investigations of the material in the sample chamber of the DAC, both with longwave radiation in the infrared range and with very shortwave X-ray radiation.[53,55,56]

The principle of the DAC is shown in Figure 8, whereby the exact geometry of the diamond stamp, as well as the type of holder and its attachment, varies according to the needs of the experiment. Two diamond anvils are arranged opposite each other to generate pressure. Furthermore, there is a metal foil between the two diamond stamps, the gasket. The sample is placed in a hole (diameter: 10-100 μm, thickness 10 μm) in the middle of the gasket. Next to the sample there is placed a crystal as standard for the calibration of pressure, usually ruby (Al_2O_3 doped with Cr^{3+}) and a pressure-transmitting hydrostatic medium (PTM). An explanation regarding the ruby as a calibration standard will be given in section 4.8 later. The pressure medium ensures that the pressure exerted by the diamonds is distributed uniformly on the sample crystal. Depending on the nature of the sample and the desired maximum pressure, a range of different PTMs can be used, including oils, gases and

organic solvents.[55] More information about the pressure cell used in this work will be given in the experimental part.
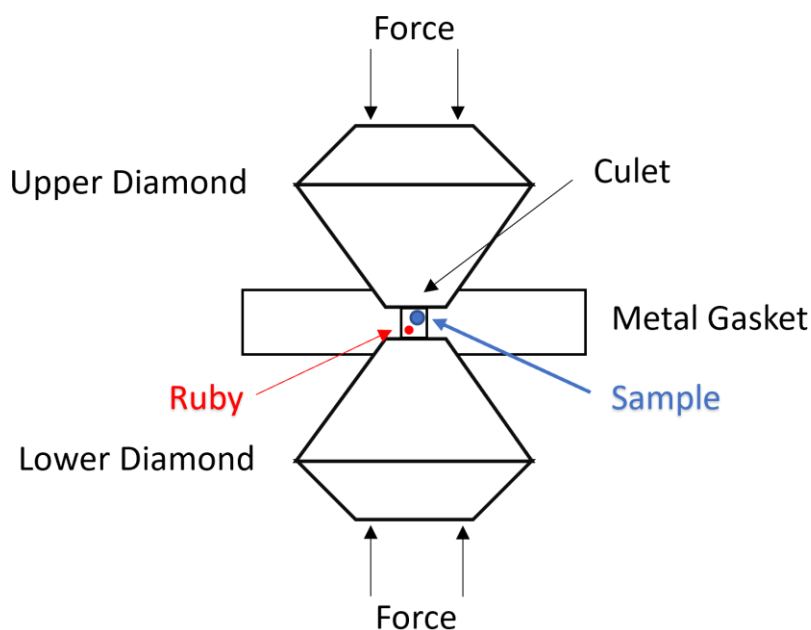
Figure 8: Schematic set up of a Diamon Anvil Cell (DAC).[55]

2.4. Excited Spin State Trapping Effects

Another phenomenon was first observed by *McGarvey* and *Lawthers* in 1982 when they found that electromagnetic radiation can be used in some Fe(II) – and Fe(III)-complex-solutions to switch from LS to HS.[57] Two years later, *Decurtins et al.[58]* followed with the same achievement in solid state and the term **L**ight **I**nduces **E**xcited **S**pin State **T**rapping (**LIESST**) was born.[58–64] Further studies on the mechanism (Figure 9) revealed spin-allowed transitions to the excited $^1T_{1g}$ and $^1T_{2g}$ states or to the metal-to-ligand charge transfer, due to exposition with pulsed green light (λ = 514 nm). Due to a pumping process from the LS state, a metastable state is created by a double intersystem crossing (ISC) via the $^3T_{1g}$ and $^3T_{2g}$ with a subsequent relaxation in the HS* state (Figure 9).[63] With an appropriate irradiation time, the photoexcited HS* state can even be fully populated with long lifetimes at very low temperatures, since the $^5T_2 \leftrightarrow {}^1A_1$ transition is not allowed, because of the selection rules. Thus, the compound becomes trapped in a photoinduced high-spin (PIHS) state. As well, it is possible to pump back the system to the LS state by irradiation into the spin-allowed $^5T_{2g} \longrightarrow {}^5E_g$ absorption band of the HS state (λ = 820 nm, red light), which is named reverse-LIESST.[65]
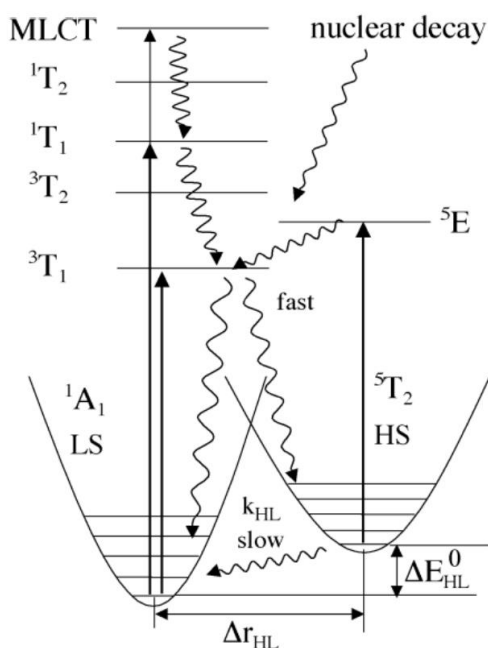
Figure 9: Schematic representation of the electronic structure of Fe-(II) SCO complexes showing the mechanisms of LIESST and reverse-LIESST effects. Adapted from reference [63].

The lifetimes of the PIHS and the relaxation as well as the activation energy of the relaxation process can be defined by analysing the kinetics. A very important characteristic of LIESST compounds is T_{LIESST}, which is the temperature at which thermal relaxation of the metastable HS state occurs.[61,66,67]

$$T_{LIESST} = T_0 + 0.3\ T_{1/2} \qquad\qquad 10$$

The problem of compounds with LIESST properties is the occurrence of this effect at very low temperatures, which is not favourable for future applications. Thus, *Létard et al.* focused the research on the LIESST effect in the year 2006 with the goal to synthesise compounds with LIESST switching properties near room temperature. He and his co-workers screened about 60 compounds with nitrogen-donor ligands and could establish empirically the correlation described by equation 10. Furthermore, the relation between photomagnetic properties and inner coordination sphere was found (Figure 10).
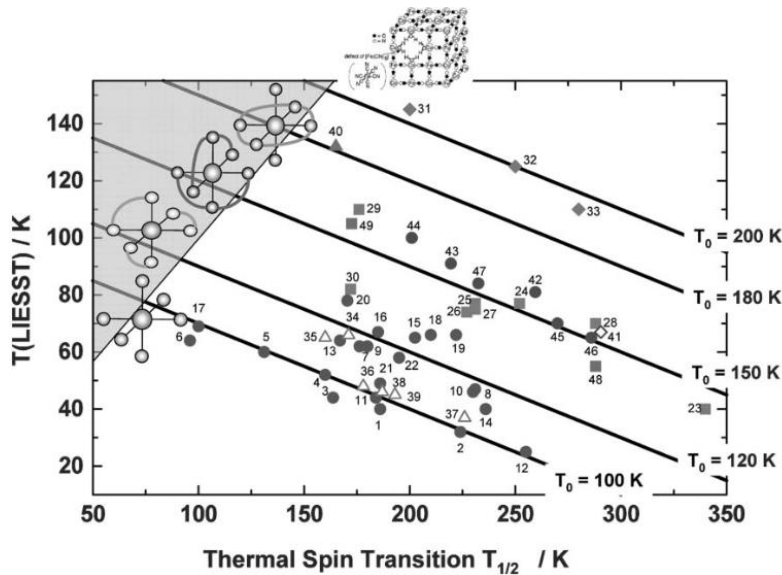
Figure 10: Correlation between T_{LIESST} and $T_{1/2}$ adapted from reference [67]. The grey region represents the impossible overlap of the two values.

An interesting scenario is found when the T_{LIESST} value is close to the $T_{1/2}$ value. In this case, the equation described above (equation 10) gives physically invalid values because the HS phase is trapped and the kinetically slow thermal HS $\longrightarrow$ LS transition is not complete. Thus, the fraction of the HS state shifts upwards (Figure 11). In summary, when T_{LIESST} and $T_{1/2}$ move towards each other, the relaxation of the excited metastable HS state is simultaneously suppressed, increasing the residual HS fraction.[68,69]
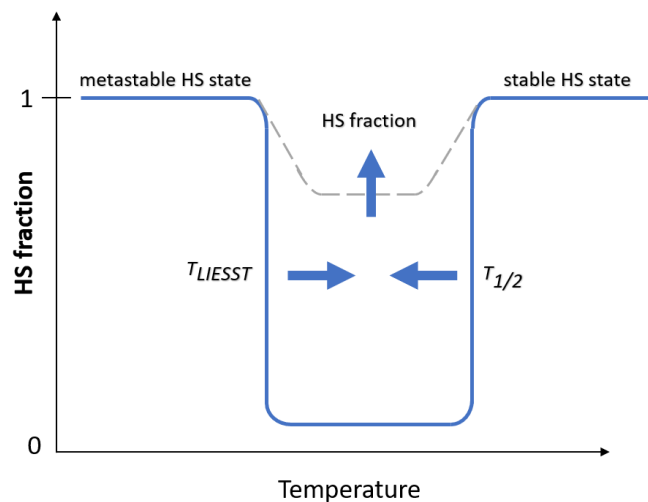
Figure 11: Schematic representation of the impact on HS fractions as a function of temperature when $T_{1/2}$ and T_{LIESST} values converge, resulting in gradually increased iron-(II) HS fractions at low temperatures. [69]

If the initial spin state at low temperatures is a mixed spin state, it is possible to obtain a bidirectional LIESST effect, with population of fully LS or HS states using different irradiation wavelengths, giving tri-stability to the system (Figure 12a). 2020, *Tong et al.* observed an additional annealing process of the magnetic susceptibility around liquid nitrogen temperature*,* after LIESST experiments and fast thermal quenching of the magnetic moment. These properties were found in a 2D Hofmann-type

polymer ([Fe(isoq)$_2$[Au(CN)$_2$]$_2$], isoq = isoquinoline) and lead to a set of novel two-step relaxation pathways named **L**ight (LASSA) – and **T**emperature (TASSA) **A**ssisted **S**pin **S**tate **A**nnealing (Figure 12).[70] These new paths expose hidden phases that remain undetected under normal conditions.
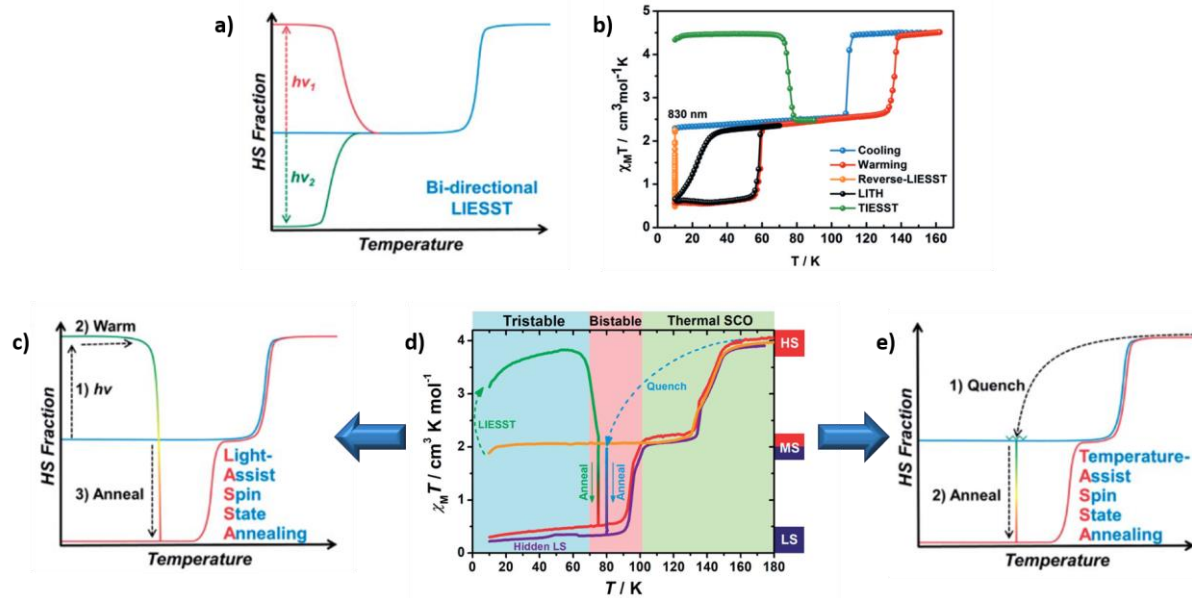
*Figure 12: Schematic representation of **a)** a bi-directional LIESST system and **b)** a multi stable Iron (III) system designed by Harding et al., showing Light Induced Thermal Hysteresis (LITH) and also Thermal Induced Excited Spin State Trapping Effect (TIESST); **c)**, and **e)** showing a schematic representation of a Light-Assisted Spin State Annealing (LASSA) and Temperature-Assisted Spin State Annealing (TASSA) phenomenon, whereas **d)** shows the original $\chi_m T$ – plot of Tong et al.[70,71]*

When speaking of multi stability and hidden phases, it is also necessary to mention the **L**ight **I**nduced **T**hermal **H**ysteresis (LITH), which was discovered and named by *Kahn* and co-workers in 1998, during the research on the spin crossover compound Fe(PM-BiA)$_2$(NCS)$_2$ (with PM-BiA = *N*-(2-pyridylmethylene)aminobiphenyl).[72] Another example of LITH and the exposure of multi stable SCO compounds is [Fe(trz-py)2{Pt(CN)4}]·3H2O (trz-py = with -(2-pyridyl)-1,2,4,4H-triazol) and was shown by *Triki et al.* in 2016.[73] LIESST (irradiation with green light at 510 *nm*) and reversed-LIESST (irradiation with red light at 830 *nm*) experiments each revealed two distinct hidden hysteresis cycles with different widths and transition temperatures, starting from a mixed spin state. The hybrid state, consisting of a 50% mixture of HS and LS state, is formed by [FePt(CN)$_4$] layers separated by meshing trz-py ligands with two non-equivalent Fe-(II) sites. This leads to a 2D network built by Fe$_4$ squares with diagonals consisting of Fe1-Pt-Fe2 bridges.

A different way to generate a metastable HS state and make use of the switching between the two states of Fe (II) is by thermal quenching (fast cooling of the sample from room temperature). This is known as **T**hermally **E**xcited **S**pin **S**tate **T**rapping (TIESST) effect and is found in systems exhibit high cooperaitivity.[68,71,74–76] Thermal relaxation to the low-spin ground state from the metastable TIESST HS state is hindered below a compound-specific temperature, which is called T_{TIESST}. These metastable HS phases at low temperatures enable additional magnetically addressable states. On the one hand, there

are examples in which the structure of the metastable phase is the same, no matter how it was obtained (by thermal quenching or light irradiation). 2012, *Létard et al.* gave an example in which the metastable HS states was generated, and compared, either by LIESST effect or by thermal quenching by studying the complex cis-[Fe(picen)(NCS)$_2$] (with picen=N,N'-bis(2-pyridylmethyl)1,2-ethanediamine).[77] The mentioned complex showed similar relaxation behaviour of the metastable state, regardless of whether it was generated after excitation by light or quenching at low temperatures. On the other hand, there are systems with different relaxation processes.[78–80] *Aromi et al.* measured the relaxation kinetics of both the photoinduced and the thermally quenched HS states of the SCO compound [Fe(H$_4$L)$_2$](ClO$_4$)$_2$·H$_2$O·2(CH$_3$)$_2$CO (with H$_4$L = 2,6-bis[5-(2-hydroxyphenyl)pyrazol-3-yl]pyridine), and they were found to differ significantly.[80] The metastable HS state produced by thermal quenching shows disorder in all acetone molecules and in half of the perchlorate anions, while the LS state shows no disorder. In conclusion, the thermal spin transition from the metastable HS to the LS state is bound to a disorder/order mechanism. Contrary, the PIHS crystal structure does not show any disorder with respect to the perchlorate anions, while the disorder of the acetone molecules is reduced (Figure 13). It was proposed, within the TIESST relaxation the phase undergoes an order/disorder transition first before the iron centre relaxes from HS to LS state. Whereas, in the LIESST relaxation, the iron centres would relax directly from the HS to the LS state. This was confirmed by kinetic measurements, this being the first example where crystallographic data was consulted to predict such relaxation mechanisms.[80]
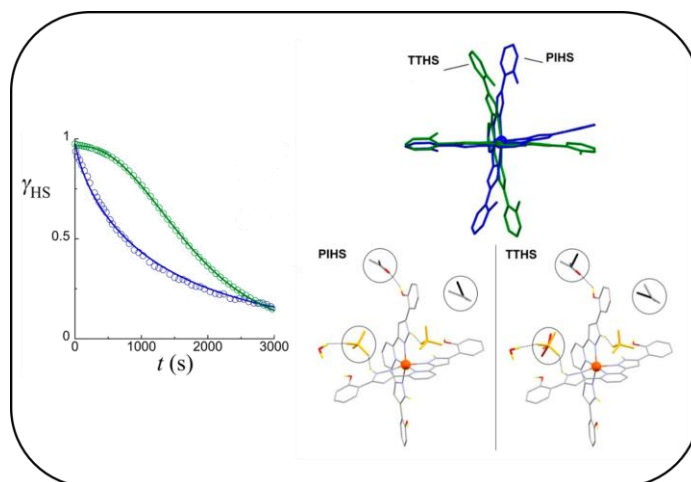
Figure 13: Representation of the two different relaxation processes of the PHIS (blue curve) and TTHS (green curve) at 90 K. Additionally, the asymmetric unit of the photoinduced HS state and the thermally quenched HS state of [Fe(H$_4$L)$_2$](ClO$_4$)$_2$·H$_2$O·2(CH$_3$)$_2$CO (with H$_4$L = 2,6-bis[5-(2-hydroxyphenyl)pyrazol-3-yl]pyridine) is shown, emphasizing the different disorder of perchlorate anions and acetone solvent molecule. Colour code: C-atoms are shown in grey/black, O-atoms in red, perchlorate anions in orange, N-atoms in blue, H-atoms in yellow and Fe-ions in dark orange. The structural distortions of the respective structures of the differently generated metastable states are shown in green and blue, respectively.[80]

Spin state trapping due to thermal quenching is not limited to Iron-(II) systems, which *Harding et al.* showed in the year 2019. He and his co-workers designed the new Fe-(III) spin crossover compound [Fe-(naphBzen)$_2$]I (with HnaphBzen = (1-{[2-(benzylamino)ethylimi-no]methyl}-2-naphthol)) with properties, never observed in SCO-molecules with iron in the oxidation state of three. Besides a hidden hysteresis, revealed by reverse-LIESST effect, which has never been observed in an iron-(III) system,

the TIESST effect, a rare phenomenon for Fe-(III), is also observed. With a T_{TIESST} value of 75 K it is the highest value observed for iron-(III) compounds (Figure 12b).[71]

2.5.   Characterization of SCO complexes

For the detection of spin transition curves, there are many different techniques like for example magnetic susceptibility measurements, Mössbauer spectroscopy, X-ray diffraction, optical and Raman/FT-IR-spectroscopy or heat capacity measurements.[1,81,82] The most common used method is the detection of the magnetic susceptibility as a function of the temperature χ(T). Solid samples of spin crossover compounds can be analysed with a **S**uperconducting **Qu**antum **I**nterference **D**evice (**SQUID**), which has a strong sensitivity to a change in magnetic susceptibility. The SQUID magnetometer is based on a superconducting loop with Josephson junctions, which allows the detection of very small magnetic fields, starting from very small amounts of crystalline samples or powders in milligram scale. Additionally, the advantage of the SQUID-magnetometry is the possibility to measure under inert gas atmosphere due to special sample holders or to measure the magnetic moment depending on external stimuli like pressure or light irradiation for the investigation of LIESST and reverse-LIESST effects.[1,65,67,81,83,84] The change of magnetic susceptibility results from the difference in number of unpaired electrons while switching between different electronic states. In the case of iron-(II)- d^6-ion, there is a spin transition from a $^5T_2$ (HS) to a $^1A_1$ (LS)-ground state and vice versa, which also results in a change of magnetic properties. In the HS situation, a paramagnetic compound (S = 2) is present, whereas the LS state can be assigned to a diamagnetic species (S = 0). If now experimentally obtained data should be compared with theoretical values, the effective magnetic moments μ_{eff} of the respective spin state can be calculated by using the pure spin formalism (equation 11) with the Landé factor g ≈ 2, the total spin S and the Bohr magneton μ_B.[25,85]

$$\mu_{Spin-only} = g_s \sqrt{S(S+2)}\, \mu_B = 2\sqrt{S(S+2)}\, \mu_B \qquad\qquad 11$$

μ_{eff} is in fact related to the χT product (equation 12), with the Avogrado number N_A, the Bohr magneton μ_B and the Bolzmann constant k_B.[25]

$$\mu_{eff} = \sqrt{\frac{3k_B}{N_A \mu_B{}^2}}\, \sqrt{X_m T} \qquad\qquad 12$$

The actual measured values are usually larger for iron-(II) HS, since further quantum mechanical effects come into play, which are not considered in the spin only formalism.[25,29]

As mentioned earlier, changes in complex volume, bond distances, or distortion parameters can be observed during a spin transition due to the redistribution of electrons between bonding and

anti-bonding 3d orbitals. By using **Single crystal X-ray diffraction** to visualise the spin transition and measuring the crystal structure before and after the SCO transition temperature $T_{1/2}$, the structures can be corelated and potential crystallographic phase changes can be detected. The electronic transition also affects the coordination geometry of an octahedral environment. The octahedral distortion parameter $\sum$ (sum of the deviation from 90° of the 12 cis-N-Fe-N angles in the FeN$_6$ coordination sphere) is given by:[86]

$$\sum = \sum_{i=1}^{12} |90°\text{-}\alpha_i|$$

3

Thus, the perfect octahedron has a distortion parameter of $\sum = 0$. *Hendrickson et al.* introduced this parameter in 1982 for the first time,[87] before *Guionneau et al.* assigned specific values to the parameter for the LS – and HS – state.[88] LS – compounds therefore usually have a distortion of less than 80°, whereas compounds in HS – state have a distortion parameter of more than 100°, due to the geometrical change associated with the spin transition.

Another way to investigate a SCO is the **Evans method**. This allows the SCO to be observed and recorded not in the solid state, but in solution.[89–95] Due to the neglectable cooperativity in solution the Evans method enables to provide information about the electronic structure of the ligand and its influence on the SCO properties. Samples are measured in special double walled NMR tubes and deuterated solvents. The blank solvent is placed in the outer tube, whereas the dissolved sample is within the inner tube. The NMR signals corresponding to the deuterated solvent in the outer tube are shifted by $\Delta\nu$ with respect to those of the sample in the inner tube as a result of the additional magnetic field of the paramagnetic substance. χ_g, the magnetic mass susceptibility is given by equation 14, with ν for the spectrometer frequency, the mass of the paramagnetic compound m, as well as the density $\rho_{solvent}$ of the deuterated solvent and ρ_{sample}, the density of the sample solution. For dilute solutions:

4

$$X_g = \frac{3\Delta\nu}{4\pi\nu m} + X_0 + \frac{X_0(\rho_{solvent} - \rho_{sample})}{m}$$

Another very powerful technique for the investigation of iron-(II) SCO compounds in solid state is the **^{57}Fe-Mössbauer** spectroscopy. While working on his Ph.D. thesis in 1958, Rudolf Ludwig Mössbauer discovered the *recoilless nuclear magnetic resonance fluorescence of gamma radiation* of ^{191}Ir.[96–98] Of the 44 elements of the periodic table on which the Mössbauer effect can be observed, iron is ideal for studying the oxidation state, bonding properties and molecular symmetry. This is possible due to the long lifetime of the excited state and an energy of 14.4 keV of the emitted γ-quantum.[98,99] In the

Mössbauer spectroscopy on iron compounds, $^{57}_{27}$Co is used as γ-ray emitting radioactive nuclide (Figure 14).
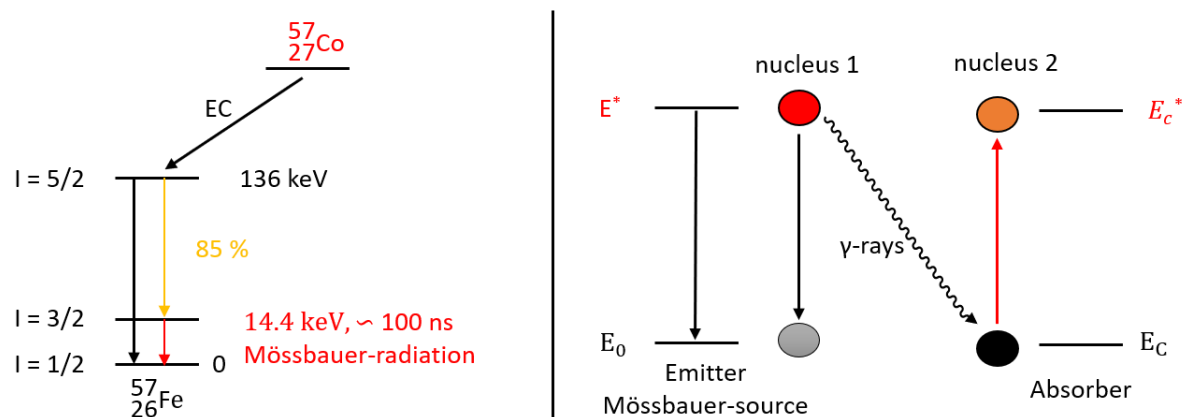

Figure 14: Schematic representation of the decay of ^{57}Co (left) and the schematic representation of the general Mössbauer-effect.[99]

This nuclide decays after an electron caption (EC) reaction from the K-shell into an excited *I* = 5⁄2 state of the $^{57}_{26}$Fe-nucleus. After the decay in the *I* = 5⁄2-excited state of iron the *I* = 3⁄2– level is populated with about 85 %, which has a relatively long lifetime of 100 ns. The energy difference of the *I* = 3⁄2 level and the *I* = 1⁄2 ground state of an Iron nuclide is 14.4 keV. The Mössbauer effect describes how, during the relaxation of the nuclide (emitter) from the *I* = 3⁄2 to the *I* = 1⁄2 state, energy is transferred to an identical nucleus (absorber) in the form of γ-rays in a recoilless manner, so that the Mössbauer absorber is put in the excited state. If the energy transfer would not take place recoiless, it would be impossible to excite the absorbing nucleus because the excitation energy would be insufficient. This is why the Mössbauer effect is just observable in solid state or in frozen solutions, where the recoil is neglectable due to fixed atom positions.[98] In order to extract information from a Mössbauer spectrum, three values are particularly important: The isomer shift δ, the quadrupole splitting ΔE_Q and the magnetic splitting ΔE_M. If the compound to be investigated has no internal magnetic field, an external magnetic field must be applied to record the magnetic splitting ΔE_M. For all compounds synthesised and measured with Mössbauer spectroscopy in the present work, all necessary information is obtained from the isomeric shift and the quadrupole splitting. Comparing the electronic environment of the emitter (the ^{57}Fe nuclide) and the absorber (a spin crossover compound) reveals that the transition metal complex differs in electron density near the atom core and in the valence shell, respectively, due to the coordination of the ligands. This difference is shown by the isomeric shift δ, which is essentially influenced by the electron density in the 4s orbital, since these have a certain probability to be present at the nucleus. In addition to the electron density in this orbital (direct effect), the electron density in the p-, d- and f-orbitals can also influence the isomeric shift δ. The more the electron density in these orbitals is reduced, for example by π-bonding, the weaker the shielding to the atom core and the s-electrons are more strongly attracted (indirect influence). Thus, the isomeric shift δ provides information about the oxidation state, the bonding characteristics and the electronegativity of the ligands.[98–100] When the electric field at the nucleus is inhomogeneous due to a non-cubic valence electron distribution and/or a non-cubic lattice environment, the electric quadrupole interaction

initiates the splitting of the degenerated $I = 3/2$ level into two sublevels with magnetic spin quantum numbers $m_I = \pm 3/2$ and $\pm \frac{1}{2}$.[101] This splitting is effected by the quadrupole moment Q, the nuclear spin I, the magnetic spin quantum number m_I and the electric field gradient (EFG). These factors result in the quadrupole splitting ΔE_Q and thus provide information about the molecular symmetry, the oxidation state and the bonding properties. [98–101] Typical values for Fe^{II} in the HS state measured by Mössbauer spectroscopy show a large quadrupole splitting of $\Delta E_Q^{HS} \approx$ 2-3 mms^{-1} and an isomer shift of $\delta^{HS} \approx$ 1 mms^{-1}, whereas those values are smaller for the LS state with $\Delta E_Q^{HS} \leq 1$ mms^{-1} and $\delta^{LS} \leq 0.5$ mms^{-1}. If both spin states are found to be present at a given temperature and the time scale of the relaxation from HS to LS is slower than the Mössbauer time scale (10^{-7} s for ^{57}Fe), it is possible to separate the two partial subspectra, although they overlap strongly. Additionally, the area fractions of the resonance lines are directly related to the concentration of the respective spin state and can be adjusted with the Lorentz fit.[1,27,81,98–101] Besides the investigation of the spin crossover phenomenon, Mössbauer spectroscopy has also been used to solve problems in archeology,[102] space research[103–105] and bioinorganic chemistry.[106–109]

The spin transition of an iron-(II) SCO complex is often observed with a colour change and is called thermochromism. The colour of the complexes originates from their d-d transitions. Usually, LS complexes have an intensive colour, whereas HS complexes are characterised by their colourlessness. Thus, the switch of magnetic states can be visualised by their optical properties, hence **UV/VIS-spectroscopy** as a favourable method is used. In order to understand the colour change, the Tanabe-Sugano diagram (Figure 5) must again be consulted. The d-d transition in the HS state ($^5T_{2g} \longrightarrow {}^5E_g$) is observed in the near infrared region at about 800-900 nm, wherein the allowed LS transitions appear in the visible region at about 500-700 nm ($^1A_{1g} \longrightarrow {}^1T_{1g}$)and 300-400 nm ($^1A_{1g} \longrightarrow {}^1T_{2g}$). The higher ligand field strength defining the molecule in the LS instead of HS state, results in a higher requirement of excitation energy (shift in the visible region) and therefore to a coloring of the compound. Consequently, when a SCO sample is cooled, the band for the HS state decreases, while the two bands for the LS state increase steadily. In this manner, the spin change from HS to LS can be tracked and its electronic nature monitored. [25,27–29,33,37]

The thermal spin transition can also be seen as a first order phase transition. This phase change occurs throughout the entire solid state via cooperative effects.[1,37,39] Due to the change in entropy ΔS and enthalpy ΔH the spin switch can be followed by **differential scanning calorimetry** (DSC) while obtaining the heat capacity C_p. This gives information about the compound specific transition temperature $T_{1/2}$ because C_p is given as a peak at this temperature. Differential scanning calorimetry also provides information about the shape of the spin transition itself and the cooperativity in between the solid state. A sharp signal for high cooperative systems with an abrupt spin transition and a broad signal for gradual spin transitions owning low cooperativity. Moreover, by integrating the peak area of the signals in the C_p vs T diagram, the values for the changes in enthalpy Δ and entropy ΔS can be calculated, since the Gibbs free energy equals zero at $T_{1/2}$.[33,81,110–116]

Another possible characterization method is the **infrared spectroscopy** (IR). The difference in the occupation of the anti-bonding e_g^*-and bonding t_{2g}-orbitals has a great influence on the vibrational mode of the metal to ligand bond lengths. In the example of the LS state, a shift towards higher frequencies can be observed due to the strengthened and shortened bonds and thus the higher bond order compared to the HS state. The stretching vibration of the M-L bond of an Fe^{II}-N_6-complex is in the far infrared region (FIR) of about 250 cm^{-1} to 500 cm^{-1}.[117] Even if these are very characteristic

vibration bands, it is sometimes difficult to classify them accurately, as there are also many additional vibrations of different chemical origin in the so-called "finger print" area. In order to observe a thermal spin change and to circumvent these difficulties, it is particularly favourable to take a look at the vibrational modes of directly coordinating anions. A good example are ligands containing a C-N motif like pseudohalide anions. This can be used as marker in the temperature dependent spin switch of SCO complexes. 2015, *Brooker et al.* monitored the spin state of an iron-(II) complex by the use of Raman spectroscopy tracking the CN-stretch of the thiocyanate ion as in between 100 K and 300 K (Figure 15).
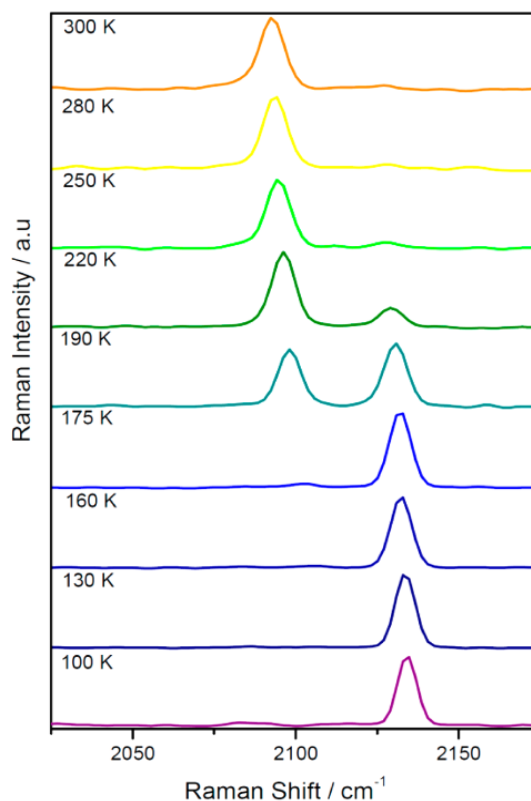

Figure 15: Raman spectra of [Fe(padpt)$_2$(SCN)$_2$] (with padpt = N-4H-1,2,4-triazole-3,5-di(2-pyridyl) palmitamide) in the temperature range of 100 K and 300 K, measured by Brooker et al.[113]

The shift of the Raman signals of the different C-N stretches of two *trans*-coordinated thiocyanate anions at different temperatures changes significantly during the spin transition, with $T_{1/2}$ = 182 K.[1,113,118]

The mentioned techniques are the most common used ones for the detection and monitoring of the spin switch in SCO compounds and especially in complexes containing Fe^{II} as the magnetic active metal centre. Of course, there are other investigation methods which are not understood as standard measurement methods, but which can be of great help and interest in certain cases of structural or electronic identification. These methods are not explained in detail but should be mentioned and appear as follows: **X**-ray **A**bsorption **S**pectroscopy (**XAS**; EXAFS; NEXAFS),[119–123] **E**lectron **P**aramagnetic **R**esonance spectroscopy (**EPR**),[124–126] **N**uclear **R**esonance **S**cattering (**NRS**),[127–129] **P**ositron **A**nnihilation **S**pectroscopy (**PAS**),[130,131] **Muon S**pin **R**elaxation (**μSR**).[132–134]

2.6. Impacts on the SCO behaviour

Ligand design

The ligand field strength Δ_O plays an essential role for the realisation of the different SCO behaviours already described in section 2.2 and 2.3. As mentioned before, each metal ion in a certain oxidation state has an individual natural splitting of the d-orbitals, therefore there are only a few suitable ligands with the right donor strength close to the critical ligand field Δ_c (crossing point of the HS and LS potentials) to show spin switching properties. Although the research in SCO has been around now for several decades, there is still no proper way to predicting the exact ligand field and thus, Δ_O often has to be adjusted, as spin switching behaviour is influenced by more effects than just the type of the donor atoms.[1,27,37,81,135] Therefore, the design of a wide spectrum of ligands with different donor sets is of special interest. The most common and investigated environment for Fe^{II}-ions as magnetic active spin crossover system is the one with six coordinated nitrogen donor atoms in octahedral surrounding, followed by N_4O_2 donor set usually represented by Schiff-Base ligands.[136–141] There are even iron(II) compounds with spin switching properties achieved with a N_4C_2 coordinating sphere.[142]

Strong-field ligands from the end of the spectrochemical series are able to provide a large splitting of the bonding t_{2g}-and anti-bonding e_g^*-orbitals, whereas the LS state of an Fe^{II} centred complex is stabilised by increasing Δ_O due to the combination of its t_{2g}-orbitals and ligand centred acceptor states with π^* symmetry.[143,144] Most recently, this concept has come into sharper focus as the molecular factors of the ligand itself of SCO complexes are not yet fully understood. This led to the relationship between ligand structure and properties of different complexes within several ligand families.[143–145] *Halcrow* and *Deeth* put a lot of effort and work in the screening of the connection of the different impacts of ligand centred electron withdrawing-and electron donating substituents and the magnetic properties of the complex series of $[Fe(bpp^{X,Y})_2]^{2+}$(with bpp=2,6-di{pyrazol-1-yl}pyridine).[146–148] This study revealed contrary effects on SCO thermodynamics by substitution at either the central pyridyl (X)-or the terminal pyrazolyl (Y)-moiety of the ligand (Figure 16).
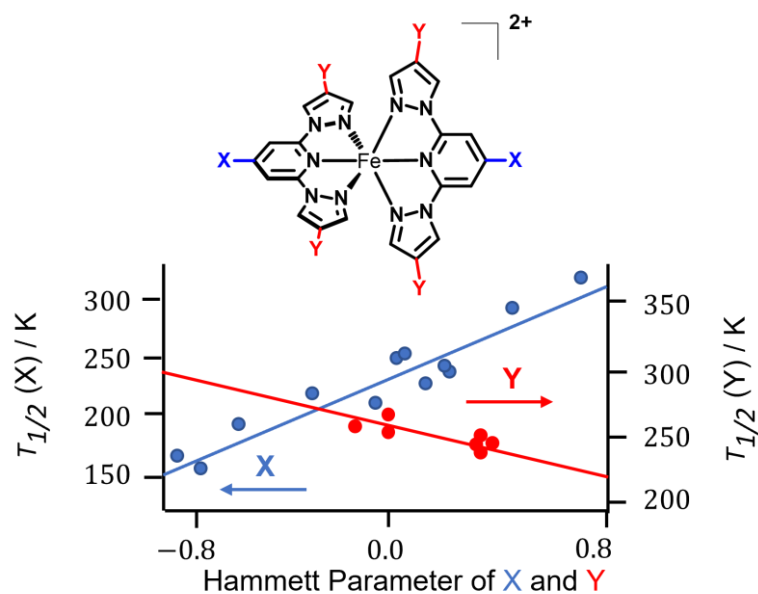
Figure 16: Plot of different values of $T_{1/2}$, according to the Hammett parameters of the different substituents at different positions in the ring moieties of the 2,6-di {pyrazol-1-yl} pyridine derivative.[146]

By correlating the transition temperature $T_{1/2}$ of 25 different SCO compounds and their corresponding Hammett parameters, which results from mesomeric and inductive effects of the respective ligand substituent.[149] The investigations were carried out on complex solutions using the Evans NMR method and revealed a strong dependency of the Fe-L σ- and π-bonding effects and the spin transition temperature. Accordingly, in solution the spin state only depends on the electronic structure of the ligand itself. Electron withdrawing groups reduce Δ_O by lowering the energy of the bpp ion pair through inductive effects and thus stabilise the HS state. However, electron withdrawing groups also decrease the energy of the π*-orbitals. This in turn leads to an increase of the ligand field Δ_O by strengthening the metal to ligand π-backbonding. In summary, since the substituents at the pyridine ring have electron-withdrawing properties and those at the pyrazole moiety have electron-donating ones, the LS state is stabilised and favoured.[146]

Besides electronic changes in the ligand itself, there are many other smart ways to fine tune the ligand field strength Δ_O, like for example the use of different coordinating co-ligands with different ligand field splitting properties. Coordinating pseudohalide anions provide a nice way to increase the ligand field strength by ascending order of $NCO^- < NCS^- < NCSe^- < N(CN)_2^- < NCBH_3^-$ towards the spin crossover region and Δ_c and vice versa. There are many examples in which the above-mentioned series of pseudohalides is used and a clear shift of the transition temperature in ascending order to higher values can be observed.[39,43,150–155]

There are by far more possible ways to influence the spin transition properties, due to ligand design like the difference between six-or five-membered heteroatomic rings and their variety of donor atoms,[95,156–158] the replacement of aromatic by aliphatic donating moieties or the difference in the chelating properties of the ligand.[1,3,32,86] Nevertheless, a careful handling is necessary, because the change of the ligand and its electronic structure is not the only crucial factor for the spin transition

properties of SCO complexes. Cooperative interactions in the solid state have a big influence on the magnetic behaviour of SCO complexes and are not predictable or controllable in most of the cases.

Cooperativity

The term cooperativity describes the degree of the crosslinking of the SCO-active metal centres within a crystal lattice and how the information of an electronic or structural change triggered by the spin change is carried on through the lattice.[3,81,159] A spin transition can be expressed as a first order phase transition, which propagates through the solid state. This was shown by *Sorai* and *Seki* with the use of DSC experiments.[39] Cooperative interactions can not only have an influence on directly neighbouring molecules, but may also be expressed in long-range interactions that are propagated through the crystal lattice. These interactions are classified as elastic interactions and can be of ferroelastic or antiferroelastic nature. The former scenario promotes the population of the same electronic spin state, while the latter case is responsible for alternating HS/LS states. The elastic frustration resulting from the existence of both types of interactions can lead to the phenomenon of symmetry breaking in the materials.[160,161] Enhanced cooperativity also increases the internal pressure in the crystal itself, which builds up and grows with each further spin change and thus affects each further non-switched SCO molecule to a greater extent.[162] This can be explained by a simple mechanoelastic model in which the spin carrying atoms are expressed as round spheres and the intermolecular cooperative interactions are expressed by a spring.[163]
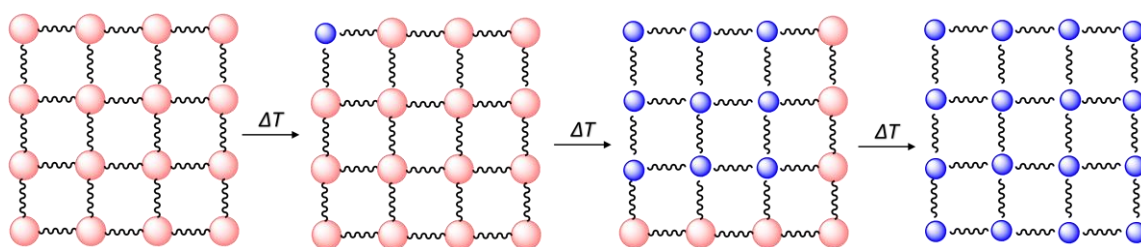

Figure 17: Evolution of a thermally induced spin transition in a macroscopic material, where the red spheres represent the metal centres in the HS state, the blue spheres the metal centres in the LS state and the springs the cooperative interactions between neighbouring SCO complexes within the crystal lattice. Due to a change in temperature the propagation of the ST starts in the top left corner and proceeds until the system is finally in the LS state (left to right).

Furthermore, as mentioned in section 2.2. the type or occurrence of a spin transition is strongly dependent on the degree of cooperativity within the system. Weak cooperativity leads to a gradual spin transition, whereas strong effects manifest themselves in an abrupt SCO or hysteretic behaviour.[33,81,159,162] This degree of networking can be enhanced by a wide variety of intermolecular interactions such as classical and non-classical hydrogen bonds directly between the complex molecules, as well as non-coordinating solvent molecules or non-coordinating counterions. Additionally, van der Waal's contacts, π-π-stacking of aromatic groups in the molecule backbone or direct linkage between the spin carrying centres have a major influence on the SCO properties.[33,41,113,164–169] There are even examples of ion-pair π and halogen bonding interactions.[170]

2015, *Tong et al.* presented a nice example for the tuning of cooperative effects in spin crossover Hoffman-like metal-organic framework by aromatic guests.[167] Due to the high porosity of the Iron(II) spin crossover system Fe(dpb){Au(CN)$_2$}$_2$]·nSolv (with dpb = 1,4-di(pyridin-4-yl)benzene and nSolv = 1.5DMF·0.3EtOH·0.2C$_6$H$_{12}$), solvent molecules of different sizes, properties and electronic structure can be incorporated into the existing cavities (Figure 18).
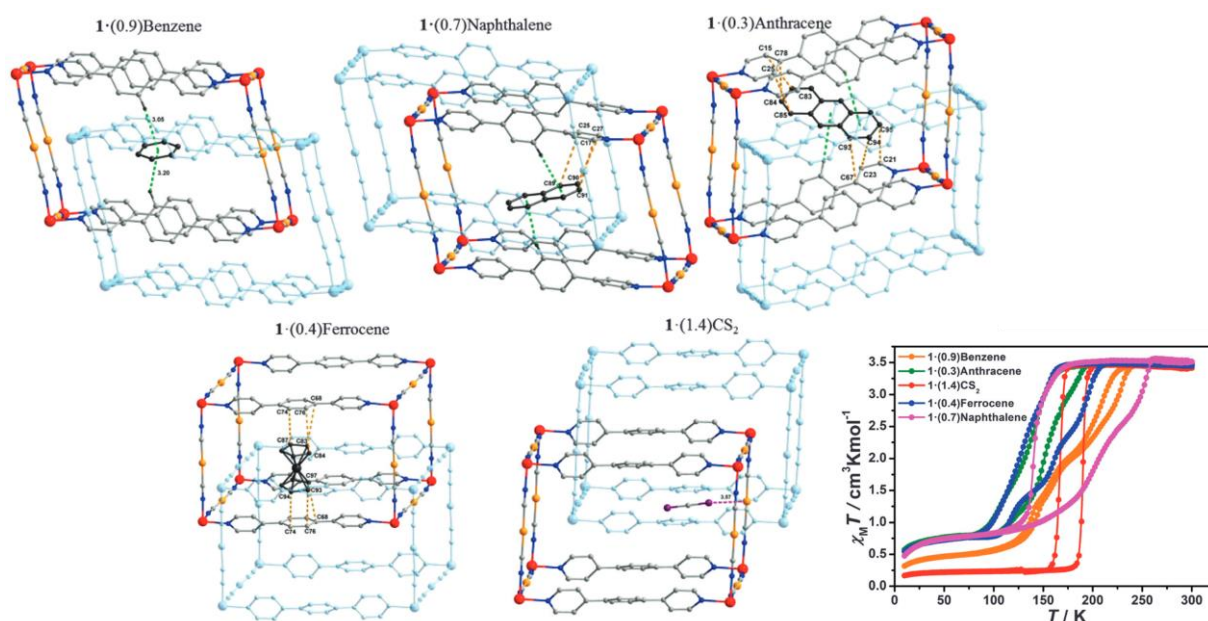

*Figure 18: 3D network of Fe(dpb){Au(CN)$_2$}$_2$]·nSolv (with dpb = 1,4-di(pyridin-4-yl)benzene and nSolv = 1.5DMF·0.3EtOH·0.2C$_6$H$_{12}$) with different solvent guest (benzene, naphthalene, anthracene, ferrocene and CS$_2$) molecules, showing different host guest interaction properties. Colour code: Dot lines: green, C–H···π distance; yellow, C···C distance; magenta, and Au···S distance. **Bottom right:** Temperature dependence of the χ$_m$T curves showing the different influences on the magnetic SCO properties provoked by the different host-guest interactions. The figure was taken from the literature.[167]*

The different host guest interactions (π-π-stacking of aromatic groups and C-S interaction) between the metal-organic framework and the incorporated solvent molecules show great impact on the magnetic spin crossover behaviour. The widths of the observed hysteresis loops are drastically influenced by the different interactions. The largest hysteresis width of 73 K is reached with naphthalene as guest in the cavity, whereas the most abrupt spin transition is observed incorporating CS$_2$ into the porose system. The intermolecular interactions between guest and host can be considered as "chemical pressure" and can strengthen the cooperativity responsible for the differences in the thermal hysteresis properties of the various systems.[167]

Another example for the influence of cooperative effects was recently given by Tuczek et al. in 2020. He and his group revealed different magnetic behaviour for two different polymorphic modifications of the new SCO complex [Fe{H$_2$B(pz)(pypz)}$_2$] (pz = pyrazole, pypz = pyridylpyrazole). One of the two polymorphic phases (phase I) forms dimers due to strong coupling of intermolecular π-π-interactions between neighbouring complex molecules, whereas π-π-interactions are not observed for the second polymorph (phase II). This leads to a stabilisation of the LS state for the polymorph with strong cooperativity via π-π-coupling and thus a shift of the transition temperature T$_{1/2}$ = 300 K. If these

interactions are disabled $T_{1/2}$ is shifted by 130 K towards lower temperatures. Furthermore, the highly cooperative phase II turns out to be metastable, which is transformed into the thermodynamically stable phase I by temperature.[169]
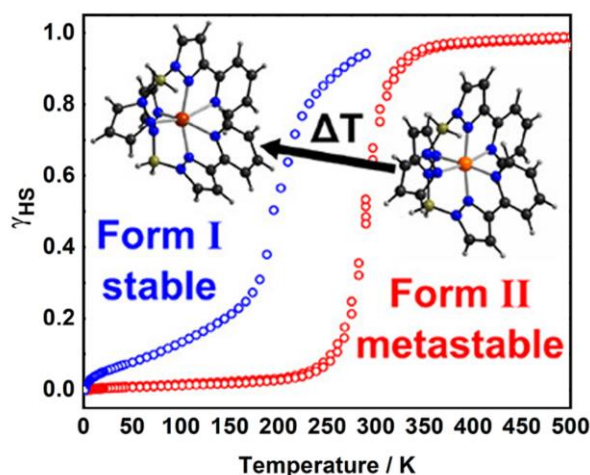

Figure 19: Different magnetic data of the two different moplymorphic phases of [Fe{H$_2$B(pz)(pypz)}$_2$] (pz = pyrazole, pypz = pyridylpyrazole). A shift of $T_{1/2}$ can be seen in relation to the presence of π-π -WW and the possible transition from phase II to phase I by temperature. The picture is reproduced from the literature.[169]

A common way to investigate the dependency of a certain SCO system is by studying the magnetic properties under the conditions of suppressed intermolecular interactions. This is the case in systems diluted or doped with other transition metals like Zn^{II}, Ni^{II}, Mn^{II} or Co^{II}. Those are either not magnetic active or at least do not own any SCO-activity with the chosen ligand system. Recalling the mechanoelastic model from Figure 17 in order to understand this, the intermolecular interactions do not disappear completely, but rather the propagation of the spin change is attenuated or buffered, since the doping metals are not subjected to any geometric and structural change due to the spin transition. Accordingly, these metal centres cannot be influenced by spin switching centres and in turn do not influence any other spin carrying centres, which results in a reduction of cooperativity. However, a main condition for this investigation method is an isostructurality of the magnetically active and the inactive species. 2012, Létard et al. reported an example for the dilution of the dehydrated [Fe$_x$Mn$_{1-x}$(bpp)$_2$](BF$_4$)$_2$ with bpp = 2,6-bis(pyrazol-3-yl-pyridine).[68] The dilution with Mn^{II} seems ideal for the decrease of the thermal spin crossover temperature because of the larger ion volume in its HS state compared to Fe^{II} with the ultimate goal of creating the situation of the overlap between the high temperature stable phase and the low temperature metastable phase. The overlap was successful below a value for the dilution of x=0.96. The $\chi_M T$ products of the diluted complexes were found to increase at low and high temperatures because of the paramagnetic contribution of the Mn^{II}-ions (d^5, S=5/2). To compare all measured data with the pure iron complex, an adjustment must be made by equations 15 and 16. The value of $(\chi_M T)_{Fe}$ is always reported to 1 mol of [Fe] entities.

$$X_M T = x \cdot (\chi T)_{Fe} + (1-x) \cdot (\chi T)_{Mn} \qquad\qquad 15$$

$$\chi_{Fe}T = \frac{\chi_M T - (1-x)\chi_{Mn}T}{x}$$

16

For the situation of increasing metal dilution $(\chi_M T)_{Fe}$ plotted against the temperature shows a conservation of the HS state and an increase of the residual paramagnetic fraction at low temperature, as well as a shift of $T_{1/2}$ to lower temperatures and a spin transition in a more gradual way. This trend of the magnetic curves is consistent with the general observations of diluted metal systems especially with those of the diluted $[Fe_xM_{1-x}(Phen)_2(NCS)_2]$ (with M = Ni^{II}, Zn^{II} and Co^{II}) SCO complex.[171–175] The only difference for this example is the preservation of the thermal hysteresis loop due to the low concentration of Mn^{II} in the compound, which does not suppress the cooperative interactions in a sufficient degree.[68]
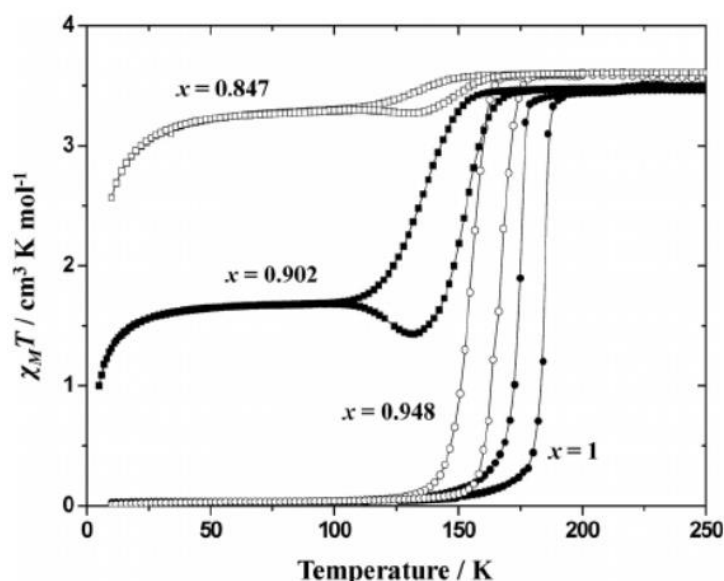
Figure 20: Thermal dependency of the $(\chi_M T)_{Fe}$ product of $[Fe_xMn_{1-x}(bpp)_2](BF_4)_2$ with bpp = 2,6-bis(pyrazol-3-yl-pyridine).[68]

Solvent and non-coordinating anion effect

Generally, direct intermolecular interactions between the complex molecules are scarce, however solvent molecules or non-coordinating anions are usually responsible for the interactions and the presence or absence of the crosslinking molecule tends to make a dramatic difference in the magnetic behaviour. The aforementioned Fe(bpp)2(X)2 · nSolv complex is a nice all-encompassing example because the magnetic properties are affected by both, different non-coordinating anions and solvent molecules (Figure 21).[64,176]

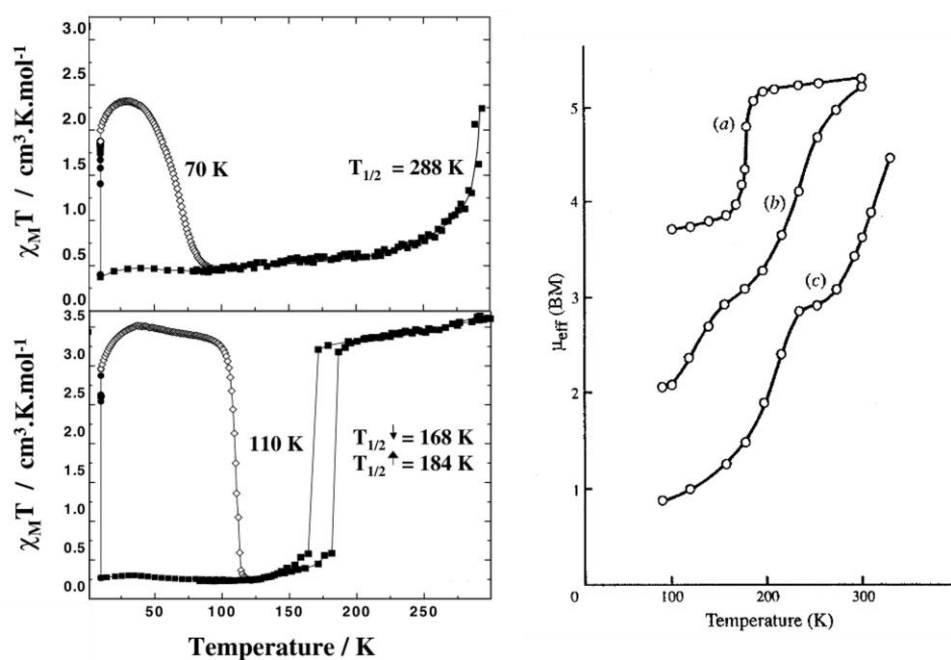*Figure 21 **left:** Temperature dependence of $\chi_M T$ for the hydrated Fe(bpp)$_2$(BF$_4$)$_2$ · 3H$_2$O complex (top) and the solvent free Fe(bpp)$_2$(BF$_4$)$_2$ complex (bottom) in the cooling mode without irradiation (▪), with irradiation at 10 K (●) and T(LIESST) experiment (◊).[64] **Right:** Temperature dependence of the magnetic moment μ_{eff} of a) [Fe(bpp)$_2$][PF$_6$]$_2$; b) [Fe(bpp)$_2$][PF$_6$]$_2$ · H$_2$O and c) [Fe(bpp)$_2$][PF$_6$]$_2$ · 2H$_2$O.[176]*

In the case of [Fe(bpp)$_2$][PF$_6$]$_2$ · n H$_2$O, with increasing number of n (0, 1, 2) there is a clear correlation between the amount of lattice water and the enhancement of the transition temperature $T_{1/2}$. More precisely, the larger n becomes and thus lattice water is present in the system, the more the LS state is stabilised (Figure 21 right). The temperature dependence of the magnetic moment of the two hydrated species, but particularly of the dihydrated one, appears unusual showing the occurrence of a two-step transition. It is determined that this behaviour results from the existence of two non-equivalent sites for the molecules in the lattice.[176,177] The change of the non-coordinating anions, from PF$_6^-$ to BF$_4^-$, results in different transition temperatures, especially for the hydrated derivative (Figure 21 left) with $T_{1/2}$ = 288 K and T_{LIESST} = 70 K. However, if the anhydrous Fe(bpp)$_2$(BF$_4$)$_2$ compound is examined a discontinuous spin switch with a broad thermal hysteresis ($T_{1/2}{\downarrow}$ = 168 K; $T_{1/2}{\uparrow}$ = 184 K and $\Delta T_{1/2}$ = 16 K) is found. Furthermore, the light induced generation of the metastable HS state is nearly quantitative at low temperatures, but the transition of the T_{LIESST} curve is more abrupt for Fe(bpp)$_2$(BF$_4$)$_2$ than the Fe(bpp)$_2$(BF$_4$)$_2$ · 3H$_2$O.[64] The mentioned complex illustrates very well how different transition curves depend on the different non-coordinating counterions and additionally on the crystal water contained in the system.

In this section, it was demonstrated how ligand design and cooperative effects interact to generate special spin switching properties. Since these factors are also to be utilised in this thesis, the following section will explain why the ligand system used in this thesis was designed and which properties should be included in this way.

3. Aim of this work

The previous sections provided an insight in the term "spin crossover" and the different properties, including all advantages and potential applications linked to the phenomenon of spin transition. The field of research has developed rapidly in the recent decades, increasingly revealing that cooperative interactions within the solid state play a central role. This is known as the "communication" between the individual spin-carrying metal ions, which can effectively propagate the local structural changes associated with the spin transition to the surrounding environment in the solid state and thus determine the properties of the system's spin transition. Abrupt spin transitions and especially thermal hysteresis are hot subjects and key components for applications, like for example molecular switches The bistable spin-switching system exhibits a memory effect, which means it provides two different adressable states (HS and LS state) in a certain range of external stimuli.

Our group has long been investigating the impact of cooperativity within the solid state on the magnetic properties of SCO materials. *Herold* in our group demonstrated the potential of highly solvent-dependant spin switching properties of bimetallic complexes using 1,3,4-thiadiazole bridging ligands.[41,158] For the synthesised complex $[Fe^{II}_2(PMTD)_2](BF_4)_4 \cdot 4DMF$ (with PMTD = 2,5-bis[(2-pyridylmethyl]amino)methyl-1,3,4-thiadiazole) all three possible spin states ([HS-HS]; [HS-LS] and [LS-LS]) were accessible upon solvent loss and rediffusion of DMF into the crystal lattice. *Fürmeyer,* recently investigated the influence on spin transition by different counterions or temperature-dependant structural phase changes.[40] The investigated binuclear SCO systems $[Fe^{II}_2(\mu2\text{-}TMAT)_2](X)_4$ (with TMAT = 2,5-bis{[(thiazol-2-ylmethyl)-amino]-methyl}-1,3,4-thiadiazole) and X = BF_4^-, ClO_4^-, $F_3CSO_3^-$) showed varying spin switching properties due to the different intermolecular distances between the spin carrying complex cations. As a result of a more and more reduced anion volume, the intermolecular distances along the form one dimensional chains decrease and thus destabilising the [LS-LS] state. Therefore, $[Fe^{II}_2(\mu2\text{-}TMAT)_2](F_3CSO_3)_4$ with the largest counterion volume consequently exhibits spin transition from the [LS-LS] to the [HS-HS] state above room temperature, while for the complex $[Fe^{II}_2(\mu2\text{-}TMAT)_2](BF_4)_4$ with the smallest anion volume the [LS-LS] state is not even reached at very low temperatures, staying at [HS-LS] intermediate level. In turn, complex $[Fe^{II}_2(\mu2\text{-}TMAT)_2](ClO_4)_4$ is able to address all three possible spin states. The special feature of this compound is that all three spin states can be achieved by a crystallographic phase change through slow cooling. Remarkably, under thermal quenching of the crystal no phase change was detected and thus the [HS-LS] state was found to be a superposition of LS and HS Fe^{II}-ions in the complex cation. These examples illustrate very well that spin crossover properties are dependent on many factors and especially on crystal packing effects inside the solid.

1,3,4-Thiadiazole based ligand systems are not only studied in our group, as it has been shown that the nitrogen atoms of the heterocycle are excellently suited as donor atoms for iron (II)-SCO compounds. The interest in this bridging motif had already been established in the international community for several years. Among the first reported SCO complexes incorporating the 1,3,4-thiadiazole motif were those using the 2,5-di-(2-pyridyl)-1,3,4-thiadiazole (dptd), by *Klingele et al.*[43,151,152] The built

mononuclear complexes with the sum formula [Fe(L^{dptd})$_2$X$_2$] · n(Solv) (with X = NCS$^-$, NCSe$^-$ and NCBH$_3^-$) showed abrupt or two-step SCO properties depending on the used counterion. The SCO binding pocket, consisting of two 1,3,4-thiadiazole-pyridyl backbones of the ligand is perfectly finetuned by two of the above mentioned pseudohalides, while the spin transition temperature T$_{1/2}$ shifts to higher temperature in the order NCS$^-$ < NCSe$^-$ < NCBH$_3^-$. In contrast to the analogous pyrazole and triazole bridging ligands, in which the central heterocycle is present in its deprotonated and negative form, no dinuclear complexes are formed.[178,179] However, the complexes show a preference for the formation of 1-D chains due to intermolecular π-π-interactions of the neighbouring complex molecules, which is illustrated in Figure 22 showing a selected part of the crystal structure of the complex [Fe^{II}(L^{dptd})$_2$(NCSe)$_2$] ·1.5DCM ·1.5H$_2$O. This seems to be an excellent cooperativity situation for the transmittance of the structural changes, associated with the SCO, to the neighbouring complex molecules via π-π-interactions.
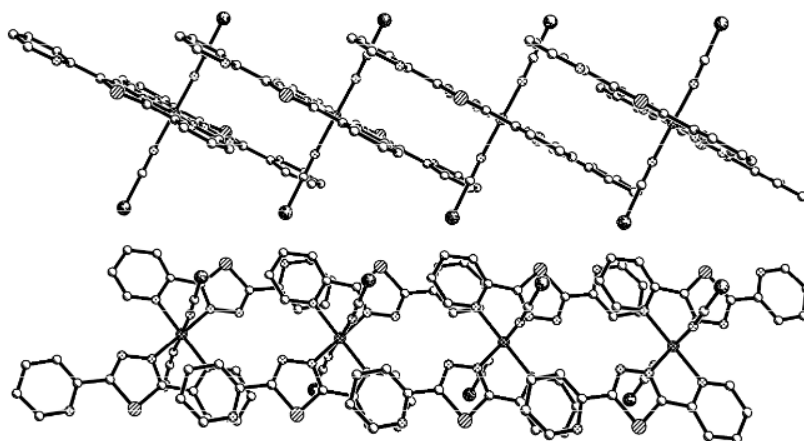

Figure 22: Side and top views of the crystal structure of [Fe^{II}(dptd)$_2$(NCSe)$_2$] ·1.5DCM ·1.5H$_2$O, emphasizing the chain motif running along the a axis. Hydrogen atoms and solvent molecules have been omitted for clarity.[151]

Since a thorough understanding of the interplay between cooperativity and hysteretic magnetic loops is of great importance for future applications, this work focused on the role of π-π-interactions between potential iron(II) SCO complexes based on the 1,3,4-thiadiazole bridging motif. [3,33,34,110] Since L^{dptd} seems to be not suitable to form dinuclear iron (II) complexes the non-coordinating pyridyl side arm will be substituted with various aromatic groups that are on purpose of non-coordinating nature (Figure 23). These structural ligand modifications are expected to improve the π-π-stacking properties between the complex molecules shown in Figure 22, providing a further insight in the relationship between SCO behavior and crystal packing effects. If there is found a higher degree of cooperativity, this should lead to even more abrupt spin transitions and above all to hysteretic magnetic properties.

Since many examples are known in the literature in which an incorporated naphthyl residue clearly increased π-π-stacking,[180–182] the ligand was first modified by replacing the pyridyl moiety with a naphthyl moiety, generating the ligand **L^1** (2-naphthy-5-pyridyl-1,2,4-thiadiazole). The structural and magnetic investigation of the resulting complexes [Fe^{II}(**L^1**)$_2$(NCX)$_2$] (with X = S, Se and BH$_3$) revealed unexpected and thus very interesting properties. More detailed insights into the interplay of

cooperative interactions and the resulting magnetic properties were gained by structurally modification of the ligand in further projects, as shown in Figure 23. By modifying the ligand, it is possible to directly influence the π-π-stacking of the individual Fe^{II}-complex molecules within the solid state. Consequently, the communication between the spin carrying molecules changes, which also alters the magnetic and hysteretic properties.

In the following, successes and shortcomings are reported and discussed, leading to a concluding outlook. This may drive the discussed projects forward, while also highlighting problems that still need to be solved.
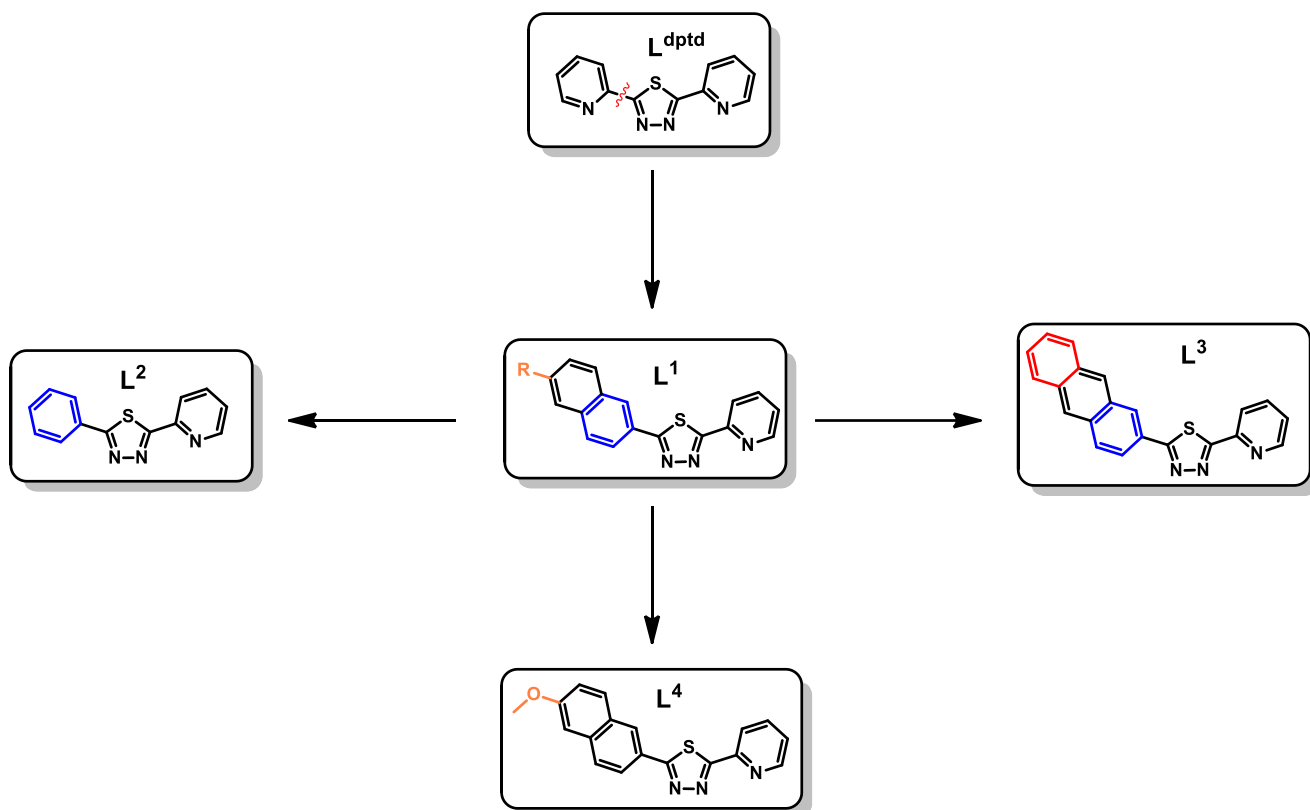

Figure 23: Different evolution of the Ligand L^{dptd}, starting with the ligand L^1 and ending with L^4.

4. Results and Discussion

4.1. Strongly cooperative mononuclear [Fe(L^1)$_2$(NCX)$_2$] complexes (X = S, Se, BH3) exhibit highly versatile magnetic bistability

The first part of the section "Results and Discussion" will be about the special and versatile magnetic properties of the complex family [Fe^{II}(L^1)$_2$(NCX)$_2$] with L^1 = 2-naphthyl-5-pyridyl-1,3,4-thiadiazol and X = S, Se and BH$_3$. A manuscript with selected data of [Fe^{II}(L^1)$_2$(NCX)$_2$] (X=S and Se) on this topic is currently in preparation.[183] Many different people were involved in this project, including ██████ ████████████ and ████████████ from the Technical University of Kaiserslautern, who were responsible for the recording and interpretation of the Mössbauer data for this project. Furthermore, ████████████ and his master student ████████████ from the University of Aarhus in Denmark were involved. Thanks to this collaboration, it was possible to record crystal structures at very low temperatures at the Spring-8 synchrotron beamline BL02B1 in Japan, and ████████████ also completed her master's thesis on pressure-induced SCO properties at the University of Aarhus, using the SCO systems described below in the same way. Finally, ████████████ from Johannes Gutenberg University carried out the single crystal structure investigation and refined the data. All other results on that topic, especially for [Fe^{II}(L^1)$_2$(NCBH$_3$)$_2$], and shortcomings that cannot be found in the manuscript are also discussed below.

4.2. Synthesis of 2-naphthyl-5-pyridyl-1,3,4-thiadiazole L1

As already mentioned in the previous section, the ligand was designed to generate the highest possible cooperative effects through π-π-interactions, without losing the SCO properties.[159,168,169,184] The chosen design of the ligand should lead to trans-coordination of pseudohalides as co-ligands and additionally to highly cooperative SCO compounds, as strong intermolecular interactions are enabled by π-π-stacking of the aromatic side residues of the ligands. Therefore, the literature known ligand 2,5-di(2-pyridyl)-1,3,4-thiadiazole,[43,151,152] was modified by replacing a pyridine moiety by a naphthyl moiety, as this seems to be particularly suitable for the conditions mentioned (Figure 23).[167] In the following, the synthesis of the ligand L^1 is described.
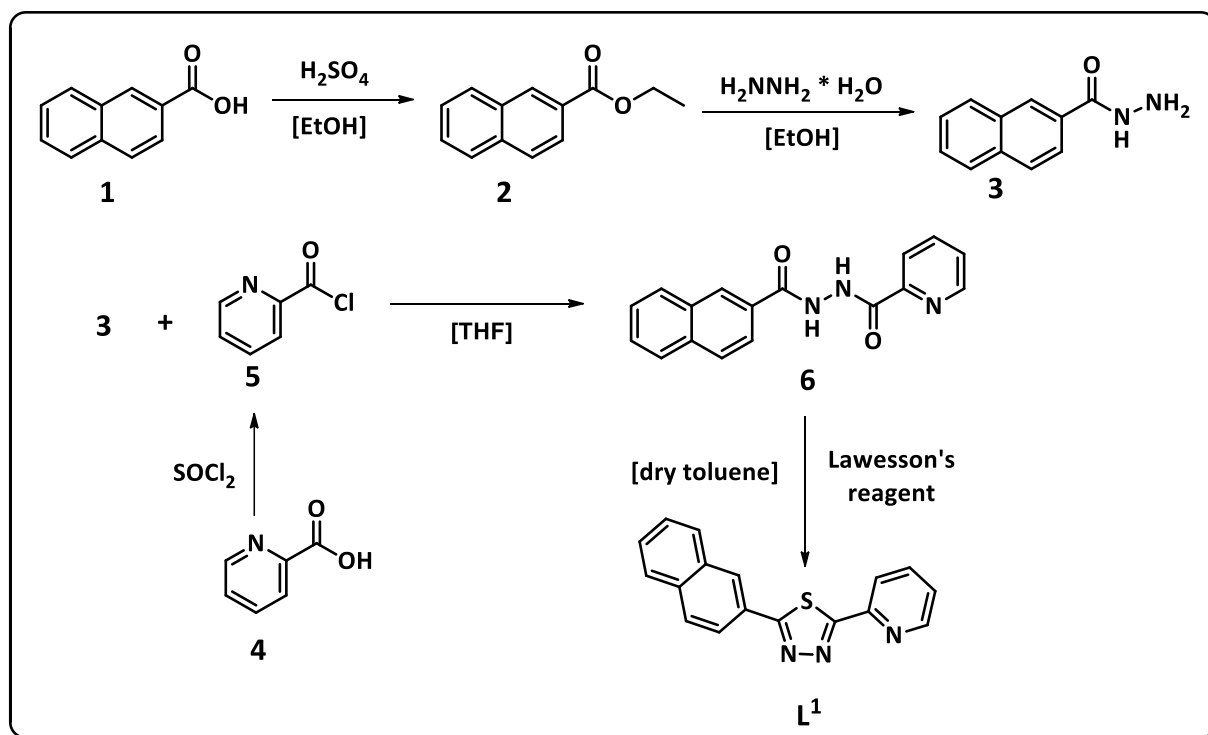
Scheme 1: Synthesis route for the preparation of L (2-naphthyl-5-pyridyl-1,3,4-thiadiazole)[1,41,158,185,186] The detailed description of the individual synthesis steps, yields and analytical characterisation can be taken from the experimental section.

The synthesis of the ligand **L¹** (2-naphthyl-5-pyridyl-1,3,4-thiadiazole) is presented in Scheme 1. Ethyl 2-naphthoate (**2**) was prepared according to procedures reported in the literature, by refluxing 2-naphthoicacid suspended in ethanol with a catalytic amount of sulfuric acid.[186] 2-Naphthohydrazide (**3**) was prepared in a nucleophilic substitution reaction of ethanol by addition of hydrazine hydrate, according to a modified literature procedure.[185] The previously formed ester was dissolved in ethanol, an excess of hydrazine hydrate was added and heated to reflux overnight. Subsequently, by stirring **3** with pyridine-2-carbonyl chloride (**5**) at room temperature in dry tetrahydrofuran (THF), which was freshly prepared from 2-pyridinecarboxylic acid (**4**) and thionyl chloride,[186] N'-(2-naphthoyl) pyridine-2-carboxylic acid hydrazide (**6**) was obtained. The ligand **L¹** was finally synthesised by a well-known method already used by *Herold*[41,158] and *Fürmeyer*[40,156,165] to design ligand systems based on coordinating 1,3,4-thiadiazoles. **6** was heated with Lawesson's reagent in dry toluene under reflux and argon atmosphere and then purified by column chromatography (DCM → DCM/diethyl ether 9:1) to give a yield of 62 % over four reaction steps. The ligand was fully characterised (¹H-NMR-, ¹³C-NMR-, COSY-NMR-, HMBC-NMR- and HSQC-NMR-, and IR-spectroscopy as well as APCI-spectrometry) and subsequently used for complexation reactions with iron (II) ions. Figure 24 displays the ¹H-NMR spectrum of **L¹**. The number of the respective signals and the integrals agree with the expected values. An exact assignment of all NMR signals, as well as additional analytics can be found in the experimental part (chapter 9).
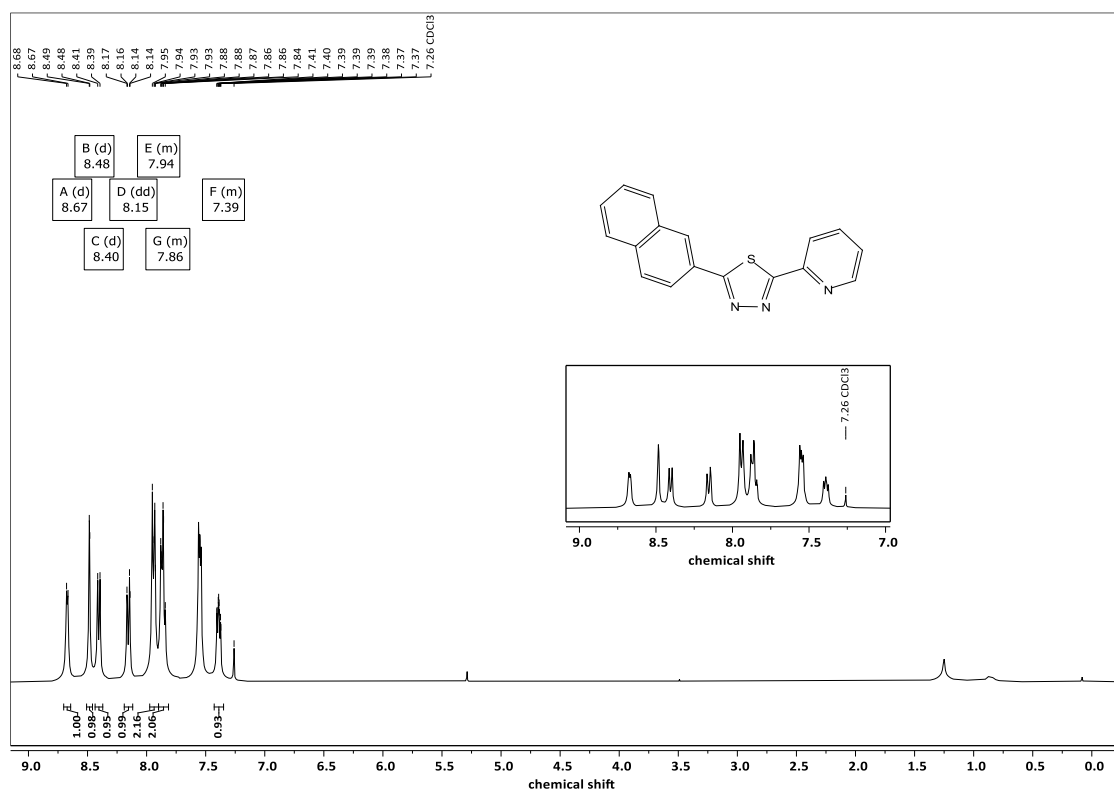
*Figure 24: ^{1}H-NMR of 2-naphthyl-5-pyridyl-1,3,4-thiadiazole (**L^1**) measured at 600 MHz. For a better understanding, only the peaks with the respective integrals, as well as a zoom of all aromatic signals that can be observed, are shown.*

4.3.   Synthesis of iron (II) complexes of the family Fe^{II}(L^1)$_2$(NCX)$_2$

The successful preparation of 2-naphthyl-5-pyridyl-1,3,4-thiadiazol (**L^1**) allowed its use for complexation reactions of iron (II)-ions. As mentioned in section 0, the combination of pseudohalides as co-ligands for the fine-tuning (increasing ligand field strength with NCS$^-$ < NCSe$^-$ < NCBH$_3^-$) of the spin crossover properties of iron (II)-complexes and the well-known 5-pyridyl-1,3,4-thiadiazole-SCO binding pocket provide the ideal situation to create versatile magnetic properties. The synthesis was carried out according to literature known procedures and under inert gas conditions.[43,152,187]
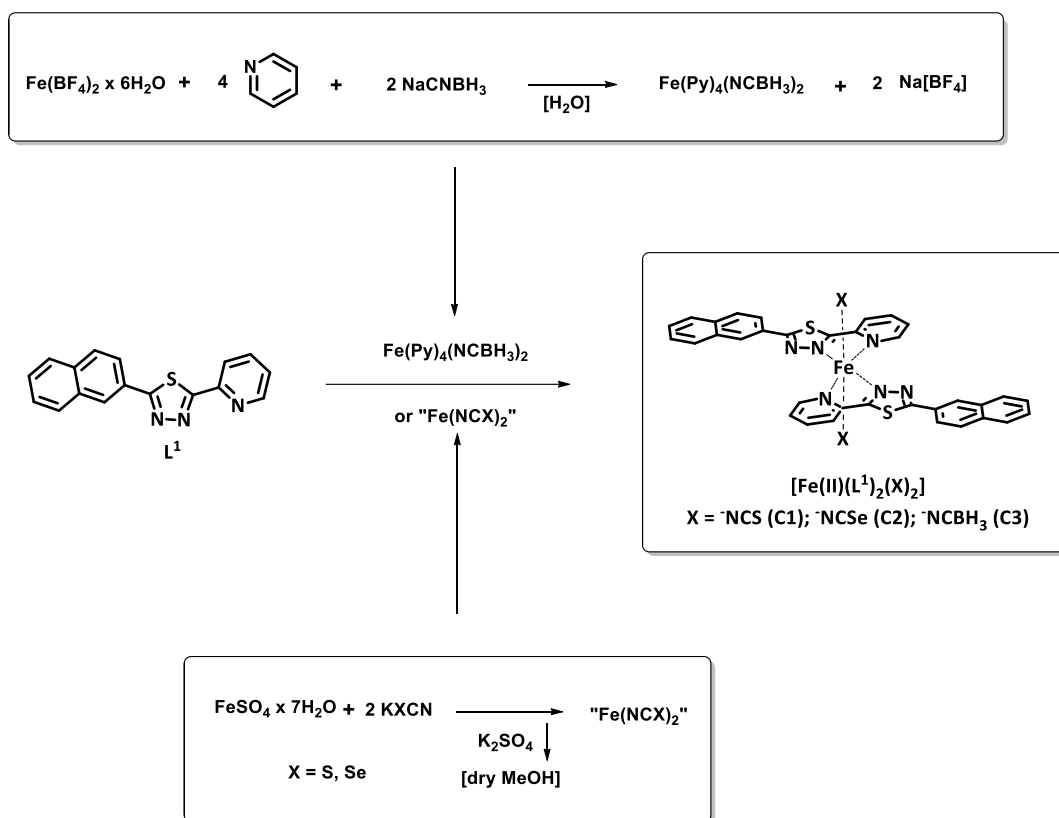
Scheme 2: Synthesis of the iron (II) complex family of Fe(L^1)$_2$(NCX)$_2$. Marked are the different synthesis routines for the complexes C1 and C2 (beneath the reaction arrow) and for C3 (above the reaction arrow). Additionally, the preparation of the reactive iron (II)-species is shown.

For the synthesis of the complexes **[Fe^{II}(L^1)$_2$(NCS)$_2$] C1** and **[Fe^{II}(L^1)$_2$(NCSe)$_2$] C2** (Scheme 2), 1 equivalent (eq.) of FeSO$_4$·7H$_2$O was dissolved in dry methanol and subsequently mixed with 2 eq. of KXCN (X = S and Se) in dry methanol and stirred for at least two hours. The built colourless precipitation of K$_2$SO$_4$ was filtered of and the resulting "Fe(XCN)$_2$" solution was layered over 2 eq. of **L^1** dissolved in dichloromethane (DCM). The layered solution was allowed to remain for liquid-liquid diffusion and crystallisation of the complex forming at the junction of both solutions. Gray to black single crystals suitable for X-ray structure analysis were obtained after 3-5 days at room temperature.

The synthesis of **[Fe^{II}(L^1)$_2$(NCBH$_3$)$_2$] C3** was also carried out according to this procedure, but with NaCNBH$_3$. However, no crystals suitable for X-ray structure analysis could be obtained, which is why an alternative route was used. For the preparation, the precursor compound [Fe^{II}(pyridine)$_4$(NCBH$_3$)$_2$] was synthesised as yellow powder according to procedures known from the literature (Scheme 2).[188,189] Fe(L^1)$_2$(NCBH$_3$)$_2$ **C3** was obtained by layering a solution of 2 eq. of **L^1** in DCM/toluene 1:1 with 1 eq. of [Fe^{II}(pyridine)$_4$(NCBH$_3$)$_2$] in Acetonitrile (MeCN). The layered solution was allowed to remain in the same way described above for liquid-liquid diffusion and crystallisation of the complex forming at the junction of both solutions. Violet block shaped crystals suitable for X-ray structure analysis were obtained after 1-2 days. The reaction mixture was filtered, and the residue was analysed by IR-spectroscopy in order to obtain a preliminary identification of the individual substances. In complexes containing pseudohalide NCX anions, the position of the CN-stretching vibration provides important information regarding the spin state of the iron (II) metal ion centre. If X = S and Se: 2020-

2080 cm^{-1} are typical values for iron (II) in the HS state, whereas the values for N-bound iron (II) in LS the state $\backsim$ 2100 cm^{-1}.[178,190–193] In addition, the location of the CN-stretching band of NCS- and NCSe-complexes can also provide information about the binding mode of the co-ligand to the metal centre. If the co-ligand is S-bound or Se-bound to the metal centre the bands are higher than $\backsim$ 2100 cm^{-1}, while values of 2020-2080 cm^{-1} are an indication for the bonding with nitrogen.[193–195] Contrary, the CN-stretch of NCBH$_3$-complexes always appear higher than $\backsim$ 2100 cm^{-1} when N-bound and additionally a strong B-H stretch can be found $\backsim$ 2300 cm^{-1}.[151,152,178,193,196–199] Figure 25 compares the infrared spectra of the ligand **L^1** (black) and the three complexes **C1** (red), **C2** (cyan) and **C3** (blue). Due to more clarity, all four spectra were normalised and shifted agaist each other.
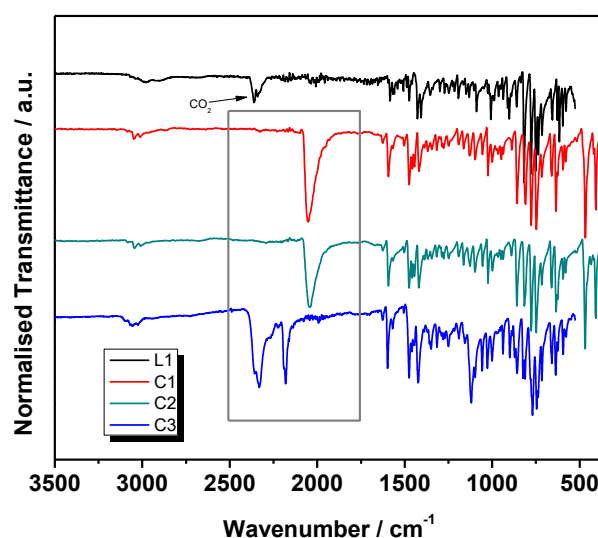
Figure 25: Normalized Infrared spectra of L1, C1, C2 and C3 in one graph. The spectra are offset from each other for more clarity. The grey box marks the characteristic IR-bands of the coordinating pseudohalides of the respective complexes; SCN$^-$ for C1, SeCN$^-$ for C2 and NCBH$_3^-$ for C3.

The CN-stretching vibrations for [Fe^{II}(L^1)$_2$(NCS)$_2$] **C1** and [Fe(L^1)$_2$(NCSe)$_2$] **C2** can be observed at 2056 cm^{-1} and 2048 cm^{-1}, respectively indicating both being N-bound. Fe(L^1)$_2$(NCBH$_3$)$_2$ **C3** exhibits a CN-stretching vibration at 2180 cm^{-1}, as well as a BH-stretch at 2330 cm^{-1}, as expected for N-bound NCBH$_3$. Additional analytical data can be taken from the appendix.

4.4. Crystal structures of C1 and C2

Figure 26: **left**: Crystal structure of C1 including the atom labelling. Hydrogen atoms are omitted for clarity **Right**: The tilted naphthyl antenna plane (blue) and the equatorial plan (red) were each marked with colour. Color Code: grey-C, yellow-sulfur, blue-N, orange-Fe, white-H. ORTEP representation with atomic displacement parameters at 50% level of probability.
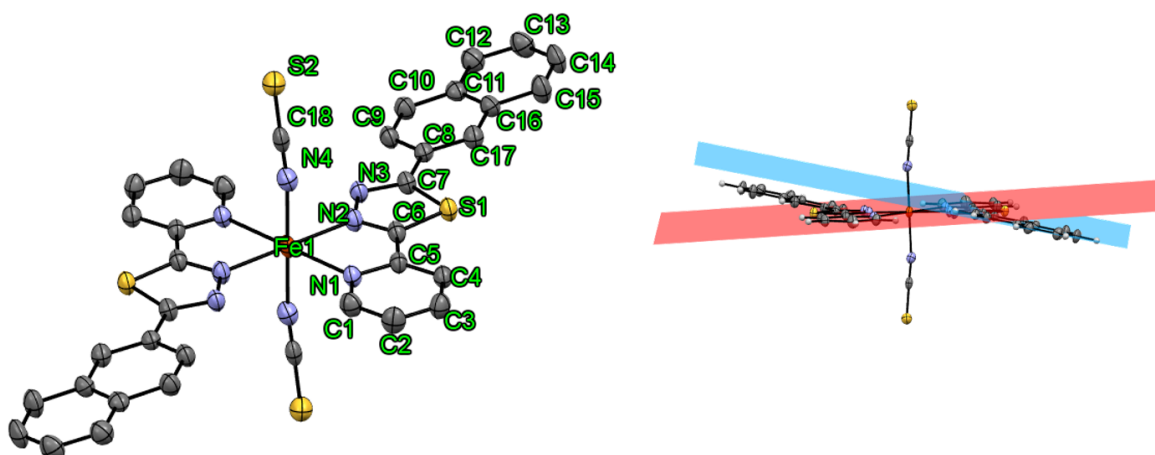
The complex **[Fe^{II}(L^1)$_2$(NCS)$_2$]** (**C1**) crystallizes in the triclinic space group $P\bar{1}$ (Figure 26). To detect a possible spin transition by the measured X-ray structure analysis, the structure was measured at 173 K and 90 K. The asymmetric unit contains half of the molecule with the iron (II)-ion located on the centre of inversion. **C1** exhibits a moderately distorted octahedral coordination environment formed by two molecules of **L^1** and two trans-coordinating thiocyanate anions, giving an overall neutral complex molecule. The chelating ligand (**L^1**) is bidentate, with the pyridyl and thiadiazole backbone spanning the equatorial plane, while the naphthyl moiety is tilted 14.79° from this plane for 173 K and 14.90° for the structure at 90 K. The average Fe-N bond length of 2.16 Å (173 K) and 1.99 Å (90 K) are in the typical range for iron(II) complexes in the HS and LS state, respectively.[1,27,33,110] The bite angle of the coordinating pyridyl and thiadiazole unit (N1-Fe-N3) is found to be 75.69° for 173 K, while the NCS$^-$ Co-ligands coordinate angularly with an angle of 168.41°. For the structure measured at 90 K, there is a widening of the bite angle observed to 80.37 °, while the coordination angle of the Co-ligands comes to 173.85°. The two N-C-S moieties are almost linear for both temperatures (178.82° at 173 K and 179.10 at 90 K). Besides the metal-ligand bond lengths, the octahedral distortion parameter Σ (sum of the deviation from 90° of the 12 cis-N-Fe-N angles in the FeN$_6$ coordination sphere) is a common measure for the spin state of the central ion. Σ equals 67.04° at 173 K and 45.00° at 90 K and differs significantly from the typical values for HS- and LS-complexes (Σ > 100°and Σ< 80°).[86] However, the difference is comparable to the literature known SCO systems coordinating equatorially via pyridine and thiadiazole and pseudohalides as axial co-ligands.[43,151,152] The values above mentioned show a clear spin transition of the complex molecule between the measured temperatures of 173 K (HS) and 90 K (LS). Due to the spin change from HS to LS, the Fe-Fe distances within the solid also change along the crystallographic axes a, b, and c. **C1** at 173 K (Figure 132) has Fe-Fe distances of 7.95 Å along the a-axis, 9.27 Å along the b-axis and 12.09 Å along the c-axis. In turn, at 90 K and thus in LS state, the Fe-Fe distances are 7.78 Å along the a-axis, 9.03 Å along the b-axis and 12.36 Å along the c-axis. Accordingly, a reduction of the Fe-Fe distances along the a- and b-axis can be observed due to the spin switch,

whereas an increase of the distances along the c-axis can be observed. As cooperativity plays a key role in SCO behaviour, it is important to note that the crystal structure does not contain any solvent molecules. As a result, strong π-π interactions form between anti-parallel aligned coordinating ligands **L¹** of the respective neighbouring complex molecules in different spatial directions (Figure 27). Distances and offsets of all π-π-interacting parts for both **C1** at 173 K (HS) and at 90 K (LS) are in the range of interactions well-known from literature (3.51 Å to 3.66 Å).[200,201] All exact values can be taken from the appendix (section 11.4.1, Table 8 and Table 10).
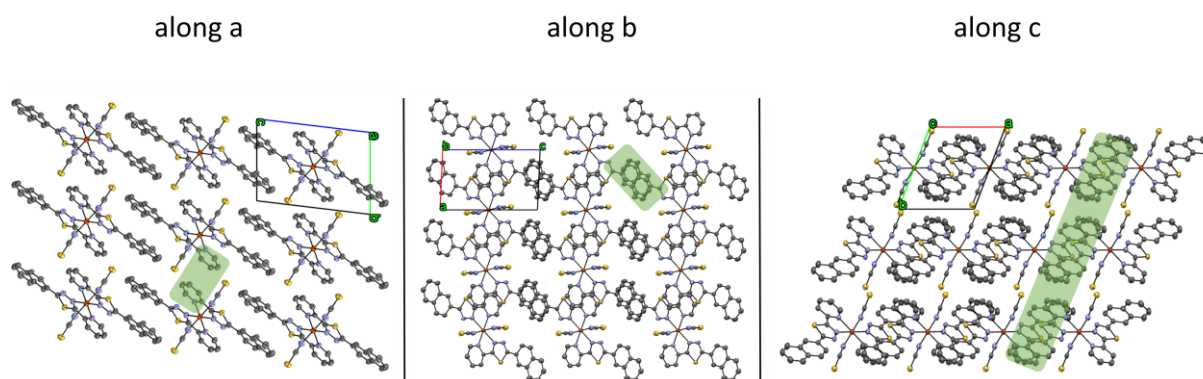

*Figure 27: **along a**: Selected part of the crystal structure of **C1** along the a-axis. Highlighted are the π-π-interactions of parallel displaced pyridyl moieties of neighbouring complex molecules; **along b**: Selected part of the crystal structure of **C1** along the b-axis. Highlighted are the π-π-interactions of parallel displaced naphthyl moieties of neighbouring complex molecules; **along c**: Selected part of the crystal structure of **C1** along the c-axis. Highlighted are the inter molecular π-π-interactions of the anti-parallel arrangement of ligand molecules of neighbouring complex molecules within the crystal. Color Code: grey-C, yellow-sulphur, blue-N, orange-Fe, white-H. ORTEP representation with atomic displacement parameters at 50% level of probability.*

The single-crystal X-ray diffraction data of **C2** at 200 K and **C1** are isostructural and consequently **C2** crystallises in space group $P\bar{1}$, as well.
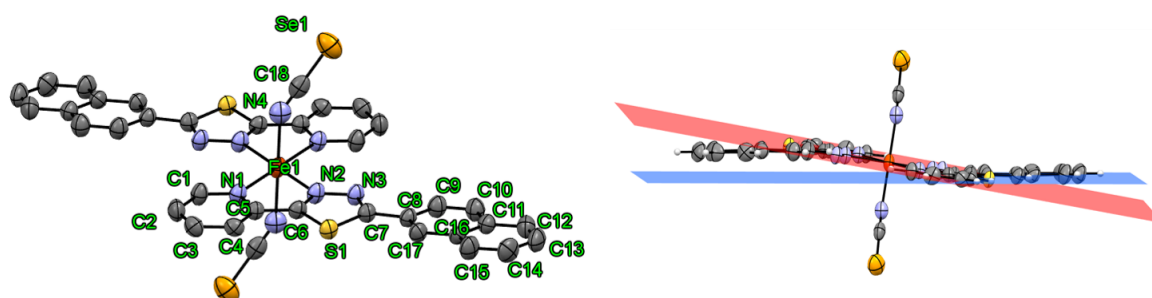
*Figure 28: Crystal structure of **C2** including the atom labelling. Hydrogen atoms are omitted for clarity **Right**: The tilted naphthyl antenna plane (blue) and the equatorial plan (red) were each marked with colour. Color Code: grey-C, yellow-sulfur, blue-N, orange-Fe, white-H. ORTEP representation with atomic displacement parameters at 50% level of probability.*

The asymmetric unit is built up as described above, as is the coordination of the ligand and the Co-ligand. The pyridyl and thiadiazole backbones of the ligands span the equatorial plane with the iron ion again, while the naphthyl group is twisted by a value of 10.51° (Figure 28). The average Fe-N bond length of 2.17 Å at 200 K is in the typical range for iron(II) complexes in the HS state.[1,27,33,110] The bite

angle of the chelating ligand (N1-Fe-N2) hardly differs from that measured in **C1** (75.61°), while the coordinating NCSe⁻ Co-ligands in this case are more angled (Fe-N4-C18 angle = 144.69°) (the two N-C-Se anions are again almost linear at 179.26°). Σ is 72.88° and thus significantly larger than for **C1** and is comparable to literature-known SCO systems using a 5-pyridyl-1,2,4-thiadiazole binding pocket.[43,151,152] The Fe-Fe distances in the case for **C2** at 200 K (Figure 137) are 8.23 Å along the a-axis, 10.46 Å along the b-axis and 10.70 Å along the c-axis. Since **C2** also crystallises without any solvent molecules, strong cooperative interactions between neighbouring complexes are established again by π-π-interactions as described above (Figure 137). Distances and offsets of all π-π-interacting parts are in the range of interactions well-known from literature (3.53 Å to 3.59 Å).[200,201] The exact values of the π-π-interaction can be taken from the appendix (section 11.4.1, Table 11).

4.5. Variable temperature magnetic susceptibility measurements of C1 and C2

Variable temperature magnetic susceptibility measurements were performed on samples stored under air conditions as well as on freshly prepared samples. For **C1** and **C2**, no differences were found between the measurements, which confirms the stability of the crystalline compounds under ambient conditions. A temperature range of 2 – 400 K under an external magnetic field of 1000 Oe was used for the data collection of the magnetic susceptibility. The cooling and heating rates were varied between 0.2 K/min and 10 K/min. Both **C1** and **C2** are in the HS state at room temperature, as shown by χ_MT values at 300 K of 3.47 cm³Kmol⁻¹ and 3.46 cm³Kmol⁻¹, respectively. Both high-temperature values are in the range typically for this kind of Fe^{II} HS complexes.[1,43,84,110,151,152,154] When cooling from room temperature, the χ_MT values of **C1** and **C2** (cooling rate of 0.35 K/min) remain at constant values until an abrupt drop in the χ_MT curve is observed at 100 K for **C1** and at about 125 K for **C2**, respectively, resulting in χ_MT values of 0.18 cm³Kmol⁻¹ for C1 and 0.44 cm³Kmol⁻¹ for **C2** at 2 K (Figure 29).
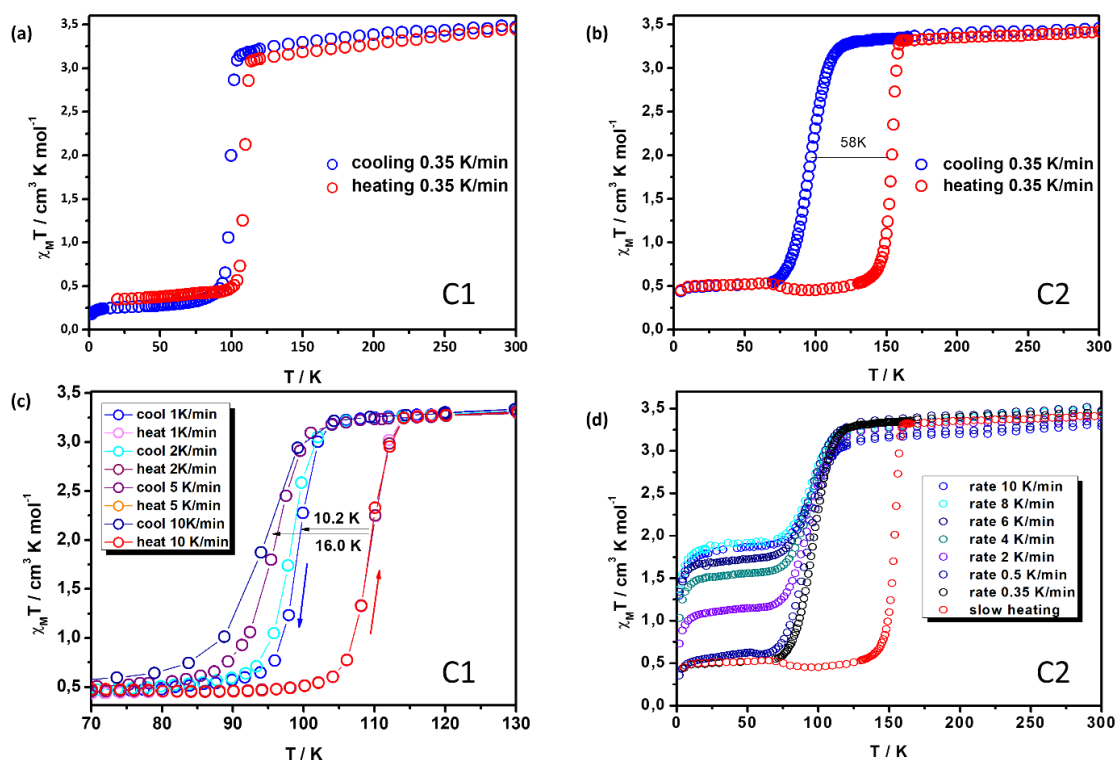
Figure 29: **(a)** Magnetic properties of [Fe(II)(L^1)$_2$(NCS)$_2$] (**C1**) displaying abrupt spin transition at 110 K while heating, but at 100 K while cooling This results in in a hysteresis of 10 K (cooling and heating rate: 0.35 K/min); **(b)** Magnetic properties of [Fe(II)(L^1)$_2$(NCSe)$_2$] (**C2**) displaying abrupt spin transition at 154 K while heating and at 96 K while cooling, resulting in a hysteresis of 58 K. The measuring speed during the heating or cooling process was 0.35 K/min; **(c)** Closer look on the hysteresis cycle of **C1** with different cooling rates (1 K/min-10 K/min). The measurements were done in sweeping mode; **(d)** Cooling of **C2** with different cooling rates from 10 K/min – 0.35 K/min. The result are different metastable states with $\chi_M T$ values between 1.9 cm^{3}Kmol^{-1} at maximum speed of 10 K/min and 0.35 cm^{3}Kmol^{-1} at minimum speed of 0.35 K/min.

According to the single crystal structure analysis data, **C1** and **C2** exhibit pronounced intermolecular interactions. This leads to abrupt SCO behaviour for **C1** and **C2**, which can be seen in Figure 29. Solvent-free crystal packing leads to reproducibility of the measurement data in either case over several heating and cooling cycles (Figure 29c and Figure 30). No decomposition or oxidation of the iron (II) centre is observed. When cooling or heating slowly at constant speed of 0.35 K/min, a hysteresis of $\Delta T_{1/2}$ = 10 K (**C1**) and $\Delta T_{1/2}$ = 58 K (**C2**) can be observed. It is known that the hysteresis curves vary depending on the cooling and heating rates, thus the hysteresis curves of **C1** and **C2** were investigated at different scan rates.[115,202–204] The heating curves were found to be independent of the heating rates and remained unaffected (Figure 29).[115,202] With increasing cooling rate for **C1**, the transition temperature $T_{1/2}$ shifts from 100 K to 94 K. This leads to a widening of the hysteresis curve from $\Delta T_{1/2}$ = 10 K to $\Delta T_{1/2}$ = 16 K (Figure 29c). Noteworthy is that neither the cooling rate nor the heating rate have an impact on the transition temperatures $T_{1/2\downarrow}$ or $T_{1/2\uparrow}$ for **C2** and the hysteresis cycle remains stable and unaffected even after several cycles with a cooling rate of 2 K/min.[202,203]
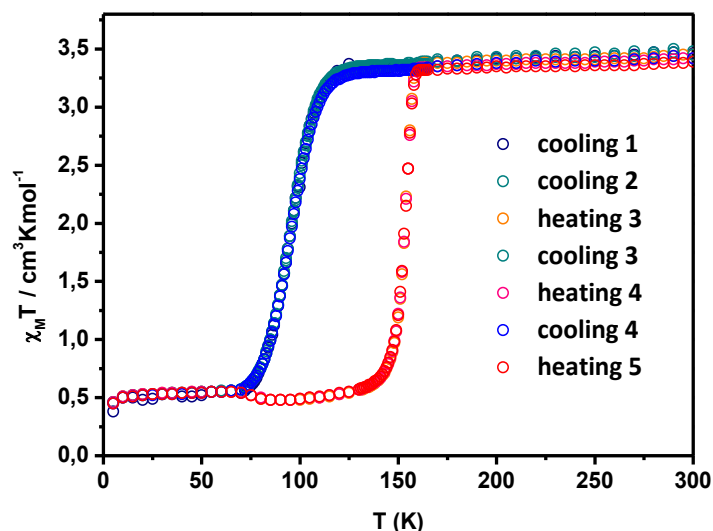
*Figure 30: **C2** showing reproducibility and stability of the complex and its magnetic properties after several hysteresis cycles at constant sweep rate of 2 K/min.*

Instead of a change in the value $T_{1/2\downarrow}$ and an associated widening of the hysteresis curve (similar to **C1**), for **C2** a more and more incomplete spin transition is observed, due to an increase in the cooling rate. Below 65 K, as shown in Figure 29d, different HS/LS fractions are revealed in the form of different plateau levels or values of $\chi_M T$ when changing the cooling rate. At maximum speed of the sweeping rate (10 K/min) up to 42 % HS state is maintained. For very slow cooling of **C2** (0.35 K/min), conservation of about 15 % of the HS fraction below 65 K can be observed. In order to exclude, that the remaining HS residue is not caused by macroscopic effects within the bulk material, or by impurities, the sample was slightly heated and the change in magnetic susceptibility of the sample was investigated over a period of 12 h at 75 K. The magnetic relaxation allows an almost complete spin change into the LS state. Another way for this kind of investigation would be to perform reverse-LIESST experiments with a laser, in the infrared range. This should allow a full conversion of the HS residual fraction into the LS state by irradiation into the $^5T_{2g}$ absorption band of the HS state. Unfortunately, this was not possible since there was no suitable experimental set-up at that time.
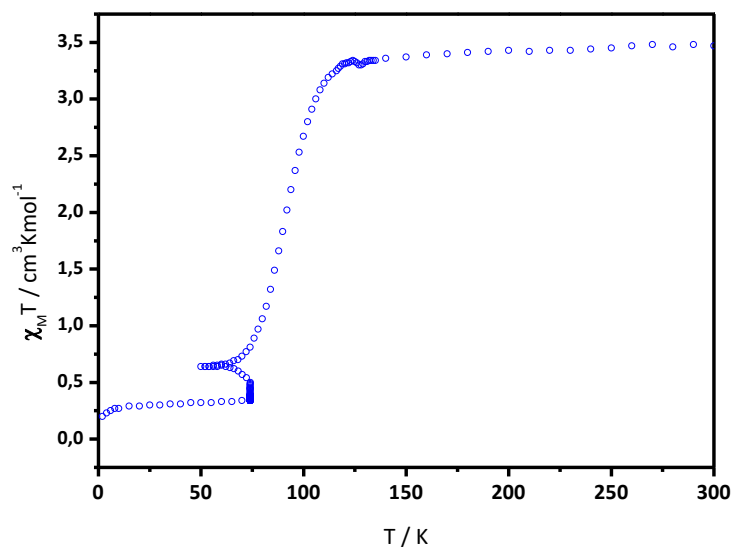
Figure 31: χMT-measurement of C2 with subsequent relaxation of the magnetic susceptibility: C2 was slowly cooled (0.5 K/min) to 50 K, leading in a magnetic susceptibility value of 0.64 cm³ K mol⁻¹ and subsequently heated to 75 K. The magnetic susceptibility was now measured over a period of 12 hours and afterwards cooled down to 2 K, leading in a χMT value of 0.2 cm³Kmol⁻¹.

Considering the isostructural nature of **C1** and **C2** and the knowledge of the hysteretic properties of **C2** just described the two complexes were investigated for the existence of metastable plateaus. In fact, if a sample of either complex is cooled down to 10 K very rapidly (by rapid insertion into the measuring chamber) in the SQUID magnetometer, a strongly pronounced TIESST effect (thermally induced excited spin state) can be observed.[68,69,75,78,153,205–207]
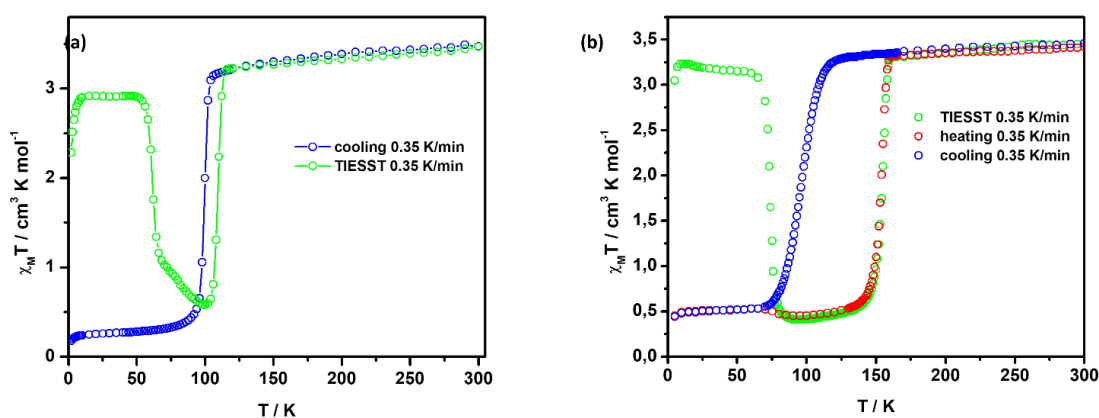
Figure 32: Magnetic properties of [Feᴵᴵ(L¹)₂(NCS)₂] (C1) and [Feᴵᴵ(L¹)₂(NCSe)₂] (C2), showing clear existence of a metastable TIESST plateau after thermal quenching at 10 K. (a) Relaxation of the generated metastable state into the LS ground state of C1 at 50 K with T_{TIESST} = 62.10 K (0.35 K/min) and an abrupt spin transition at 110 K and 100 K while cooling. (b) Relaxation of the generated metastable state into the LS ground state of C2 at 65 K with T_{TIESST} = 70.15 K (0.35 K/min) and an abrupt spin transition at 154 K and 96 K during the cooling process.

Hence, by quenching the sample at very low temperatures, it is possible to preserve the magnetic information given by the thermal HS state. This information is consequently stored in the newly formed metastable HS plateau or state.[68,69] The (thermal) relaxation of the magnetic moment into the LS ground state is blocked below a critical temperature characteristic for each compound. The magnetic moment relaxes below 50 K for **C1** and below 65 K for **C2**. The thermally metastable HS state can be preserved at 84% at low temperatures for **C1** and at 92% for **C2**. The temperature T_{TIESST} at which half of the molecules of the metastable state are in the HS state is determined with 62.10 K for **C1** and 70.15 K for **C2** when the samples are heated to room temperature at a rate of 0.35 K/min. Similar to the investigations of the hysteresis behaviour of **C1** and **C2**, T_{TIESST} of the metastable state was also investigated for potential shifts to higher temperatures. This was done by heating with different heating rates (0.5 K/min – 10 K/min) in sweeping mode after quenching at 10 K and subsequent heating to room temperature. With increasing heating rates, T_{TIESST} shifts to higher temperatures for **C1** (from T_{TIESST} = 62.10 K to 76.50 K; ΔT_{TIESST} = 14.40 K) and **C2** (from T_{TIESST} = 70.15 K to 86.10 K; ΔT_{TIESST} = 15.95 K). It is also worth mentioning that T_{TIESST} and the scan rate are in a proportional relationship to each other (Figure 176). This shift of T_{TIESST} closer to $T_{1/2\downarrow}$ is reflected in a less and less complete spin transition (Figure 33). The increase in T_{TIESST} values obviously favours the overlap of T_{TIESST} and the thermal hysteresis. In other words, there is an increasing overlap or mixing of the kinetic state of the metastable phase and the thermodynamic state of the hysteresis. This favours the kinetic distortion of the hysteresis loop, which mainly explains the increase of the HS residual at low temperatures. These observations correlate with observations from the past regarding the behaviour of the remaining HS fraction as T_{LIESST}/T_{TIESST} and $T_{1/2\downarrow}$ move towards each other.[69,208]
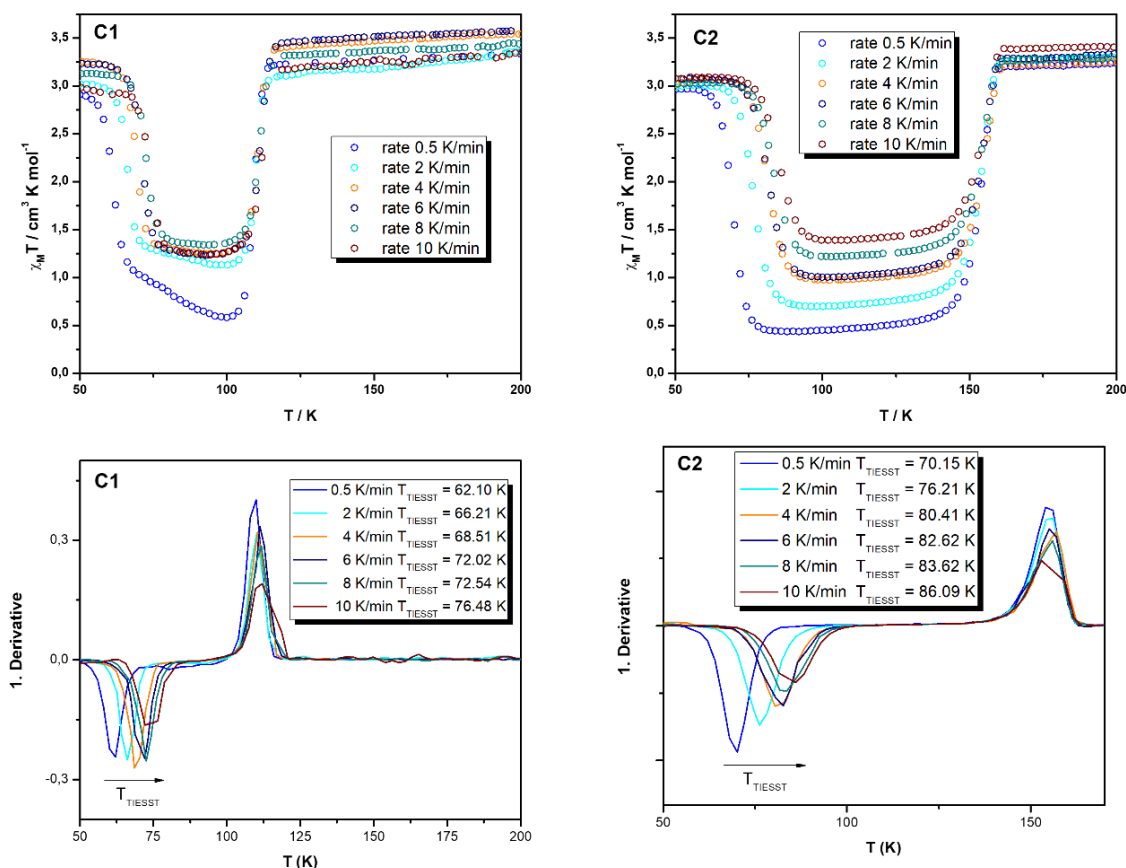
*Figure 33: **Top:** TIESST experiments of **C1** and **C2** respective different heating rates. The sample was re-quenched for every measurement at 10 K and heated to RT with different heating rates (0.5 K/min – 10 K/min). A shift from T_{TIESST} to higher temperatures and steady increase of the $\chi_M T$ value after relaxation can be observed. **Bottom:** First Derivatives of each $\chi_M T$ curve of **C1** and **C2** to calculate all T_{TIESST} and $T_{1/2}$ values.*

Additionally, **C1** exhibits an altered relaxation velocity around 68 K, which is, however, less pronounced with increasing sweeping rate (Figure 32a, green curve). To ensure that the relaxation behaviour of **C1** is not caused by impurities, the bulk material was investigated by powder X-ray diffraction (Figure 174 of section 0). It was found that the very good agreement between the diffraction calculated from the single crystal structure data and the measured powder data shows no indication of (paramagnetic) contamination of the sample. This suggests that **C1** exhibits two different relaxation trajectories while relaxing from the metastable TIESST state back to the ground state. Another way to come to the same conclusion is to look at the actual relaxations of the magnetic susceptibility using time-dependent decay measurements of the magnetic moment. The measurements were each carried out at constant temperatures, with magnetic susceptibility measured over specific time rates (700 min – 50 min). At 30 K both systems do not show any significant relaxation over 11 h. The HS to LS relaxation is observable in the temperature range of 50 K-61 K for **C1** and 61 K-70 K for **C2**.
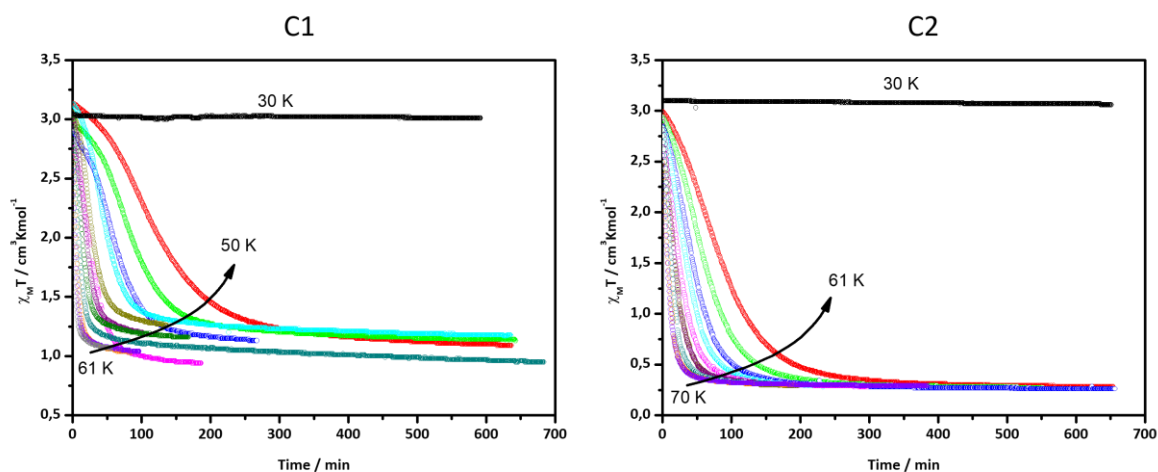
*Figure 34:Time-depended relaxation measurements of the change in magnetic susceptibility of **C1** and **C2** at the given temperatures as function of time in minutes.*

The values for $\chi_M T$, does not settle at a certain value after the time-depended relaxation of **C1** (Figure 34), thus the final values of the magnetic susceptibility do not converge to a threshold of $\chi_M T$ and vary around the value of 1.25 cm^3 K mol^{-1}. Exactly the value at which the slope of the decay of the $\chi_M T$-product changes after quenching of the sample at 10 K and subsequent heating to RT (Figure 32a, green curve). This is another indicator suggesting that **C1** exhibits two different relaxation trajectories after relaxing from the metastable TIESST-plateau into the LS ground state, as already assumed after measuring the temperature-dependent magnetic susceptibility at 0.35 K/min (Figure 32). Contrary, looking at all relaxation curves of the relaxation measurement of **C2**, the values all converge to the specific $\chi_M T$ value of 0.25 cm^3 K mol^{-1}. This matches the value of the measured $\chi_M T$-product and the residual HS fraction after quenching and subsequent heating (0.35 K/min) of the sample, which can be seen in Figure 32 and Figure 33.

Further insights are possible from the relaxation measurements, but these also raise questions. The deviation of the decay curves for **C1** and **C2** at lower relaxation temperatures from a single exponential is striking. The decay curves clearly show sigmoidal behaviour, which is in agreement with the prediction of the self-accelerated decay of high cooperative systems.[209,210] Elastic long-range interactions play an important role in the self-acceleration process. These act as a kind of internal pressure resulting from the difference in the metal to ligand bond length distances caused by the spin transition, leading to a progressive reduction of the energy barrier.[33,162,209,210] This observation coincides perfectly with the high cooperativity suggested from the crystal structure and the resulting abrupt spin transitions and wide hysteresis loops. Accordingly, the relaxation rate $k_{HL}{}^*$(T, γ_{HS}) is written, in the thermal activation regime:[152,208]

$$\frac{d\gamma HS}{dt} = - k_{HL}{}^*(T) \cdot \gamma_{HS} \qquad 17$$

with

$$k_{HL}*(T, \gamma_{HS}) = k_{HL}(T)\ exp[\alpha(1- \gamma_{HS})]$$

18

α = acceleration factor

If the data of **C1** and **C2** are simulated with the above mathematical relationship, it is very clear that the relaxation does not only follow a sigmoidal course. This behaviour was expected for **C1** as a second relaxation pathway was already visible and thus predicted. In contrast, **C2** at first glance only shows a relaxation path from the metastable HS state to the LS ground state and only becomes visible through mathematical simulation. The following figure (Figure 35) shows the relaxation curves at 51 K for **C1** and at 61 K for **C2**. As time progresses, the sigmoidal model fails and takes a slower, presumably an exponential progression. This trend is even more pronounced for **C1** than for **C2**. With increasing relaxation temperature, the relaxation is less dominated by the sigmoidal progression. All simulations made with the sigmoidal self-acceleration model can be taken from the appendix (Figure 175 and Figure 177).
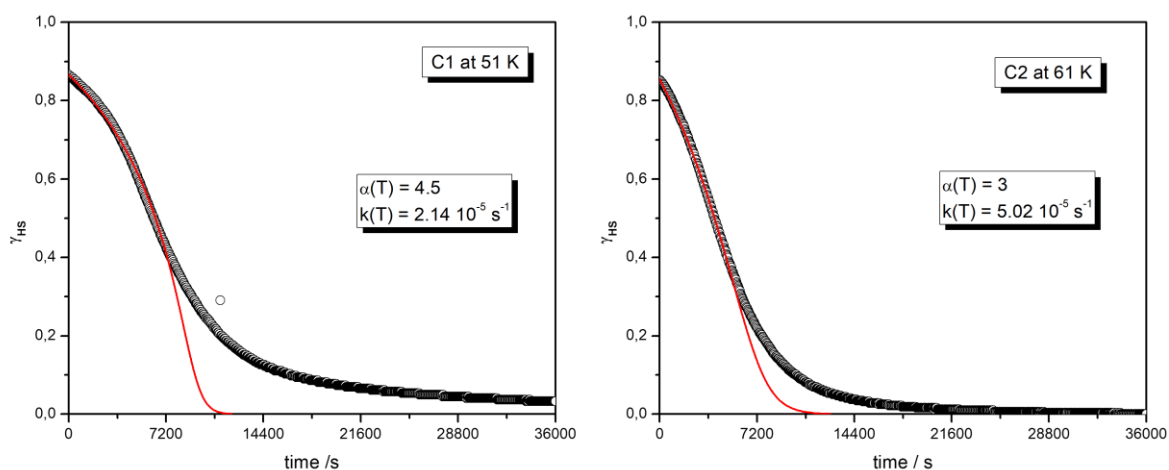
*Figure 35: Relaxation of **C1** at 51 K and **C2** at 61 K (black curve) as function of the time in seconds and the respective sigmodial simulation (red) at the given temperatures. The simulation clearly shows a deviation of a pure sigmodial relaxation behaviour.*

Due to the mixture of different relaxation trajectories, an exact determination of the reaction rates and the associated parameters is only possible to a limited extent. The model used results in an activation energy of 538.14 cm^{-1} (α = 4.5) for **C1** (Figure 178, section 11.8) and 631.83 cm^{-1} (α = 3) for **C2** (Figure 179, section 11.8). Although these values are within the range of systems known from literature,[68,152,208] they should be considered with caution, as the model is not representative for multiple relaxation pathways. The mixture of both relaxation trajectories is probably a result of the crossing point of the kinetic regime of the relaxation of the metastable low temperature HS-state and the thermodynamic hysteretic regime.[208] Looking more closely, this phenomenon can be seen very clearly. The higher the scan rate is chosen, the closer the kinetic and thermodynamic processes move towards each other, until they finally cross. Shown here representatively as blue and red boxes in Figure 36.

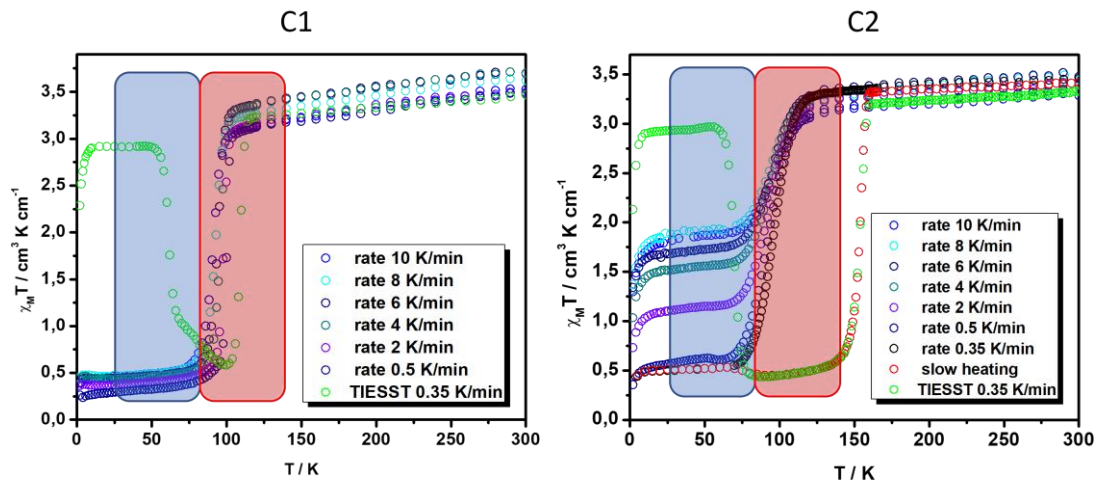*Figure 36: Representation of the molar magnetic susceptibility of **C1** and **C2** as a function of the scan rate. The faster the scan rate, the closer the kinetic (blue) and thermodynamic (red) spin transition processes.*

4.6. Mössbauer experiments of C1 and C2

The results of the magnetic SCO properties of **C1** and **C2** presented above were also investigated using [57]Fe-Mössbauer spectroscopy at different temperatures. Therefore, freshly prepared, and dried samples of both compounds were investigated respectively. The measurements were done by ████ ████████ of the group of ██████████████████ of the technical University of Kaiserslautern. Information on the experimental set-up can be found in the experimental section.

*Figure 37: **Left column:** Mössbauer spectra of slow cooled **C1** down from RT at the given temperatures with a cooling rate of 1 K/min. The cooling sequence starts at 298 K ends at 77 K and is chronologically referenced (**a-d**). **Middle and right column:** Mössbauer spectra of **C1** cooled to very low temperatures with a cooling rate of 1.25 K/min and a subsequent heating rate of 1 K/min. The temperature sequence starts at 15 K and is chronologically referenced (**e-l**). **Colour code:** HS-states are depicted in red; LS-states are depicted in blue, the overall fits are depicted in black, while the black circles represent the actual measurement values. Solid lines are fits with parameters given Table 36.*

Figure 37 shows twelve selected spectra of **C1** recorded in cooling and heating mode: **(a)** measured at RT, **(b)** slowly cooled with a cooling rate of 1 K/min to 180 K from room temperature, **(b)** further cooled

to 110 K, **(c)** 100 K and **(d)** 77 K. The spectrum for **C1** collected at RT (Figure 37a) shows one species with an isomer shift δ = 1.05 mms⁻¹, a quadrupole splitting ΔE_Q = 2.83 mms⁻¹ and a linewidth of Γ = 0.35 mms⁻¹, parameters typical for iron (II) HS ions.[40,211–216] When cooling the sample, the spin switch is observed at 110 K (**b**), 100 K (**c**) and 77 K (**d**) indicated by the spectra exhibiting two different components of iron (II). Both species can be assigned to iron (II) HS and LS respectively, whereby the LS portion increases with decreasing temperature. [40,158,211–216] Due to the presence of a metastable TIESST plateau, seen in the magnetic SQUID data, which is due to thermal quenching or rapid cooling of the sample to very low temperatures, the compound was also investigated by ⁵⁷Fe-Mössbauer spectroscopy at very low temperatures (Figure 37 **e-l**). The same sample of **C1** which was used for the previous series of Mössbauer experiments was cooled to 15 K (**e**) at a cooling rate of 1.25 K/min and then heated to room temperature at a heating rate of 1 K/min to 25 K (**f**), 77 K (**g**), 85 K (**h**), 95 K (**i**), 110 K (**j**), 120 K (**k**) and 298 K (**l**) (Figure 37 **e-l**). It is observed that the isomer shift δ and quadrupole splitting ΔE_Q of the observed HS state at 15 K (**e**) (δ = 1.149 mms⁻¹, ΔE_Q = 2.97 mms⁻¹, Table 36) are similar to the values measured at higher temperatures (e.g. at 298 K: δ = 1.05 mms⁻¹, ΔE_Q = 2.83 mms⁻¹, Table 36). The small difference in δ can be explained by the temperature-dependent second-order Doppler shift.[213] This suggests a similar electronic environment for both iron(II) ions in the metastable HS state and in the high temperature HS state. The line broadening in the Mössbauer spectra in Figure 37 are due to the inherent vibrations of the cryogenic closed cycle cryostat used for these measurements. However, this has no influence on the determination of the given δ and ΔE_Q values and the relative area of the corresponding HS and LS iron species. Thus, it can be concluded that thermal quenching or rapid cooling of the sample does not result in a crystallographic phase change. Compared to SQUID magnetometry, it is possible to preserve up to 33 % of the HS state at very low temperatures (**e** and **f**). Although the preserved HS fraction is significantly smaller here, due to the slower cooling properties of the experimental setup, the results are in good agreement with the data of the SQUID magnetometry of the metastable state of C1. T$_{TIESST}$ and T$_{1/2↑}$ is also confirmed by the subsequent heating of the sample, which is confirmed by the decrease of the metastable HS-fraction (Figure 37 **g**) and subsequent spin switch between 110 K and 120 K (Figure 37 **j** and **k**). All other values and Mössbauer spectra, which are not shown in Figure 37, can be found in the appendix (Table 36, section 11.5.1).

C2 was also investigated using ⁵⁷Fe-Mössbauer spectroscopy at different temperatures, using the same experimental set up and conditions as used in the previous experiments and results are described in the following.
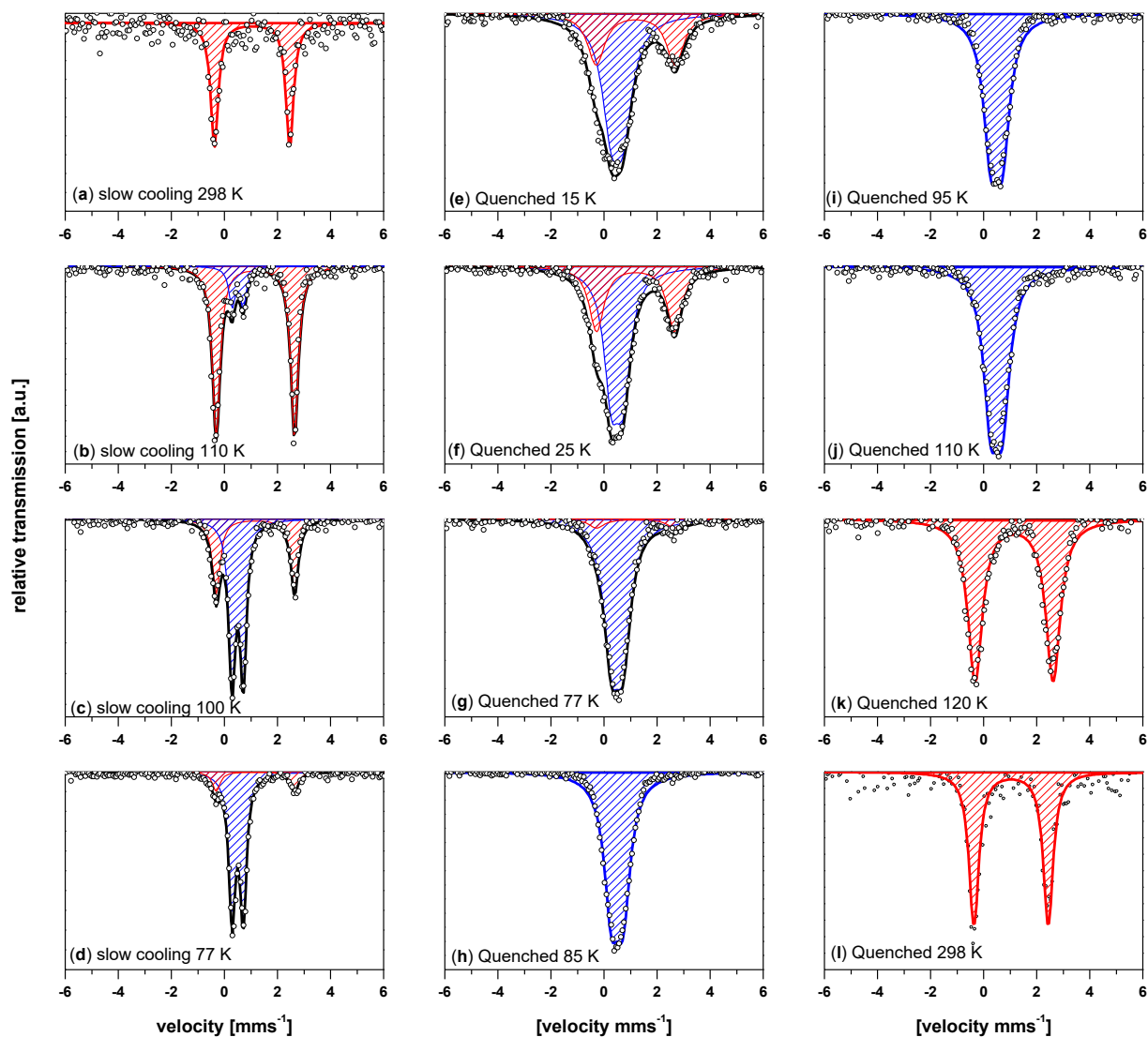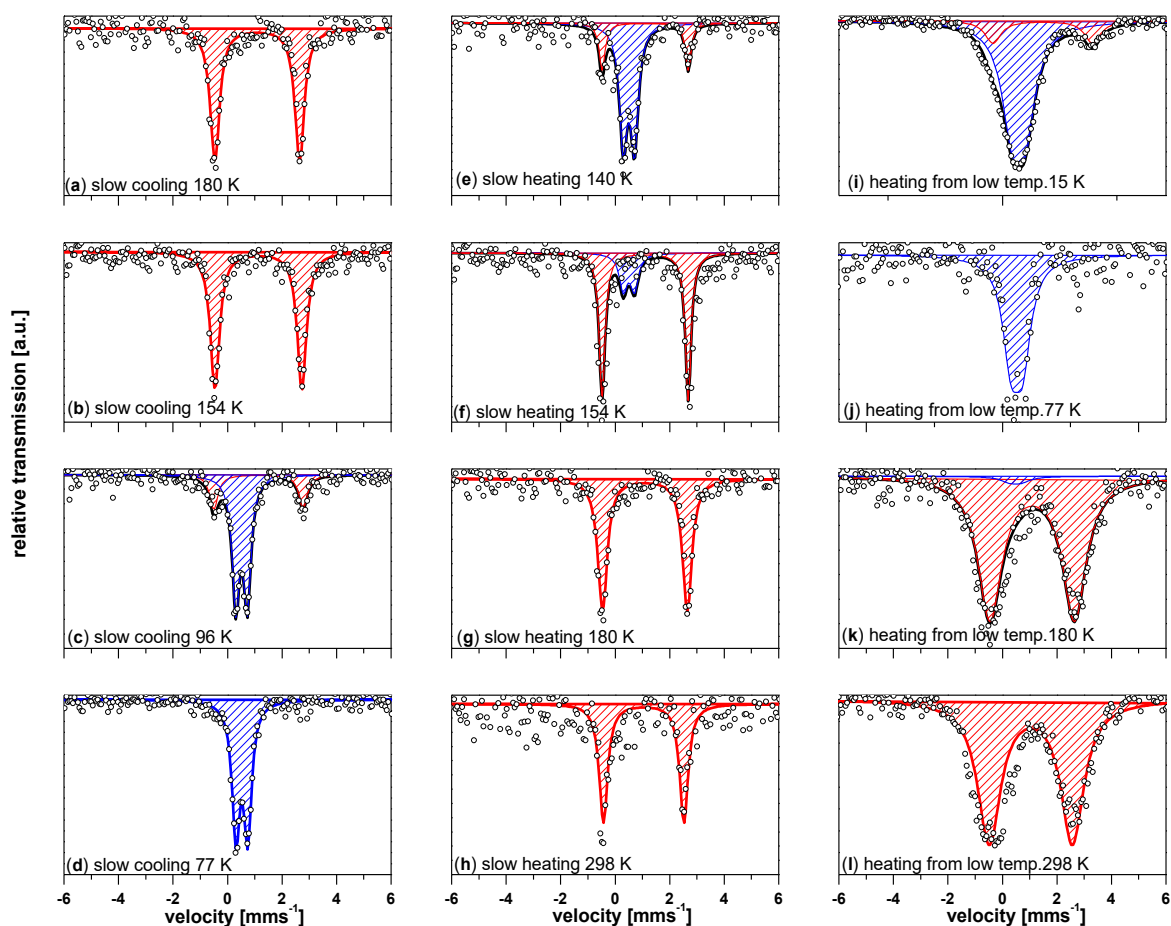
*Figure 38: **Left:** Mössbauer spectra of slow cooled **C2** down from RT at the given temperatures with a cooling rate of 1 K/min. The cooling sequence starts at 180 K ends at 77 K and and is chronologically referenced (**a-d**). **Middle:** Subsequent slow heating of **C2** from 77 K to RT (**e-h**); **Right:** Mössbauer spectra of **C2** cooled to very low temperatures with a cooling rate of 1.25 K/min and a subsequent heating rate of 1 K/min. The temperature sequence starts at 15 K and is chronologically referenced (**i-l**). **Colour code**: HS-states are depicted in red; LS-states are depicted in blue, the overall fits are depicted in black, while the black circles represent the actual measurement values. Solid lines are fits with parameters given in Table 37.*

Figure 38 also shows twelve spectra, but this time taken from **C2** recorded in cooling and heating mode: (**a**) slow cooling from room temperature at a cooling rate of 1 K/min to 180 K, (**b**) further cooling to 154 K, (**c**) 96 K and (**d**) 77 K, respectively. The sample was then heated directly to 140 K (**e**) at the same heating rate of 1 K/min, further heated to (**f**) 154 K, (**g**) 180 K and (**h**) 298 K. During the slow cooling process, the spectrum recorded at 180 K (Figure 38 **a**) shows a single species with an isomer shift δ = 1.09 mms^{-1}, a quadrupole splitting ΔE_Q = 3.10 mms^{-1} and a linewidth Γ = 0.42 mms^{-1}. These values are typical for iron (II) ions in HS state. [40,211–216] When cooling, the spin change is observed at 96 K (**c**), as shown by the spectra with two components, indicating the presence of iron (II) ions in the HS and LS state. Contrary, the spectrum at 77 K (**d**) shows one component with δ = 0.53 mms^{-1}, ΔE_Q = 0.43 mms^{-1} and Γ = 0.35 mms^{-1}, indicating the LS state of iron (II). [40,158,211–216] Once the LS state was reached at 77 K, the sample was again heated to room temperature. Spectra (**e**) and (**f**) in Figure 38 illustrate the spin switch at $T_{1/2}\uparrow$ (154 K). The data obtained from the Mössbauer analyses agree well with the collected magnetic susceptibility data (Figure 29), as both methods conclude again similar values for $T_{1/2}\downarrow$ and $T_{1/2}\uparrow$. In the case of **C2**, the TIESST plateau was also investigated using ^{57}Fe-Mössbauer spectroscopy at very low temperatures, based on the findings of SQUID

magnetometry. The experimental conditions for the low temperature measurements for **C2** were exactly as those described above for **C1**. Precisely the same Mössbauer sample of **C2** used for the previous experiments at nitrogen temperature was cooled to 15 K (**i**) at a cooling rate of 1.25 K/min and then heated to room temperature at a heating rate of 1 K/min with respective measurements at 77 K (**j**), 180 K (**k**) and 298 K (**l**) (Figure 38). The isomer shift δ and quadrupole splitting ΔE_Q of the observed HS state at 15 K (**i**) (δ = 1.14 mms^{-1}, ΔE_Q = 3.10 mms^{-1}) are observed to be similar to those at higher temperatures (e.g. at 180 K: δ = 1.09 mms^{-1}, ΔE_Q = 3.10 mms^{-1}). All other values and spectra not shown in Figure 38 can be taken from the appendix (Table 37, section 11.5.2). The small difference in δ of high and low temperature spectra is again due to the temperature dependent second order Doppler shift.[213] From this it can again be concluded, as in the above example, that thermal quenching or rapid cooling of the sample does not lead to a crystallographic phase change. The line broadening in the Mössbauer spectra in Figure 38 are due to the inherent vibrations of the cryogenic closed cycle cryostat used for these measurements. However, this has no influence on the determination of the given δ and ΔE_Q values and the relative area of the corresponding HS and LS iron species. By comparison with SQUID magnetometry, it is possible to preserve up to 15 % of the HS state at very low temperature (**i**). However, this result agrees well with the SQUID magnetic data of the metastable state at a cooling rate of 0.35 K/min. (**j**) shows only one species which can be assigned to iron (II) ions in the LS, while the spectrum measured at 180 K (**k**) shows an HS component with a share of 97 % and an LS component with a share of 3 %, which is comparable to the spectrum shown in (**g**). Spectrum (**l**) shows only one doublet with typical values for an iron (II) HS state. [40,158,211–216] Thus, the same spin transition temperature T$_{1/2}$↑ and the same thermal transition above 77 K results for the closed-loop cryostat when the sample is heated.

4.7.   Synchrotron X-ray diffraction at very low temperatures

For the confirmation of the correlation between the high-temperature phase and the metastable TIESST phase, crystal structures of **C1** at very low temperatures were recorded. These measurements were carried out at the BL02B1 beamline at Synchrotron Spring 8 in Japan and were done by ███████ ████████ of the University of Aarhus, Denmark. First, a single crystal was quenched to 20 K. The resulting structure was clearly in the HS state. Subsequently, the crystal was slowly cooled down from room temperature to 70 K. The compound was now in the LS state. The slow cooling from RT to 70 K consequently allows a complete spin transition from HS to LS. The distortion parameter of the iron ion in octahedral nitrogen coordination (∑=45.00°) and the average Fe-N bond distances of 1.956 Å are comparable to the values of the measured LS structure (Fe-N = 1.99 Å; ∑=43.96°) measured at 90 K with a conventional X-ray source. No crystallographic phase change and thus no change in the crystal system and space group ($P\overline{1}$) is observed despite the spin change from HS to LS. Moreover, the crystal structure of **C1** at 173 K and the structure of the thermally quenched **C1** at 20 K are very similar. The distortion parameter of the iron ion in octahedral nitrogen coordination comes to ∑=65.20° with the average Fe-N bond distance being 2.14 Å at 20 K. These values compare well with the values of the

measured HS structure at 173 K (<Fe N> = 2.16 Å; ∑=67.04°) and with literature values. [1,27,33,86,110] In the same way, no phase change and thus no change in the crystal system and space group type due to the rapid thermal quenching from **C1** to 20 K can be observed. Expressed differently: Based on the X-ray structure analysis of the metastable HS state, the molecule is in exactly the same HS state at 20 K as at 173 K, which confirms the results of the Mössbauer spectroscopy described in the previous section. The metastable HS state of the observed TIESST plateau can thus be identified as the frozen HS state observed at high temperatures. All data can be taken from the appendix (Table 2).

4.8. Pressure-induced Spin Crossover studies on [Fe^{II}(L^1)$_2$(NCS)$_2$] C1

In this section, the results of investigations on pressure-induced spin crossover phenomena in the [Fe(L^1)$_2$(NCS)$_2$] **C1** complex are presented. The measurements were carried out in collaboration with ▮▮▮▮▮▮▮▮▮▮, a master's student of ▮▮▮▮▮▮▮▮▮ at Aarhus University in Denmark. Selected results of the pressure study, which are presented with permission below, were produced in ▮▮▮▮▮▮▮▮▮ group. The samples used were prepared by me in the laboratory of ▮▮▮▮▮ ▮▮▮▮▮▮ group at the Johannes Gutenberg-University and provided for the study.

The investigations are based on structural research carried out with high-pressure X-ray diffraction methods using a diamond anvil cell to generate pressure in the range of 0.0-3.22(4) GPa. The investigations are designed to detect the occurrence of spin crossover due to external pressure stimuli as well as the determination of the pressure at which the crossover occurs. The effect of pressure on structural parameters such as unit cell parameters, volume, void space, Fe-N bond lengths, angle and torsion were investigated to identify a spin transition. In the following, however, only the influences of external pressure on selected data of cell volumes, bond lengths and bond angles will be discussed. In the high-pressure experiments described, the pressure was continuously measured using the ruby fluorescence method. This method uses a fluorescent material as a calibrant. Ruby, which is Cr^{3+}-doped Al$_3$O$_2$, strongly exhibits pressure-dependent peaks in its fluorescence wavelength. When excited by a laser, ruby emits fluorescently and produces two very distinct R-line signals at 692.86 nm and 694.25 nm under ambient pressure. The wavelength of the R-line shifts when the system is exposed to pressure. Subsequently, the pressure can be determined from the wavelength according to the following formula, Suggested by *Syassen et al.*[217,218]

$$P = A \cdot (\frac{\lambda}{\lambda_0} - 1) \cdot [1 + B^\lambda \cdot (\frac{\lambda}{\lambda_0} - 1)]$$

19

With A = 1870 GPa, B = 5.9

Single crystal high pressure X-ray diffraction on **C1** was performed at room temperature using a Boehler Almax diamond anvil cell (more details about the set up can be taken from section 9). To cover

the pressure range in small pressure steps, two different crystals were used. The pressures used for the measurement are given in Table 1.[219]

Pressure point	Pressure (GPa)
P0	0.0
P1	0.24(2)
P2	0.40(2)
P3	0.52(5)
P5	0.8(3)
P6	1.02(6)
P7	1.14(3)
P8	1.74(2)
P9	2.7(1)
P10	3.22(4)

Table 1: Naming scheme of pressure points with corresponding pressure.[183,219]

The data sets for the pressure points P0-P10 cover a pressure range of 0.0-3.22(4) GPa. More information about the measured structures at the given pressure points are given in Table 38 of the appendix (section 11.7). The volume of the unit cell decreases continuously with increasing pressure. Between the pressure points P5 and P6 with pressure values of 0.8(3) and 1.02(6) GPa, respectively, a more pronounced decrease in volume is observed (Figure 39). The decrease in volume can be seen even more clearly if not the entire volume of the unit cell is considered, but only the volume of the empty voids that are present in the unit cell. A clear indication of a possible spin change between the two pressure points P5 (0.8(3) GPa) and P6 (1.02(6) GPa) is detected (Figure 39 right).
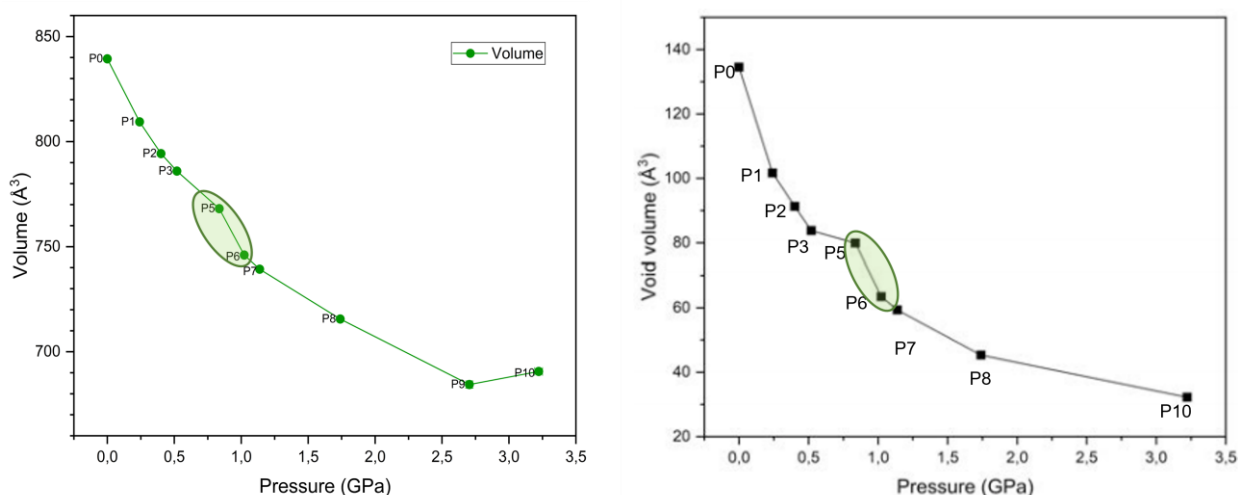
Figure 39: (left) Unit cell volume as a function of pressure with labelling of pressure points for clarity. (right) Void volume as a function of pressure. P9 was omitted due to insufficient data. The figure was reproduced with permission.[219]

The bond lengths between the iron atoms and the surrounding nitrogen atoms of the respective solved structures as a function of pressure are shown in Figure 40. In the pressure range of 0.0-0.8(3) GPa

(P0-P5), the changes in Fe-N1 and Fe-N2 bond lengths are relatively small. In general, the bond lengths are observed to be slightly shorter than for the structure at ambient pressure, and a decreasing trend can be seen, but minor variations are observed, which can be related to the uncertainties. The uncertainty limits for the Fe-N1 bond lengths are more pronounced than for Fe-N2. In contrast, the variation for the Fe-N4 bond lengths is more pronounced with changes in bond length of up to 0.05 Å in the same pressure range. This is consistent with the fact that the thiocyanate ligands are monodentate and thus more flexible than the chelating pyridine-thiadiazole binding pocket of the ligand and consequently more likely to be affected by increased pressure. This also becomes visible in the dependence of the bond angles as a function of the pressure, which will be discussed in more detail later. In the pressure range of 0,8(3)-1,02(6) GPa (P5 and P6), a clear decrease is observed for all bond lengths considered, especially for Fe-N1 and Fe-N2.
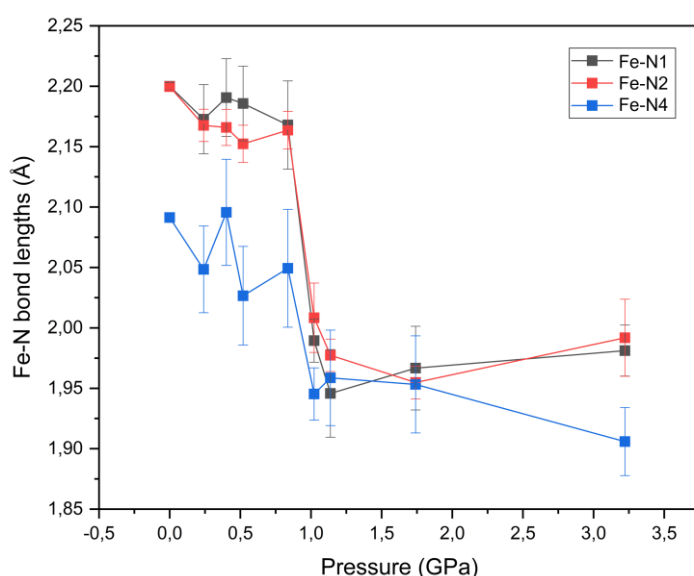

Figure 40: Fe-N bond lengths as a function of pressure. A significant decrease between P5 and P6 can be detected for all Fe-N bond lengths. The figure was reproduced with permission.[219]

The differences of the Fe-N_x bond lengths of the structures at 0.0 GPA (P0), 0.8(3) GPa (P5) and 1.02(6) GPa (P6) are compared in

	Fe-N1 bond	Fe-N2 bond	Fe-N4 bond
P0 bond length (Å)	2.200(3)	2.200(3)	2.091(4)
P5 bond length (Å)	2.17(3)	2.16(2)	2.05(5)
P6 bond length (Å)	1.99(1)	2.01(3)	1.95(2)
Difference P5-P6 (Å)	0.18(5)	0.16(4)	0.10(7)
Difference P5-P6 (%)	8.2	7.2	5.1
Difference P0-P6 (Å)	0.21(2)	0.19(3)	0.15(3)
Difference P0-P6 (%)	9.5	8.6	7.2
Difference P0-P5 (Å)	0.03(4)	0.04(2)	0.04(5)
Difference P0-P5 (%)	1.4	1.8	1.9

Table 39 of the appendix (section 11.7). The structures have values for the bond lengths, which can be assigned to different spin states for iron (II) and are typical for LS and HS. Clearly, this is an indication of a pressure-induced spin transition.

The success of the pressure-induced SCO is also illustrated by the bond angles of atoms N4-C18-S2 and Fe-N4-C18 of the monodentate thiocyanate ligand which is shown in Figure 41.
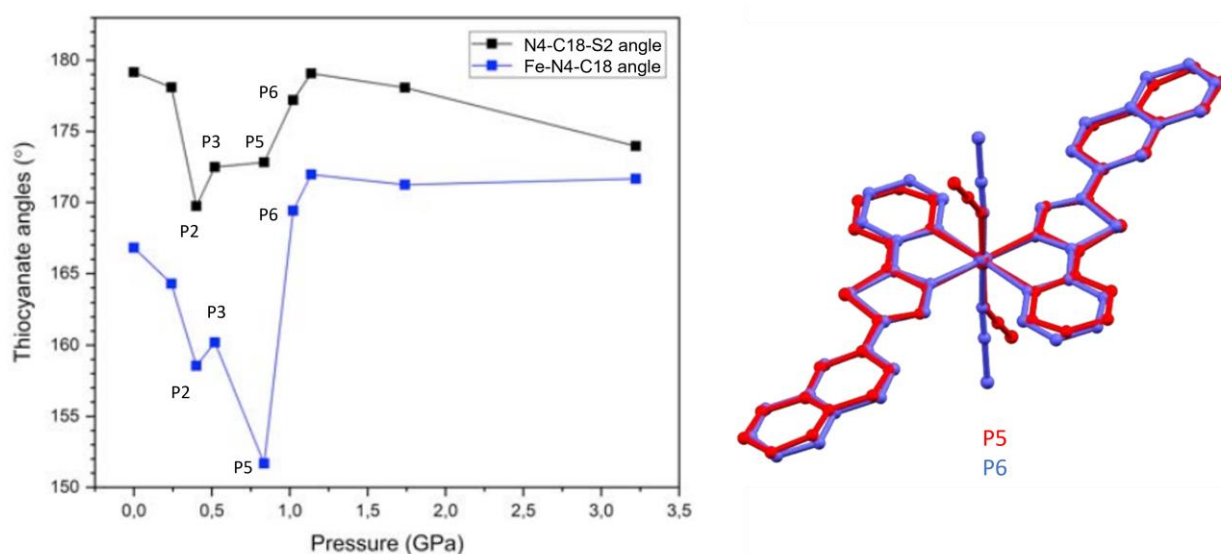

Figure 41: (left) Thiocyanate bond angles of atoms N4-C18-S2 and Fe-N4-C18 as function of pressure. (right) Superimposition of P5 (red) and P6 (blue) with indication of the two HS and LS structures, respectively, just before and after the pressure-induced spin transition. The pressure points P4 and P9 are omitted, due to insufficient data. The figure is reproduced with permission.[219]

Under ambient pressure, the thiocyanate ligand is approximately linear, but under applied pressure, the bond angle deviates from 180°, which is particularly pronounced at the P2, P3 and P5 pressure points. More striking, however, is the angle between the atoms Fe-N4-C18. With increasing pressure, the angle decreases steadily and at the same time the difference to 180° as under normal pressure increases (Figure 41). This deviation from 180° is at a maximum at the pressure point P5. As we can see from the above changes in volume or bond lengths, there is a spin transition between 0.8(3) and

1.02(6) GPa (P5 and P6). Due to this spin transition and the associated reduction of the ion radii, the mentioned angle increases again and approaches 180° again. The difference between the two structures at given pressures P5 and P6 is also shown in Figure 41 by superimposing them with the Mercury programme.[220] The different angle at different spin states (HS⟷LS) of the thiocyanate ligand is clearly visible.

In conclusion, this chapter shows that the collaborative work with ███████████████ and ███████ ███████ has successfully demonstrated that **C1** exhibits pressure-induced SCO behaviour in the pressure range of 0.8(3) and 1.02(6) GPa. Due to the similar behaviour of **C1** and **C2**, both structurally and magnetically, it would be very interesting to investigate **C2** for these properties as well. Furthermore, the change in magnetic susceptibility and thus the influence on the existing hysteresis properties and the metastable states created by quenching at low temperatures due to external pressure willbe interesting to investigate.

4.9. Further investigations on the complex family [Fe(L^1)$_2$(NCX)$_2$]

4.9.1. Investigations on C3

As described in chapter 4.3, complex **C3** with the molecular formula [Fe^{II}(**L^1**)$_2$(NCBH$_3$)$_2$] was also synthesised and characterised. The results and shortcomings of the investigation of this compound and why **C3** behaves differently from complexes **C1** and **C2** are presented below.
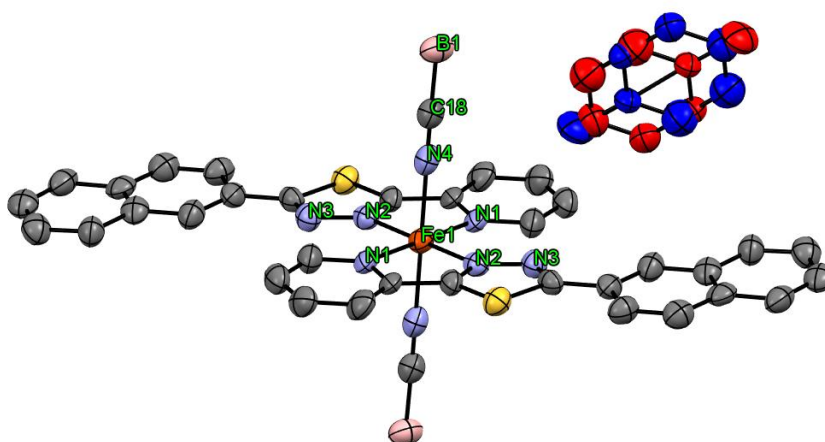
4.9.2. Crystal structure of C3

*Figure 42: Crystal structure of **[Fe(L^1)$_2$(NCBH$_3$)$_2$] · C$_7$H$_8$ C3**. Hydrogen atoms omitted for clarity. Disordered toluene molecules with occupancy of 0.5, respectively are coloured in red and blue regarding their symmetry operation. Color Code: grey-C, yellow-sulfur, blue-N, orange-Fe, white-H. ORTEP representation with atomic displacement parameters at 50% level of probability.*

The complex with the molecular formula **[Fe(L^1)$_2$(NCBH$_3$)$_2$] · C$_7$H$_8$ C3** crystallizes in the triclinic space group $P\overline{1}$ at 160 K. The asymmetric unit contains half of the molecule with the iron (II)-ion located on the centre of inversion and one molecule of toluene with occupancy of 0.5. Thus, the unit cell exhibits two molecules of respective disordered toluene. Due to the sterically demanding NCBH$_3^-$ counterions, it is most likely possible that toluene can be deposited as a solvent in the resulting voids in this example. Additionally, **C3** exhibits a distorted octahedral coordination environment formed by two trans-coordinating cyanoborohydride anions and by two molecules of **L^1**, giving an overall neutral complex molecule. **L^1** coordinates using the nitrogen atoms of the 2-pyridyl group and one of the thiadiazole group. Thus, the pyridyl and thiadiazole backbones of the ligands span the equatorial plane with the iron (II) ion in the middle, while the naphthyl group is tilted 8.99° from the coordination plane. Furthermore, it is striking that the naphthyl unit of the ligand rotates in the direction of the

coordination sphere, as shown schematically in Figure 43. Presumably this is caused by the incorporated toluene, as this interacts with the ligand as described later.
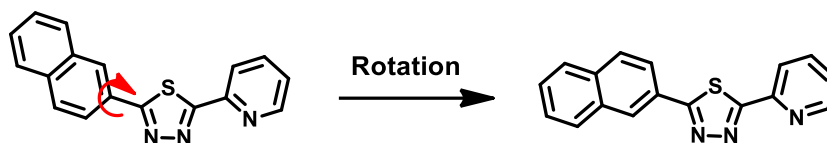

Figure 43: rotation of the naphthyl moiety towards the coordination sphere.

The average Fe-N bond length of 2.08 Å at 160 K is smaller than expected typical for HS state and higher than expected for low spin state, possibly indicating the crystal structure was measured around a spin transition point.[1,27,33,110] The bite angle of the coordinating pyridyl and thiadiazole unit (N1-Fe-N3) is found to be 77.95°, while the NCS-Co ligands coordinate with an angle of 177.90°. The two NCBH$_3^-$ moieties are almost linearly coordinated to each other (178.84°). The octahedral distortion parameter Σ is 59.48°. The value is comparable to the literature known SCO systems coordinating equatorially via pyridine and thiadiazole and pseudohalides as axial co-ligands.[43,151,152] Due to the π-π-interactions (3.33 Å-3.58 Å) of the anti-parallel coordinating ligands **L^1** of the neighbouring complex molecules, the **C3** complex molecules propagate as chains along the b-axis. Along the c-axis, these **C3** chains alternate with a layer of solvent of disordered toluene in an ABAB-sequence. The toluene is building a T-shaped C-H···π-interactions (distance 2.74 Å) with the ligand molecules of the complex (Figure 44). Distances and offsets of all π-π-interacting parts are in the range of interactions well-known from literature (3.33 Å to 3.58 Å)..[200,201] All exact values can be taken from the appendix (Table 14 of section 11.4.1).
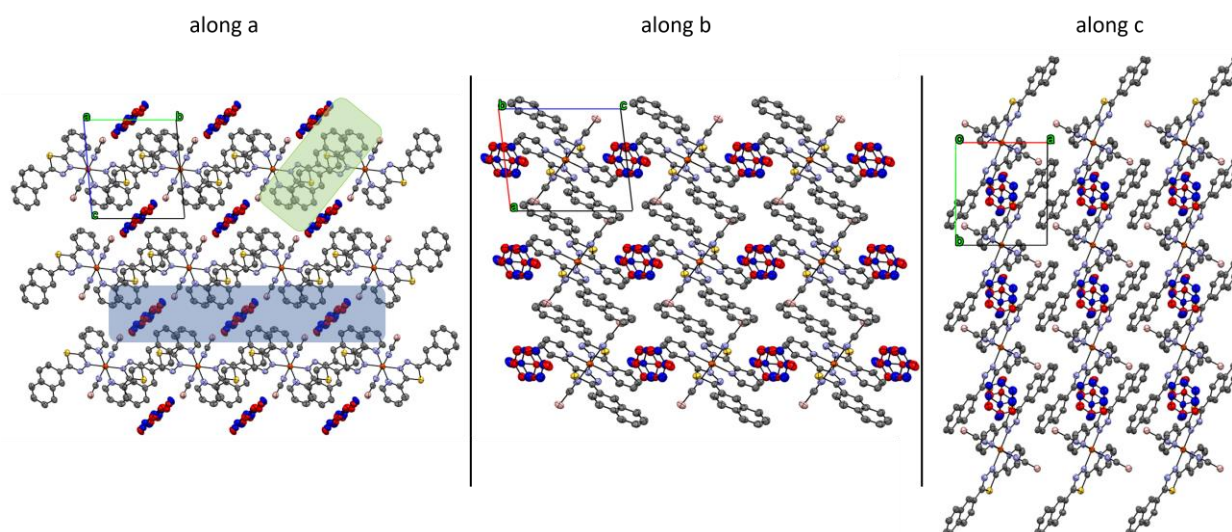

*Figure 44: **along a**: Selected part of the crystal structure of **C3** along the a-axis. Highlighted in green are the π-π-interactions of the anti-parallel oriented ligands of neighbouring complex molecules. Additionally, highlighted in blue are the incorporated disordered toluene molecules building T-shape C-H···π-interactions; **along b:** Selected part of the crystal structure of **C3** along the b-axis; **along c:** Selected part of the crystal structure of **C3** along the c-axis. Color Code: grey-C, yellow-sulphur, blue-N, orange-Fe, white-H. The disordered toluene solvent molecules are marked in dark blue and red, respectively, depending on their symmetry operation. ORTEP representation with atomic displacement parameters at 50% level of probability.*

4.9.3. Variable temperature magnetic susceptibility measurements of [Fe(L^1)$_2$(NCBH$_3$)$_2$] · C$_7$H$_8$ **C3**

Variable temperature magnetic susceptibility measurements were performed on dried samples stored under air conditions as well as on freshly prepared samples measured with mother liquor. For **C3**, significant differences between the two measurement methods were found, leading to a solvent dependency of the crystalline compounds under the given conditions. A temperature range of 2 – 400 K under an external magnetic field of 1000 Oe was used for the data collection of the magnetic susceptibility. The cooling and heating rate (2 K/min) was not varied in both cases.

Whereas **C1** and **C2** are very similar in their magnetic properties, **C3** shows clearly different behaviour (Figure 45). The magnetic susceptibility acquisition was started at 300 K with a $\chi_M T$ value of 2.71 cm^3 K mol^{-1}. At 2 K, a $\chi_M T$ value of 0.14 cm^3 K mol^{-1} was obtained. A clear two-step SCO behavior with abrupt spin transitions was observed. The spin transition is almost complete. The $\chi_M T$ value of the intermediate plateau can be read as 2.03 cm^3 K mol^{-1}. The small drop in $\chi_M T$ at very low temperatures can possibly be assigned to zero field splitting effects.[37,205] It is also worth mentioning that quenching at low temperatures does not cause any trapping of the metastable spin state. Subsequently, the sample was again heated to 400 K showing unchanged spin transition temperatures at $T_{1/2\downarrow\uparrow}(1) = 160$ K and $T_{1/2\downarrow\uparrow}(2) = 300$ K for the cooling and heating process measured in mother liquor and thus no hysteresis is observed. In the previous section it was already assumed, based on the X-ray structure analysis that the structure of **C3** could not be assigned to a clearly definable spin state (HS or LS) at 160 K. This is now confirmed by the measurement of the molar magnetic susceptibility, as shown in Figure 45. The plateau of magnetic saturation with $\chi_M T = 3.34$ cm^3 K mol^{-1} of the HS state is slowly reached at 400 K. The sample was kept at 400 K for 10 minutes until cooling to low temperatures was repeated. **C3** exhibits different behaviour for the second cooling process showing a slightly different $T_{1/2\downarrow}(3) = 290$ K, while the region of the plateau at $\chi_M T$ of 2.03 cm^3 K mol^{-1} is almost completely vanished.

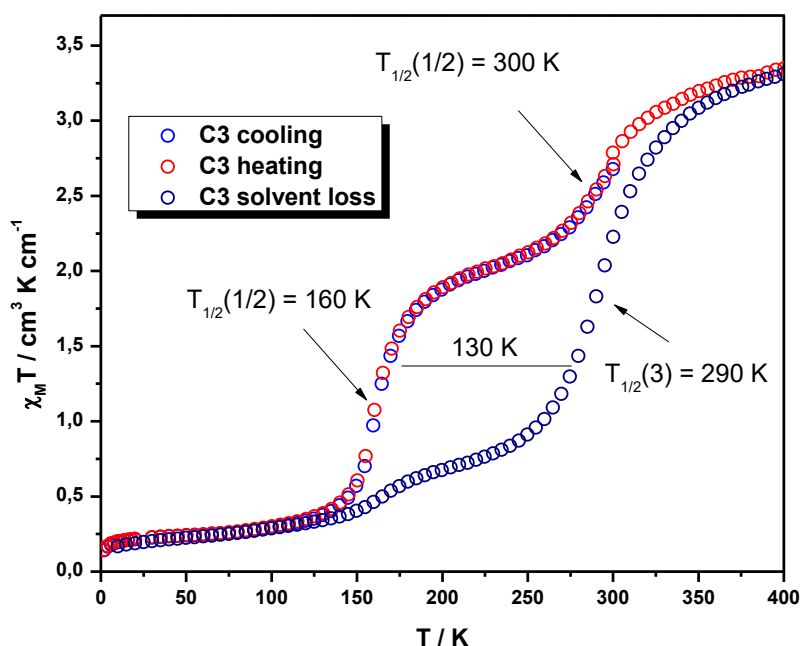*Figure 45: Measurement of the magnetic susceptibility of $[Fe(L^1)_2(NCBH_3)_2] \cdot C_7H_8$ C3 at variable temperature. The spin transition temperatures are respectively $T_{1/2}\downarrow\uparrow(1) = 160$ K and $T_{1/2}\downarrow\uparrow(2) = 300$ K measured in mother liquor. $T_{1/2}\downarrow\uparrow(1) = 160$ K disappears under solvent loss during the measurement, showing clear solvent dependency. Additionally, $T_{1/2}\downarrow$ shifts from 300 K to 290 K.*

Most often, two-step SCO is observed in complexes exhibiting two crystallographically non-equal metal sites in the LS and/or in the HS phase.[40,221,222] However, two-step transitions can also occur in compounds with crystallographically equivalent metal ions.[223–225] In this case, the two-step spin transition behaviour can be explained by either long range elastic interactions or inter- and intramolecular antagonistic short range interactions.[42] However, the lack of crystal structures at different temperatures other than 160 K or detailed Mössbauer investigations means that the exact nature of the two-step spin crossover remains to be determined. However, based on the results of the magnetic measurements, it can be assumed that this is a solvent-driven two-step SCO due to temperature-dependent release of the toluene molecules. Different solvatomorphs of complexes are well known from literature and the observed disappearance of the two-step SCO is mostly assigned to the loss of solvent molecules in the crystal lattice.[41,226,227] In addition, the disorder of the solvent could also play a decisive role and thus have an influence on the elastic interactions within the solid through the C-H⋯π interaction with the complex molecules. Similar examples of the influence of disordered molecules within the crystal have been reported in the past.[79,80] In order to make a precise statement for **C3**, further experiments are necessary.

Further results and projects

Due to the abundance of successful and very informative results of the research on the complex family [Fe(L^1)$_2$(NCX)$_2$] (X = S (**C1**), Se (**C2**), BH$_3$ (**C3**)), which was built up by the ligand **L^1**, the ligand was modified in several further projects. These changes are intended to show the structural influence of the ligand on the magnetic properties.

<u>5.</u>   Family of mononuclear [Fe(L^2)$_2$(NCX)$_2$] complexes (X = S, Se, BH$_3$)
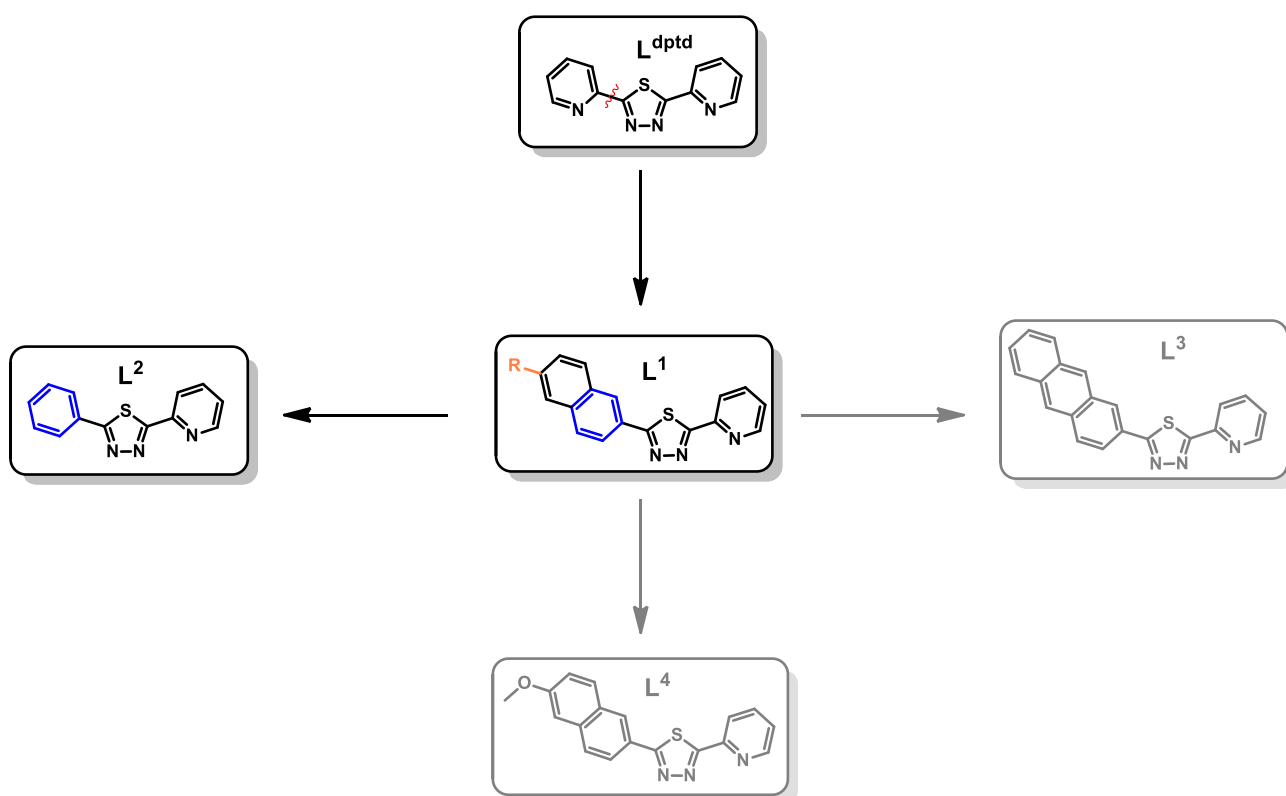

Figure 46: Evolution of ligand L^1 leading to the preparation of ligand L^2.

All magnetic properties of the complex family formed by the ligand **L^1** were dominated by high cooperativity within the crystalline bulk material. **L^1** formed strong π-π-interactions with surrounding ligand molecules of neighbouring complexes, which propagate across all spatial directions. Coupled with the appropriate ligand field, ensured by the well-known SCO binding pocket consisting of a pyridyl and a thiadiazole unit as well as pseudohalides as co-ligands, [43,151,152] many exciting properties could be discovered. Based on these findings, the new ligand **L^2** was developed (Figure 46), which does not differ fundamentally from ligand **L^1**, but which has a smaller π-system (a phenyl group instead of naphthyl group). By replacing the naphthyl group with a phenyl group, a reduction of the intermolecular cooperativity and therefore differences in the magnetic properties is expected. The question is hence: How do the complexes formed with ligand **L^2** behave in the solid state and what exactly is the role of the π-π-interaction described in the previous examples in the generation of the

intrinsic magnetic properties? Presented here is to what extent the changes of the ligand affect the properties of the complex series. The following ligand **L²** (2-phenyl-5-(pyridin-2-yl)-1,3,4-thiadiazole) and most of the results were obtained in cooperation with one of my bachelor students during his thesis, ▮▮▮▮▮▮▮▮▮.

5.1. Synthesis of 2-phenyl-5-(pyridin-2-yl)-1,3,4-thiadiazole L²
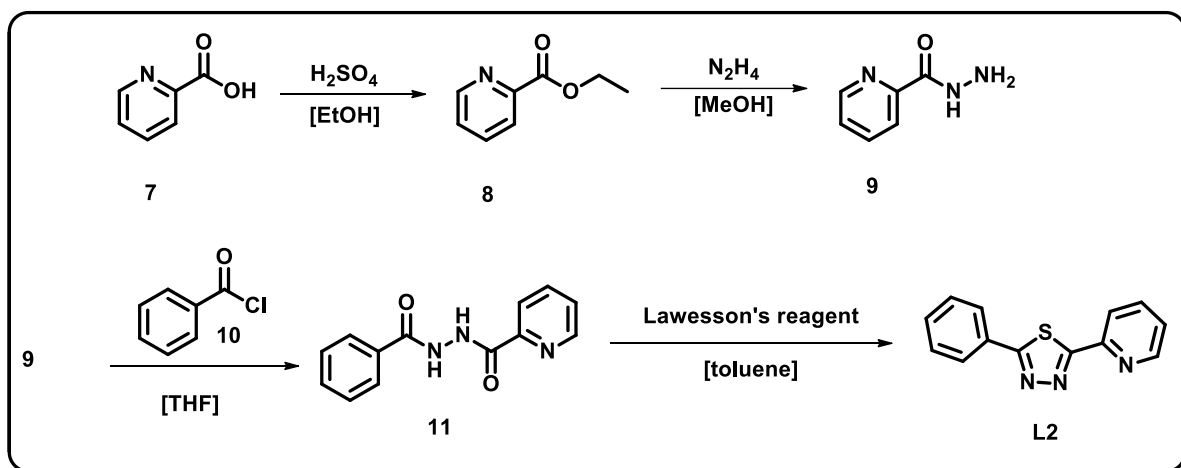
*Scheme 3: Synthesis route of **L²** (2-phenyl-5-(pyridin-2-yl)-1,3,4-thiadiazole).[41,158,185,186] The detailed description of the individual synthesis steps, yields and analytical characterisation can be taken from the experimental section.*

The ligand 2-(pyridin-2-yl)-5-phenyl-1,3,4-thiadiazole (**L²**) was prepared in a four-step synthesis (Scheme 3). Starting with pyridine-2-carboxylic acid (**7**), the acidic esterification was carried out in ethanol to give ethyl 2-pyridine carboxylate (**8**). Subsequently, compound **8** was reacted in a nucleophilic substitution with hydrazine hydrate in methanol to give pyridine-2-carboxylic acid hydrazide (**9**), according to a modified literature procedure.[185] Compound **9** and benzoyl chloride (**10**) reacted in a nucleophilic substitution to give N`-(2-benzoyl)-pyridine-2-carboxylic acid hydrazide (**11**). Compound **8** was reacted to 2-(pyridin-2-yl)-5-phenyl-1,3,4-thiadiazole (**L²**) with Lawesson's reagent in an intramolecular cyclisation reaction already used by *Herold*[41,158] and *Fürmeyer*[40,156,165] to synthesize ligand systems based on coordinating 1,3,4-thiadiazoles. The successful synthesis of **L²** was verified by NMR- (¹H, ¹³C, COSY, HMBC, HSQC), IR-spectroscopy and mass spectrometry. Figure 47 shows the ¹H-NMR spectra of **L²**. The number of the respective signals and the integrals agree with the expected values. The assignment of the protons and all other spectra are shown in the experimental part (chapter 9) and the additional appendix (chapter 11).
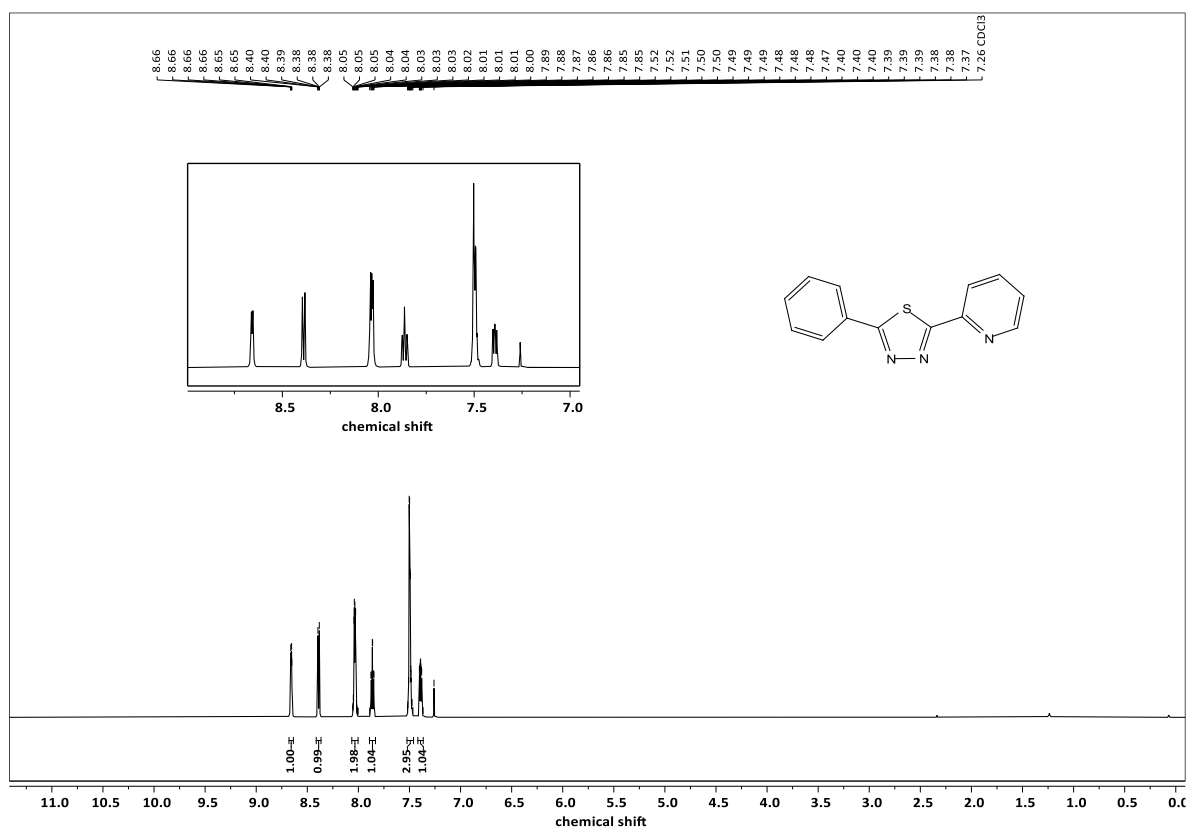
*Figure 47: ^{1}H-NMR of 2-phenyl-5-(pyridin-2-yl)-1,3,4-thiadiazole (**L^2**) measured at 600 MHz. For a better understanding, only the peaks with the respective integrals, as well as a zoom of all aromatic signals that can be observed, are shown. A precise assignment of all signals can be found in the experimental part.*

5.2. Synthesis of the complex family [Fe^{II}(NCX)$_2$(L^2)$_2$] (X = S, Se, BH$_3$).

Successful preparation and isolation of the ligand **L^2** enabled its use for the preparation of iron (II) complexes with the molecular formula [Fe^{II}(NCX)$_2$(L^2)$_2$] (X = S, Se, BH3). The complexes were synthesised by liquid-liquid diffusion. A solution of the ligand in several solvents was layered with a solution of the corresponding dissolved metal salt. All reactions were done under inert gas atmosphere and were carried out with degassed and dried solvents. Methanol, acetonitrile and dichloromethane proved to be the most suitable solvents for complex formation via liquid-liquid diffusion. The salts used to form the complexes **C4** [Fe^{II} (NCS)$_2$(L^2)$_2$], **C5** [Fe(NCSe)$_2$(L^2)$_2$] and **C6** [Fe^{II} (NCBH$_3$)$_2$(L^2)$_2$] were FeSO$_4$·7H$_2$O, KSCN, KSeCN and [Fe^{II} (py)$_4$(NCBH$_3$)$_2$]. Single crystals as well as microcrystalline powders were obtained of all complexes. The complexes were crystallized in the same way than **C1**, **C2** and **C3** (section 4.3). Only the ratio of the used solvents MeOH and DCM was varied to find the most suitable concentration for the formation of single crystals. For complexes **C4** and **C5**, the best results were obtained with a 2:1 methanol: DCM ratio. For complex **C6**, an acetonitrile: DCM mixture in the same 2:1 ratio was used. Single crystals of **C4** and **C5** suitable for X-ray structure analysis were obtained after 72 hours as grey-violet, rod-shaped crystals. Crystals were obtained for **C6** as purple very small cubic crystals, after approximately 72 hours. Except for **C6**, the complexes were characterised by IR

spectroscopy, X-ray structure analysis and measurements of the molar magnetic susceptibility. For **C6**, no X-ray structure analysis was possible because the obtained single crystals were too small and very fragile. In the following (Figure 48), the infrared spectra of the synthesised complexes **C4** (red), **C5** (cyan) and **C6** (blue) are compared with the ligand **L²** (black). Due to more clarity, the spectra were normalised and vertically shifted. Intense bands can be observed in the spectra for **C4** at 2055 cm⁻¹, for **C5** at 2061 cm⁻¹ and for **C6** at 2192 cm⁻¹ and 2332 cm⁻¹, respectively. These bands can be assigned to the co-ligands NCS⁻ (1990-2140 cm⁻¹), NCSe⁻ (2072 cm⁻¹) and NCBH₃⁻ (v_{CN}=2070-2240 cm⁻¹; v_{BH}=2315-2380 cm⁻¹), respectively. [151,152,178,193,196–199]
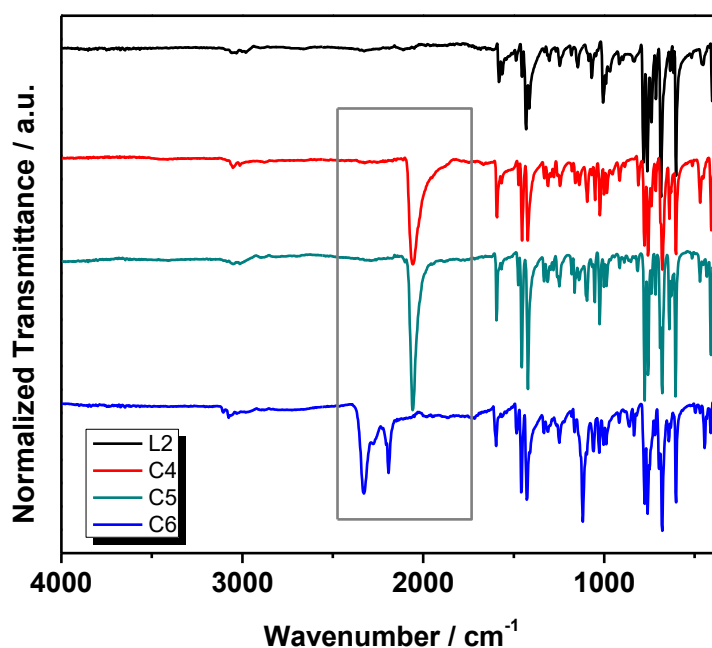

*Figure 48: Normalized Infrared spectra of **L2**, **C4**, **C5** and **C6** in one graph. The spectra are offset from each other for more clarity. The grey box marks the characteristic IR-bands of the coordinating pseudohalides of the respective complexes; SCN⁻ for **C4**, SeCN⁻ for **C5** and NCBH₃⁻ for **C6**.*

By comparing the measured infrared spectra of the respective complexes and the spectrum of the ligand, a successful complex formation can be assumed. However, by means of infrared spectroscopy alone, no statement can be made about the crystal structure, packing effects or cooperative effects. Therefore, the X-ray structure analyses of the complexes must be included and are discussed in the following chapter. A brief comparison to the previously obtained complexes will be given where necessary. All associated magnetic properties are discussed in section 5.4. Based on the results of previous studies, it is assumed that the complexes are similarly coordinated as already seen in the complex series [Fe^{II}(NCX)₂(**L¹**)₂] (X = S (**C1**), Se (**C2**), BH₃ (**C3**))

5.3. Crystal structure of C4 and C5
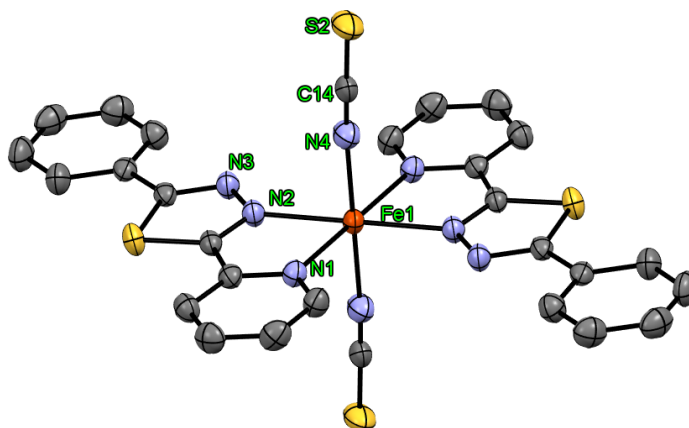
*Figure 49: Molecular structure of **[Fe^{II}(L^2)$_2$(NCS)$_2$] · 2 CH$_2$Cl$_2$ C4**. Hydrogen atoms and solvent molecules (disordered DCM) are omitted for clarity Color Code: grey-C, yellow-sulfur, blue-N, orange-Fe, white-H. ORTEP representation with atomic displacement parameters at 50% level of probability.*

The complex with the molecularformula **[Fe^{II}(L^2)$_2$(NCS)$_2$] · 2 CH$_2$Cl$_2$ (C4)** crystallizes in the triclinic space group $P\bar{1}$ at 173 K (Figure 49). The asymmetric unit (Figure 141) contains half of the molecule with the iron (II) ion located on the centre of inversion and one disordered dichloromethane solvent molecule. A moderately distorted octahedral coordination environment for the central atom is formed by two molecules of **L^2** and two trans-coordinating thiocyanate anions formed by the coordinating nitrogen atoms, resulting in a neutral complex molecule. **L^2** coordinates with the nitrogen atoms of the 2-pyridyl group and one of the thiadiazole core. The pyridyl and thiadiazole backbones of the ligands span the equatorial plane with the iron ion centre, while the phenyl group is just slightly twisted by 1.10°. In contrast to complex **C1**, the coordinating ligand is therefore almost planar. The bite angle of the chelating ligand (N1-Fe-N2) is 75.36° with NCS co-ligands coordinating at an angle (Fe-N4-C14) of 174.24° (the two N-C-S anions are nearly linear at 178.64°). The average Fe-N bond length of 2.17 Å at 173 K is in the range for iron(II) complexes and is typical for HS state.[1,27,33,110] The octahedral distortion parameter Σ comes to 67.94° and clearly differs from the typical values for HS complexes (Σ > 100°).[86] However, the values are in good agreement as in the previous cases with comparable SCO systems known in the literature that coordinate equatorially via pyridine and thiadiazole and pseudohalides as axial co-ligands[43,151,152] As already mentioned, dichloromethane solvent molecules are incorporated into the structure. As a result of this intercalation, the complex and solvent molecules arrange as a layer structure of the sequence ABAB (Figure 50), with **C4** propagating as a 2D-scaffold along the crystallographic a- and b-axis via π-π-interactions, build by the interaction of pyridyl and phenyl groups. Distances and offsets of all π-π-interacting parts are in the range of interactions well-known from literature (3.45 Å to 3.60 Å).[200,201] All exact values can be taken from the appendix (Table 17 in section 11.4.2).The dichloromethane molecules move along the crystallographic b-axis in a zig-zag pattern with alternating distances of 2.99 Å and 2.51 Å each, while the Fe-Fe distances come to 7.68 Å along the a-axis, 9.50 Å along the b-axis and 12.83 Å along the c-axis (Figure 142). The inversion

symmetry of the complex molecules leads to an anti-parallel arrangement of the coordinating ligands L^2 of two neighbouring complex molecules, respectively. However, there is no cooperative interaction pathway via hydrogen bonding between the two different layers and the distance is 4.98 Å.
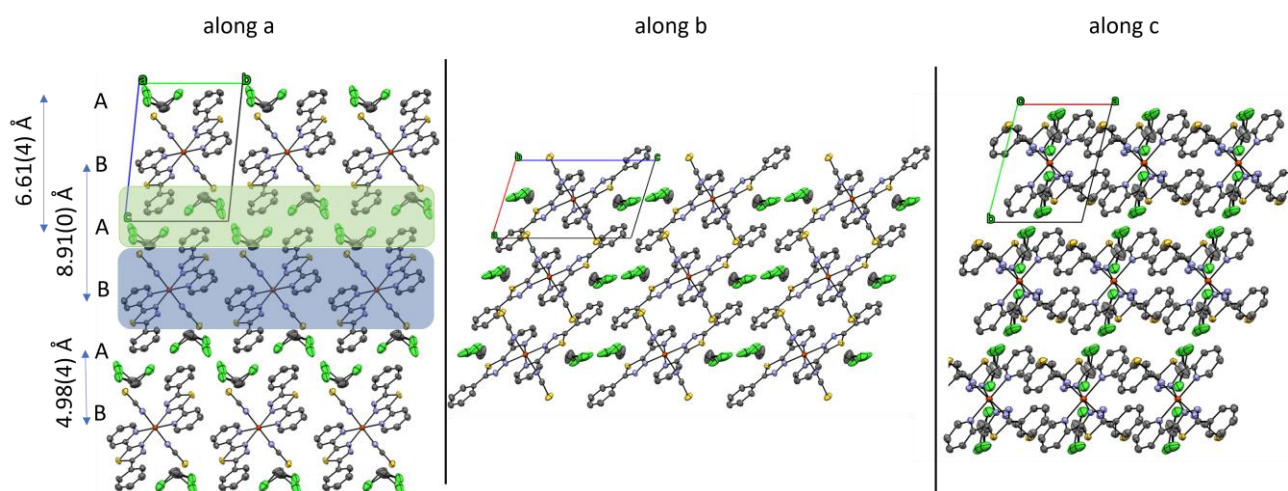

*Figure 50: **along a**: Selected part of the crystal structure of **C4** at 173 K along the a-axis. The complex molecules as well as the DCM solvent molecules are arranged alternately along the b-axis in an ABAB sequence. **along b**: Selected part of the crystal structure of **C4** at 173 K along the b-axis. The complex molecules as well as the DCM solvent molecules are arranged alternately along the b-axis in an ABAB sequence. **along c**: Selected part of the crystal structure of **C4** at 173 K along the c-axis. Highlted are the different layers in green (A) and blue (B) and the respective distances. Color Code: grey-C, yellow-sulphur, blue-N, orange-Fe, green-Cl white-H. ORTEP representation with atomic displacement parameters at 50% level of probability.*

As shown in the figure below (Figure 51), **[Fe^{II}(L^2)$_2$(NCSe)$_2$] · MeOH** (**C5**) has the same trans-coordination geometry as **C4**, but the complexes are not isostructural. Furthermore, the incorporated solvent is methanol instead of dichloromethane. The reaction conditions were the same for **C4** and **C5**. The single crystal diffraction for **C5** was measured at 90 K and 240 K. The structures are the same for both temperatures and so the structure is just described for 90 K. More information can be taken from the appendix (Table 15 in section 11.4.2)
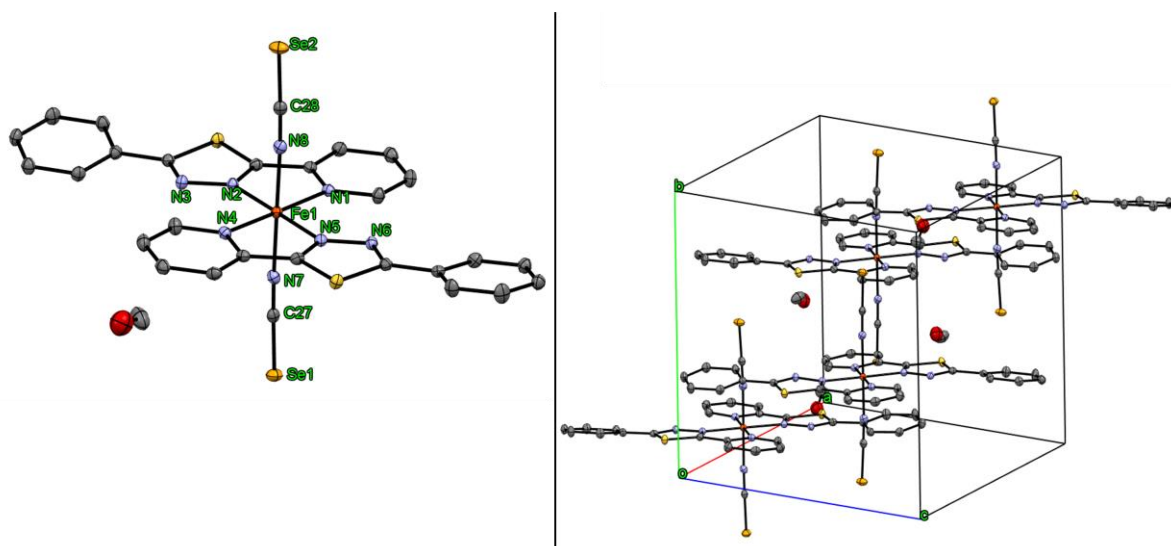
*Figure 51: (**left**) asymmetric unit of **C5**, containing one complex molecule and one solvent molecule of methanol. (**Right**) Unit cell of **C5**. Hydrogens have been omitted for clarity. Color Code: grey-C, yellow-sulphur, blue-N, orange-Fe, red-O white-H. ORTEP representation with atomic displacement parameters at 50% level of probability.*

The complex crystallises in a monoclinic crystal system and exhibits the space group $P2_1/c$ at 90 K. Accordingly, the structure is symmetrically generated by a 2-fold screw axis along the b-axis and a c-glide (translation along c axis) in the ac-plane, perpendicular to the b-axis (Figure 144). The asymmetric unit of the structure thus consists of a full complex molecule, i.e. the iron(II) ion with two ligand molecules of L^2 and two coordinating NCSe$^-$ anions plus one solvent molecule methanol. This results in four complex molecules and four molecules of methanol per unit cell. The iron (II) centre of the complex is located in an octahedral nitrogen coordination sphere. The atoms N1, N3, N5 and N7 span the equatorial plane of the octahedron with the atoms N4 and N8 in apical positions. Due to the missing inversion centre located at the iron (II) ion position, the bite angles of the two coordinating ligands slighty differ (80.33° for N1-Fe-N2 and 80.15° for N4-Fe-N5). The two different NCSe$^-$ anions coordinate at angles of 177.57° (Fe-N8-C28) and 177.97° (Fe-N7-C27) and are almost linear at angles of 178.44° (N8-C28-Se1) and 178.48° (N7-C27-Se2). The average Fe-N bond distance comes to 1.98 Å and indicates that the system is in the LS state.[1,27,33,110] The octahedral distortion parameter ∑ is 41.24°. As in all the examples already given, this parameter deviates from the Fe (II)-SCO systems known from the literature but is comparable to systems using the same binding pocket.[43,151,152] The complexes also enter into π-π-interactions with each other as in all the examples described so far, but due to the different packing properties of **C5**, these are only propagated by the coordinating pyridine- or the phenyl-moiety, leading to leass dense crystal packing. Distances and offsets of all π-π-interacting parts are in the range of interactions well-known from literature (3.24 Å to 3.34 Å).[200,201] All exact values (Table 19) and additional data can be taken from the appendix (11.4.2)

5.4. Variable temperature magnetic susceptibility measurements of the complex family [Fe^{II}(NCX)$_2$(L^2)$_2$] (X = S, Se, BH$_3$).

All three complexes were investigated by variable temperature magnetic susceptibility measurements. A temperature range of 2 - 400 K under an external magnetic field of 1000 Oe was used for the data collection of the magnetic susceptibility. The cooling and heating rates (2 K/min) were hold constant in all measurements. The samples were each dried and measured as fine crystalline powder. At room temperature, **[Fe^{II}(L^2)$_2$(NCS)$_2$] · 2 CH$_2$Cl$_2$ C4** (Figure 52) is in the HS state as indicated by the χ_MT values at 300 K of 3.62 cm^{3}Kmol^{-1}, which is in the range typically observed for mononuclear iron(II)-HS complexes.[43,84,152,228,229] At cooling (2 K/min) **C4** undergoes an abrupt but not complete spin transition with T$_{1/2\downarrow}$ = 116 K. After the SCO a plateau is reached with remaining χ_MT values around 0.73 cm^{3}Kmol^{-1}. The drop at low temperatures can be dedicated to zero field splitting effects, reaching in a minimum of the magnetic susceptibility of 0.45 cm^{3}Kmol^{-1}. [37,205] Subsequently, the sample was heated again to room temperature. During the heating process a small drop of the magnetic susceptibility values is observed at 90 K, indicating a spin transition process, i.e. a relaxation process from HS to LS. Further heating reveals an abrupt SCO with T$_{1/2\uparrow}$ = 124 K, leading in a hysteresis of Δ T$_{1/2\downarrow\uparrow}$ = 8 K. It is noticeable that the spin transition of the cooling curve is not quite as steep as the heating curve, causing the hysteresis. Considering the knowledge gained from the investigation of the magnetic properties of **C1** and **C2** and the observation of the small decrease in the χ_MT values at 90 K while heating, the complex **C4** was investigated for the presence of metastable plateaus, which can be achieved by thermal quenching of the sample. The procedure was the same as described in chapter 4.5. When the sample is cooled very rapidly to 10 K in the SQUID magnetometer, a strongly pronounced TIESST effect is indeed observed, similar to **C1** and **C2**. [68,69,75,78,153,205–207] The (thermal) relaxation of the magnetic moment into the LS ground state is inhibited below a critical temperature characteristic for each compound. The TIESST plateau exhibits constant χ_MT values around 2.6 cm^{3}Kmol^{-1} in the temperature range of 10 K to 60 K, before the complex relaxes in the LS state. According to this, it is possible to preserve 72% of the thermal HS state at low temperatures. The temperature T$_{TIESST}$ at which half of the molecules of the metastable state are in the HS state is determined at 80 K for **C4** when the sample is heated to room temperature at a rate of 2 K/min. Compared to the NCS$^-$ complex **C1** (T$_{TIESST}$ = 76.48 K at 10 K/min), T$_{TIESST}$ of **C4** is shifted to higher temperatures, even with a lower heating rate. The minimum χ_MT value reached of the relaxation from the metastable HS-state into the LS-state comes to 0.70 cm^{3}Kmol^{-1}.

Due to the magnetic behaviour of **C4** described above, the question arises why the complex system behaves similarly to **C1** and **C2**, although **C4** exhibit a less pronounced π-π-stacking and additionally contains dichloromethane as solvent. In this case, the evaporation of the solvent (drying in ultra-high vacuum) may cause the present layer structure of **C4** to eventually become closer to the situation of the π-π-interacting 3D-network in **C1** and **C2**. Examples from literature show that solvent loss can be responsible for more cooperativity and thus more abrupt spin transitions and even hysteretic

behaviour[230,231] Therefore, it would be very interesting to carry out another measurement of freshly prepared **C4** in mother liquor to confirm this hypothesis.
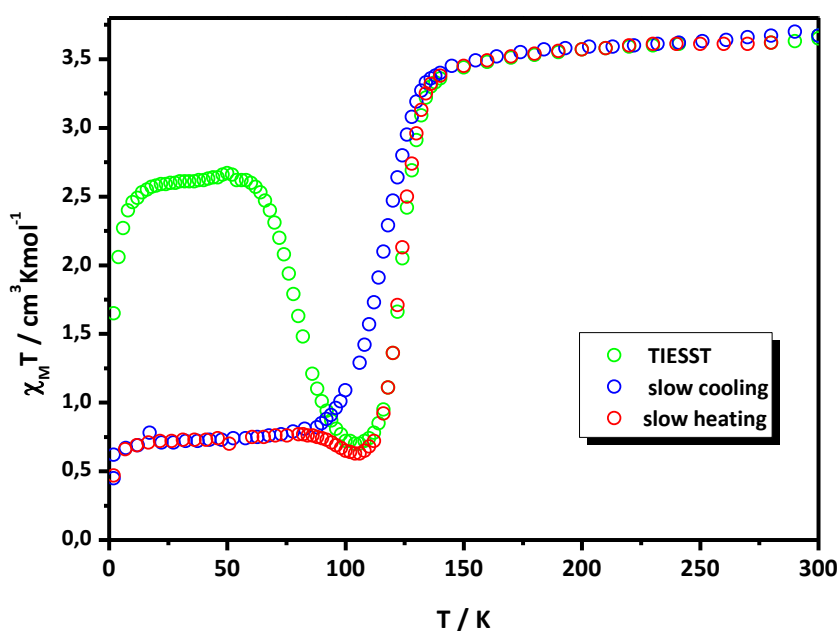

*Figure 52: Magnetic properties of **[Fe^{II}(L^2)$_2$(NCS)$_2$] · 2 CH$_2$Cl$_2$ (C4)**, showing clear existence of a metastable TIESST plateau after thermal quenching at 10 K. Relaxation of the generated metastable state into the LS ground state of **C4** at 60 K with T$_{TIESST}$ = 80 K (2 K/min) and an abrupt spin transition at T$_{1/2}\uparrow$ = 124 K while heating. Directly successive cooling (T$_{1/2}\downarrow$ = 116 K) and heating processes (T$_{1/2}\uparrow$ = 124 K) reveal a hysteresis of 8 K*

The relaxation from the metastable TIESST state into the LS ground state was investigated (like **C1** and **C2**) by time-dependent relaxation measurements of the magnetic susceptibility (Figure 53). The experiments were performed as in the previous examples. A sample of **C4** was quenched, for each new measurement, at 10 K and subsequently heated to the "drop region" of the plateau. Afterwards, the temperature was ssettled at a specific value and measured over 700 min - 50 min. At 30 K both systems do not show any significant relaxation over 11 h. The HS to LS relaxation is observable in the temperature range of 70 K-79 K.
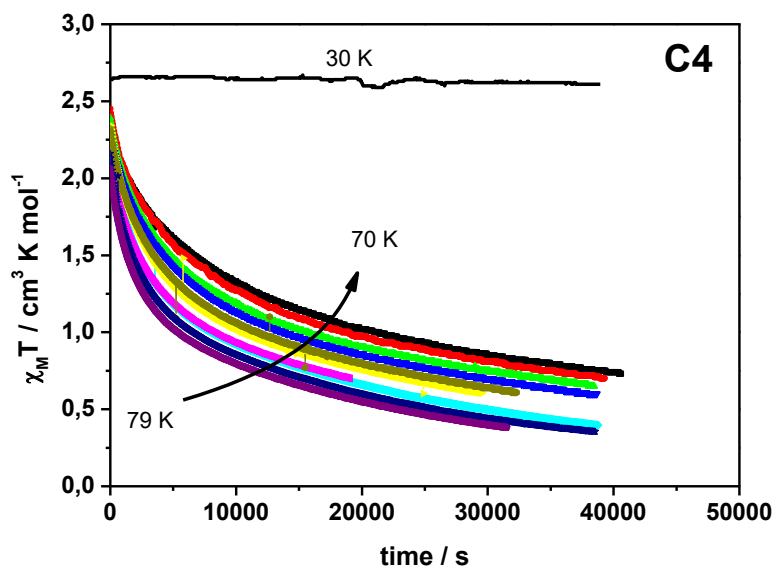
*Figure 53: Time-depended relaxation measurements of the change in magnetic susceptibility of **C4** at the given temperatures as function of time in minutes.*

The relaxation curves clearly do not show any sigmoidal shape, but rather an exponential one. Thus, indicating a weak cooperative system what is also reflected by the more gradual spin transition from the metastable state into the LS ground state.[209,210] The values of $\chi_M T$ do not converge towards a specific value, but after relaxation they vary between the values 1.0 cm^{3}Kmol^{-1} and 0.5 cm^{3}Kmol^{-1}. This is consistent with the TIESST curve from Figure 52. In addition, it can be observed that the relaxation is not yet complete after 11 h for **C4** at the different temperatures which is indicative for a slow decay process. Trying to fit the data with a single exponential function did not give a satisfactory result, whereas a biexponential function gave an excellent fit.

$$\chi_M T \,(\mathrm{t}) = A_1 \cdot e^{-k_1 \cdot t} + A_2 \cdot e^{-k_2 \cdot t} \qquad\qquad 20$$

with the prefactors A_1 and A_2 and the decay constants k_1 and k_2.

The relaxation curves are therefore assumed to be composed of two different exponential processes (process 1 and process 2). The reason is not known yet. Both processes were weighted 50 percentage each in the equation. After the extraction of the decay constants k_1 and k_2, the values were used to calculate the energy barrier with help of the Arrhenius-plot (Figure 182), leading to values for the energy barrier of 226,24 cm^{-1} for process 1 and 28, 14 cm^{-1} of process 2. The calculated values must not be over-interpreted in any way, as it is not known which process has the strongest weighting. This only allows a qualitative statement about the relaxation process, meaning that there are two individual exponential processes, each with unknown mathematical weighting. All fits and data can be taken from the appendix (Figure 181, Figure 182 and Table 40 of section 11.8).

By increasing the ligand field strength of the complex by using different pseudohalide anions as co-ligands, $T_{1/2}$ is shifted to higher temperatures and consequently the LS state is stabilised. In Figure

54 the variable temperature magnetic susceptibility measurements of dried samples of **C5** and **C6** are shown, where the effect described is readily observed.
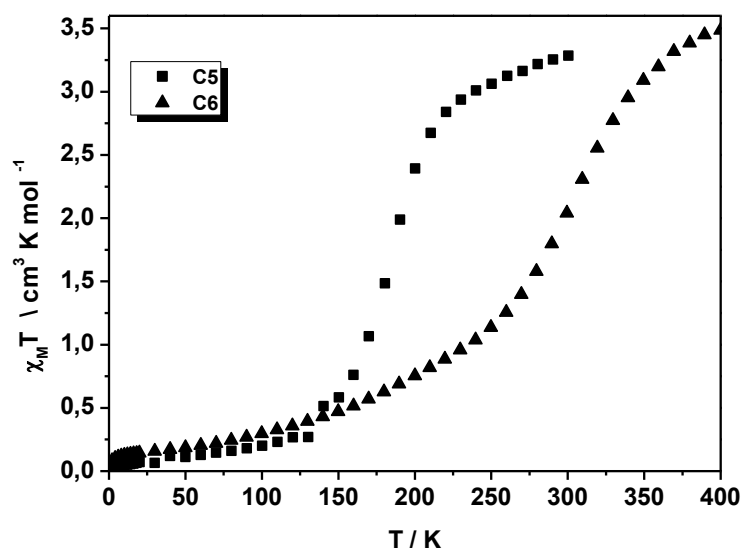

Figure 54: Magnetic properties of [Fe(II)(L²)₂(NCSe)₂] · MeOH (C5, squares) and [Fe(II)(L²)₂(NCBH₃)₂] (C6, triangles) with $T_{1/2\downarrow}$ = 180 K for C5 and $T_{1/2\downarrow}$ = 309 K for C6 at constant colling rates of 2 K/min.

At high temperatures, **C5** and **C6** are present as HS complexes as indicated by the $\chi_M T$ values at 300 K of 3.28 $cm^3 Kmol^{-1}$ for **C5** and at 400 K of 3.49 $cm^3 Kmol^{-1}$ for **C6**. The values are in the range typically observed for mononuclear iron(II)-HS complexes.[43,84,152,228,229] While cooling to very low temperatures **C5** undergoes an abrupt full spin transition at $T_{1/2\downarrow}$ = 180 K. Compared to **C4** ($T_{1/2\downarrow}$ = 116 K), an increase of $T_{1/2\downarrow}$ to higher temperatures of ΔT = 64 K is observed. When the sample is heated again to room temperature, neither a hysteretic effect is observed, nor is a metastable TIESST state found when the sample is thermally quenched. **C6**, on the other hand, exhibits a gradual and fully converted spin transition over the entire temperature range and thus a $T_{1/2\downarrow}$ value of 309 K is found. Consequently, **C6** has a spin transition around room temperature. However, the gradual nature of the curve is indicative of a low cooperative effect within the complex in the solid state.[1,27,34,110] Due to the finding of solvent molecules in the crystal structures of **C4** and **C5**, it is very likely that solvent molecules are also present in the structure of **C6**. However, without investigating the crystal structure of **C6**, no precise conclusion can be drawn. The assumption of enhancing cooperativity through solvent loss (like **C4**) does not apply in the cases of **C5** and **C6**, whereby a gradual SCO over a wider temperature range is observed.

In summary, the magnetic properties of the complexes **[Fe(II)(L²)₂(NCS)₂] · 2 CH₂Cl₂ (C4)**, **[Fe(II)(L²)₂(NCSe)₂] · MeOH (C5)** and **[Fe(II)(L²)₂(NCBH₃)₂] (C6)** are clearly different from those already described in chapter 4.1. Only **C4** resembles the complex properties of **C1** and **C2**. Like these two complexes, **C4** exhibits a hysteretic properties and a clearly pronounced metastable TIESST plateau, which can be achieved by quenching the sample at 10 K. Noticeably, the measured crystal structures of **C1** and **C2** are isostructural, whereas in the structure of **C4** solvent molecules are found. Nevertheless, the complexes propagate in the different spatial directions as a network, which is formed

by π-π-interactions. **C5**, in contrast, does not have the same structural properties and thus differs in the magnetic behaviour. This leads to the assumption that the hysteretic as well as the TIESST-properties of the investigated complex families are strongly influenced by the structural properties in the bulk material and the present coupling of the complex molecules. [160,161] **C6**, on the other hand, exhibits a clearly different and gradual SCO in contrast to the comparable NCBH$_3$-complex **C3**, which is characterised by a two-step SCO. Unfortunately, the crystal structure of **C6** could not be investigated yet. The significant differences in the magnetic behaviour and packing properties of the complex molecules are due to the exchange of the naphthyl unit with the pyridyl unit in the coordinating ligand system. The use of a larger naphthyl moiety allows for a greater degree of π-π-stacking in contrast to a pyridyl group, as illustrated by the direct stacking of the naphthyl moieties of neighbouring complex molecules in **C1** and **C2** (Figure 27 and Figure 137). In the case of the pyridyl residue, there is less π-π-stacking due to the smaller residue and thus smaller ligand. The complex molecules within the solid would have to come much closer to each other to generate a comparable stacking behaviour of **L^1**. However, most likely due to steric hindrance and electromagnetic repulsion, this is not possible. This allows the conclusion that larger aromatic side chains are better suited to construct a π-π-stacked 3D network, which leads to the next evolution step of the ligand.

6. Family of mononuclear [Fe(L^3)$_2$(NCX)$_2$] complexes (X = S, Se, BH3)

By decreasing the π-system of the ligand side arm in **L^2** compared to **L^1** (phenyl instead of naphthyl unit), a reduction of the cooperative properties has been found and thus, a less pronounced π-π-stacking of the ligand molecules to neighbouring complex molecules can be observed. In addition, the decreased ligand stacking enables the incorporation of solvent molecules into the crystal structure which turned out to be unfavorable for the desired properties.
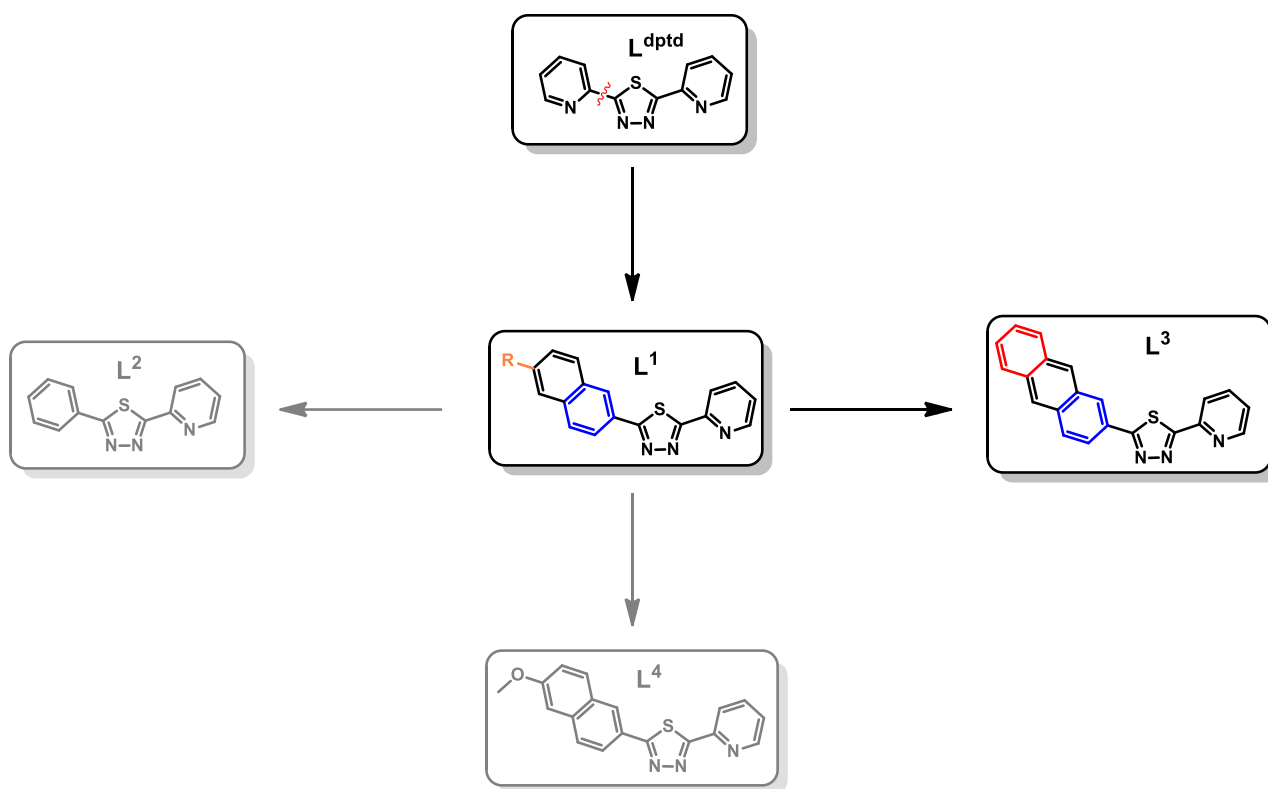

*Figure 55: Evolution of the Ligand **L^1** to the diffferent projects presented in this thesis.*

The structural and magnetic discoveries of the above-mentioned project of the ligand **L^2** and the complexes (**C4**, **C5**, **C6**) formed, suggest that the next evolution step of the ligand system should be the opposite direction and therefore an enlargement of the ligand's π-system. For this reason, an anthracene unit was linked to the SCO binding pocket consisting of pyridine and thiadiazole already mentioned in the above examples.[43,151,152] It is expected that an increase of the ligands π-system and thus higher aromatic stacking properties will again allow crystallisation (likewise **C1** and **C2**) of the complex system without any solvent molecules, leading to a significant increase of the intermolecular cooperative interactions. The higher cooperative interactions in turn, are intended to increase T$_{TIESST}$ and the width of the magnetic hysteresis and thus, improve the magnetic properties observed in the [Fe(L^1)$_2$(NCX)$_2$] (**C1**, **C2** and **C3**) complex series.

6.1. Synthesis of 2-(anthracen-2-yl)-5-(pyridin-2-yl)-1,3,4-thiadiazole L[3]
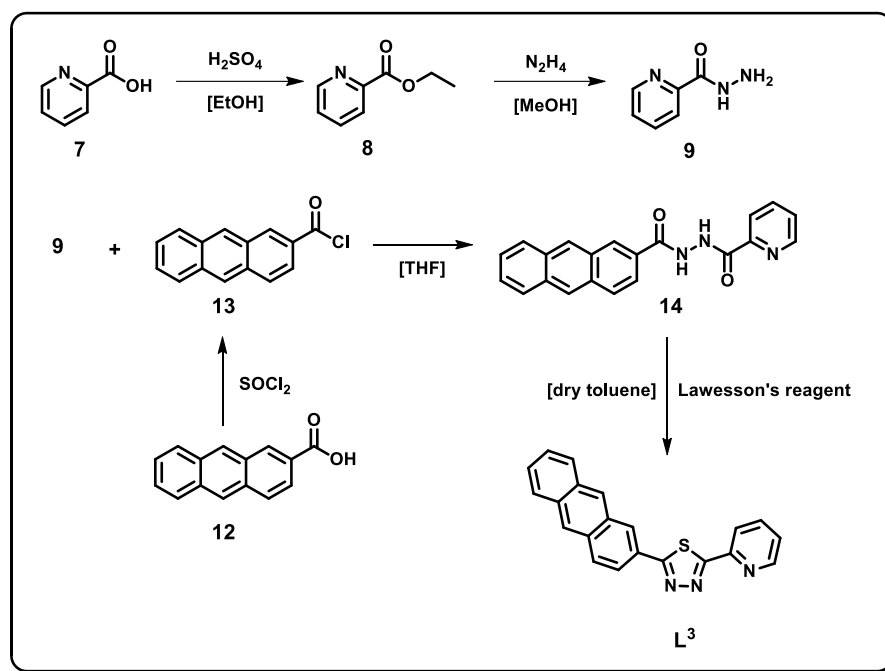
*Scheme 4: Synthesis route of 2-(anthracen-2-yl)-5-(pyridin-2-yl)-1,3,4-thiadiazole **L[3]**. [41,158,185,186] The detailed description of the individual synthesis steps, yields and analytical characterisation can be taken from the experimental section.*

The synthesis of the ligand **L[3]** (2-(anthracen-2-yl)-5-(pyridin-2-yl)-1,3,4-thiadiazole) is presented in Scheme 4. Ethyl 2-pyridine carboxylate (**8**) was prepared according to the following procedures reported in the literature, by refluxing pyridine-2-carboxylic acid suspended in ethanol with a catalytic amount of sulfuric acid.[186] 2-pyrdinecarboxylic acid hydrazide (**9**) was prepared in a nucleophilic substitution reaction of ethanol by addition of hydrazine hydrate, according to a modified literature procedure.[185] The previously formed ester was dissolved in methanol, an excess of hydrazine hydrate dissolved in methanol was added and stirred overnight. Removing the solvent and residual hydrazine monohydrate under reduced pressure afforded (**9**). Subsequently, by stirring **9** with anthracene-2-carbonyl chloride (**13**) at room temperature in dry tetrahydrofuran (THF), which was freshly prepared from anthracene-2-carboxylic acid (**12**) and thionyl chloride,[186] N'-(2-anthracenyl) pyridine-2-carboxylic acid hydrazide (**14**) was obtained. The ligand **L[3]** was again synthesised according to the above mentioned procedure by *Herold*[41,158] and *Fürmeyer.* [40,156,165] **14** was heated with Lawesson's reagent in dry toluene under reflux and argon atmosphere and then purified by column chromatography (toluene → toluene/ethyl acitate 9:1) to give a yield of 82 % over four reaction steps. The ligand was fully characterised (^{1}H-NMR-, ^{13}C-NMR-, COSY-NMR-, HMBC-NMR- and HSQC-NMR-, and IR-spectroscopy as well as mass spectrometry) and subsequently used for complexation reactions with iron (II) ions. The coordination is expected to not differ from the previous synthesised ligands. Figure 56 displays the ^{1}H-NMR spectrum of **L[3]**. The number of the respective signals and the integrals agree with the expected values. All exact assignments of the signals can be taken from the

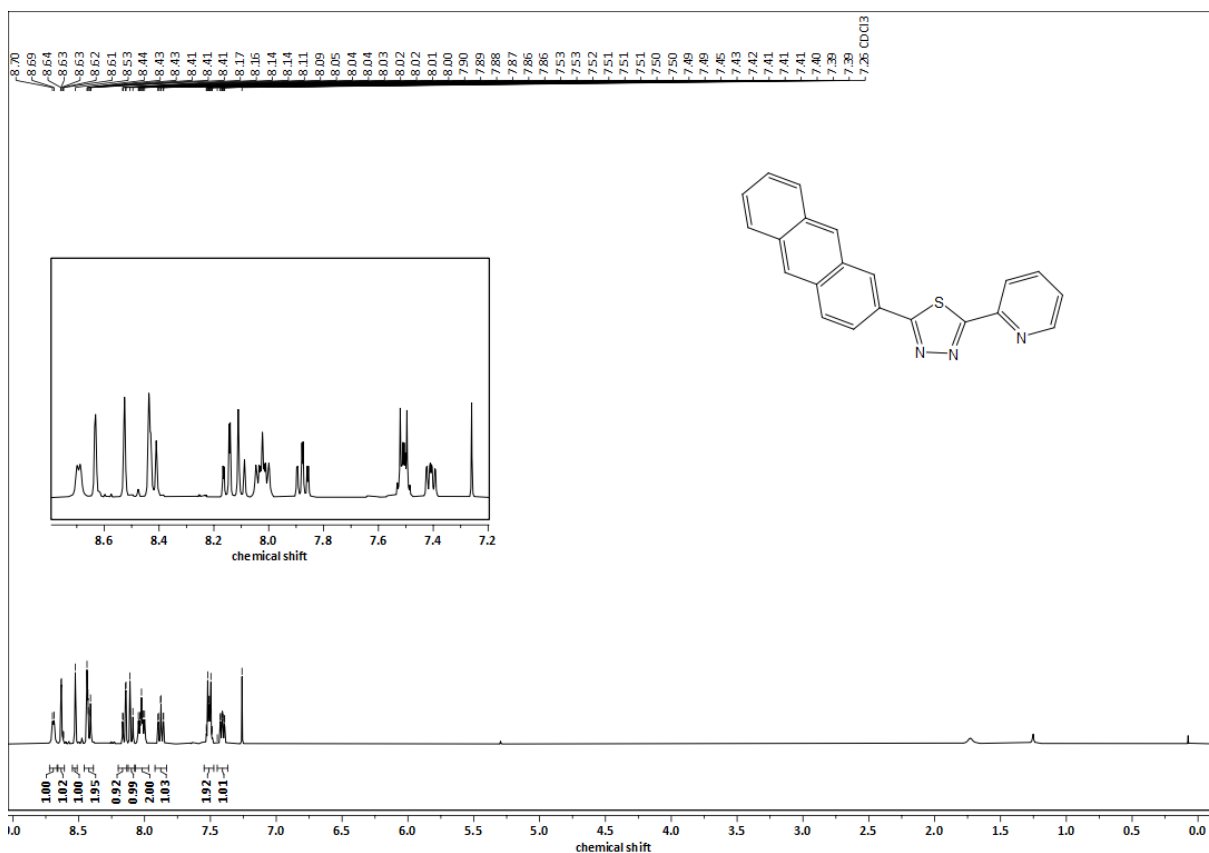experimental part (section 9). All other analytics can be taken from the additional appendix (section 11).

Figure 56: ¹H-NMR of 2-(anthracen-2-yl)-5-(pyridin-2-yl)-1,3,4-thiadiazole (L³) measured at 600 MHz. For a better understanding, only the peaks with the respective integrals, as well as a zoom of all aromatic signals that can be observed, are shown. A precise assignment of all signals can be found in the experimental part.

6.2.   Synthesis of the complex family [Fe^{II}(NCX)$_2$(L^3)$_2$] (X = S, Se, BH3).

Access to iron (II) complexes of the molecularformula [Fe^{II}(NCX)$_2$(L^3)$_2$] (X = S, Se, BH$_3$) was made possible by the successful preparation and isolation of the ligand **L³**. Liquid-liquid diffusion was used for the complex synthesis. A solution of the ligand in different solvents, with highest possible density among the used solvents, was placed at the bottom of a tube. Then a solvent mixture (1:1) of the solvents used for ligand and iron salt solution was carefully layered over the ligand solution. This layer serves as a non-reactive transport medium and was always doubled in volume compared to the two reactant volumes. In other words, if a volume of 5 mL was chosen for the ligand and iron salt solution, for example, the solvent mixture of the transport layer was set at 10 mL. The transport layer was then layered with an iron salt solution in a solvent having the lowest density of all solvents used in this procedure. The built three-phase system was then allowed to settle for several weeks. The reactants used besides **L³** were FeSO$_4$ · 7H$_2$O, KSCN, KSeCN and NaNCBH$_3$. Single crystals as well as crystalline powder with the anions (SCN$^-$, SeCN$^-$ and BH$_3$$^-$) could be obtained. For **C7** and **C8**, FeSO$_4$·7H$_2$O and KXCN

76

were dissolved in equimolar amounts in dry methanol and stirred for at least 2 hours. The colourless precipitate of K_2SO_4 was filtered. The resulting colourless metal salt solution was then used as reactant in the three-phases system. **C9** was prepared in the same way, by using a $NaNCBH_3$ dissolved in methanol. Small yellow block-shaped single crystals could be obtained after approximately four weeks and were used for X-ray structure analysis and the investigation of the molar magnetic susceptibility.

The complexes were characterised by IR-spectroscopy, X-ray structure analysis and measurement of the molar magnetic susceptibility. In the following figure (Figure 57), the infrared spectra of all synthesised complexes **C7** (NCS^-, red), **C8** ($NCSe^-$, cyan) and **C9** ($NCBH_3^-$, blue), with increasing ligand field strength are compared with the ligand **L³** (black). The spectra were normalised and vertically shifted from each other for more clarity. The observation of intense bands in the spectra for **C7** at 2066 cm^{-1}, for **C8** at 2071 cm^{-1} and for **C9** at 2188 cm^{-1} and 2340 cm^{-1}, again provides first indication of successful complexation. These bands can be assigned to the coordinating co-ligands NCS^- (1990-2140 cm^{-1}), $NCSe^-$ (2072 cm-1) and $NCBH_3^-$ (v_{CN}=2070-2240 cm^{-1}; v_{BH}=2315-2380 cm^{-1}), respectively.[151,152,178,193,196–199]
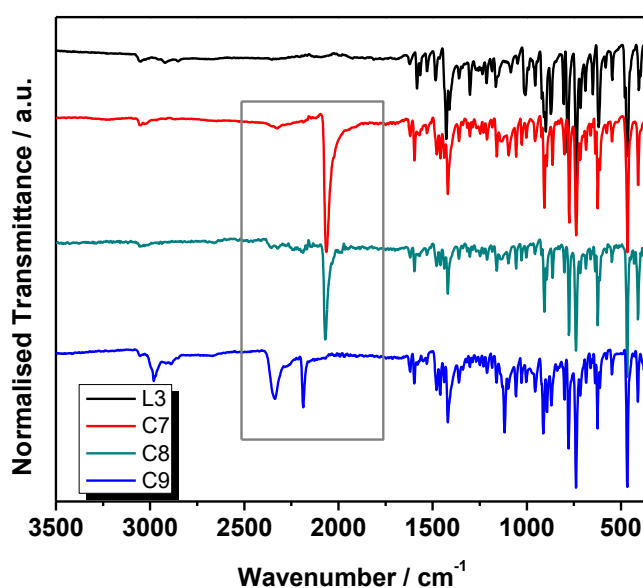
*Figure 57: Normalized Infrared spectra of **L3, C7, C8** and **C9** in one graph. The spectra are offset from each other for more clarity. The grey box marks the characteristic IR-bands of the coordinating pseudohalides of the respective complexes; SCN⁻ for **C7**, SeCN⁻ for **C8** and NCBH₃⁻ for **C9**.*

X-ray structural analysis of the samples was performed to obtain information on packing effects, cooperative effects, and intermolecular interactions.
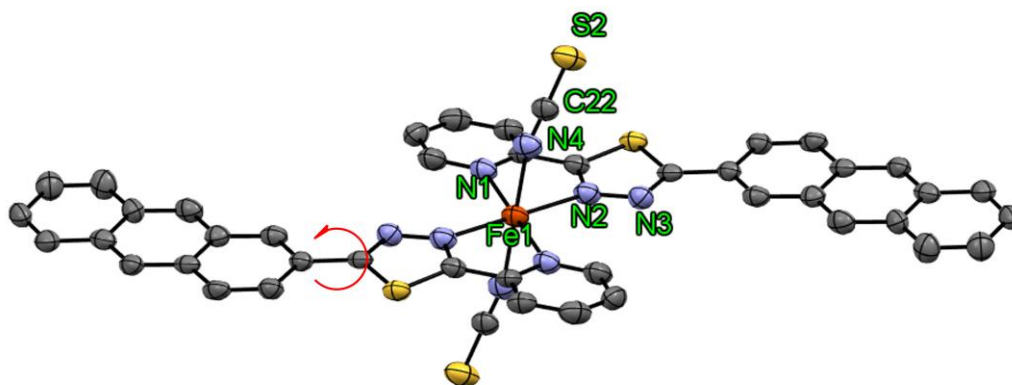
6.3. Crystal structure of C7, C8 and C9

*Figure 58: Molecular structure of [Fe^{II}(NCS)$_2$(**L^3**)$_2$] **C7**. Hydrogen atoms are omitted for clarity Color Code: grey-C, yellow-sulfur, blue-N, orange-Fe, white-H. ORTEP representation with atomic displacement parameters at 50% level of probability.*

The built complex **[Fe^{II}(L^3)$_2$(NCS)$_2$]** (**C7**) crystallizes in the triclinic space group $P\bar{1}$ (Figure 58) at 120 K. The asymmetric unit (Figure 147, section 11.4.3) contains half of the complex molecule with the iron(II)-ion on the centre of inversion. Thus, the octahedral coordination sphere is formed by two ligand molecules of **L^3** and two trans-coordinating thiocyanate anions, leading to an overall neutral complex molecule. The coordinating equatorial plane is spanned by the pyridyl and thiadiazole backbone of the bidentate ligand **L^3**. The anthracene moiety is tilted 6.69° in contrast to the equatorial plane, while the coordinating pyridyl group is tilted 5.95° from the octahedral plane. The ligand is therefore deformed, which indicates a high strain within the ligand molecule and coordination sphere. In addition, contrary to the naphthyl moiety of complex family [Fe^{II}(L^1)$_2$(NCx)$_2$], the anthracenyl moiety is rotated towards the coordination plane, depicted with a red arrow in Figure 58. The average iron to nitrogen bond distance of 2.17 Å is typical for iron (II)-complexes in HS-state.[1,27,33,110] The bite angle of the coordinating nitrogen atoms (N1-Fe-N2) is found to be 75.71° for 173 K, while the NCS$^-$ co-ligands coordinate with an angle of 166.12°. The co-ligand moiety (N4-C22-S2) is almost linear with an angle of 178.20°. The octahedral distortion parameter Σ is 77.72°. Again this value differs from the typical values for HS complexes[86], but the difference is comparable to the literature known SCO systems coordinating equatorially via pyridine and thiadiazole and pseudohalides as axial co-ligands.[43,151,152] However, if the value is compared with the distortion parameter of the mother complex **C1** (67.04°) in HS-state, a significantly greater distortion of the coordination environment is found. This is consistent with the observations of the existing high strain in the coordinating ligand. The crystal structure of **C7** is also characterised by the absence of any solvent molecules, due to building of a highly cooperative system via strong π-π-stacking. The π-π-interactions are formed between anti-parallel aligned coordinating ligands **L^3** of the neighbouring complex molecules in different spatial directions. Distances and offsets of all π-π-interacting parts are in the range of interactions well-known from literature (3.14 Å to 3.40 Å).[200,201] All exact values can be taken from the appendix (Table 24 of section 11.4.3). Compared to **C1** (3.51 Å to 3.66 Å), the found π-π-distances are way shorter in **C7** indicating stronger π-π-interactions and thus higher cooperativity.
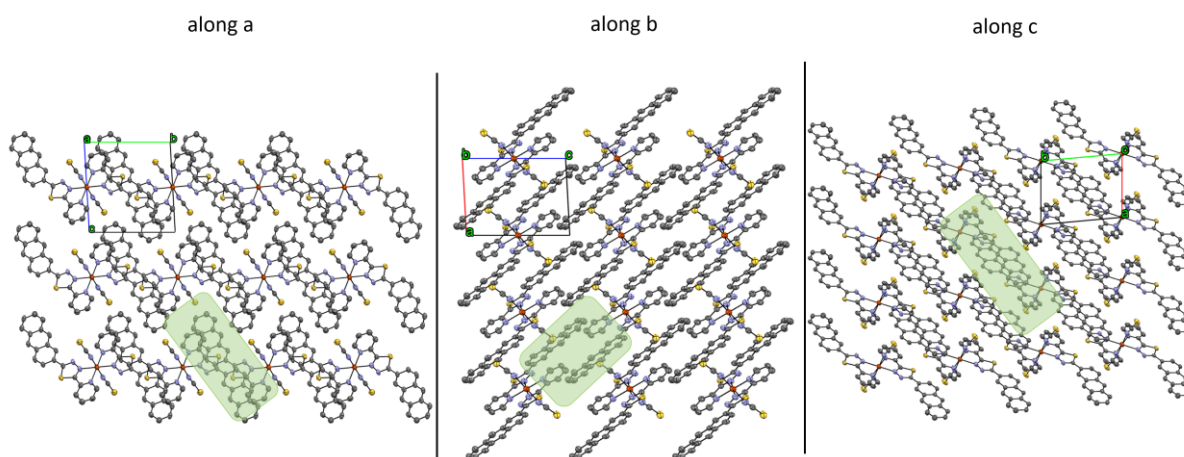
along a   along b   along c

*Figure 59: **along a**: Selected part of the crystal structure of **C7** at 120 K along the a-axis. **along b:** Selected part of the crystal structure of **C7** at 120 K along the b-axis. **along c:** Selected part of the crystal structure of **C7** at 120 K along the c-axis. Color Code: grey-C, yellow-sulphur, blue-N, orange-Fe, green-Cl white-H. ORTEP representation with atomic displacement parameters at 50% level of probability. Highlighted are the π-π-interacting anti-parallel aligned ligands of neighbouring complex molecules, respectively.*

The single-crystal X-ray diffraction data of **C8** at 173 K and **C7** are isostructural.
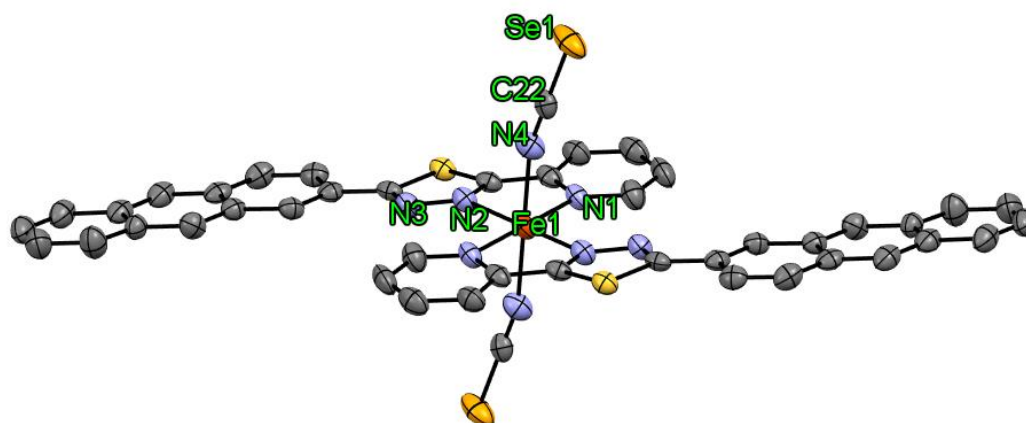

*Figure 60: Crystal structure of **C8** including the atom labelling. Hydrogen atoms are omitted for clarity Color Code: grey-C, yellow-sulfur, blue-N, orange-Fe, white-H, light orange-Se. ORTEP representation with atomic displacement parameters at 50% level of probability.*

The asymmetric unit (Figure 150) is identical to that of **C7** and differs only in one atom of the co-ligand (Se instead of S). Thus, the equatorial coordination sphere is again spanned by the pyridyl and thiadiazole backbone of the bidentate ligand **L³**. The twist of the anthracenyl residue (7.25°) and the pyridyl residue (3.98°) of **C8** is in the same range as for **C7**. In combination with the high value of the octahedral parameter Σ of 79.52° for systems using a 5-pyridyl-1,2,4-thiadiazole binding pocket and pseudohalides as co-ligands,[43,151,152] a similar strain in the ligand and thus in the coordination environment of the complex molecule can be seen. Additionally to this value, the identical average Fe-N bond distance of 2.17 Å at 173 K compared to **C7** indicates that **C8** is in the HS-state. [1,27,33,110] The bite angle of the chelating ligand (N1-Fe-N2) hardly differs from that measured in **C7** (75.49°), while the coordinating NCSe⁻ Co-ligands in this case are more angled (Fe-N4-C22 angle = 164.69°) (the two

N-C-Se anions are again almost linear at 179.62°). Since **C7** and **C8** are isostructural, again there are no solvent molecules in the crystal structure, which leads to strong cross-linking of the complex molecules through strong π-π-interactions. The π-π-interactions are again generated by anti-parallel aligned coordinating ligands **L³** of the neighbouring complex molecules. Distances and offsets of all π-π-interacting parts are in the range of interactions well-known from literature (3.20 Å to 3.46 Å) and just differ hardly from those found in **C7**, thus leading to a similar degree of cooperativity through π-π-stacking.[200,201] All exact values can be taken from the appendix (Table 26 of section 11.4.3).
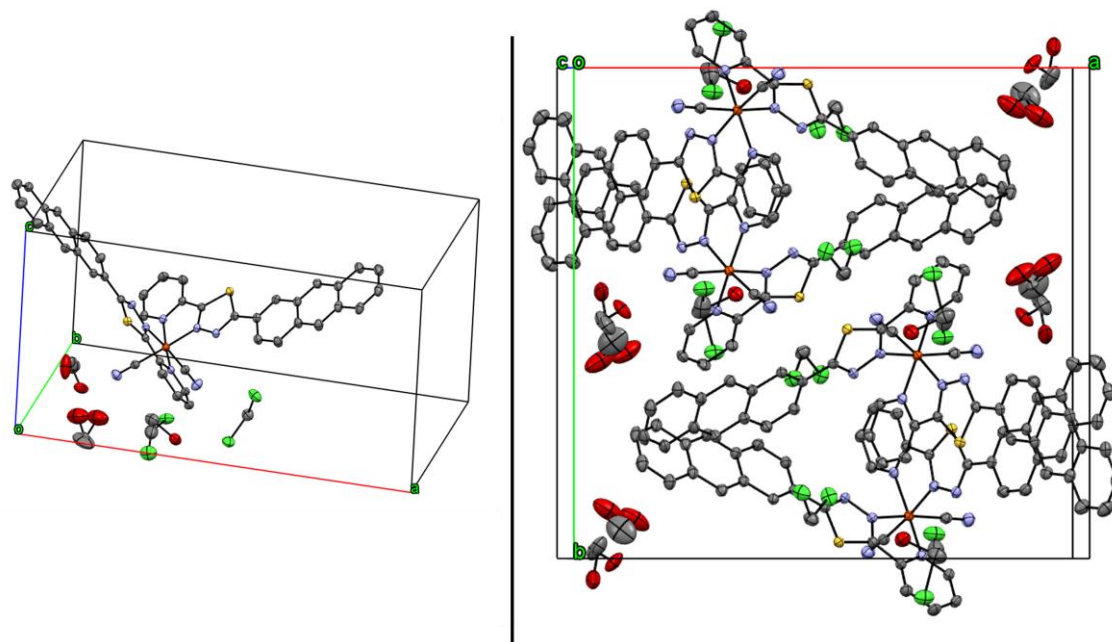

*Figure 61: **Left;** Asymmetric Unit of **C9** at 120 K. **Right;** packing of the unit cell of **C9**: Color Code: grey C, yellow-sulfur, blue-N, orange-Fe, red-O, green-Cl, white-H. ORTEP representation with atomic displacement parameters at 50% level of propability.*

If, on the other hand, one takes a closer look at the structure of **C9** **[Fe^{II}(L³)$_2$(CN)$_2$] · 1.15 CH$_2$Cl$_2$ · 2.85 MeOH**, it clearly deviates from the complex series of the previous examples. In fact, the measured crystal structure did not reflect the desired product. Rather than showing the cyanoborohydride anions as co-ligands the complex shows coordinated cyanide anions. Nevertheless, why the structure is representative for the desired complex is discussed below. **C9** crystallizes in the monoclinic space group *P*2$_1$/*c* at 120 K with four complex molecules in the uni cell (Figure 61 right). Thus, the entire complex molecule is found in the asymmetric unit. Also, part of the asymmetric unit are 1.15 molecules of dichloromethane and 2.85 molecules of methanol, while the methanol solvent shows certain degree of disorder. One complex molecule contains one iron (II) ion, coordinated in cis-conformation by two molecules of the ligand **L³** and two cyanides as co-ligands giving a neutral complex overall. The coordinating equatorial plane is spanned by the pyridyl and the thiadiazole backbone of one bidentate coordinating ligand (N4 and N5), one pyridyl backbone (N1) unit of the second coordinating ligand and one cyanide anion (C43), while the tip of the octahedral coordination sphere is generated by the second cyanide anion (C44) and one coordinating nitrogen atom (N2) of the thiadiazole backbone of the second coordinating ligand. Noticeably, the anthracene

unit of the ligand is rotated away from the coordination plane, in contrast to the examples discussed above. The average Fe-N bond distance is 1.97 Å, while the average Fe-C bond distance is 1.91 Å indicating the measured complex is in LS state. [1,27,33,110,142] The biting angles of the coordinating ligands are found to be 80.30° (N1-Fe-N2) and 81.06° (Fe4-Fe-N5), while the angle of the coordination CN^- co-ligands are 176.23° (Fe-C43-N7) and 179.22° (Fe-C44-N8). Due to the cis-conformation and the resulting different packing of the complex and solvent molecules, the crystal packing is significantly less dense as in the previous examples. The different complexes interact again by π-π-interactions (Figure 154) through mostly anti-parallel aligned ligands of the neighbouring complexes, but also by T-shape CH···π-interactions (Figure 155). Distances and offsets of all π-π- (3.38 Å to 3.51 Å) as well as CH···π-(3.38 Å to 4.09 Å) interacting parts are in the range of interactions well-known from literature.[200,201] All exact values can be taken from the appendix (Table 28 of section 11.4.3). The major question, however, remains why, contrary to the expectations, CN^- and not $NCBH_3^-$ is present as co-ligand. Most likely, the co-ligand was substituted by a ligand exchange reaction.[232] Since several months laid between the preparation of the sample and the single-crystal X-ray structure analysis, it is very likely that unreacted $NCBH_3^-$ has decomposed under acidic conditions. However, all other measurements such as infrared or magnetic susceptibility measurements were carried out shortly after complexation and are not affected. Although the reaction took place in a glovebox and thus in the absence of oxygen, the reaction vessel was not darkened, so it is possible that the dichloromethane may have decomposed under the influence of light. It is known that under radical reaction and non-aerobic conditions, one decomposition product of dichloromethane is hydrogen chloride (HCl).[233] The HCl in turn enables the acidic cleavage of unreacted $NaBH_3CN$, producing, among other side products, HCN as a ligand exchange reagent. Since a ligand exchange reaction is predicted, it can be assumed that the targeted complex $[Fe^{II}(L^3)_2(NCBH_3)_2]$ · (xSolv) coordinates (cis-manner) and crystallises in a similar way.

The idea to create a system with even stronger intermolecular π-π-interactions, contrary to the complexes of the $[Fe(L^1)_2(NCX)_2]$ (**C1**, **C2** and **C3**) series, to force crystallisation without solvent was successful for the complexes $[Fe^{II}(L^3)_2(NCS)_2]$ **C7** and $[Fe^{II}(L^3)_2(NCSe)_2]$ **C8**. In turn, $[Fe^{II}(L^3)_2(CN)_2]$ · 1.15 CH_2Cl_2 · 2.85 MeOH **C9** on the other hand, crystallises in a different space group and thus solvent molecules are incorporated into the structure. Additionally, the complex exhibits a cis-configuration. Nevertheless, the complexes **C7**, **C8** and **C9** are expected to have optimal characteristics to possess SCO properties. On the one hand, there is a SCO coordination pocket, which has been found in the past and in this work to be characterised by a well-adjusted ligand field. And on the other hand, a high (and even stronger than that in **C1**-**C3**) cooperativity and communication of the individual complex molecules within the solid is present. How the complexes behave magnetically is explained in the next section.

6.4. Variable temperature magnetic susceptibility measurements of the complex family [Fe(NCX)$_2$(L^3)$_2$] (X = S, Se, BH3)

All three complexes were investigated by variable temperature magnetic susceptibility measurements. A temperature range of 2 - 300 K under an external magnetic field of 1000 Oe was used for the data collection of the magnetic susceptibility. The cooling and heating rates (2 K/min) were hold constant in all measurements. The samples were dried and measured as fine crystalline powder as well as crystals. **[Fe^{II}(NCS)$_2$(L^3)$_2$] C7**, **[Fe^{II}(NCSe)$_2$(L^3)$_2$] C8** and **[Fe^{II}(NCBH$_3$)$_2$(L^3)$_2$] C9** are in HS state as indicated at 300 K by the χ_MT values of 3.56 cm^{3}Kmol^{-1} for **C7** and 3.48 cm^{3}Kmol^{-1} for **C9** (Figure 62). Since the measurement of **C8** is very error-prone, this is only described qualitatively. **C7** and **C8** are in HS state over the whole temperature scale with almost constant values for χ_MT. The drop at low temperatures (below 20 K) can be dedicated to zero field splitting effects, reaching in a minimum of the magnetic susceptibility of 2.15 cm^{3}Kmol^{-1} for **C7**.[37,205] In turn, **C9** shows spin switching properties, indicated by a fully converted gradual SCO between the temperature range of 250 K and 150 K and T$_{1/2\downarrow}$ = 230 K.
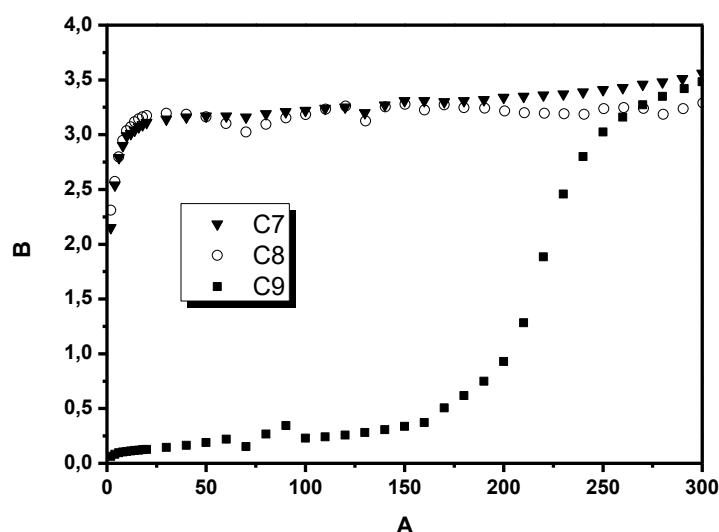

Figure 62: Magnetic properties of [Fe^{II}(L^3)$_2$(NCS)$_2$] (C7, triangles), [Fe^{II}(L^3)$_2$(NCSe)$_2$] (C8, open circles) and [Fe^{II}(L^3)$_2$(NCBH$_3$)$_2$] (C9, squares) with T$_{1/2\downarrow}$ = 230 K for C9 at constant colling rates of 2 K/min.

C7 and **C8** clearly show different magnetic behavior in contrast to the mother complex **C1** and **C2**. No spin crossover properties can be detected at all. Most likely, the introduced anthracenyl moiety, contrary to the naphthyl moiety in the complex family [Fe^{II}(L^1)$_2$(NCX)$_2$] (X = S, Se, BH$_3$), is responsible for a more compact crystal packing, due to the enlargement of the intermolecular π-π -interactions. This would inhibit any structural changes associated with a spin transition.[231] In turn, **C9** is able to switch spin state in a temperature range of 100 K and shows gradual SCO with T$_{1/2\downarrow}$ = 230 K. Due to the structure (Figure 61) described in Section 6.3, it is assumed that **C9** is present in a cis-conformation. In contrast to **C7** and **C8**, the crystal packing is much less compact. Therefore, the required structural changes are no longer inhibited, and it is possible for the complex to switch spin states. In addition, a

further single crystal X-ray structure analysis of the unit cell of complex **[Fe^{II}(L^3)$_2$(CN)$_2$] · 1.15 CH$_2$Cl$_2$ · 2.85 MeOH** at 240 K (Table 22) also showed the complex existing in LS state and thus does not correlate with the χ_MT curve of Figure 62.Since the χ_MT curve at 240 K indicates a complex in the HS state, the thesis of ligand exchange of complex **C9** by decomposition of unreacted NaBH$_3$CN is supported.

In summary, the basic idea of "crystal engineering" was successful, and the complexes **C7** and **C8** have the desired structural properties. Unfortunately, however, the increase in intermolecular interactions did not improve the spin crossover properties compared to the [Fe^{II}(L^1)$_2$(NCX)$_2$] (X = S, Se, BH$_3$) complex family. However, the example of **C9** shows very nicely how important it is not only to use a well-tuned SCO binding pocket, but also how strongly spin transition properties depend on the interaction of the complex molecules in the solid.

7. **Family of mononuclear [Fe(L^4)$_2$(NCX)$_2$] complexes (X = S, Se, BH3)**

The insights gained into the structural and associated magnetic properties of the various complex families so far, led to the development of a new ligand and thus a new complex family. The reduction or enlargement of the π-system of the ligand, starting from **L^1** (2-naphthyl-5-pyridyl-1,3,4-thiadiazole), resulted in a significant change of the magnetic properties of the formed complexes compared to those exhibiting multistable magnetic behaviour.
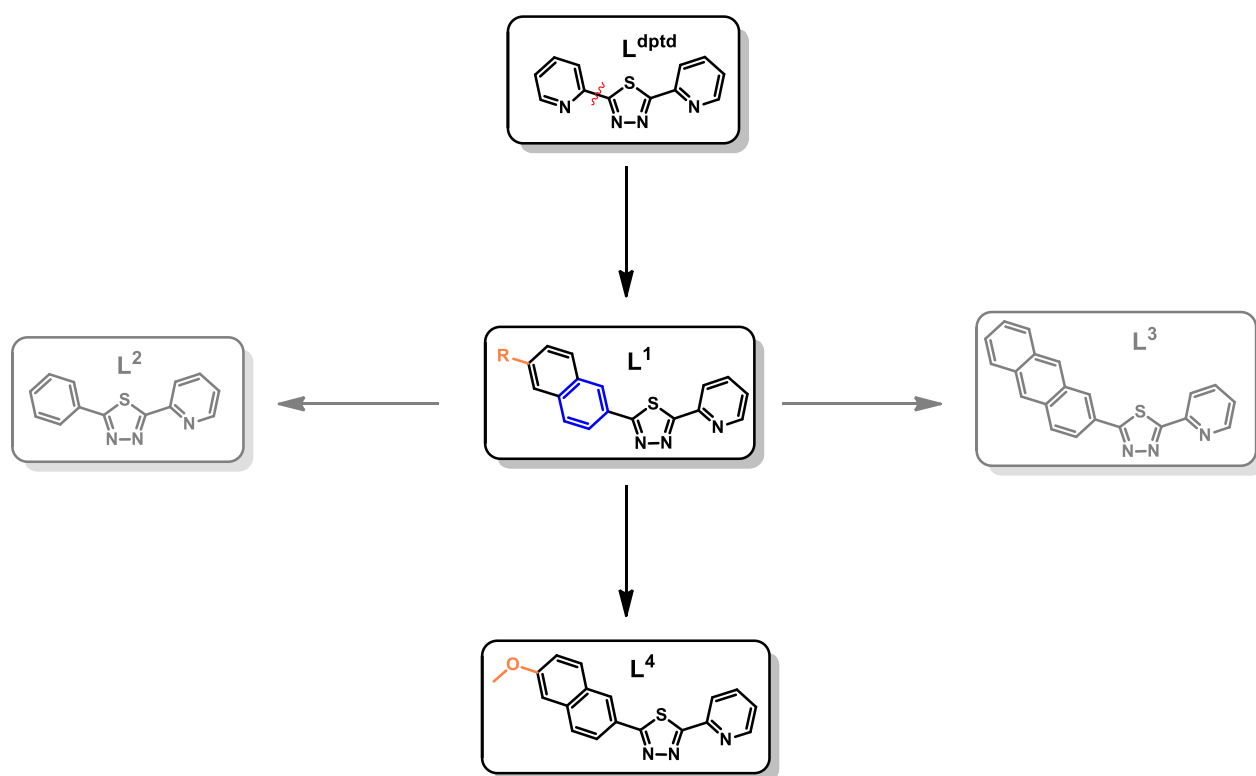
*Figure 63: Evolution of the different ligands used in this thesis starting from ligand **L¹** with the focus on **L⁴**.*

With the introduction of **L³** (anthracenyl side chain) in the complex system [Fe^{II}(**L^Y**)$_2$(NCX)$_2$] (X = S, Se, BH$_3$) discussed in the previous section, the spin crossover properties were partially lost due to excessive intermolecular interactions within the solid state. If, on the other hand, a smaller ligand is introduced into the complex system, as in the example of the already discussed ligand **L²**, the spin crossover properties are retained in all cases, but the spin transition behaviour is rather gradual (**C5** [Fe^{II}(**L²**)$_2$(NCSe)$_2$] · MeOH and **C6** [Fe^{II}(**L²**)$_2$(NCBH$_3$)$_2$]). Except for complex **C4** [Fe^{II}(**L²**)$_2$(NCS)$_2$] · 2 CH$_2$Cl$_2$, the magnetic properties are like those of **C1** [Fe^{II}(**L¹**)$_2$(NCS)$_2$] and **C2** [Fe^{II}(**L¹**)$_2$(NCSe)$_2$], although here the exact nature can only be hypothesised, and further experiments are needed. Overall, it turned out that the magnetic properties in **C1** and **C2** are strongly dependent on the degree of cross-linking of the intermolecular interactions (in this case π-π-interactions) and the replication of the magnetic properties is not trivial, even if the ligand is only slightly changed in the different discussed case (phenyl←naphthyl→anthracenyl). Based on this knowledge, which was gained through the ligand modification, the ligand **L⁴** (2-(6-methoxynaphthalen-2-yl)-5-(pyridin-2-yl)-1,3,4-thiadiazole) was developed (Figure 63). The idea behind this is to return to the master motif of the ligand **L¹** (2-naphthyl-5-pyridyl-1,3,4-thiadiazole) and to modify it by introducing a methoxy group at the 6th position of the naphthyl ring. It is essential that the change of the ligand takes place in the aromatic side chain and not in the coordinating pyridine, as the ligand field should only be marginally influenced. The question to be addressed is to what extent it is possible to structurally move away from the master motif of the ligand **L¹** to preserve the solid-state properties, dependent on the degree of the intermolecular π-π-interaction and the associated magnetic properties. Furthermore, the new modification leading to the ligand **L⁴** will help, in combination with the findings for **L²** and **L³**, to generate a better understanding of the interplay between solid state and the resulting magnetic properties of

the complexes discussed in this work. The following ligand **L⁴** (2-(6-methoxynaphthalen-2-yl)-5-(pyridin-2-yl)-1,3,4-thiadiazole) and all produced results were obtained in cooperation with one of my bachelor students during her thesis, ██████████.

7.1. Synthesis of 2-(6-methoxynaphthalen-2-yl)-5-(pyridin-2-yl)-1,3,4-thiadiazole L⁴
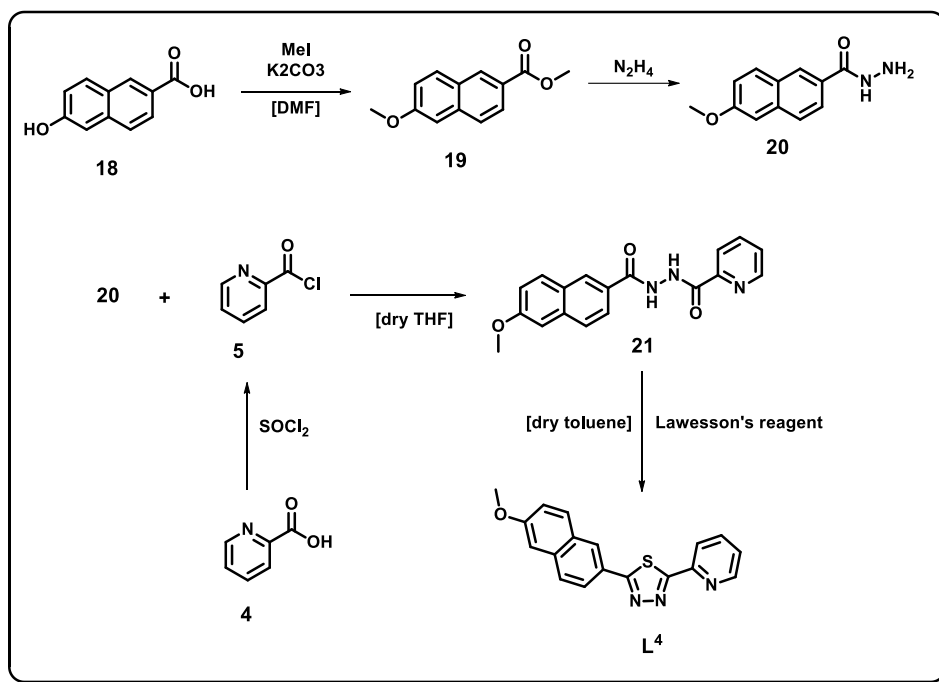
*Scheme 5: Synthesis route of 2-(6-methoxynaphthalen-2-yl)-5-(pyridin-2-yl)-1,3,4-thiadiazole **L⁴**. [41,158,185,186] The detailed description of the individual synthesis steps, yields and analytical characterisation can be taken from the experimental section.*

2-(6-methoxynaphthalen-2-yl)-5-(pyridin-2-yl)-1,3,4-thiadiazole **L⁴** was prepared in a four-step synthesis. Starting from 6-hydroxy-2-naphthoic acid (**18**), 6-methoxy-2-naphthoic acid methyl ester (**19**) was obtained by a methylation reaction with methyl iodide in dimethyl formamide. 6-methoxynaphthalene-2-carbohydrazide (**20**) was synthesised in a nucleophilic substitution reaction of ethanol by addition of hydrazine hydrate, according to a modified literature procedure.[185] Hydrazine hydrate was used as reactant as well as reaction solvent. N'-(6-methoxy-2-naphthoyl) pyridine-2-carboxylic acid hydrazide **21** could be prepared by nucleophilic substitution with 2-pyridinecarboxylic acid chloride **5** and **20**. The acid chloride **5** was previously obtained by the reaction of the corresponding carboxylic acid with thionyl chloride with the cleavage of sulphur dioxide and hydrogen chloride, according to a literature known procedure. [186] **L⁴** 2-(6-methoxynaphthalen-2-yl)-5-(pyridin-2-yl)-1,3,4-thiadiazole was again synthesised in a cyclisation reaction according to *Fürmeyer*[40,156,165] and *Herold*[41,158]. **21** was heated with Lawesson's reagent in dry toluene under reflux

and argon atmosphere and then purified by column chromatography (DCM → DCM/diethyl ether 9:1) to give a yield of 20 % over four reaction steps. The ligand was fully characterised (^{1}H-NMR-, ^{13}C-NMR-, COSY-NMR-, HMBC-NMR- and HSQC-NMR-, and IR-spectroscopy as well as mass-spectrometry). Figure 64 displays the ^{1}H-NMR spectrum of **L[4]**. The number of the respective signals and the integrals agree with the expected values. The introduced methoxy group is marked in the spectrum with an orange ellipse. All exact assignments of the signals can be taken from the experimental part (chapter 9). All other analytics can be taken from the additional appendix (chapter 11).
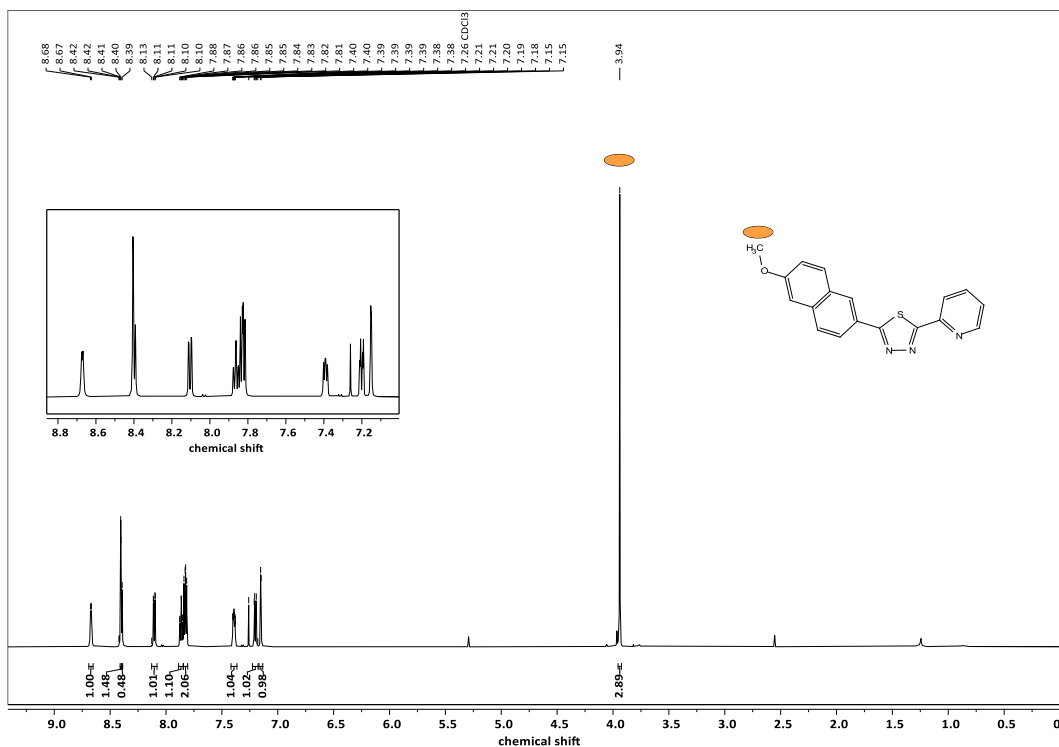

*Figure 64: ^{1}H-NMR of 2-(6-methoxynaphthalen-2-yl)-5-(pyridin-2-yl)-1,3,4-thiadiazole **L[4]** measured at 600 MHz. For a better understanding, only the peaks with the respective integrals, as well as a zoom of all aromatic signals that can be observed, are shown. A precise assignment of all signals can be found in the experimental part.*

7.2. Synthesis of the complex family [Fe(NCX)$_2$(L[4])$_2$] (X = S, Se, BH3).

The synthesis of the complex series [Fe(NCX)$_2$(L[4])$_2$] (X = S, Se, BH$_3$) was carried out by liquid-liquid diffusion. A solution of the ligand in different solvents was layered with a solution of the corresponding dissolved metal salt. All reactions were done under inert gas atmosphere and were carried out with degassed and dried solvents. The reactants used besides **L[4]** were FeSO$_4$ · 7H$_2$O, KSCN, KSeCN and [Fe(Py)$_4$NCBH$_3$]. Single crystals with the anions (SCN[-], SeCN[-] and BH$_3$[-]) could be obtained. For this purpose, both solvents and experimental procedure of the liquid-liquid diffusion were varied. For **C10** and **C11**, FeSO$_4$·7H$_2$O and KXCN were dissolved in equimolar amounts in dry methanol and stirred for at least 2 hours. The resulting colourless precipitate of K$_2$SO$_4$ was filtered and the solution obtained was carefully layered over the ligand dissolved in DCM (2eq.). Small grey rod-shaped single crystals

could be obtained after several days and were used for X-ray structure analysis and the investigation of the molar magnetic susceptibility. **C12** was synthesised in the same way, however, a previously synthesised precursor of the molecularformula $[Fe(py)_4(NCBH_3)_2]$ dissolved in acetonitrile was used. The complexes were characterised by IR-spectroscopy, X-ray structure analysis and measurement of the molar magnetic susceptibility. In the following (Figure 48), the infrared spectra of the synthesised complexes **C10** (red), **C11** (cyan) and **C12** (blue) are compared with the ligand **L⁴** (black). Due to more clarity, the spectra were normalised and shifted relative to each other. Intense bands can be observed in the spectra for **C10** at 2051 cm⁻¹, for **C11** at 2066 cm⁻¹ and for **C12** at 2185 cm⁻¹ and 2340 cm⁻¹, respectively. These bands can be assigned to the coordinating co-ligands NCS⁻ (1990-2140 cm⁻¹), NCSe⁻ (2072 cm-1) and NCBH₃⁻ (v_{CN}=2070-2240 cm⁻¹; v_{BH}=2315-2380 cm⁻¹), respectively. [151,152,178,193,196–199]
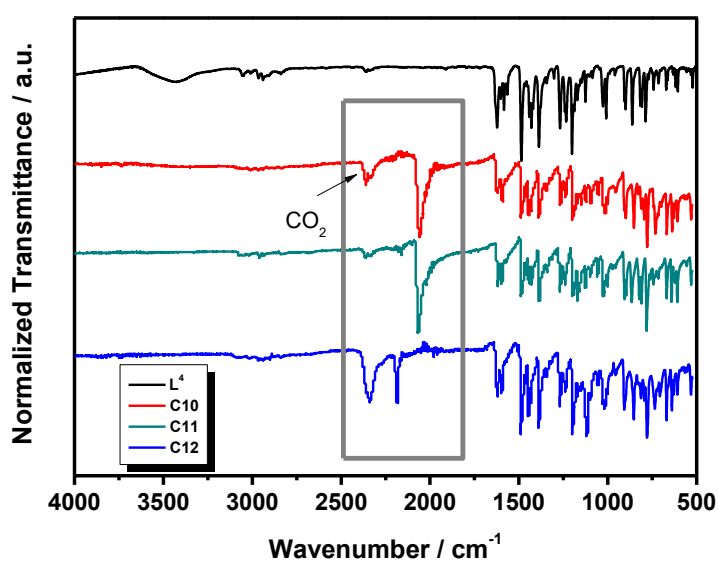
Figure 65: Normalized Infrared spectra of L⁴, C10, C11 and C12 in one graph. The spectra are offset from each other for more clarity. The grey box marks the characteristic IR-bands of the coordinating pseudohalides of the respective complexes; SCN⁻ for C10, SeCN⁻ for C22 and NCBH₃⁻ for C12.

Compared to the IR spectrum of the **L⁴** a successful coordination of the ligand and the coordinating anions can be assumed for C**10**-C**12**. However, infrared spectroscopy cannot be used to draw conclusions about the crystal structure, packing or cooperative effects. Therefore, X-ray structural analyses of the complexes must be included, which are discussed in the following chapter. Where necessary, a brief comparison is made with the previously obtained complexes. Any associated magnetic properties are discussed in section 7.4.

7.3. Crystal structures of C10, C11 and C12

C10, **C11** and **C12** are isostructural, which is why only **C10** is described in detail. All further information on **C11** and **C12** can be found in section 11.4.4.
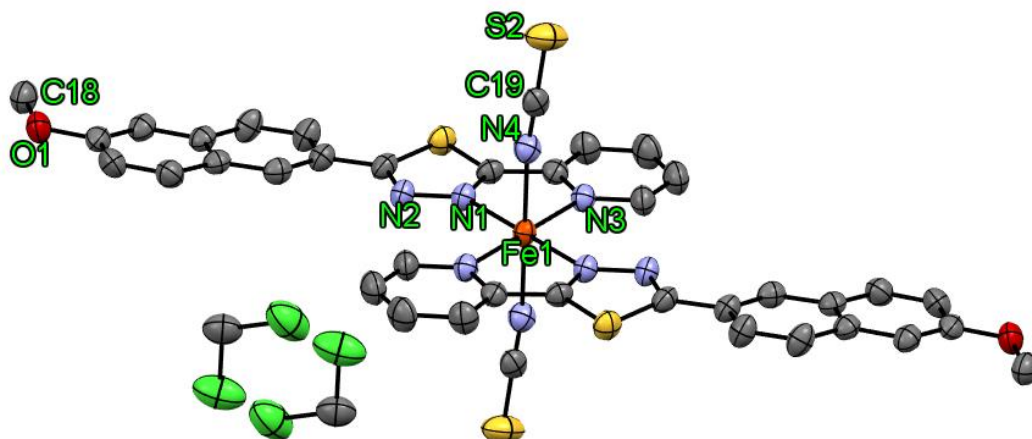

*Figure 66: Crystal structure of **C10** including the atom labelling. Hydrogen atoms are omitted for clarity Color Code: grey-C, yellow-sulfur, blue-N, orange-Fe, white-H, red-O, Cl-green. ORTEP representation with atomic displacement parameters at 50% level of probability.*

The complex **[Fe^{II}(L^4)$_2$(NCS)$_2$] · 2 CH$_2$Cl$_2$ C10** crystallises in the triclinic space group $P\bar{1}$ at 173 K. The asymmetric unit of the complex contains half of the complex molecule, consisting of one molecule of **L^4**, one NCS$^-$ co-ligand, one solvent molecule of DCM and one iron atom sitting on the centre of inversion. Thus, the octahedral coordination sphere is formed by two ligand molecules of **L^4**, building the equatorial coordination sphere and two trans-coordinating thiocyanate anions, representing the tip of the octahedron. This leads to an overall neutral complex molecule. The equatorial plane of the octahedron is built by the pyridyl (N3) and thiadiazole (N1) backbone of the bidentate ligand **L^4**, while the naphthyl-plane is twisted about 6.34° from this plane. In contrast to **C1** and **C2**, this value is reduced by half. The average iron to nitrogen bond distance of 2.16 Å is typical for iron (II)-complexes in HS-state.[1,27,33,110] The bite angle between N1-N3 of bidentate **L^4** (pyridyl-thiadiazole backbone) is 75.77°, while the angle between the coordinated NCS$^-$ and the iron (II) ion is found to be 171.86°. The NCS$^-$ moiety itself is almost linear with an angle of 178.50°. The octahedral distortion parameter Σ is 66.88° and is almost identical with the parent complex **C1** (67.04°). This value of octahedral distortion is again in the expected range of an iron (II) HS complex exhibiting and pyridyl-thiadiazole coordinating motive and pseudohalides as axial co-ligands. [43,151,152] As in the previous examples, the complexes are aligned anti-parallel to each other and again a 3D cross-linked network through π-π-interactions, formed by the coordinated ligand **L^4** is generated. Distances and offsets of all π-π-interacting parts are in the range of interactions well-known from literature (3.27 Å to 3.41 Å).[200,201] All exact values can be taken from the appendix (Table 31 of section 11.4.4). However, this network is not as pronounced as in the parent complex **C1**. Due to the introduced methoxy-group, the 6-methoxy-naphthyl side chain

is rotated towards the coordination sphere instead of away from it likewise **C1** (Figure 67). A similar behaviour could already be observed in the complexes **C3** [Fe^{II}(**L^1**)$_2$(NCS)$_2$] · C$_7$H$_8$, **C7** [Fe^{II}(**L^3**)$_2$(NCS)$_2$] and **C8** [Fe^{II}(**L^3**)$_2$(NCSe)$_2$]. Additionally, the methoxy group hinders the ligand to undergo π-π-stacking in its full extend (Figure 68).
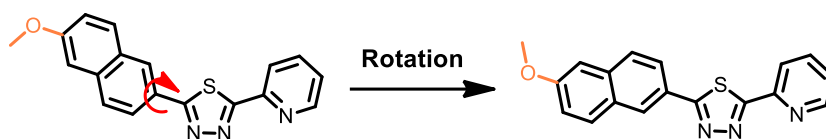

Figure 67: Rotation of the 6-methoxy-naphthyl moiety towards the coordination sphere.

This effects the iron-iron distances of **C10** compared to **C1** (C1:7.95 Å along a, 9.27 Å along b, 12.09 Å along c) which are 9.14 Å along the a-axis, 9.31 Å along the b-axis and 12.34 Å along the c-axis, leading to a less compact crystal packing. The consequence of this is the formation of cavities within the structure, which is marked as a black box in Figure 63. In the centre of these cavities sits an inversion centre, whereby two DCM molecules are located within the cavity. Since the iron (II) ions are also located on an inversion centre, the iron-iron distances and the distances of the cavity centres are equal. All values and figures for **C11** and **C12** are in the same range as described and can be taken from the appendix (Figure 160 and Figure 164 of section 11.4.4)
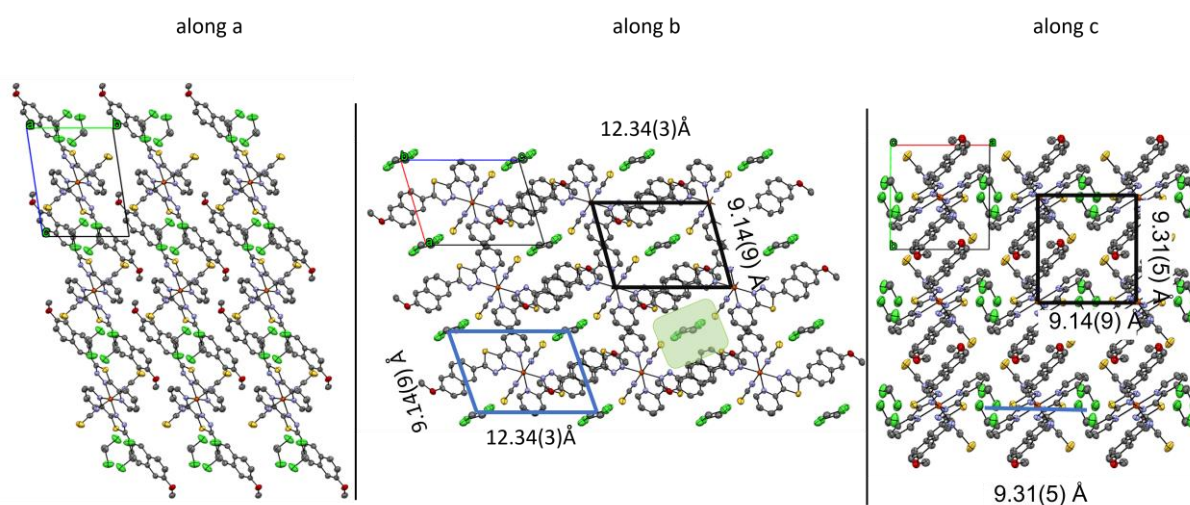
Figure 68: ***along a****: Selected part of the crystal structure of* ***C10*** *at 173 K along the a-axis.* ***along b:*** *Selected part of the crystal structure of* ***C10*** *at 173 K along the b-axis.* ***along c:*** *Selected part of the crystal structure of* ***C10*** *at 173 K along the c-axis. Color Code: grey-C, yellow-sulphur, blue-N, orange-Fe, green-Cl white-H. ORTEP representation with atomic displacement parameters at 50% level of probability. Highlighted are the π-π-interacting anti-parallel aligned ligands of neighbouring complex molecules, respectively. Highlighted are the Fe-Fe distances (black boxes) along the different axis and the distances of the centre of the cavities (blue box).*

7.4. Variable temperature magnetic susceptibility measurements of C10, C11 and C12

The successfully synthesised and describedcomplexes **C10**, **C11** and **C12** were also investigated by variable temperature magnetic susceptibility measurements. The temperature was varied between 2 and 400 K. An external magnetic field of 1000 Oe was used for the data collection of the magnetic susceptibility. The cooling and heating rates (2 K/min) were hold constant in all measurements. The complex samples were filtered, dried and measured as fine crystalline powder as well as crystals. **C11** are in the HS state at 300 K, indicated by the $\chi_M T$ values of 3.56 cm^{3}Kmol^{-1} for **C10** and 3.52 cm^{3}Kmol^{-1} for **C11** and $[Fe(NCBH_3)_2(L^4)_2] \cdot 2\,CH_2Cl_2$ **C12** is in HS state at 400 K, showing a $\chi_M T$ value of 3.26 cm^{3}Kmol^{-1} (Figure 69). The complex **C11** undergoes an abrupt (not as abrupt as **C2**) spin transition of $T_{1/2\downarrow}$ = 150 K while cooling the sample from room temperature, leading in a final $\chi_M T$ value of 0.16 cm^{3}Kmol^{-1}. This indicates an almost complete spin transition. Likewise, **C12** shows spin crossover behavior in a rather gradual manner over a temperature range of 100 K with $T_{1/2\downarrow}$ = 268 K while cooling, also showing almost complete spin transition with a final value of $\chi_M T$ = 0.17 cm^{3}Kmol^{-1}. Both complexes **C11** and **C12** do not show any hysteretic behavior after subsequent heating to room temperature, as well as no metastable states after thermal quenching at 10 K. In turn, the situation for **C10** is somewhat different and closer to that of **C1**, **C2** and **C4**. After quenching the sample at low temperatures due to fast insertion into the measuring chamber at 10 K, **C10** reveals the existence of a metastable TIESST-plateau with a maximum $\chi_M T$ value of 1.48 cm^{3}Kmol^{-1}.[68,69,75,78,153,205–207] This amounts to a recovery of 44 % HS centres through thermal quenching, which is way less than compared to the parent complex **C1**. The drop at low temperatures (below 10 K) can be attributed to zero field splitting effects, leading to a minimum of the magnetic susceptibility of 1.04 cm^{3}Kmol^{-1}.[37,205] After reaching the critical temperature of 50 K, the quenched and preserved HS centres building the metastable plateau are relaxing to the LS ground state with T_{TIESST} = 60 K and a minimum of $\chi_M T$ = 0.99 cm^{3}Kmol^{-1}. The critical relaxation temperature and T_{TIESST} is comparable with the parent complex **C1**. Additionally, the kinetic region (TIESST) and the thermodynamic region (thermal SCO) of **C10** and **C1** exhibit a comparable overlap indicating the actual crossing point around 75 K. [208] Contrary, the spin transitions at T_{TIESST} = 60 K and $T_{1/2\uparrow}$ = 100 K, have more gradual character than those of **C1**. After reaching room temperature, the sample was subsequently cooled again to low temperature (2 K). No hysteresis is observed and the spin transition temperature stays the same with $T_{1/2\downarrow}$ = 100 K. The sample do not undergo a complete spin transition with a final $\chi_M T$ value of 0.78 cm^{3}Kmol^{-1}. Why the magnetic properties of **C11** in this case, although **C10** and **C11** are isostructural, differ from **C10** and did not exhibit a metastable state (like **C1** and **C2**) is unclear so far.
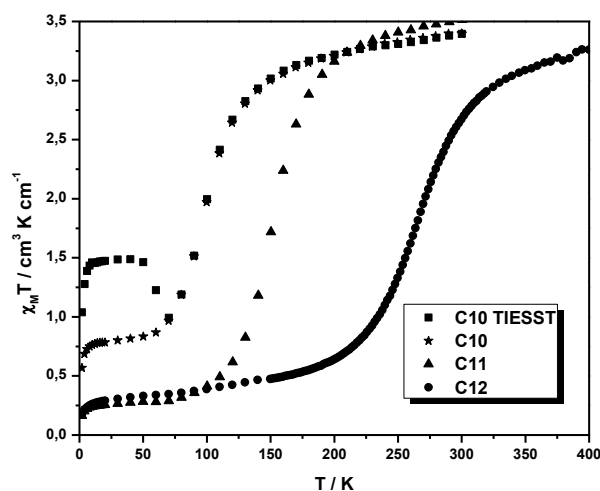
Figure 69: Magnetic properties of [Fe(II)(L⁴)₂(NCS)₂] (C10, squaress), [Fe(II)(L⁴)₂(NCSe)₂] (C11, squares) and [Fe(II)(L⁴)₂(NCBH₃)₂] (C12, cyrcles) with $T_{1/2}\uparrow\downarrow$ = 100 and T_{TIESST} = 60 K for C10, $T_{1/2}\downarrow$ = 150 K for C11 and $T_{1/2}\downarrow$ = 268 K for C12 at constant colling and heating rates of 2 K/min.

In summary, returning to the master motif the use ligand **L⁴** as complex ligand was only moderately successful. Although the SCO properties could be maintained for all three complexes **C10**, **C11** and **C12**, the elastic long-range coupling of the metal centres in the solid state, generated by strong π-π-interactions is clearly affected by the introduced methoxy group at the 6th position of the naphthyl side chain. This is indicated by the disappearance of the hysteretic properties in all three cases and the more gradual spin transitions. Additionally, for **C10**, a much weaker TIESST effect than in the parent complex **C1** could also be observed. This another indication that the degree of high elastic long-range coupling of the magnetic centres in the [Fe^{II}(**L$^{1-4}$**)₂(NCX)₂] (X = S, Se, BH₃) complex families play a decisive role while quenching at low temperatures. This needs to be further investigated.

<u>8.</u> Summary and Outlook

The present work aimed at the synthesis and characterisation of new mononuclear iron (II) spin crossover systems with highly versatile magnetic bistability using 1,3,4-thiadiazole ligands. Previous works from our group, as well as works from literature showed great potential in the use of the 1,3,4-thiadiazole in combination with the pyridyl heterocycle in the coordination sphere. Coordination is completed with pseudohalides (likewise NCS^-, $NCSe^-$ or $NCBH_3^-$) as co-ligands, this results in a very effective spin crossover coordination sphere for iron (II) ions. Special emphasis was placed on the creation of complex system exhibiting a high degree of cooperativity between the individual complex centers within the solid to generate abrupt and hysteretic magnetic properties.[3,33,34,110] SCO compounds with a wide thermal hysteresis loop, if possible around or above room temperature, are most desired[202,234] as both magnetic states, HS or LS, can be observed in the same temperature range. The strong intermolecular interactions required, can be mediated for example by hydrogen bonding[235,236] or π-π-stacking.[180,237] Since a thorough understanding of the interplay between cooperativity and hysteretic magnetic loops is of great importance for future applications, this work focused on the role of π-π-interactions to enhance intermolecular "communication". Therefore, the known ligand 2,5-di(2-pyridyl)-1,3,4-thiadiazole[43,152] was modified by replacing the pyridyl moiety with a naphthyl moiety, leading to the ligand L^1 (2-naphthy-5-pyridyl-1,2,4-thiadiazole), which was used for the successful synthesis of the complex family [$Fe^{II}(L^1)_2(NCX)_2$] (with X = S, Se and BH$_3$). The anionic co-ligands coordinate trans to the metal ions and the complexes are isostructural for [$Fe^{II}(L^1)_2(NCS)_2$] **C1** and [$Fe^{II}(L^1)_2(NCS)_2$] **C2** with no solvent molecules present in the crystal structure. As desired, high communication is observed between the complex molecules within the single crystal due to a huge network of π π-interactions and thus led to abrupt and pronounced hysteretic SCO behavior (**C1**, $T_{1/2}\downarrow$ 100 K and $T_{1/2}\uparrow$110 K; $\Delta T_{1/2}$ = 10 K and **C2**, $T_{1/2}\downarrow$ 96 K and $T_{1/2}\uparrow$ 154 K; $\Delta T_{1/2}$ = 58 K). In addition, **C1** and **C2** show a very pronounced thermally excited spin state capture (TIESST) after thermal quenching of the sample at 10 K. Consequently, a metastable HS state (with T_{TIESST} = 62 K for **C1** and T_{TIESST} = 70 K for **C2**) is obtained at low temperatures, so that the magnetic information contained in the metastable HS state is maintained. The preservation of the thermal HS state at very low temperatures due to thermal quenching was further proven by ^{57}Fe-Mössbauer spectroscopy and low temperature single crystal X-ray diffraction. When cooling the sample from room temperature with different cooling rates, sweeping measurements show a broadening of the hysteresis curve for **C1**. However, for **C2** this is not observable, but different thermally metastable states with different HS fractions are formed in each case, indicating the kinetic trapping of the HS state becomes more favourable with increasing cooling rate. Beyond that, both compounds are stable for several hysteresis cycles at a constant cooling rate. Possible shifts of the transition temperature T_{TIESST} due to different heating rates in sweeping mode were also investigated for the TIESST-plateau. As the heating rate increases after thermal quenching at 10 K of **C1** and **C2**, T_{TIESST} shifts to higher temperatures (from T_{TIESST} = 62.10 K to 76.50 K; ΔT_{TIESST} = 14.40 K for **C1** and from T_{TIESST} = 70.15 K to 86.10 K; ΔT_{TIESST} = 15.95 K for **C2**). This shift from T_{TIESST} closer to $T_{1/2}\downarrow$ is reflected in a less and less complete spin transition, indicating a kinetic distortion of the thermodynamic hysteresis curve. Finally, high pressure single crystal diffraction showed that the

HS-LS change of **C1** could be induced by external compression of the crystal. The spin transition from HS to LS is seen at pressures between 0.8 and 1.02 GPa, the crystal structure changes completely from HS to LS. In turn, the complex $Fe^{II}(L^1)_2(NCBH_3)_2] \cdot C_7H_8$ **C3** shows clearly different behavior. Due to the crystallisation of solvent molecules of toluene into the crystal structure, **C3** exhibits a two-step SCO ($T_{1/2\downarrow\uparrow}(1)$ = 160 K and $T_{1/2\downarrow\uparrow}(2)$ = 300 K). Neither TIESST-properties due to thermal quenching nor any hysteresis are observed. Surprisingly, the second spin transition at 160 K of the two-step SCO disappears when the sample is kept for 10 min at 400 K. Only, one abrupt spin transition is left at $T_{1/2\downarrow}$ = 290 K when cooling the sample again to room temperature, showing a solvent dependent hysteresis opening. This needs further investigation. It would be very interesting to understand whether and to what extent it is possible to revive the two-step SCO by rediffusion of different solvents into the solid.

To gain further insight on the dependence of the above-mentioned findings and the cooperative properties through π-π-stacking, the ligand **L¹** was structurally modified in different projects. To address the issue of how the magnetic properties differ due to the different structural properties as the π-system of the ligand is reduced by replacing the naphthyl side chain with a smaller phenyl ring. The complex family $[Fe^{II}(L^2)_2(NCX)_2]$ (with X = S (**C4**), Se (**C5**) and BH_3 (**C6**)) could only maintain the previously discovered magnetic SCO properties to a limited extent. All three complexes show spin transitions ($T_{1/2\downarrow\uparrow}$ = 180 K for **C5** and $T_{1/2\downarrow\uparrow}$ = 309 K for **C6**), but these tend to be of more gradual nature. Only **C4** (T_{TIESST} = 80 K; $T_{1/2\downarrow}$ = 116 K and $T_{1/2\uparrow}$ = 124 K; $\Delta T_{1/2}$ = 8 K) exhibits a metastable TIESST plateau and hysteretic properties, similar to the parent complex **C1**. It was found that small solvent molecules (DCM and MeOH) were incorporated in the respective crystal structures, presumably due to significantly smaller π-π-stacking because of the ligand's smaller π-system. Since the comparison of the structural properties of the complexes formed with ligand **L¹** and **L²** gave clear indications that the degree of cooperativity through π-π-stacking is decisive for the exciting magnetic properties, ligand **L³** (2-(anthracen-2-yl)-5-(pyridin-2-yl)-1,3,4-thiadiazole) was designed in a further project and used for the synthesis of iron (II) complexes. Due to the solvent-free crystallisation of complexes **C1** and **C2** which are responsible for the great stability of the bulk material and thus the magnetic properties, like the magnetic hysteresis loop, the complex family $[Fe^{II}(L^3)_2(NCX)_2]$ (with X = S (**C7**), Se (**C8**) and BH_3 (**C9**)) was attempted to force crystallising without any crystal solvent by increased π-π-interactions of the ligand **L³**. This "crystal-engineering" approach was successful for **C7** and **C8**, as these have a significantly higher degree of cooperativity and stronger π-π-stacking. However, both complexes no longer show SCO properties, as the intermolecular interactions are so strong that the spin transition is blocked. Presumably, this happens because of a too dense crystal packing, so that the geometric changes a SCO requires cannot be realised. This is a perfect example that crystal-engineering works in principle, but crystal packing effects play such a crucial role, making it much more difficult to accurately predict the desired magnetic properties. Only **C9** of this complex series shows SCO properties ($T_{1/2\downarrow\uparrow}$ = 230 K). The reason for this is the found cis-configuration of the complex, which leads to an expanded crystal packing, allowing the required volume change of the individual spin crossover molecules. The findings, that the control of cooperativity via modified π-π-stacking just needed to be slightly varied for the complexes dealt in this work, led to the synthesise of **L⁴**. The challenge to be addressed was to understand to what extent **L¹** (the so-called master motif) can be modified to eliminate, preserve, or

even improve the desired structural and/or magnetic properties. For this reason, the ligand was modified with the smallest possible synthetic effort by introducing a methoxy group at the 6th position in the naphthyl ring, leading to the ligand L^4 (2-(6-methoxynaphthalen-2-yl)-5-(pyridin-2-yl)-1,3,4-thiadiazole). As expected, π-π-stacking decreased with the introduction of the methoxy group. However, it was also seen that the small change in the ligand had a drastic effect on the magnetic behaviour. Again, for all three complexes, rather gradual spin transitions (**C10** $T_{1/2\downarrow\uparrow}$ = 100 K, **C11** $T_{1/2\downarrow}$ = 100 K, and **C12** $T_{1/2\downarrow}$ = 268 K) without hysteretic properties were observed. However, **C10** showed a less pronounced metastable state due to thermal quenching of the sample with a T_{TIESST} = 60 K equal to that of the mother complex **C1**.

In conclusion, twelve new complexes have been synthesised with different bidentate ligands showing different structural and magnetic properties. The most promising spin crossover system exhibiting magnetic bistability presented in that work is probably the complex family $[Fe^{II}(L^1)_2(NCX)_2]$ (with X = S, Se and BH$_3$ and L^1 = 2-naphthy-5-pyridyl-1,2,4-thiadiazole), which exhibits many exciting properties at constant structural stability. In addition, the manipulation of the desired hysteretic and TIESST properties through the targeted structural influence (ligand design) on the intermolecular π-π-interactions is difficult for various reasons and can only be predicted to a limited extent. For this reason, a return to the already great functioning complex system $[Fe^{II}(L^1)_2(NCX)_2]$ is recommended for future research work, as it still has a lot of exciting potential.

To get closer to answering the question of why the systems, especially **C1** and **C2** behave magnetically in the presented way, various approaches could be made. To generate a better understanding and insight into the processes occurring within the solid state, low temperature X-ray scattering could be used to track and compare the structural features with the magnetic curve at different temperatures, after thermal quenching of the sample and subsequent heating to room temperature.[238] The comparison of the different structural diffraction patterns of the solid state of the kinetic spin transition from the metastable state to the LS ground state (TIESST) and of the subsequent thermodynamic spin transition ($T_{1/2}$) could provide information on how the SCO is propagating through the the solid crystal.[238] In addition, the approach of metal dilution by non-SCO active metal ions (for example Mn^{II} or Zn^{II}) could be applied and combined with the previous described experiment to moderate or buffer the cooperativity and thus the intermolecular interactions. This would provide further insight into the structural mechanism of the different spin transitions.[238] Dilution experiments also could be used to control and directly manipulate the spin transitions of the hysteresis loop as well as those of the metastable state as desired. Due to the non-SCO active metal centres within the solid, the cooperativity of the intermolecularly communicating complex molecules is affected, which should consequently influence the transition curves as well.[68] Furthermore, it would be beneficial to generate metastable states with light (LIESST) instead of thermal quenching with subsequent investigation of their relaxation processes in a similar way as it was done in this work for the TIESST plateaus of some complexes.[70] This would require a low temperature UV/VIS to determine the exact irradiation wavelength of the $^1A_{1g}$- band of the respective complex. In contrast, the principle of the reverse LIESST effect can also be applied to **C1** and **C2**, for instance, to convert a thermally generated

metastable state back to the LS ground state by irradiating into the $^5T_{2g}$ band of the complex.[71] Another approach aims to influence the magnetic properties of the active SCO complexes through macroscopic effects of the grown nanocrystals. With the so-called reverse micelle technique,[239,240] it is possible to grow SCO nanocrystals in different shapes and sizes, depending on how the solvent and surfactant are chosen. The principle is based on the ratio of surface and volume of the grown particle/crystal. Because of a small volume ratio compared to the surface, the incomplete coordination at the particle surface increases and thus there is a partial loss of "chemical pressure" at the nearby Fe^{II} centres. Consequently, the transition temperature of the SCO system is affected.[241] This should also have a major impact on the hysteretic properties and the TIESST plateau of **C1** and **C2**. Thus, the solvent-free crystallisation of the two complexes could result in a structurally controllable system with equally controllable magnetic properties at any time. Finally, Since **C1** showed pressure induced SCO properties, the same bevavior should be studied for **C2**, as well as the influence on the different $\chi_M T$ curves of **C1** and **C2** at varied pressure to investigate how the TIESST and the hysteretic properties are affected.

9. Experimental Section

9.1. General working methods

Commercially available chemicals were purchased by abcr, Acros Organics, Alfa Aesar, Deutero, Fisher Scientific, Roth, Sigma Aldrich and TCI and used without further purification. Solvents were dried according to literature procedures.[242] To prevent any oxidation processes of the iron(II) compounds during the complex syntheses, work was carried out in a glovebox (MBraun) with argon atmosphere. Anhydrous solvents degassed with argon were used. The acetonitrile and tetrahydrofuran used were dried using an SPS 800 Manual solvent drying unit from MBraun. Ligand **L²** was synthesised in cooperation with ▓▓▓▓▓▓▓▓ during his Bacherlor thesis, as well as **L⁴** was synthesised by ▓▓▓ ▓▓▓ during her Bachelor thesis.

9.2. Instrumental Details

9.2.1. Mössbauer spectroscopy

Transmission Mössbauer spectra were measured by two Mössbauer spectrometers operating in constant acceleration mode in conjunction with a 512-channel analyzer working in the time-scale mode (WissEl GmbH). The sources contained ^{57}Co diffused in Rh with an activity of 1.4 GBq. Temperature-dependent Mössbauer spectroscopy was performed using a continuous flow cryostat (OptistatDN, Oxford Instruments) and a helium closed cycle cryostat (CRYO Industries of America Inc.). The spectrometers were calibrated against α-iron at room temperature. Spectral data were transferred from multi-channel analyzers to PCs for further analysis, employing the public domain

program Vinda running on an Excel 2003R platform.[243] The spectra were analyzed by least-squares fits using Lorentzian line shapes with the line width at half maximum given as Γ.

9.2.2. IR-Spectroscopy

The IR spectra were all measured at room temperature. An FT/IR Nicolet5700 from ThermoFischer was used. All further evaluations were carried out with the Omnic software. In addition, an FT-IR from Bruker was used. All further evaluations were carried out with the Opus software. In each case, the bands with the highest intensity and the characteristic bands of the material were indicated.

9.2.3. Chromatography

For the chromatographic purification of the respective raw products, column chromatography was used according to the principle of flash chromatography.[53] Silica gel from the company Acros Organics, which has a particle size of 35-70 μm, was used as the stationary phase. Controls of the individual reactions were carried out using aluminium prefabricated plates with silica gel coating and were obtained from the company Macherey-Nagel (Alugram SIL G/UV_{254}). Detection of the fractions was performed by UV light of wavelength λ = 254 nm and λ = 365 nm and using the following staining reagents:

- Vanillin: 100 mL methanol, 1.0 g vanillin, 4 mL conc. sulphuric acid, 12 mL acetic acid.

- Ninhydrin: 0.2 g ninhydrin, 3 mL acetic acid100 mL ethanol

- p-anisaldehyde: 5.1 mL p-anisaldehyde, 1.7 mL acetic acid, 150 mL ethanol, 5.6 mL conc. sulphuric acid.

9.2.4. Mass spectrometry

ESI mass and APCI mass spectra were recorded by the department of mass spectrometry at Johannes Gutenberg University Mainz on an Agilent 6545 QTOF-MS with positive ion mode. For preparation, the samples were dissolved in appropriate solvents. The spectra were visualized with Origin8.

All FD mass spectra were carried out at the Institute for Analytical and Inorganic Chemistry at the Johannes Gutenberg University Mainz. The Trace 1310 DFS mass spectrometer used for this purpose was provided by ThermoFisher.

9.2.5. NMR-Spektroskopie

All samples were dissolved in deuterated solvent and analysed with the following instruments: Bruker DRX 400 DRX 400 (v(^{1}H)= 400.13 MHz, v(^{13}C) = 100.61 MHz); Avance III HD 300 (v(^{1}H)= 400 MHz, v(^{13}C) = 100.1 MHz); Avance II 400 (v(^{1}H)= 400.13 MHz, v(^{13}C) = 100.1 MHz); Avance III 600 (v(^{1}H)= 600 MHz, v(^{13}C) = 151 MHz).

The chemical shift, which is given in ppm, refers to the signal of the deuterated solvent used and trimethylsilane as standard. δ [ppm] = 7.26 { ^{1}H}, 77.16 {^{13}C}, MeOD-d4 δ [ppm] = 3.31{ ^{1}H}, 49.00 {^{13}C}, DMSO-d6 δ [ppm] = 2.50 { ^{1}H}, 39.52 {^{13}C}).[244] All deuterated solvents were obtained from the company Deutero. The spectra were evaluated by the MestReNova programme from the company Mestrelab Research.

9.2.6. Single Crystal X-Ray Structure Analysis

X-ray crystallographic data were collected and refined by ▮▮▮▮▮▮▮▮ on a STOE STADIVARI at Johannes Gutenberg University Mainz or by ▮▮▮▮▮▮▮▮ on a STOE IPDS 2T diffractometer at Johannes Gutenberg University Mainz. The crystal structures were solved with SHELXT[245] and refined with SHELXL[246] implemented in the program Olex².[247] The other crystal structures were solved and refined by ▮▮▮▮▮▮. The structures were visualized with Mercury3.8, Mercury4.2.[220]

9.2.7. Magnetische Suszeptibilitätsmessungen

Variable temperature magnetic susceptibility measurements were performed in the range of 2 to 400 K at an applied field of 1 kOe (0.1 T), unless not specified, using a Quantum Design MPMSXL SQUID magnetometer. Sweeping measurements were carried out at heating or cooling rates between 0.35 K/min and 10 K/min. The crystalline samples were placed in a gelatin capsule and fixed in a plastic straw. The magnetic contribution of the capsule and straw was determined experimentally and subtracted from the measured value. The molar magnetic susceptibilities χ_M were calculated using the molar masses of the compounds and taking the diamagnetic contribution χ_D into account. The calculation of the diamagnetic contribution χ_D of the sample was done using the following equation.[248]

$$\chi_D \backsim \frac{M}{2} \cdot 10^{-6} \, emu \, mol^{-1} \qquad\qquad 21$$

9.2.8. Elemental Analysis

Elemental analyses (C, H, N) were performed at the Johannes Gutenberg-University in Mainz in the analytical department of the Institute of Organic Chemistry using a vario EL cube element analyzer from *Elementar*.

9.2.9. Pressure induced SCO experiments

The high-pressure single crystal X-ray diffraction on **C1** was carried out at room temperature using a Boehler-Almax diamond anvil cell. In order to cover the pressure range in small steps of pressure, two different crystals were used. The pressures used for measurement are given in Table 1. The pressures were obtained using the ruby fluorescence method.

Data reduction and integration of all HP data were completed in CrysAlisPRO using the same strategy, which was adapted for HP experiments. Standard tricks to avoid contamination from gasket rings and diamond reflections was used to extract the orientation matrix before data integration. A cell opening angle of 38° was implemented, reflections with bad profiles were discarded, and the data resolution was truncated at 1.05 Å. A crystal structure from ambient data at room temperature was used as starting point for all HP refinements, ensuring identical naming schemes. In the refinement, only iron and sulfur atoms were refined using anisotropic thermal parameters, while all other atoms were treated isotropically.

9.3. Ligand Synthesis

9.3.1. Ethyl-2-naphthoate (2)[186]

1   →   H₂SO₄ [EtOH]   →   **2**

$$\text{H}_2\text{SO}_4 \quad [\text{EtOH}]$$
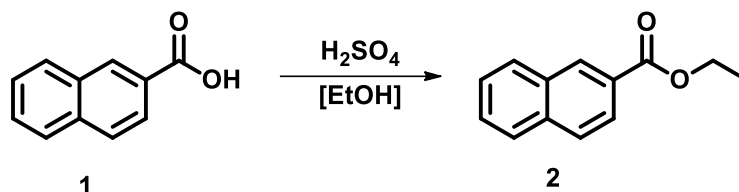
**C₁₃H₁₂O₂**   **REN-JMK-073**

2-Naphthoic acid (**1**) (10.00 g, 57.50 mmol, 1.0 eq.) was dissolved in ethanole (65 mL) and 95% sulphuric acid (3.91 mL) was added dropwise. The solution was refluxed over night, neutralized with sodium carbonate, and extracted with ethyl acetate (4 x 20 mL). The organic layer was dried over manganese sulfate and the solvent was removed under reduced pressure. The resulting yellowish oil (**2**) crystallises as colourless needles.**Yield**: 9.85 g (49.19 mmol, 84 %).**¹H-NMR** (400 MHz, Chloroform-d, 25 °C) δ = 1.45 (t, J=7.1, 3H), 4.45 (q, J=7.1, 2H), 7.57 (m, 2H), 7.88 (d, J=8.4, 2H), 7.96 (d, J = 8.0, 1H), 8.07 (dd, J=8.6, 1.7, 1H), 8.62 (s, 1H).**APCI-MS** (MeCN): m/z = 129.0703 $[\text{C}_{10}\text{H}_9]^+$ (cacld. = 129.0704), 155.0498 $[\text{C}_{11}\text{H}_7\text{O}]^+$ (calc.= 155.0497), 173.0599 $[\text{C}_{11}\text{H}_9\text{O}_2]^+$ (calc. = 173.0603). **R$_f$** (cyclohexane/ethyl acetate on silica) = 0.47.

9.3.2. 2-Naphthohydrazide (3)[185]

2   →   H₂NNH₂ [EtOH]   →   **3**

$$\text{H}_2\text{NNH}_2 \quad [\text{EtOH}]$$
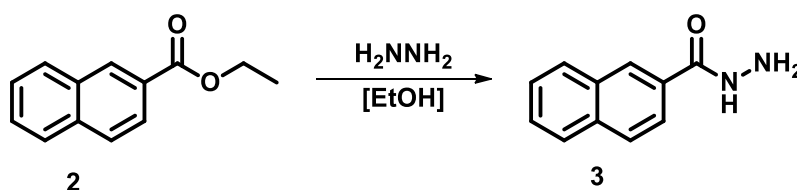
C₁₁H₁₀N₂O   **REN-JMK-074**

Ethyl-2-naphthoate (**2**) (9.87 g, 49.29 mmol, 1eq.) was dissolved in ethanol (70 mL) and hydrazine hydrate (3.48 g, 54.22 mmol, 3.37 mL, 1.1 eq) diluted in ethanol (10 mL), was added dropwise to the previous solution. The reaction mixture was refluxed until the reaction was finished, controlled by TLC. Subsequently, the solvent and hydrazine were removed under reduced pressure to obtain a light-yellow solid (**3**). **Yield:** 9.14 g (49.08 mmol, 99%). **¹H-NMR** (400 MHz, DMSO-d_6, 25 °C) δ = 4.58 (s,

3H), 7.59 (tt, *J*=7.2, 5.1, 2H), 7.97 (m, 4H), 8.43 (s, 1H), 9.93 (s, 1H).**IR** (ATR): $\tilde{v}$ (cm^{-1}) 3311 (m), 3174 (m), 1713 (s), 1651 (s), 1615 (s), 1095 (s), 1000(s), 912 (s), 900 (s), 722 (s), 483 (s).

### 9.3.3. N'-(2-naphthoyl)-picolinohydrazide (6)
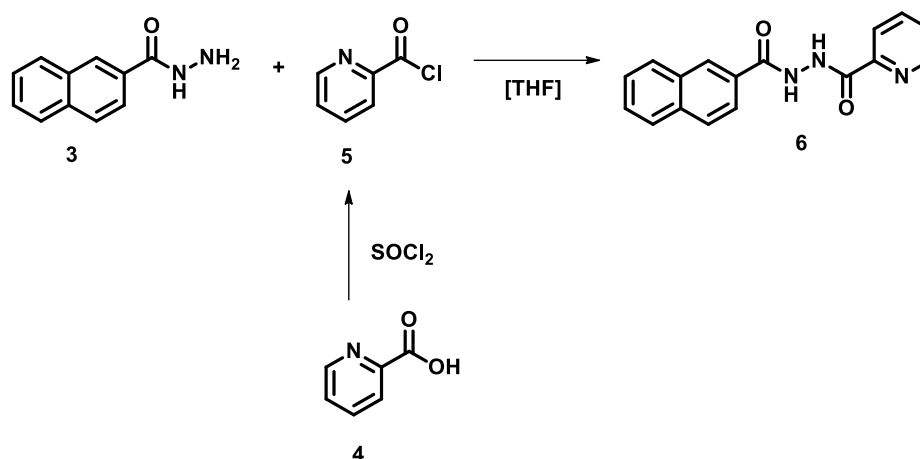
C₁₇H₁₃N₃O₂   **REN-JMK-082**

2-Naphthohydrazide (**3**) (1.20 g, 6.44 mmol, 1 eq.) was suspended in dry THF. Pyridine-2-carbonyl chloride (**5**) (1.00 g, 7.09 mmol, 1.1 eq) , freshly prepared by literature procedure[186], was dissolved in dry THF and added to the suspension dropwise under exclusion of oxygen. After the reaction mixture was stirred for 24h, the brown solid formed was filtered and washed with ether. Thereafter, the dried solid was suspended in ethyl acetate and the solution was made alkaline (pH = 8) with a saturated sodium bisulfate solution to get rid of the formed hydrochloride. The suspension was stirred until all crude product was dissolved. The aqueous layer was extracted with ethyl acetate (3 x 5 mL), all organic layers combined, dried over manganese sulfate and the solvent removed giving a brown solid (**6**). **Yield**: 1.37 g (4.72 mmol, 73.19 %).**¹H-NMR** (300 MHz, DMSO-*d₆*, 25 °C) δ = 7.66 (m, 3H), 8.01 (m, 2H), 8.07 (m, 4H), 8.56 (m, 1H), 8.73 (m, 1H), 10.71 (s, 2H).**APCI-MS** (MeCN): *m/z (%)* = 292.1085 ([M]+H⁺)⁺ (100 %) (calc. = 292.1081).**IR** (ATR): $\tilde{v}$ (cm^{-1}): 3169 (m), 3009 (m), 1684 (m), 1644 (s), 1505 (m), 1283 (m), 815 (m), 773 (m), 750 (m), 744 (m).

9.3.4. 2-naphthyl-5-pyridyl-1,3,4-thiadiazol (L^1)[40,41,156,158,165,186]

6

L^1
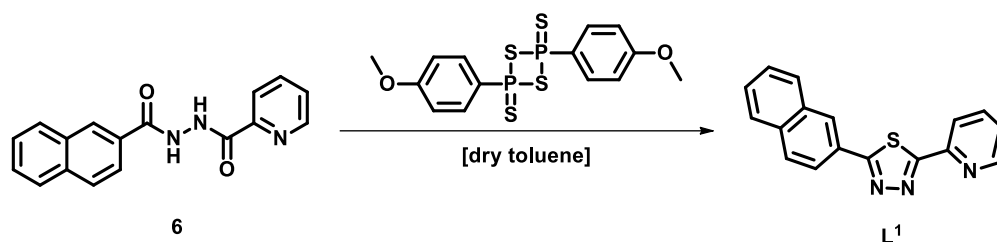
C$_{17}$H$_{11}$N$_3$S   **REN-JMK-098**

6 (1.37 g, 4.72 mmol, 1 eq.) and Lawesson's reagent (2.41 g, 5.66 mmol, 1.20 eq.) were suspended in dry toluene (230 mL) and refluxed under nitrogen atmosphere for 24h. The reaction solution was then cooled to room temperature, filtrated and the solvent was removed under reduced pressure. The resulting orange-brown oil was purified by column chromatography (SiO$_2$, gradient from DCM to DCM/diethyl ether 9:1). By-products formed of reacting Lawesson's reagent were eluated with pure dichloromethane. The product (**L^1**) was isolated by changing the solvent gradually to DCM/diethyl ether 9:1. **Yield**: 1.04 g (3.56 mmol, 75 %) as pale yellow needles. **^{1}H-NMR** (400 MHz, Chloroform-*d*, 25 °C) δ = 7.39 (dd, *J*=7.6, 4.8, 1H,H$_{31}$), 7.55 (tt, *J*=6.8, 3.6, 2H, H$_{28,22}$), 7.86 (m, 2H, H$_{30,27}$), 7.94 (d, *J*=8.2, 2H, H$_{26,23}$), 8.15 (dd, *J*=8.6, 1.8, 1H, H$_{25}$), 8.40 (d, *J*=7.9, 1H, H$_{29}$), 8.48 (d, *J*=1.7, 1H, H$_{24}$), 8.67 (d, *J*=4.9, 1H, H$_{32}$). **^{13}C-NMR** (101 MHz Chloroform-*d*, 25 °C) δ = 121.03 (C$_{12}$), 124.53 (C$_{17}$), 125.31 (C$_{10}$), 127.06 (C$_{20}$), 127.64 (C$_6$), 127.71 (C$_{19}$), 127.93 (C$_{21}$), 128.29 (C$_{13}$), 128.83 (C$_{16}$), 129.08 (C$_{18}$), 133.12 (C$_{14}$), 134.60 (C$_{15}$), 137.21 (C$_{11}$), 149.22 (C$_7$), 149.85 (C$_9$), 169.94 (C$_4$), 170.19 (C$_1$).**APCI-MS** (MeCN): *m/z* (%) = 290.0747 ([M]+H$^+$)$^+$ (100%) (calc. = 290.0752) , 291.0776 ([M]+H$^+$)$^+$ (19.7%) (calc. = 291.0785), 292.0739 ([M]+H$^+$)$^+$ (4.7%) (calc. = 292.07).**IR** (ATR): $\tilde{v}$ (cm^{-1}): 3036 (w), 2919 (w), 1583 (m), 1474 (m), 1427 (m), 817 (s), 777 (s), 751 (s), 735 (s), 615 (s). **R$_f$** (DCM on silica) = 0.1, (DCM/diethyl ether 9:1 on silica) = 0.74.

9.3.5. Ethyl 2-pyridine carboxylate(**8**)[249]

7   **8**
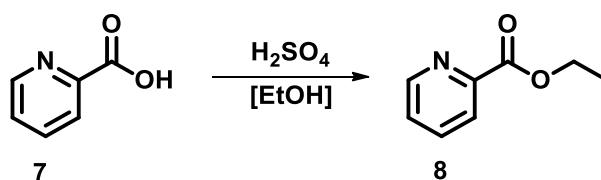
C$_8$H$_9$NO$_2$ **REN-HG-001**

2-picolinic acid (**7**) (10.82 g, 87.89 mmol, 1.0 eq.) was placed in a round bottom flasked in ethanole (130 mL) and 95% sulphuric acid (2 mL, 8.62 g, 87.89 mmol, 1 eq.) was added dropwise. The solution was refluxed over night. The solvent was removed under reduced pressure and the crude product was redissolved in 30 mL of DCM and washed several times with a sodium bicarbonate solution (5%). The organic layer was dried over manganese sulfate and the solvent was evaporated. The resulting

yellowish oil (**8**) crystallises as colourless needles. **Yield**: 9.86 g (65.23 mmol, 74%).**¹H-NMR** (400 MHz, Chloroform-d) δ 8.76 (m, 1H), 8.14 (m, 1H), 7.84 (td, J = 7.7, 1.7 Hz, 1H), 7.47 (ddd, J = 7.5, 4.8, 1.3 Hz, 1H), 4.48 (q, J = 7.2 Hz, 2H), 1.44 (t, J = 7.1 Hz, 3H). **IR** (ATR): $\tilde{\nu}$ (cm^{-1}) 3065 (w), 2979 (w), 1713 (s), 1584 (m), 1438 (m), 1367 (m), 1290 (s), 993 (m), 856 (w), 746 (s), 705 (s), 618 (w). **R$_f$** (cyclohexane/ethyl acetate 9:1 on silica) = 0.62.

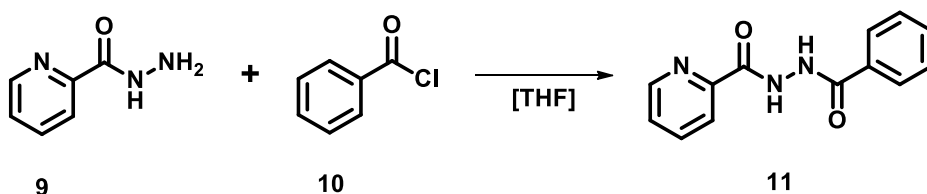## 9.3.6. 2-Pyridinecarboxylic acid hydrazide (**9**)[249]

8　　　　　　　　　　　　　　**9**
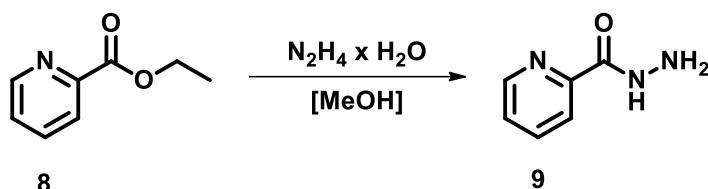
C$_6$H$_7$N$_3$O　　　　　　　　　　　　　　　　　　　　　　　　**REN-HG-003**

Ethyl 2-pyridine carboxylate (**8**) (11.00 g, 72.77 mmol, 1.0 eq.) was added dropwise to a solution of hydrazine monohydrate (5.13 g, 80.05 mmol, 1.10 eq.) in 20 mL methanol. The resulting mixture was stirred at room temperature over night. Removing the solvent and the residual hydrazine monohydrate under reduced pressure afforded picolinohydrazide (**9**) as a pale yellow oil, which crystallised at room temperature. **Yield**: 8.31 g (60.59 mmol, 83%). **¹H-NMR** (400 MHz, DMSO-d6) δ 9.86 (s, 1H), 8.60 (dt, J = 4.8, 1.3 Hz, 1H), 7.97 (m, 2H), 7.57 (ddd, J = 5.8, 4.7, 3.2 Hz, 1H), 4.62 (s, 3H). **IR** (ATR): $\tilde{\nu}$ (cm^{-1}) 3290 (w), 3211 (w), 2979 (w), 2331 (w), 1636 (s), 1567 (m), 1518 (m), 1381 (m), 1201 (m), 993 (m), 818 (w), 748 (m), 705 (s), 618 (m), 454 (w).

## 9.3.7. N`-(2-benzoyl)-pyridine-2-carboxylic acid hydrazide (**11**)[186]

9　　　　　　　**10**　　　　　　　　　　　**11**

C$_{13}$H$_{11}$N$_3$O$_2$　　　　　　　　　　　　　　　　　　　　　**REN-PR-023**

2-Pyridinecarboxylic acid hydrazide (**9**) (4.00 g; 29.17 mmol; 1 eq) was placed in 70 mL THF and a solution of benzoyl chloride (**10**) (4.14 g; 29.17 mmol; 1 eq) in 10 mL THF was added. A colourless solid precipitated immediately. The solid was filtered and washed with THF. A beige solid (**11**) was obtained and used without further purification. **Yield:** 4.28 g (17.74 mmol, 61 %). **IR** (ATR): $\tilde{\nu}$ (cm^{-1}): 3035 (m), 2926 (m), 1700 (s), 1653 (s), 1601 (s), 1521 (s), 1282 (s), 1178 (m), 867 (m), 801 (m), 749 (s), 702 (s), 636 (s).

9.3.8. 2-phenyl-5-(pyridin-2-yl)-1,3,4-thiadiazole (L^2)[40,41,156,158,165,186]

11   **L^2**
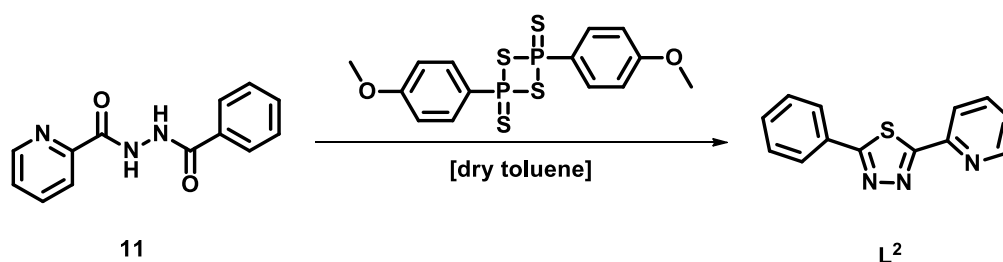
C$_{13}$H$_9$N$_3$S   **REN-PR-014**

N`-(2-benzoyl)-picoline hydrazide (**11**) (4.20 g; 17.12 mmol; 1 eq) was placed in about 750 mL dry toluene and Lawesson's reagent (8.75 g, 20.55 mmol, 1.2 eq) was added and the suspension was then refluxed for 24 h under inert gas atmosphere. The reaction solution was then cooled to room temperature, filtrated and the solvent was removed under reduced pressure. Subsequently, the resulting orange-brown oil was purified by column chromatography (SiO$_2$, toluene). A colourless solid was obtain (**L^2**). **Yield:** 3.05 g (12.75 mmol, 74 %). **^{1}H-NMR** (600 MHz, CDCl$_3$) δ = 8.66 (dt, J=4.9, 1.3, 1H, H$_{26}$), 8.39 (dt, J=7.9, 1.1, 1H, H$_{23}$), 8.06 – 8.00 (m, 2H, 18, H$_{22}$), 7.86 (td, J=7.7, 1.7, 1H, H$_{24}$), 7.52 – 7.46 (m, 3H, H$_{19,20,21}$), 7.39 (ddd, J=7.6, 4.8, 1.2, 1H, H$_{25}$). **^{13}C-NMR** (151 MHz, CDCl$_3$) δ = 170.06 (C$_4$), 169.82 (C$_1$), 149.76 (C$_9$), 149.09 (C$_7$), 137.29 (C$_{11}$), 131.27 (C$_{15}$), 130.20 (C$_6$), 129.22 (C$_{14,16}$), 127.97 (C$_{13,17}$), 125.34 (C$_{10}$), 121.02 (C$_{12}$). **APCI-MS** (MeCN): m/z (%) = 240,060 ([M]+H$^+$)$^+$ (100%) (calc. = 240.0595), 241,063 ([M]+H$^+$)$^+$ (4,5%) (calc. = 241.0629). **IR** (ATR): $\tilde{v}$ (cm^{-1}): 3043 (w), 2981 (w), 1582 (m), 1432 (m), 1248 (w), 1071 (w), 1007 (m), 783 (s), 762 (s), 686 (s), 604 (s).

9.3.9. N'-(2-anthracenyl) pyridine-2-carboxylic acid hydrazide (**17**)[186,250]
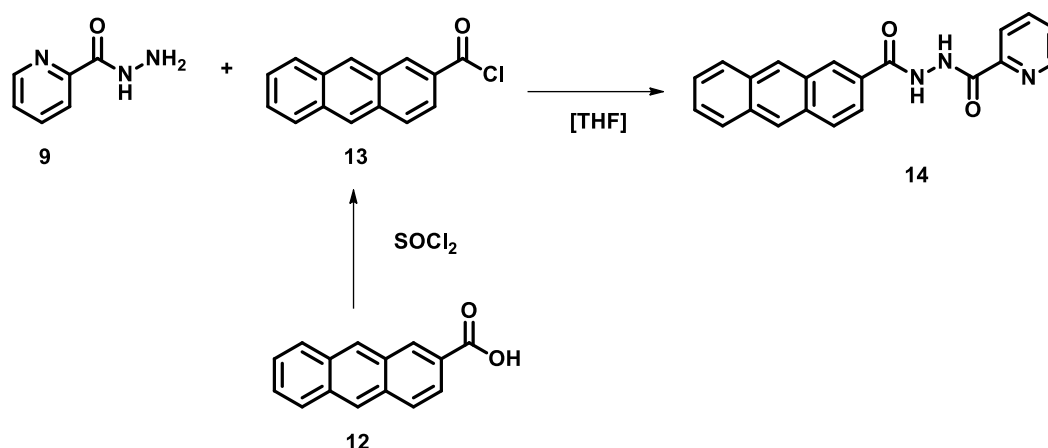
C$_{21}$H$_{15}$N$_3$O$_2$ **REN-JMK-145**

Anthracene-2-carbonyl chloride (**13**) (1.00 g, 5.28 mmol, 1.0 eq) , freshly prepared by literature procedure[186], was suspended in dry THF. Picolinohydrazide (**9**) (0.724 g, 5.28 mmol, 1.0 eq.) was dissolved in dry THF and added to the suspension dropwise under exclusion of oxygen. Subsequently, the reaction mixture was stirred for 24h, the bright yellow solid formed was filtered and washed with ether.The product (**14**) was used without further purification. **Yield**: 1.75 g (5.12 mmol, 97 %).**^{1}H-NMR** (400 MHz, DMSO-d_6) δ 10.80 (s, 1H), 10.75 (s, 1H), 8.75 (m, 3H), 8.67 (s, 1H), 8.13 (m, 6H), 7.95 (dd, J = 8.9, 1.7 Hz, 1H), 7.69 (ddd, J = 6.9, 4.8, 1.8 Hz, 1H), 7.59 (m, 2H). **APCI-MS** (MeCN): m/z = 705.2229 ([2M]+Na$^+$)$^+$ (100 %) (calc. = 705.2221), 324.1239 ([M]+H$^+$)$^+$ (42.52 %) (calc. = 341.1164).

9.3.10. 2-(anthracen-2-yl)-5-(pyridin-2-yl)-1,3,4-thiadiazole (**L³**) [40,41,156,158,165,186]
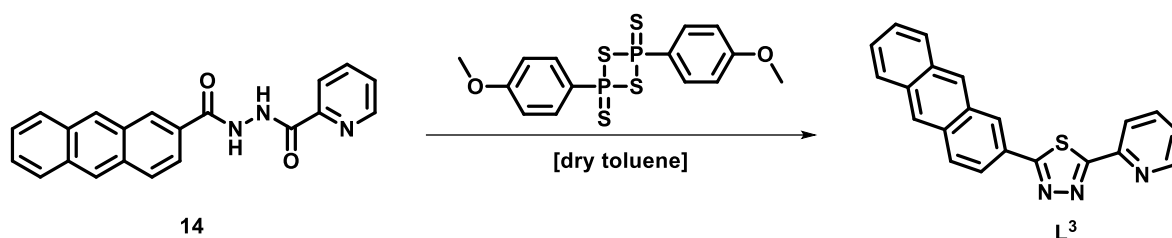
**C$_{21}$H$_{13}$N$_3$S**   **REN-JMK-147**

14 (1.90 g, 5.57 mmol, 1 eq.) and Lawesson's reagent (2.61 g, 6.12 mmol, 1.20 eq.) were suspended in dry toluene (300 mL) and refluxed under inert gas atmosphere for 24h. Afterwards, the reaction solution was cooled to room temperature, filtrated and the solvent was removed under reduced pressure. The resulting orange solid was purified by column chromatography (SiO$_2$, gradient from toluene to toluene/ethyl acetate 9:1). By-products formed of reacting Lawesson's reagent were eluated with pure toluene. The product (**L³**) was isolated by changing the solvent gradually to toluene/ethyl acetate 9:1. **Yield**: 1.56 g (4.55 mmol, 82 %) as bright yellow powder. **^{1}H-NMR** (600 MHz, Chloroform-*d*) δ 8.69 (d, *J* = 4.9 Hz, 1H, H$_{38}$), 8.63 (d, *J* = 1.6 Hz, 1H, H$_{33}$), 8.52 (m, 1H, H$_{30}$), 8.42 (m, 2H, H$_{31,35}$), 8.14 (dd, *J* = 8.8, 1.7 Hz, 1H, H$_{34}$), 8.10 (d, *J* = 8.9 Hz, 1H, H$_{32}$), 8.03 (m, 1H, H$_{29}$), 8.01 (m, 1H, H$_{27}$), 7.88 (td, *J* = 7.7, 1.7 Hz, 1H, H$_{36}$), 7.50 (m, 2H, H$_{26,28}$), 7.42 (ddd, *J* = 7.5, 4.8, 1.2 Hz, 1H, H$_{37}$). **^{13}C-NMR** (151 MHz, Chloroform-*d*) δ 170.27 (C$_1$), 169.62 (C$_4$), 149.71 (C$_9$), 149.04 (C$_7$), 137.35 (C$_{11}$), 132.74 (C$_{20}$), 132.26 (C$_{19}$), 131.91 (C$_{15}$), 130.82 (C$_{14}$), 129.42 (C$_{16}$), 129.10 (C$_{13}$), 128.35 (C$_{25}$), 128.24 (C$_{22}$), 127.89 (C$_{18}$), 127.07 (C$_6$), 126.50 (C$_{23}$), 126.39 (C$_{21}$), 126.05 (C$_{24}$), 125.36 (C$_{10}$), 123.66 (C$_{17}$), 121.12 (C$_{12}$). **APCI-MS** (MeCN): *m/z* = 340.091 ([M]+H$^+$)$^+$ (100 %) (calc. = 340.0903), 341.094 ([M]+H$^+$)$^+$ (23.90 %) (calc. = 341.0937), 342.091 ([M]+H$^+$)$^+$ (5.46 %) (calc. = 342.091), 362.073 ([M]+Na$^+$)$^+$ (23.90 %) (calc. = 362.073), 701.156 ([2M]+Na$^+$)$^+$ (77.33 %) (calc. = 701.155), 702.159 ([2M]+Na$^+$)$^+$ (37.04 %) (calc. = 701.158). **R$_f$** (toluene on silica) = 0.1, (toluene/ ethyl acetate 9:1 on silica) = 0.37.

9.3.11. 6-methoxy-2-naphthoic acid methyl ester (**19**)[251]
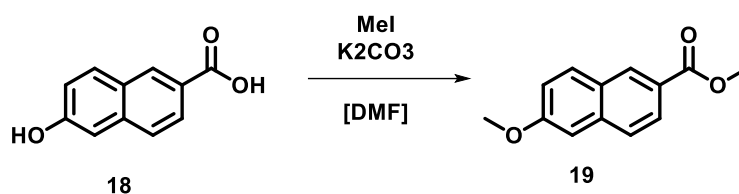
C$_{13}$H$_{12}$O$_3$ **REN-DCM-002**

6-Hydroxy-2-naphthoic acid (**18**) (2.50 g; 13.02 mmol; 1.0 eq.) was dissolved in 18 mL dimethylformamide and potassium carbonate (4.50 g; 32.55 mmol; 2.5 eq.) was added in portions.

Subsequently, 1.80 mL of methyl iodide (4.11 g; 28.64 mmol; 2.2 eq.) was added and the reaction mixture was heated at 45°C overnight with stirring. The next day, the yellow reaction mixture obtained was filtered and all volatile components were distilled (40°C, 2 mbar). It was then extracted with saturated sodium carbonate solution and ethyl acetate. The combined organic phases were dried over magnesium sulphate, filtered and freed from the extractant. A yellow crystalline solid was obtained (**19**). **Yield**: 2.05 g, (9.50 mmol, 73 %). **^{1}H-NMR** (400 MHz, CDCl3): δ (ppm) = 8.53 (s, 1H), 8.03 (d, 1H), 7.80 (dd, 2H), 7.18 (m, 2H), 3.96 (s, 3H), 3.94 (s, 3H). **FT-IR** (KBr): $\tilde{\nu}$ (cm^{-1}) = 3063 (w), 3033 (w), 2950 (m), 2844 (m), 1712 (s), 1628 (s), 1272 (s), 917 (m), 865 (s), 756 (s), 468 (m). **APCI-MS** (MeCN): m/z = 157.0353 ([$C_{11}H_9O$])$^+$ (100 %) (calc. = 157.064), 158.038 ([$C_{11}H_9O$])$^+$ (7.40 %) (calc. = 158.068), 159.0316 ([$C_{11}H_{11}O$])$^+$ (11.86 %) (calc. = 159.0805). **R_f** (Cyclohexane/EtOAc 9:1) = 0.50.

9.3.12.   6-methoxynaphthalene-2-carbohydrazide (**20**)[252]
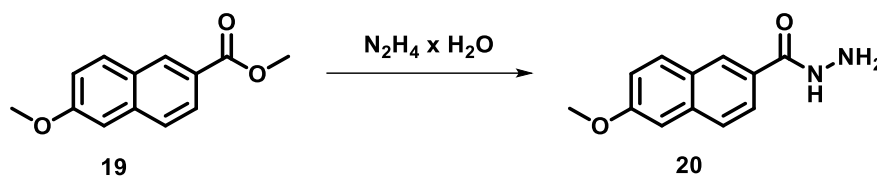
$C_{12}H_{12}N_2O_2$ **REN-DCM-005**

6-Methoxy-2-naphthoate 2 (2.42 g; 11.19 mmol; 1.0 eq.) was heated with 5 mL hydrazine hydrate (5.145 g; 12.31 mmol; 1.1 eq.) at 130°C under reflux overnight. The obtained pale yellow reaction mixture was freed from the hydrazine hydrate and azeotropically distilled twice with toluene. **Yield:** 2.04 g (9.43 mmol; 84 %) as yellow powder. **1H-NMR** (400 MHz, CDCl3): δ (ppm) = 9,82 (s, 1H); 8,35 (s, 1H); 7,88 (m, 3H); 7,37 (d, 1H); 7,22 (dd, 1H); 4,57 (s, 2H); 3,89 (s, 3H). **FT-IR** (KBr): $\tilde{\nu}$ (cm^{-1}) = 3447 (w), 3314 (m), 3017 (m), 2958 (m), 1620 (s), 1551 (s), 1262 (m), 1121 (s), 848 (m), 803 (m), 469 (m).
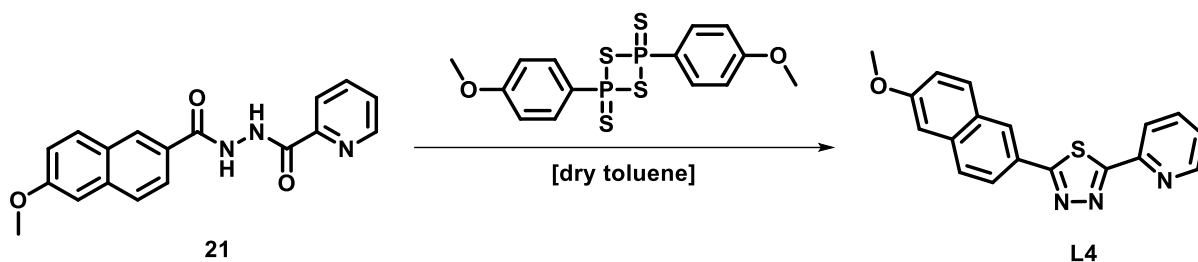
9.3.13. N'-(6-methoxy-2-naphthoyl) pyridine-2-carboxylic acid hydrazide (21)[186]
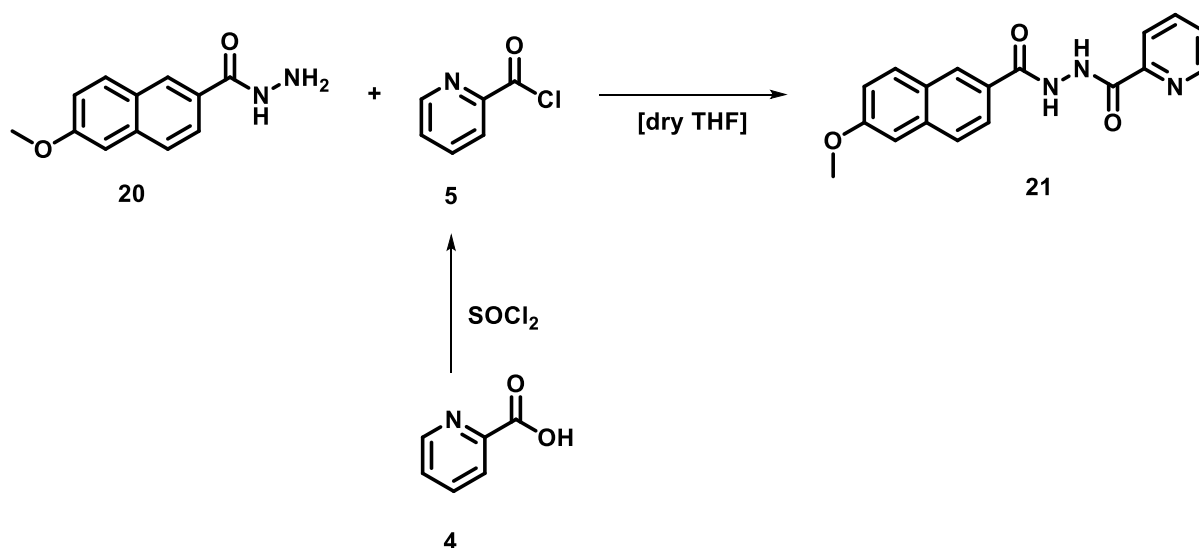
C₁₈H₁₅N₃O₃

$C_{18}H_{15}N_3O_3$

Picolinic acid (**4**) (1.80 g, 14.33 mmol, 1.0 eq.) was placed in a Schlenk flask and freshly distilled thionyl chloride (17.10 g; 143.29 mmol, 10.0 eq.) was added while a green colouration was observed. Subsequently, the mixure was heated at 90°C under reflux. After 6 h, no more gas evolution was observed and the black reaction mixture was freed from excess thionyl chloride under reduced pressure. The Pyridine-2-carbonyl chloride (**5**) (2.03 g, 14.33 mmol, 1.1 eq.) (brown oil) was dissolved in 10 mL dry THF and added dropwise to the 6-methoxy-2-naphthohydrazide (**20**) (2.00 g; 9.25 mmol; 1 eq.) suspended in 25 mL dry THF. The reaction mixture was stirred at room temperature overnight. The resulting brown solid was filtered and washed with THF. The brown solid obtained was redissolved in chloroform and washed with NaHCO₃ solution. The organic phases were combined, dried over magnesium sulfate and the solvent was removed under reduced pressure. **Yield:** 2.19 g (6.82 mmol, 74 %) as light brown powder. **¹H-NMR** (400 MHz, CDCl3): δ (ppm) = 10,40 (s, 2H); 8,72 (s, 1H); 8,48 (s, 1H); 8,00 (m, 5H); 7,68 (ddd,1H); 7,42 (d, 1H); 7,26 (dd, 1H); 3,92 (s, 3H). **FT-IR** (KBr): $\tilde{\nu}$ (cm⁻¹) = 3306 (m), 3000 (w), 2938 (w), 1710 (s), 1653 (s), 1620 (s), 1505 (s), 1277 (m), 1023 (m), 858 (s), 748 (m), 505 (m). **APCI-MS** (MeCN): m/z = 101.003 ([C₆H₆]+Na⁺)⁺ (100 %) (calc. = 101.0363, 157.0351 ([C₁₁H₉O])⁺ (30.63 %) (calc. = 157.064), 344.101 ([M] + Na⁺)⁺ (33.75 %) (calc. = 344.1006), 345.103 ([M] + Na⁺)⁺ (7.72 %) (calc. = 344.1040).

9.3.14. 2-(6-methoxynaphthalen-2-yl)-5-(pyridin-2-yl)-1,3,4-thiadiazole (L⁴)[40,41,156,158,165,186]

21 → **L4**

$C_{18}H_{13}N_3OS$ **REN-DCM-004**

N'-(6-methoxy-2-naphthoyl) pyridine-2-carboxylic acid hydrazide (**21**) (2.10 g; 6.54 mmol; 1.0 eq.) and Lawesson's reagent (3.34 g; 7.84 mmol; 1.2 eq.) were suspended in dry toluene (250 mL) and refluxed under nitrogen atmosphere for 24h. The reaction solution was then cooled to room temperature, filtrated and the red solution was freed from solvent. The resulting red oil was purified by column chromatography (SiO$_2$, gradient from DCM to DCM/diethyl ether 9:1). By-products formed of reacting Lawesson's reagent were eluated with pure dichloromethane. **L⁴** was isolated by changing the solvent gradually to DCM/diethyl ether 9:1. Yield: 0.6 g (1.88 mmol, 30 %) as yellow powder. **¹H-NMR** (600 MHz, Chloroform-d) δ 8.67 (d, J = 4.8 Hz, 1H, H$_{36}$), 8.40 (s, 1H, H$_{28}$), 8.39 (s, 1H, H$_{33}$), 8.10 (dd, J = 8.6, 1.8 Hz, 1H, H$_{29}$), 7.86 (td, J = 7.7, 1.6 Hz, 1H, H$_{34}$), 7.83 (dd, J = 8.7, 5.9 Hz, 2H, H$_{25,27}$), 7.39 (ddd, J = 7.5, 4.7, 1.1 Hz, 1H, H$_{35}$), 7.20 (dd, J = 8.9, 2.5 Hz, 1H, H$_{24}$), 7.15 (d, J = 2.5 Hz, 1H, H$_{26}$). **¹³C NMR** (151 MHz, Chloroform-d) δ 170.38 (C$_1$), 169.48 (C$_4$), 159.09 (C$_{20}$), 149.81 (C$_9$), 149.24 (C$_6$), 137.19 (C$_{11}$), 136.10 (C$_{15}$), 130.36 (C$_{18}$), 128.49 (C$_{14}$), 128.07 (C$_{13}$), 127.76 (C$_{16}$), 125.44 (C$_7$), 125.22 (C$_{10}$), 125.11 (C$_{17}$), 120.97 (C$_{12}$), 119.97 (C$_{12}$), 105.83 (C$_{21}$), 55.42 (C$_{23}$). **FT-IR** (KBr): $\tilde{\nu}$ (cm^{-1}) = 3054 (w), 2964 (w), 2835 (w), 1622 (m), 1486 (s), 1387 (s), 1234 (m), 1201 (s), 862 (m), 787 (m), 472 (m). **APCI-MS** (MeCN): m/z = 320.0855 ([M] + H⁺)⁺ (48.18 %) (calc. = 320.0853), 342.0676 ([M] + Na⁺)⁺ (47.13 %) (calc. = 342.0672), 358.0411 ([M] + K⁺)⁺ (5.87 %) (calc. = 358.0411), 661.1452 ([2M] + Na⁺)⁺ (100 %) (661.1451). **R$_f$** (DCM on silica) = 0.21, (DCM/Diethyl ether 9:1 on silica) = 0.86.

9.4. Complex Synthesis

All complex syntheses were carried out in a glovebox under argon atmosphere. DCM, toluene, and methanol were each dried, according to literature procedure[242] before usage.

9.4.1. $Fe^{II}(py)_4(NCBH_3)_2$
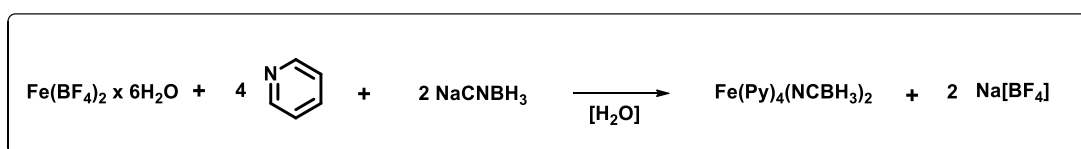
**C$_{22}$H$_{26}$B$_2$FeN$_6$**   **REN-JMK-125**

H_2O (18 mL) and pyridine (22.99 mmol, 1.86 mL, 4 eq.) were degassed and placed in a flask. Subsequently, $Fe^{II}(BF_4)_2$ - 6 H_2O (2.00 g, 5.75 mmol, 1 eq.) was added. This was followed by the addition of $NaCNBH_3$ (0.72 g, 11.49 mmol, 2 eq.). Filtration was carried out under inert gas and the solid obtained was dried in vacuo. **IR** (ATR): $\tilde{\nu}$ (cm^{-1}) 2341 (s), 2178 (s), 1598 (m), 1486 (w), 1439 (s), 1216 (w), 1120 (m), 765 (m), 753 (m), 696 (s).

9.4.2. $[Fe^{II}(L^1)_2(NCX)_2] \cdot$ n (Solv) (**C1, C2, C3**)[43,151,152]
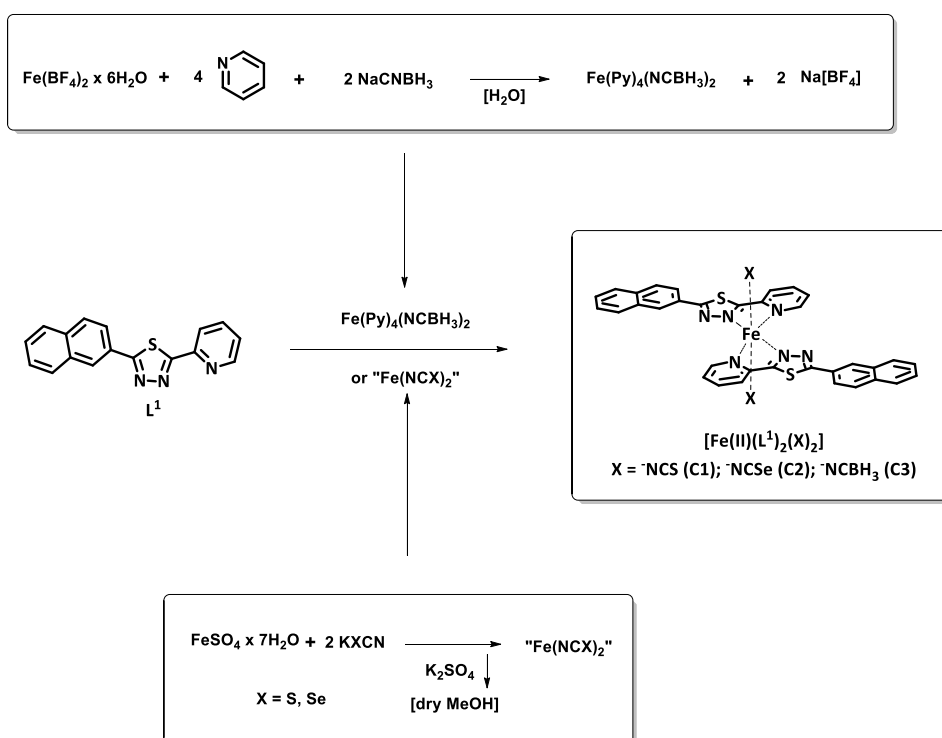
[Fe^{II}(**L^1**)$_2$(NCS)$_2$] (**C1**): FeSO$_4\cdot$7H$_2$O in methanol (25.02 mg, 0.09 mmol, 1 eq, 3 mL) was mixed with KSCN in methanol (17.50 mg, 0.18 mmol, 2 eq, 3 mL) and stirred for 24 h. The precipitate was filtrated and the resulting "Fe(NCS)$_2$" solution was layered over **L^1** in dichloromethane (52.10 mg, 0.18 mmol, 2 eq, 10 mL). Single crystals suitable for X-ray structure analysis were obtained after 3-5 d at room temperature. **IR** (ATR): $\tilde{\nu}$ (cm^{-1}): 3049 (w), 3014 (w), 2051 (s), 1593 (m), 1475 (m), 1419 (m), 859 (s), 809 (s), 777 (s), 748 (s).**Elemental analysis** for C$_{36}$H$_{22}$FeN$_8$S$_4$ (750.72 g/mol): calculated C 57.60, H 2.95, N 14.93; found: C 56.98, H 2.90, N 14.84

[Fe^{II}(**L^1**)$_2$(NCSe)$_2$] (**C2**): FeSO$_4\cdot$7H$_2$O in methanol (25.02 mg, 0.09 mmol, 1 eq, 3 mL) was mixed with KSeCN in methanol (25.93 mg, 0.18 mmol, 2 eq, 3 mL) and stirred for 24 h. The precipitate was filtrated and the resulting "Fe(NCSe)$_2$" solution was layered over **L^1** in dichloromethane (52.10 mg, 0.18 mmol, 2 eq, 10 mL). Single crystals suitable for X-ray structure analysis were obtained after 3-5 d at room temperature. **IR** (ATR): $\tilde{\nu}$ (cm^{-1}): 3051 (w), 2049 (s), 1594 (m), 1475 (m), 1445 (s), 1420 (m), 860 (s), 816 (s), 777 (s), 750 (s). **Elemental analysis** for C$_{36}$H$_{22}$FeN$_8$S$_2$Se$_2$ (844.51 g/mol) calculated: C 51.20, H 2.63, N 13.27; found: C 50.38, H 2.42, N 13.01, S 7.75. Equivalent to C$_{36}$H$_{22}$FeN$_8$S$_2$Se$_2$ x H$_2$O (862.52 g/mol).

[Fe^{II}(**L^1**)$_2$(NCBH$_3$)$_2$] · n (Solv) (**C3**): [Fe(py)$_4$(NCBH3)$_2$] in Acetonitrile (40.67 mg; 0.09 mmol, 1 eq, 3 mL) was layered over **L^1** in dichloromethane (52.10 mg, 0.18 mmol, 2 eq, 10 mL). Red parallelogram-shaped crystals suitable for X-ray structure analysis were obtained after 3 days at room temperature. **IR** (ATR): $\tilde{\nu}$ (cm^{-1}): 3065 (w), 2331 (s), 2181 (s), 1598 (s), 1475 (s), 1423 (s), 1119 (s), 1098 (s),1001 (m), 769 (s).

9.4.3. [Fe^{II}(L^2)$_2$(NCX)$_2$] · n (Solv) (X = S, Se, BH$_3$) (**C4, C5, C6**)

[Fe(II)(L^2)$_2$(X)$_2$]
X = ⁻NCS (**C4**); ⁻NCSe (**C5**); ⁻NCBH$_3$ (**C6**)
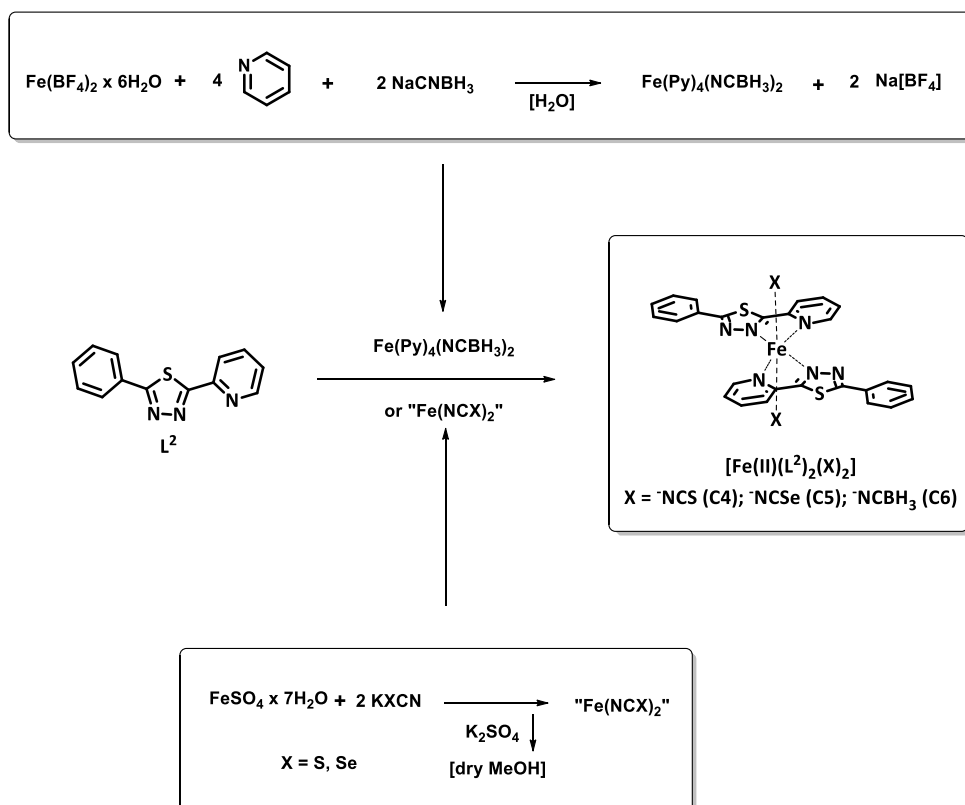
[Fe^{II}(**L^2**)$_2$(NCS)$_2$] · n (Solv) (**C4**): FeSO$_4$·7H$_2$O (25.02 mg; 0.09 mmol; 1 eq) was placed in 3 mL methanol in a snap cap vessel and mixed with a solution of KSCN (17.49 mg; 0.18 mmol; 2 eq) in 3 mL methanol. The mixture was stirred for 24 h. The precipitate was filtrated and the resulting "Fe(NCS)$_2$" solution was layered over **L^2** in dichloromethane (43.02 mg; 0.18 mmol; 2eq, 10 mL) for liquid-liquid diffusion. Violet-red rod shaped crystalls suitable for X-ray structure analysis were formed, after approximately 72 h. **IR** (ATR): $\tilde{v}$ (cm^{-1}): 3053 (w), 3010 (w), 2062 (s), 1595 (m), 1473 (m), 1419 (m), 1455 (s), 1424 (s), 1023 (m), 811 (m), 778 (s), 758 (s), 679 (s), 603 (s), 472 (m).

[Fe^{II}(**L^2**)$_2$(NCSe)$_2$] · n (Solv) (**C5**): Complex **C5** was synthesised in the similar way as **C4**. FeSO$_4$·7H$_2$O (25.02 mg, 0.09 mmol, 1 eq) was placed in 3 mL methanol in a snap cap vessel and mixed with a solution of KSeCN (25.93 mg, 0.18 mmol, 2 eq) in 3 mL methanol. The mixture was stirred for 24 h. The precipitate was filtrated and the resulting "Fe(NCSe)$_2$" solution was layered over **L^2** in dichloromethane (43.02 mg, 0.18 mmol, 2eq, 10 mL) for liquid-liquid diffusion. Violet-red rod shaped crystalls suitable for X-ray structure analysis were formed, after approximately 72 h. **IR** (ATR): $\tilde{v}$ (cm^{-1}): 3051 (w), 3014 (w), 2060 (s), 1595 (m), 1475 (m), 1456 (m), 1421 (s), 1026 (m), 817 (w), 776 (s), 760 (s), 679 (s), 605 (s), 409 (s).

[Fe^{II}(**L^2**)$_2$(NCBH$_3$)$_2$] · n (Solv) (**C5**): [Fe(py)$_4$(NCBH3)$_2$] in acetonitrile (40.68 mg; 0.09 mmol; 1 eq, 5 mL) was layered over a solution of **L^2** in dichloromethane (43.02 mg, 0.18 mmol, 2eq, 5 mL). After approximately 72 h, brown-violet crystals were obtained. **IR** (ATR): $\tilde{v}$ (cm^{-1}): 3106 (w), 3076(w) 2328 (s), 2192 (s), 1598 (s), 1486 (m), 1464 (s), 1426 (s), 1119 (s), 777 (s), 760 (s), 681 (s), 604 (s).

9.4.4. [Fe^{II}(L^3)$_2$(NCX)$_2$] · n (Solv) (X = S, Se, BH$_3$) (C7, C8, C9)
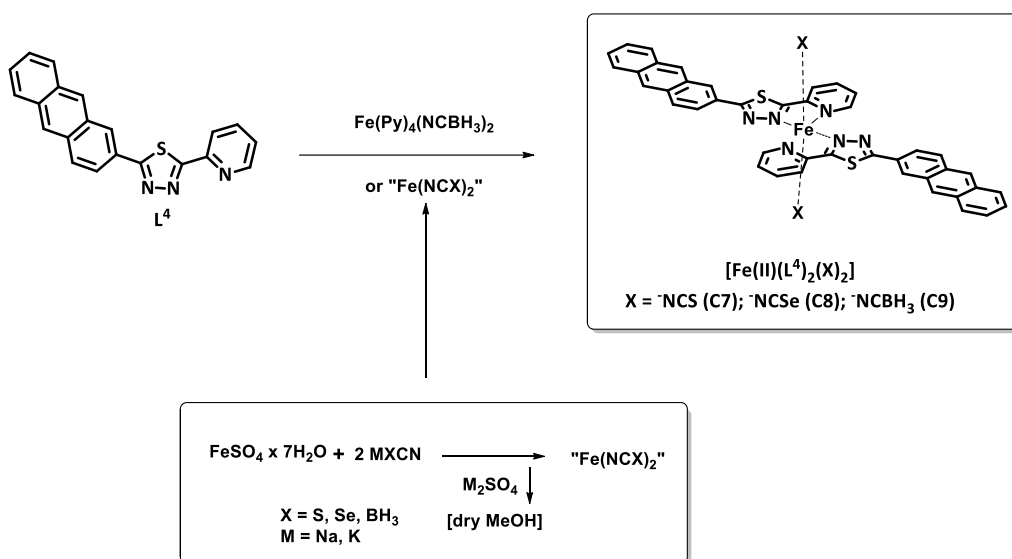
[Fe^{II}(L^3)$_2$(NCS)$_2$] (C7): L^3 (30.06 mg; 0.9 mmol; 2eq) was dissolved in 10 mL of dichloromethane and the solution was placed in a reaction tube and a mixture of DCM and MeOH (1:1→10 mL) was layered above as transporting solvent. Subsequently, FeSO$_4$·7H$_2$O (12.52 mg; 0.045 mmol; 1 eq) was placed in 2.5 mL methanol in a snap cap vessel and mixed with a solution of KSCN (8.75 mg; 0.9 mmol; 2 eq) in 2.5 mL methanol. The mixture was stirred for 24 h. The precipitate was filtrated and the resulting "Fe(NCS)$_2$" solution was layered over the transporting layer, resulting in a three phase liquid-liquid diffusion system. Yellow parallelogram shaped crystalls suitable for X-ray structure analysis were formed, after several weeks. IR (ATR): $\tilde{v}$ (cm^{-1}): 3055 (w), 3030 (w), 3020 (w), 2066 (s), 1597 (m), 1479 (m), 1459 (m), 1438 (m), 1419 (m), 1455 (s), 1424 (s), 1057 (m), 1028 (m), 906 (s), 863 (m) 774 (s), 737 (s), 624 (s), 465 (s), 410 (m).

[Fe^{II}(L^3)$_2$(NCSe)$_2$] (C8): L^3 (30.06 mg; 0.9 mmol; 2eq) was dissolved in 10 mL of dichloromethane and the solution was placed in a reaction tube and a mixture of DCM and MeOH (1:1→10 mL) was layered above as transporting solvent. Subsequently, FeSO$_4$·7H$_2$O (12.52 mg; 0.045 mmol; 1 eq) was placed in 2.5 mL methanol in a snap cap vessel and mixed with a solution of KSeCN (13.0 mg; 0.9 mmol; 2 eq) in 2.5 mL methanol. The mixture was stirred for 24 h. The precipitate was filtrated and the resulting "Fe(NCSe)$_2$" solution was layered over the transporting layer, resulting in a three phase liquid-liquid diffusion system. Yellow parallelogram shaped crystalls suitable for X-ray structure analysis were formed, after several weeks. IR (ATR): $\tilde{v}$ (cm^{-1}): 3053 (w), 3030 (w), 3014 (w), 2070 (s), 1596 (m), 1479 (w), 1459 (w), 1438 (w), 1419 (m), 1159 (w), 1057 (w), 906 (s), 863 (m), 801 (m), 776 (s), 739 (s), 624 (s), 467 (s), 410 (s).

[Fe^{II}(L^3)$_2$(NCBH$_3$)$_2$] · n (Solv) (C9): L^3 (30.06 mg; 0.9 mmol; 2eq) was dissolved in 10 mL of dichloromethane and the solution was placed in a reaction tube and a mixture of DCM and MeOH

(1:1→10 mL) was layered above as transporting solvent. Subsequently, $FeSO_4 \cdot 7H_2O$ (12.52 mg; 0.045 mmol; 1 eq) was placed in 2.5 mL methanol in a snap cap vessel and mixed with a solution of $NaBH_3CN$ (5.60 mg; 0.9 mmol; 2 eq) in 2.5 mL methanol. The mixture was stirred for 24 h. The precipitate was filtrated and the resulting "$Fe(NCBH_3)_2$" solution was layered over the transporting layer, resulting in a three phase liquid-liquid diffusion system. Dark green parallelogram shaped crystalls suitable for X-ray structure analysis were formed, after several weeks. **IR** (ATR): $\tilde{v}$ (cm^{-1}): 3055 (w), 2981(m), 2340 (s), 2187 (s), 1598 (m), 1479 (w), 1460 (w), 1438 (w), 1419 (m), 1160 (w), 1118 (m), 912 (m), 894 (m), 869 (m), 799 (w), 778 (s), 739 (s), 624 (m), 465 (s), 410 (m).

9.4.5. [Fe^{II}(L^4)$_2$(NCX)$_2$] · n (Solv) (X = S, Se, BH$_3$) (C7, C8, C9)
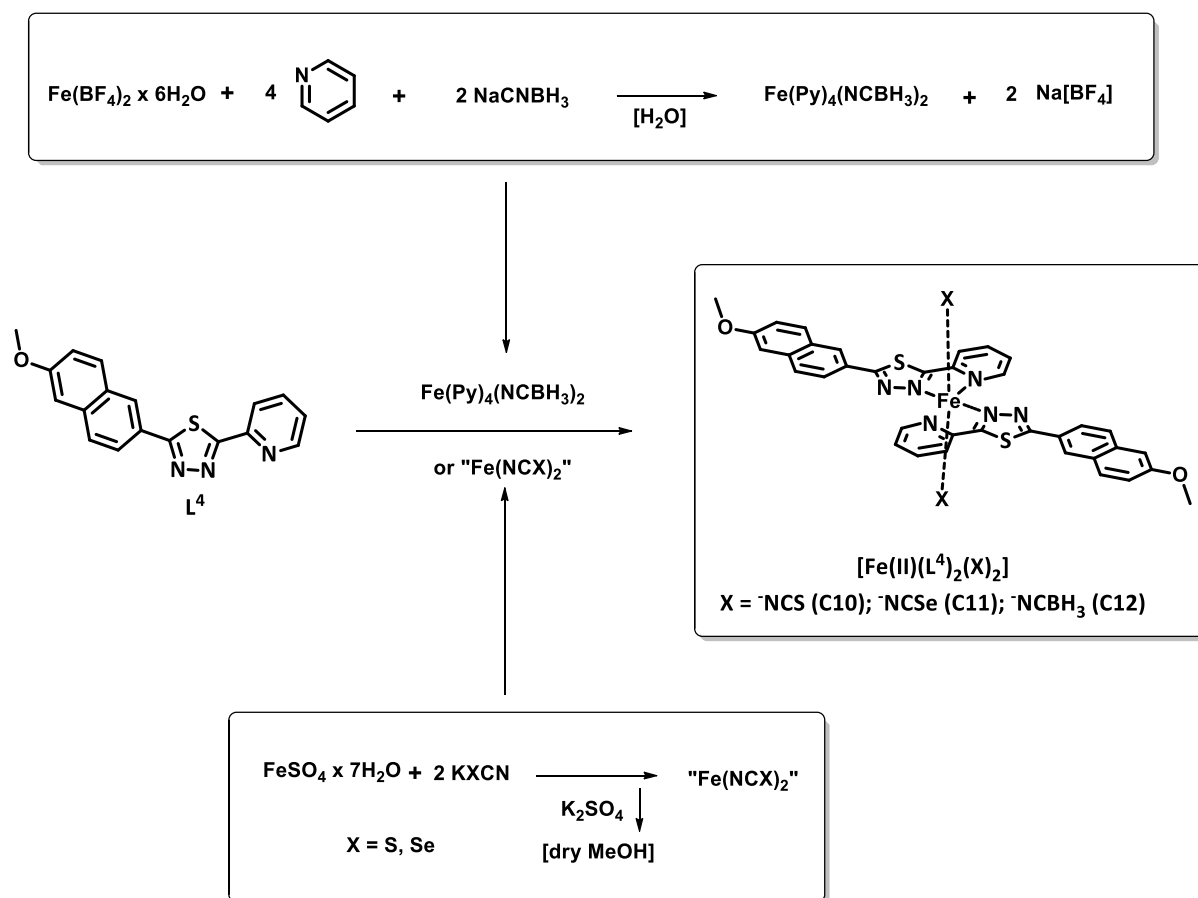
[Fe^{II}(L^4)$_2$(NCS)$_2$] · n (Solv) (C10): FeSO$_4$·7H$_2$O in dry methanol (25.02 mg, 0.09 mmol, 1 eq, 3 mL) was mixed with KSCN in methanol (18.01 mg, 0.18 mmol, 2 eq, 3 mL) and stirred for at least 2 h. The precipitate was filtrated and the resulting "Fe(NCS)$_2$" solution was layered over L^4 in dichloromethane (57.50 mg, 0.18 mmol, 2 eq, 10 mL). A micro crystallinic powder was obtained after approximately 4 days, which was used for variable temperature magnetic susceptibility measurements. To obtain single crystals suitable for X-ray structural analysis, a 3-phase system was formed within an H-tube. Red cubic crystalls formed after one week. All steps mentioned above were carried out identically, except that acetonitrile was layered over the respective solutions as a transport layer. **IR** (ATR): $\tilde{\nu}$ (cm^{-1}): 3050 (w), 3010 (w), 2051 (s), 1620 (m), 1590 (m), 1490 (m), 1440 (m), 1390 (m), 1270 (m), 1020 (m) 899 (m), 855 (m), 810 (w), 776 (s), 778 (s), 743 (w), 668 (m), 638 (m).

[Fe^{II}(L^4)$_2$(NCSe)$_2$] · n (Solv) (C11): The procedure for the synthesis of C11 is identical to that of C10. FeSO$_4$·7H$_2$O in methanol (25.02 mg, 0.09 mmol, 1 eq, 3 mL) was mixed with KSeCN in methanol (25.93 mg, 0.18 mmol, 2 eq, 3 mL) and stirred for 24 h. The precipitate was filtrated and the resulting "Fe(NCSe)$_2$" solution was layered over L^1 in dichloromethane (57.50 mg, 0.18 mmol, 2 eq, 10 mL). Single crystals suitable for X-ray structure analysis were obtained after 3-5 d at room temperature. **IR** (ATR): $\tilde{\nu}$ (cm^{-1}): 3051 (w), 2060 (s), 1620 (m), 1590 (m), 1490 (m), 1440 (w), 1432 (w), 1389 (m), 1270 (m), 1169 (m), 910 (m), 867 (m), 808 (m), 778 (s), 668 (m), 641 (m), 609 (m).

[Fe^{II}(**L^4**)$_2$(NCBH$_3$)$_2$] · n (Solv) (**C12**): [Fe(py)$_4$(NCBH3)$_2$] in Acetonitrile (40.67 mg; 0.09 mmol, 1 eq, 3 mL) was layered over **L^4** in dichloromethane (57.50 mg, 0.18 mmol, 2 eq, 10 mL). The solution was allowed to stand for liquid-liquid diffusion. Red parallelogram-shaped crystals suitable for X-ray structure analysis were obtained after one week at room temperature. **IR** (ATR): $\tilde{v}$ (cm^{-1}): 3030 (w), 2960 (w), 2340 (s), 2180 (s), 1620 (s), 1590 (s), 1490 (s), 1440 (s), 1380 (s), 1268 (s), 1201 (s),1114 (m), 899 (m), 856 (m), 779 (s), 664 (m), 636 (m).

<u>10.</u>   References

(1) Gütlich, P.; Goodwin, H. A. Spin Crossover—An Overall Perspective. In *Spin crossover in transition metal compounds*; Gütlich, P., Garcia, Y., Eds.; Topics in current chemistry, Vol. 233; Springer, 2004; pp 1–47. DOI: 10.1007/b13527.

(2) Kahn, O. Spin-Transition Polymers: From Molecular Materials Toward Memory Devices. *Science* **1998**, *279* (5347), 44–48. DOI: 10.1126/science.279.5347.44.

(3) Halcrow, M. A. *Spin-crossover materials [Elektronische Ressource]:Properties and applications*; Wiley-Blackwell, 2013.

(4) Coronado, E.; Giménez-Marqués, M.; Mínguez Espallargas, G.; Rey, F.; Vitórica-Yrezábal, I. J. Spin-crossover modification through selective CO2 sorption. *Journal of the American Chemical Society* **2013**, *135* (43), 15986–15989. DOI: 10.1021/ja407135k. Published Online: Oct. 22, 2013.

(5) Halder, G. J.; Kepert, C. J.; Moubaraki, B.; Murray, K. S.; Cashion, J. D. Guest-dependent spin crossover in a nanoporous molecular framework material. *Science* **2002**, *298* (5599), 1762–1765. DOI: 10.1126/science.1075948.

(6) Nowak, R.; Prasetyanto, E. A.; Cola, L. de; Bojer, B.; Siegel, R.; Senker, J.; Rössler, E.; Weber, B. Proton-driven coordination-induced spin state switch (PD-CISSS) of iron(ii) complexes. *Chemical communications (Cambridge, England)* **2017**, *53* (5), 971–974. DOI: 10.1039/c6cc08618g. Published Online: Jan. 3, 2017.

(7) Muller, R. N.; Vander Elst, L.; Laurent, S. Spin transition molecular materials: intelligent contrast agents for magnetic resonance imaging. *Journal of the American Chemical Society* **2003**, *125* (27), 8405–8407. DOI: 10.1021/ja0349599.

(8) Stavila, V.; Allali, M.; Canaple, L.; Stortz, Y.; Franc, C.; Maurin, P.; Beuf, O.; Dufay, O.; Samarut, J.; Janier, M.; Hasserodt, J. Significant relaxivity gap between a low-spin and a high-spin iron(ii) complex of structural similarity: an attractive off–on system for the potential design of responsive MRI probes. *New J. Chem.* **2008**, *32* (3), 428–435. DOI: 10.1039/b715254j.

(9) NobelPrize.org. Nobel Prize Outreach AB 2021. *Press release: The Nobel Prize in Chemistry 2016.* https://www.nobelprize.org/prizes/chemistry/2016/press-release/ (accessed 2021-07-20).

(10) Feringa, B. L. The Art of Building Small: From Molecular Switches to Motors (Nobel Lecture). *Angew. Chem. Int. Ed. Engl.* **2017**, *56* (37), 11060–11078. DOI: 10.1002/anie.201702979. Published Online: Jul. 27, 2017.

(11) Feringa, B. L.; Koumura, N.; van Delden, R. A.; ter Wiel, M. Light-driven molecular switches and motors. *Appl Phys A* **2002**, *75* (2), 301–308. DOI: 10.1007/s003390201338.

(12) Qiu, Y.; Zhang, L.; Pezzato, C.; Feng, Y.; Li, W.; Nguyen, M. T.; Cheng, C.; Shen, D.; Guo, Q.-H.; Shi, Y.; Cai, K.; Alsubaie, F. M.; Astumian, R. D.; Stoddart, J. F. A Molecular Dual Pump. *Journal of the American Chemical Society* **2019**, *141* (44), 17472–17476. DOI: 10.1021/jacs.9b08927. Published Online: Oct. 25, 2019.

(13) Schoevaars, A. M.; Kruizinga, W.; Zijlstra, R. W. J.; Veldman, N.; Spek, A. L.; Feringa, B. L. Toward a Switchable Molecular Rotor. Unexpected Dynamic Behavior of Functionalized Overcrowded Alkenes. *J. Org. Chem.* **1997**, *62* (15), 4943–4948. DOI: 10.1021/jo962210t.

(14) Kudernac, T.; Ruangsupapichat, N.; Parschau, M.; Maciá, B.; Katsonis, N.; Harutyunyan, S. R.; Ernst, K.-H.; Feringa, B. L. Electrically driven directional motion of a four-wheeled molecule on a metal surface. *Nature* **2011**, *479* (7372), 208–211. DOI: 10.1038/nature10587. Published Online: Nov. 9, 2011.

(15) Trauner, D. Molecular switches and cages. *Beilstein journal of organic chemistry* **2012**, *8*, 870–871. DOI: 10.3762/bjoc.8.97. Published Online: Jun. 13, 2012.

(16) Zhang, J. L.; Zhong, J. Q.; Lin, J. D.; Hu, W. P.; Wu, K.; Xu, G. Q.; Wee, A. T. S.; Chen, W. Towards single molecule switches. *Chem. Soc. Rev.* **2015**, *44* (10), 2998–3022. DOI: 10.1039/C4CS00377B. Published Online: Mar. 11, 2015.

(17) Feringa, B. L., Ed. *Molecular switches*, 2., completely rev. and enl. ed.; Wiley-VCH-Verl., 2011. DOI: 10.1002/9783527634408.

(18) Balzani, V.; Credi, A.; Venturi, M. *Molecular devices and machines*:*Concepts and perspectives for the nanoworld*, 2. ed.; WILEY-VCH, 2008. DOI: 10.1002/9783527621682.

(19) Venkataramani, S.; Jana, U.; Dommaschk, M.; Sönnichsen, F. D.; Tuczek, F.; Herges, R. Magnetic bistability of molecules in homogeneous solution at room temperature. *Science* **2011**, *331* (6016), 445–448. DOI: 10.1126/science.1201180.

(20) Thies, S.; Bornholdt, C.; Köhler, F.; Sönnichsen, F. D.; Näther, C.; Tuczek, F.; Herges, R. Coordination-induced spin crossover (CISCO) through axial bonding of substituted pyridines to nickel-porphyrins: sigma-donor versus pi-acceptor effects. *Chem. Eur. J.* **2010**, *16* (33), 10074–10083. DOI: 10.1002/chem.201000603.

(21) Dommaschk, M.; Schütt, C.; Venkataramani, S.; Jana, U.; Näther, C.; Sönnichsen, F. D.; Herges, R. Rational design of a room temperature molecular spin switch. The light-driven coordination induced spin state switch (LD-CISSS) approach. *Dalton transactions (Cambridge, England : 2003)* **2014**, *43* (46), 17395–17405. DOI: 10.1039/C4DT03048F.

(22) Dommaschk, M.; Peters, M.; Gutzeit, F.; Schütt, C.; Näther, C.; Sönnichsen, F. D.; Tiwari, S.; Riedel, C.; Boretius, S.; Herges, R. Photoswitchable Magnetic Resonance Imaging Contrast by Improved Light-Driven Coordination-Induced Spin State Switch. *Journal of the American Chemical Society* **2015**, *137* (24), 7552–7555. DOI: 10.1021/jacs.5b00929. Published Online: May. 5, 2015.

(23) Thies, S.; Sell, H.; Schütt, C.; Bornholdt, C.; Näther, C.; Tuczek, F.; Herges, R. Light-induced spin change by photodissociable external ligands: a new principle for magnetic switching of molecules. *Journal of the American Chemical Society* **2011**, *133* (40), 16243–16250. DOI: 10.1021/ja206812f. Published Online: Sep. 19, 2011.

(24) Wellm, V.; Näther, C.; Herges, R. Molecular Spin State Switching and Photochromism in the Red and Near Infrared with Ni(II) Chlorin and Ni(II) Bacteriochlorin. *J. Org. Chem.* **2021**, *86* (14), 9503–9514. DOI: 10.1021/acs.joc.1c00806. Published Online: Jun. 28, 2021.

(25) Gade, L. H. *Koordinationschemie*, 1. Aufl.; WILEY-VCH, 1998.

(26) Shriver, D. F.; Atkins, P. W.; Langford, C. H. *Anorganische Chemie*:*Ein weiterführendes Lehrbuch*; VCH, 1992.

(27) Gütlich, P.; Garcia, Y.; Goodwin, H. A. Spin crossover phenomena in Fe(ii) complexes. *Chem. Soc. Rev.* **2000**, *29* (6), 419–427. DOI: 10.1039/B003504L.

(28) Riedel, E.; Meyer, H.-J.; Janiak, C., Eds. *Moderne anorganische Chemie:Hans-Jürgen Meyer. Autoren: C. Janiak*, 4. Aufl.; De-Gruyter-Studium; de Gruyter, 2012.

(29) Atkins, P. W.; Paula, J. de. *Physikalische Chemie*, 4., vollst. überarb. Aufl.; WILEY-VCH, 2006.

(30) Janiak, C.; Meyer, H.-J.; Gudat, D.; Kurz, P.; Riedel, E. *Riedel Moderne Anorganische Chemie*; de Gruyter, 2018. DOI: 10.1515/9783110441635.

(31) Housecroft, C. E.; Sharpe, A. G. *Anorganische Chemie*, 2., aktualisierte Aufl. [der engl. Ausg.]; che - Chemie; Pearson- Studium, 2006.

(32) Halcrow, M. The Effect of Ligand Design on Metal Ion Spin State—Lessons from Spin Crossover Complexes. *Crystals* **2016**, *6* (5), 58. DOI: 10.3390/cryst6050058.

(33) Gütlich, P.; Hauser, A.; Spiering, H. Thermal and Optical Switching of Iron(II) Complexes. *Angew. Chem. Int. Ed. Engl.* **1994**, *33* (20), 2024–2054. DOI: 10.1002/anie.199420241.

(34) Gütlich, P.; Garcia, Y., Eds. *Spin crossover in transition metal compounds*; Topics in current chemistry, Vol. 233; Springer, 2004.

(35) Jørgensen, C. K. The interelectronic repulsion and partly covalent bonding in transition-group complexes. *Discuss. Faraday Soc.* **1958**, *26* (0), 110–115. DOI: 10.1039/DF9582600110.

(36) Tanabe, Y.; Sugano, S. On the Absorption Spectra of Complex Ions II. *J. Phys. Soc. Jpn.* **1954**, *9* (5), 766–779. DOI: 10.1143/JPSJ.9.766.

(37) Real, J. A.; Gaspar, A. B.; Muñoz, M. C. Thermal, pressure and light switchable spin-crossover materials. *Dalton transactions (Cambridge, England : 2003)* **2005** (12), 2062–2079. DOI: 10.1039/B501491C. Published Online: May. 6, 2005.

(38) Haberditzl, W. Einführung in die Ligandenfeldtheorie: Von H. L. Schläfer und G. Gliemann. Akademische Verlagsgesellschaft, Frankfurt am Main 1967. XIV/522 Seiten mit 147 Bildern und 63 Tabellen, Format 16×23,5 cm, Ln. 59, - DM. *Z. Chem.* **1968**, *8* (3), 119–120. DOI: 10.1002/zfch.19680080329.

(39) Sorai, M.; Seki, S. Phonon coupled cooperative low-spin 1A1high-spin 5T2 transition in [Fe(phen)2(NCS)2] and [Fe(phen)2(NCSe)2] crystals. *Journal of Physics and Chemistry of Solids* **1974**, *35* (4), 555–570. DOI: 10.1016/S0022-3697(74)80010-7.

(40) Fürmeyer, F.; Carrella, L. M.; Ksenofontov, V.; Möller, A.; Rentschler, E. Phase Trapping in Multistep Spin Crossover Compound. *Inorg. Chem.* **2020**, *59* (5), 2843–2852. DOI: 10.1021/acs.inorgchem.9b03170. Published Online: Feb. 11, 2020.

(41) Herold, C. F.; Shylin, S. I.; Rentschler, E. Solvent-dependent SCO Behavior of Dinuclear Iron(II) Complexes with a 1,3,4-Thiadiazole Bridging Ligand. *Inorg. Chem.* **2016**, *55* (13), 6414–6419. DOI: 10.1021/acs.inorgchem.6b00163. Published Online: Jun. 13, 2016.

(42) Bonnet, S.; Siegler, M. A.; Costa, J. S.; Molnár, G.; Bousseksou, A.; Spek, A. L.; Gamez, P.; Reedijk, J. A two-step spin crossover mononuclear iron(II) complex with a HS-LS-LS intermediate phase. *Chemical communications (Cambridge, England)* **2008** (43), 5619–5621. DOI: 10.1039/b811746b. Published Online: Sep. 29, 2008.

(43) Klingele, J.; Kaase, D.; Klingele, M. H.; Lach, J.; Demeshko, S. Two-step spin crossover in the mononuclear iron(II) complex Fe(II)(L)(2)(NCS)(2) (L = 2,5-di-(2-pyridyl)-1,3,4-thiadiazole). *Dalton*

transactions (Cambridge, England : 2003) **2010**, *39* (7), 1689–1691. DOI: 10.1039/b924223f. Published Online: Dec. 15, 2009.

(44) Steinert, M.; Schneider, B.; Dechert, S.; Demeshko, S.; Meyer, F. Spin-State Versatility in a Series of Fe4 2 × 2 Grid Complexes: Effects of Counteranions, Lattice Solvent, and Intramolecular Cooperativity. *Inorg. Chem.* **2016**, *55* (5), 2363–2373. DOI: 10.1021/acs.inorgchem.5b02762. Published Online: Feb. 16, 2016.

(45) Ewald, A. H., Martin, R. L., Ross, I. G., White, A. H., Anomalous behaviour at the 6A1-2T2 crossover in iron (III) complexes. *Proc. R. Soc. Lond. A* **1964**, *280* (1381), 235–257. DOI: 10.1098/rspa.1964.0143.

(46) Gütlich, P., Ksenofontov, V., Gaspar, A. Pressure effect studies on spin crossover systems. *Coordination Chemistry Reviews* **2005**, *249* (17-18), 1811–1829. DOI: 10.1016/j.ccr.2005.01.022.

(47) Granier, T.; Gallois, B.; Gaultier, J.; Real, J. A.; Zarembowitch, J. High-pressure single-crystal x-ray diffraction study of two spin-crossover iron(II) complexes: Fe(Phen)2(NCS)2 and Fe(Btz)2(NCS)2. *Inorg. Chem.* **1993**, *32* (23), 5305–5312. DOI: 10.1021/ic00075a058.

(48) Jeftic, J.; Hinek, R.; Capelli, S. C.; Hauser, A. Cooperativity in the Iron(II) Spin-Crossover Compound Fe(ptz)(6)(PF(6))(2) under the Influence of External Pressure (ptz = 1-n-Propyltetrazole). *Inorg. Chem.* **1997**, *36* (14), 3080–3087. DOI: 10.1021/ic961404o.

(49) Ksenofontov, V.; Levchenko, G.; Spiering, H.; Gütlich, P.; Létard, J.-F.; Bouhedja, Y.; Kahn, O. Spin crossover behavior under pressure of Fe(PM-L)2(NCS)2 compounds with substituted 2'-pyridylmethylene 4-anilino ligands. *Chemical Physics Letters* **1998**, *294* (6), 545–553. DOI: 10.1016/S0009-2614(98)00901-4.

(50) Shepherd, H. J.; Bartual-Murgui, C.; Molnár, G.; Real, J. A.; Muñoz, M. C.; Salmon, L.; Bousseksou, A. Thermal and pressure-induced spin crossover in a novel three-dimensional Hoffman-like clathrate complex. *New J. Chem.* **2011**, *35* (6), 1205. DOI: 10.1039/C0NJ00845A.

(51) Linares, J.; Codjovi, E.; Garcia, Y. Pressure and temperature spin crossover sensors with optical detection. *Sensors (Basel, Switzerland)* **2012**, *12* (4), 4479–4492. DOI: 10.3390/s120404479. Published Online: Apr. 10, 2012.

(52) Rissanen, K. *Advanced X-Ray Crystallography*, Vol. 315; Springer Berlin Heidelberg, 2012. DOI: 10.1007/978-3-642-27407-7.

(53) Weir, C. E.; Lippincott, E. R.; van Valkenburg, A.; Bunting, E. N. Infrared Studies in the 1- to 15-Micron Region to 30,000 Atmospheres. *Journal of research of the National Bureau of Standards. Section A, Physics and chemistry* **1959**, *63A* (1), 55–62. DOI: 10.6028/jres.063A.003. Published Online: Aug. 1, 1959.

(54) Wei, Q.; Dubrovinskaia, N.; Dubrovinsky, L. Ruby and Sm:YAG fluorescence pressure gauges up to 120 GPa and 700 K. *Journal of Applied Physics* **2011**, *110* (4), 43513. DOI: 10.1063/1.3624618.

(55) Jayaraman, A. Diamond anvil cell and high-pressure physical investigations. *Rev. Mod. Phys.* **1983**, *55* (1), 65–108. DOI: 10.1103/RevModPhys.55.65.

(56) Wiehl, L.; Friedrich, A.; Haussühl, E.; Morgenroth, W.; Grzechnik, A.; Friese, K.; Winkler, B.; Refson, K.; Milman, V. Structural compression and vibrational properties of Bi12SiO20 sillenite from experiment and theory. *Journal of physics. Condensed matter : an Institute of Physics journal* **2010**, *22* (50), 505401. DOI: 10.1088/0953-8984/22/50/505401. Published Online: Nov. 26, 2010.

(57) McGarvey, J. J.; Lawthers, I.; Heremans, K.; Toftlund, H. Spin-state relaxation dynamics in iron(II) complexes: solvent on the activation and reaction and volumes for the 1 A ⇌ 5 T interconversion. *J. Chem. Soc., Chem. Commun.* **1984** (23), 1575–1576. DOI: 10.1039/C39840001575.

(58) Decurtins, S.; Gütlich, P.; Köhler, C. P.; Spiering, H.; Hauser, A. Light-induced excited spin state trapping in a transition-metal complex: The hexa-1-propyltetrazole-iron (II) tetrafluoroborate spin-crossover system. *Chemical Physics Letters* **1984**, *105* (1), 1–4. DOI: 10.1016/0009-2614(84)80403-0.

(59) Bressler, C.; Milne, C.; Pham, V.-T.; Elnahhas, A.; van der Veen, R. M.; Gawelda, W.; Johnson, S.; Beaud, P.; Grolimund, D.; Kaiser, M.; Borca, C. N.; Ingold, G.; Abela, R.; Chergui, M. Femtosecond XANES study of the light-induced spin crossover dynamics in an iron(II) complex. *Science* **2009**, *323* (5913), 489–492. DOI: 10.1126/science.1165733. Published Online: Dec. 11, 2008.

(60) Gütlich, P. Photoswitchable coordination compounds. *Coordination Chemistry Reviews* **2001**, *219-221*, 839–879. DOI: 10.1016/S0010-8545(01)00381-2.

(61) Létard, J.-F.; Capes, L.; Chastanet, G.; Moliner, N.; Létard, S.; Real, J.-A.; Kahn, O. Critical temperature of the LIESST effect in iron(II) spin crossover compounds. *Chemical Physics Letters* **1999**, *313* (1-2), 115–120. DOI: 10.1016/S0009-2614(99)01036-2.

(62) Marchivie, M.; Guionneau, P.; Howard, J. A. K.; Chastanet, G.; Létard, J.-F.; Goeta, A. E.; Chasseau, D. Structural characterization of a photoinduced molecular switch. *Journal of the American Chemical Society* **2002**, *124* (2), 194–195. DOI: 10.1021/ja016980k.

(63) Hauser, A. Light-Induced Spin Crossover and the High-Spin→Low-Spin Relaxation. In *Spin crossover in transition metal compounds*; Gütlich, P., Boillot, M.-L., Eds.; Topics in current chemistry, Vol. 234; Springer, 2004; pp 155–198. DOI: 10.1007/b95416.

(64) Marcén, S.; Lecren, L.; Capes, L.; Goodwin, H. A.; Létard, J.-F. Critical temperature of the LIESST effect in a series of hydrated and anhydrous complex salts [Fe(bpp)2]X2. *Chemical Physics Letters* **2002**, *358* (1-2), 87–95. DOI: 10.1016/S0009-2614(02)00590-0.

(65) Hauser, A. Reversibility of light-induced excited spin state trapping in the Fe(ptz)6(BF4)2, and the Zn1−xFex(ptz)6(BF4)2 spin-crossover systems. *Chemical Physics Letters* **1986**, *124* (6), 543–548. DOI: 10.1016/0009-2614(86)85073-4.

(66) Hauser, A. Intersystem crossing in Fe(II) coordination compounds. *Coordination Chemistry Reviews* **1991**, *111*, 275–290. DOI: 10.1016/0010-8545(91)84034-3.

(67) Létard, J.-F. Photomagnetism of iron(ii) spin crossover complexes—the T(LIESST) approach. *J. Mater. Chem.* **2006**, *16* (26), 2550–2559. DOI: 10.1039/B603473J.

(68) Paradis, N.; Chastanet, G.; Létard, J.-F. When Stable and Metastable HS States Meet in Spin-Crossover Compounds. *Eur. J. Inorg. Chem.* **2012**, *2012* (22), 3618–3624. DOI: 10.1002/ejic.201200297.

(69) Sciortino, N. F.; Neville, S. M.; Desplanches, C.; Létard, J.-F.; Martinez, V.; Real, J. A.; Moubaraki, B.; Murray, K. S.; Kepert, C. J. An investigation of photo- and pressure-induced effects in a pair of isostructural two-dimensional spin-crossover framework materials. *Chemistry (Weinheim an der Bergstrasse, Germany)* **2014**, *20* (24), 7448–7457. DOI: 10.1002/chem.201400367. Published Online: May. 7, 2014.

(70) Chen, Y.-C.; Meng, Y.; Dong, Y.-J.; Song, X.-W.; Huang, G.-Z.; Zhang, C.-L.; Ni, Z.-P.; Navařík, J.; Malina, O.; Zbořil, R.; Tong, M.-L. Light- and temperature-assisted spin state annealing: accessing the

hidden multistability. *Chemical science* **2020**, *11* (12), 3281–3289. DOI: 10.1039/c9sc05971g. Published Online: Feb. 26, 2020.

(71) Boonprab, T.; Lee, S. J.; Telfer, S. G.; Murray, K. S.; Phonsri, W.; Chastanet, G.; Collet, E.; Trzop, E.; Jameson, G. N. L.; Harding, P.; Harding, D. J. The First Observation of Hidden Hysteresis in an Iron(III) Spin-Crossover Complex. *Angew. Chem.* **2019**, *131* (34), 11937–11941. DOI: 10.1002/ange.201907619.

(72) Létard, J.-F.; Guionneau, P.; Rabardel, L.; Howard, J. A. K.; Goeta, A. E.; Chasseau, D.; Kahn, O. Structural, Magnetic, and Photomagnetic Studies of a Mononuclear Iron(II) Derivative Exhibiting an Exceptionally Abrupt Spin Transition. Light-Induced Thermal Hysteresis Phenomenon. *Inorg. Chem.* **1998**, *37* (17), 4432–4441. DOI: 10.1021/ic980107b.

(73) Milin, E.; Patinec, V.; Triki, S.; Bendeif, E.-E.; Pillet, S.; Marchivie, M.; Chastanet, G.; Boukheddaden, K. Elastic Frustration Triggering Photoinduced Hidden Hysteresis and Multistability in a Two-Dimensional Photoswitchable Hofmann-Like Spin-Crossover Metal-Organic Framework. *Inorg. Chem.* **2016**, *55* (22), 11652–11661. DOI: 10.1021/acs.inorgchem.6b01081. Published Online: Jul. 21, 2016.

(74) Marchivie, M.; Guionneau, P.; Létard, J. F.; Chasseau, D.; Howard, J. Thermal trapped iron(II) high spin state investigated by X-ray diffraction. *Journal of Physics and Chemistry of Solids* **2004**, *65* (1), 17–23. DOI: 10.1016/j.jpcs.2003.09.002.

(75) Schönfeld, S.; Lochenie, C.; Thoma, P.; Weber, B. 1D iron(ii) spin crossover coordination polymers with 3,3'-azopyridine – kinetic trapping effects and spin transition above room temperature. *CrystEngComm* **2015**, *17* (29), 5389–5395. DOI: 10.1039/C5CE00800J.

(76) Wang, H.; Sinito, C.; Kaiba, A.; Costa, J. S.; Desplanches, C.; Dagault, P.; Guionneau, P.; Létard, J.-F.; Negrier, P.; Mondieig, D. Unusual Solvent Dependence of a Molecule-Based Fe II Macrocyclic Spin-Crossover Complex. *Eur. J. Inorg. Chem.* **2014**, *2014* (29), 4927–4933. DOI: 10.1002/ejic.201402666.

(77) Létard, J.-F.; Asthana, S.; Shepherd, H. J.; Guionneau, P.; Goeta, A. E.; Suemura, N.; Ishikawa, R.; Kaizaki, S. Photomagnetism of a sym-cis-dithiocyanato iron(II) complex with a tetradentate N,N'-bis(2-pyridylmethyl)1,2-ethanediamine ligand. *Chemistry (Weinheim an der Bergstrasse, Germany)* **2012**, *18* (19), 5924–5934. DOI: 10.1002/chem.201102637. Published Online: Mar. 27, 2012.

(78) Buchen, T.; Gütlich, P.; Sugiyarto, K. H.; Goodwin, H. A. High-Spin → Low-Spin Relaxation in [Fe(bpp)2](CF3SO3)2 H2O after LIESST and Thermal Spin-State Trapping—Dynamics of Spin Transition Versus Dynamics of Phase Transition. *Chem. Eur. J.* **1996**, *2* (9), 1134–1138. DOI: 10.1002/chem.19960020915.

(79) Craig, G. A.; Costa, J. S.; Roubeau, O.; Teat, S. J.; Aromí, G. Coupled crystallographic order-disorder and spin state in a bistable molecule: multiple transition dynamics. *Chem. Eur. J.* **2011**, *17* (11), 3120–3127. DOI: 10.1002/chem.201003197. Published Online: Feb. 15, 2011.

(80) Craig, G. A.; Costa, J. S.; Teat, S. J.; Roubeau, O.; Yufit, D. S.; Howard, J. A. K.; Aromí, G. Multimetastability in a spin-crossover compound leading to different high-spin-to-low-spin relaxation dynamics. *Inorg. Chem.* **2013**, *52* (12), 7203–7209. DOI: 10.1021/ic400776x. Published Online: Jun. 4, 2013.

(81) Gütlich, P.; Gaspar, A. B.; Garcia, Y. Spin state switching in iron coordination compounds. *Beilstein journal of organic chemistry* **2013**, *9*, 342–391. DOI: 10.3762/bjoc.9.39. Published Online: Feb. 15, 2013.

(82) Hiller, W.; Straehle, J.; Datz, A.; Hanack, M.; Hatfield, W. E.; Haar, L. W. ter; Guetlich, P. Synthesis, structure, and magnetic properties of catena-(.mu.-oxo)(hemiporphyrazinato)iron(IV), the first polymeric .mu.-oxo-bridged complex of iron. *Journal of the American Chemical Society* **1984**, *106* (2), 329–335. DOI: 10.1021/ja00314a013.

(83) Gaspar, A. B.; Levchenko, G.; Terekhov, S.; Bukin, G.; Valverde-Muñoz, J.; Muñoz-Lara, F. J.; Seredyuk, M.; Real, J. A. The Effect of Pressure on the Cooperative Spin Transition in the 2D Coordination Polymer {Fe(phpy) 2 [Ni(CN) 4]}. *Eur. J. Inorg. Chem.* **2014**, *2014* (3), 429–433. DOI: 10.1002/ejic.201301374.

(84) Ltard, J.-F.; Chastanet, G.; Nguyen, O.; Marcn, S.; Marchivie, M.; Guionneau, P.; Chasseau, D.; Gtlich, P. Spin Crossover Properties of the [Fe(PM - BiA) 2 (NCS) 2] Complex - Phases I and II. *Monatshefte fr Chemie / Chemical Monthly* **2003**, *134* (2), 165–182. DOI: 10.1007/s00706-002-0537-0.

(85) Riedel, E.; Janiak, C. *Anorganische Chemie*, 9. Auflage; De Gruyter Studium; de Gruyter, 2015.

(86) Halcrow, M. A. Structure:function relationships in molecular spin-crossover complexes. *Chem. Soc. Rev.* **2011**, *40* (7), 4119–4142. DOI: 10.1039/C1CS15046D. Published Online: Apr. 11, 2011.

(87) McCusker, J. K.; Rheingold, A. L.; Hendrickson, D. N. Variable-Temperature Studies of Laser-Initiated 5 T 2 → 1 A 1 Intersystem Crossing in Spin-Crossover Complexes: Empirical Correlations between Activation Parameters and Ligand Structure in a Series of Polypyridyl Ferrous Complexes. *Inorg. Chem.* **1996**, *35* (7), 2100–2112. DOI: 10.1021/ic9507880.

(88) Gütlich, P.; Boillot, M.-L., Eds. *Spin crossover in transition metal compounds*; Topics in current chemistry, Vol. 234; Springer, 2004.

(89) Evans, D. F. 400. The determination of the paramagnetic susceptibility of substances in solution by nuclear magnetic resonance. *J. Chem. Soc.* **1959**, 2003. DOI: 10.1039/JR9590002003.

(90) Hogue, R. W.; Feltham, H. L. C.; Miller, R. G.; Brooker, S. Spin Crossover in Dinuclear N4S2 Iron(II) Thioether-Triazole Complexes: Access to HS-HS, HS-LS, and LS-LS States. *Inorg. Chem.* **2016**, *55* (9), 4152–4165. DOI: 10.1021/acs.inorgchem.5b02851. Published Online: Apr. 15, 2016.

(91) Milek, M.; Heinemann, F. W.; Khusniyarov, M. M. Spin crossover meets diarylethenes: efficient photoswitching of magnetic properties in solution at room temperature. *Inorg. Chem.* **2013**, *52* (19), 11585–11592. DOI: 10.1021/ic401960x. Published Online: Sep. 24, 2013.

(92) O'Connor, C. J. Magnetic-Susceptibility Measurement Techniques. In *Molecule-Based Magnetic Materials*; Turnbull, M. M., Sugimoto, T., Thompson, L. K., Eds.; ACS Symposium Series; American Chemical Society, 1996; pp 44–66. DOI: 10.1021/bk-1996-0644.ch004.

(93) Ortega-Villar, N.; Thompson, A. L.; Muñoz, M. C.; Ugalde-Saldívar, V. M.; Goeta, A. E.; Moreno-Esparza, R.; Real, J. A. Solid- and solution-state studies of the novel mu-dicyanamide-bridged dinuclear spin-crossover system {(Fe(bztpen)2mu-N(CN)2}(PF6)3 x n H2O. *Chem. Eur. J.* **2005**, *11* (19), 5721–5734. DOI: 10.1002/chem.200500171.

(94) Turnbull, M. M.; Sugimoto, T.; Thompson, L. K., Eds. *Molecule-Based Magnetic Materials*; ACS Symposium Series; American Chemical Society, 1996. DOI: 10.1021/symposium.

(95) Singh, S.; Brooker, S. Extension of Azine-Triazole Synthesis to Azole-Triazoles Reduces Ligand Field, Leading to Spin Crossover in Tris-L Fe(II). *Inorg. Chem.* **2020**, *59* (2), 1265–1273. DOI: 10.1021/acs.inorgchem.9b02993. Published Online: Jan. 7, 2020.

(96) Mössbauer, R. L. Recoilless Nuclear Resonance Absorption of Gamma Radiation: A new principle yields gamma lines of extreme narrowness for measurements of unprecedented accuracy. *Science* **1962**, *137* (3532), 731–738. DOI: 10.1126/science.137.3532.731.

(97) Mssbauer, R. L. Kernresonanzabsorption von Gammastrahlung in Ir191. *Naturwissenschaften* **1958**, *45* (22), 538–539. DOI: 10.1007/BF00632050.

(98) Gütlich, P. Fifty Years of Mössbauer Spectroscopy in Solid State Research - Remarkable Achievements, Future Perspectives. *Z. anorg. allg. Chem.* **2012**, *638* (1), 15–43. DOI: 10.1002/zaac.201100416.

(99) Gütlich, P. Physikalische Methoden in der Chemie: Mößbauer-Spektroskopie I. *Chemie in unserer Zeit* **1970**, *4* (5), 133–144. DOI: 10.1002/ciuz.19700040502.

(100) Gütlich, P. Physikalische Methoden in der Chemie: Mößbauer-Spektroskopie II. *Chemie in unserer Zeit* **1971**, *5* (5), 131–141. DOI: 10.1002/ciuz.19710050502.

(101) Gütlich, P.; Bill, E.; Trautwein, A. X. *Mössbauer Spectroscopy and Transition Metal Chemistry*; Springer Berlin Heidelberg, 2011. DOI: 10.1007/978-3-540-88428-6.

(102) Souza Jr., P. A. de; Bernhardt, B.; Klingelhöfer, G. Surface Analysis in Archaeology Using the Miniaturized Mössbauer Spectrometer MIMOS II. *Hyperfine Interactions* **2003**, *151/152* (1-4), 125–130. DOI: 10.1023/B:HYPE.0000020408.92554.a6.

(103) Klingelhöfer, G.; Morris, R. V.; Bernhardt, B.; Schröder, C.; Rodionov, D. S.; Souza, P. A. de; Yen, A.; Gellert, R.; Evlanov, E. N.; Zubkov, B.; Foh, J.; Bonnes, U.; Kankeleit, E.; Gütlich, P.; Ming, D. W.; Renz, F.; Wdowiak, T.; Squyres, S. W.; Arvidson, R. E. Jarosite and hematite at Meridiani Planum from Opportunity's Mossbauer Spectrometer. *Science* **2004**, *306* (5702), 1740–1745. DOI: 10.1126/science.1104653.

(104) Morris, R. V.; Klingelhöfer, G.; Schröder, C.; Rodionov, D. S.; Yen, A.; Ming, D. W.; Souza, P. A. de; Fleischer, I.; Wdowiak, T.; Gellert, R.; Bernhardt, B.; Evlanov, E. N.; Zubkov, B.; Foh, J.; Bonnes, U.; Kankeleit, E.; Gütlich, P.; Renz, F.; Squyres, S. W.; Arvidson, R. E. Mössbauer mineralogy of rock, soil, and dust at Gusev crater, Mars: Spirit's journey through weakly altered olivine basalt on the plains and pervasively altered basalt in the Columbia Hills. *J. Geophys. Res.* **2006**, *111* (E2), n/a-n/a. DOI: 10.1029/2005JE002584.

(105) Morris, R. V.; Klingelhöfer, G.; Schröder, C.; Rodionov, D. S.; Yen, A.; Ming, D. W.; Souza, P. A. de; Wdowiak, T.; Fleischer, I.; Gellert, R.; Bernhardt, B.; Bonnes, U.; Cohen, B. A.; Evlanov, E. N.; Foh, J.; Gütlich, P.; Kankeleit, E.; McCoy, T.; Mittlefehldt, D. W.; Renz, F.; Schmidt, M. E.; Zubkov, B.; Squyres, S. W.; Arvidson, R. E. Mössbauer mineralogy of rock, soil, and dust at Meridiani Planum, Mars: Opportunity's journey across sulfate-rich outcrop, basaltic sand and dust, and hematite lag deposits. *J. Geophys. Res.* **2006**, *111* (E12), n/a-n/a. DOI: 10.1029/2006JE002791.

(106) Frankel, R. B.; Blakemore, R. P.; Wolfe, R. S. Magnetite in freshwater magnetotactic bacteria. *Science* **1979**, *203* (4387), 1355–1356. DOI: 10.1126/science.203.4387.1355.

(107) Khalil, M. I.; Al-Zahem, A. M.; Al-Qunaibit, M. H. Synthesis, Characterization, Mössbauer Parameters, and Antitumor Activity of Fe(III) Curcumin Complex. *Bioinorganic chemistry and applications* **2013**, *2013*, 982423. DOI: 10.1155/2013/982423. Published Online: Mar. 27, 2013.

(108) Rao, K. K.; Cammack, R.; Hall, D. O.; Johnson, C. E. Mössbauer effect in Scenedesmus and spinach ferredoxins. The mechanism of electron transfer in plant-type iron-sulphur proteins. *The Biochemical journal* **1971**, *122* (3), 257–265. DOI: 10.1042/bj1220257.

(109) van Stappen, C.; Davydov, R.; Yang, Z.-Y.; Fan, R.; Guo, Y.; Bill, E.; Seefeldt, L. C.; Hoffman, B. M.; DeBeer, S. Spectroscopic Description of the E1 State of Mo Nitrogenase Based on Mo and Fe X-ray Absorption and Mössbauer Studies. *Inorg. Chem.* **2019**, *58* (18), 12365–12376. DOI: 10.1021/acs.inorgchem.9b01951. Published Online: Aug. 23, 2019.

(110) Gütlich, P. Spin Crossover - Quo Vadis? *Eur. J. Inorg. Chem.* **2013**, *2013* (5-6), 581–591. DOI: 10.1002/ejic.201300092.

(111) Boča, R.; Boča, M.; Ehrenberg, H.; Fuess, H.; Linert, W.; Renz, F.; Svoboda, I. Spin crossover in iron(II) tris(2-(2′-pyridyl)benzimidazole) complex monitored by variable temperature methods: synchrotron powder diffraction, DSC, IR spectra, Mössbauer spectra, and magnetic susceptibility. *Chemical Physics* **2003**, *293* (3), 375–395. DOI: 10.1016/S0301-0104(03)00375-6.

(112) Chen, W.-B.; Leng, J.-D.; Wang, Z.-Z.; Chen, Y.-C.; Miao, Y.; Tong, M.-L.; Dong, W. Reversible crystal-to-crystal transformation from a trinuclear cluster to a 1D chain and the corresponding spin crossover (SCO) behaviour change. *Chemical communications (Cambridge, England)* **2017**, *53* (55), 7820–7823. DOI: 10.1039/C7CC04036A.

(113) Feltham, H. L. C.; Johnson, C.; Elliott, A. B. S.; Gordon, K. C.; Albrecht, M.; Brooker, S. "Tail" tuning of iron(II) spin crossover temperature by 100 K. *Inorg. Chem.* **2015**, *54* (6), 2902–2909. DOI: 10.1021/ic503040f. Published Online: Mar. 2, 2015.

(114) Hora, S.; Hagiwara, H. High-Temperature Wide Thermal Hysteresis of an Iron(II) Dinuclear Double Helicate. *Inorganics* **2017**, *5* (3), 49. DOI: 10.3390/inorganics5030049.

(115) Kulmaczewski, R.; Olguín, J.; Kitchen, J. A.; Feltham, H. L. C.; Jameson, G. N. L.; Tallon, J. L.; Brooker, S. Remarkable scan rate dependence for a highly constrained dinuclear iron(II) spin crossover complex with a wide thermal hysteresis loop. *Journal of the American Chemical Society* **2014**, *136* (3), 878–881. DOI: 10.1021/ja411563x. Published Online: Jan. 8, 2014.

(116) Sorai, M.; Yumoto, Y.; Dost M., H.; Larkworthy, L. F. Calorimetric study on the spin-crossover phenomenon between 3T1 and 5E in trans-bis[1,2-bis(diethylphosphino) ethane]diiodochromium(II), [CrI2(depe)2]. *Journal of Physics and Chemistry of Solids* **1993**, *54* (4), 421–430. DOI: 10.1016/0022-3697(93)90323-J.

(117) Takemoto, J. H.; Streusand, B.; Hutchinson, B. Far-infrared spectra of some Fe(1,10-phenanthroline) 2X2 complexes. *Spectrochimica Acta Part A: Molecular Spectroscopy* **1974**, *30* (3), 827–834. DOI: 10.1016/0584-8539(74)80199-6.

(118) Craig, G. A.; Costa, J. S.; Roubeau, O.; Teat, S. J.; Shepherd, H. J.; Lopes, M.; Molnár, G.; Bousseksou, A.; Aromí, G. High-temperature photo-induced switching and pressure-induced transition in a cooperative molecular spin-crossover material. *Dalton transactions (Cambridge, England : 2003)* **2014**, *43* (2), 729–737. DOI: 10.1039/C3DT52075G.

(119) Garcia, Y.; van Koningsbruggen, P. J.; Bravic, G.; Guionneau, P.; Chasseau, D.; Cascarano, G. L.; Moscovici, J.; Lambert, K.; Michalowicz, A.; Kahn, O. Synthesis, Crystal Structure, EXAFS, and Magnetic Properties of catena -Poly[μ-tris(4-(2-hydroxyethyl)-1,2,4-triazole- N1 , N2)copper(II)] Diperchlorate

Trihydrate: Relevance with the Structure of the Iron(II) 1,2,4-Triazole Spin Transition Molecular Materials. *Inorg. Chem.* **1997**, *36* (27), 6357–6365. DOI: 10.1021/ic970895p.

(120) Hosoya, K.; Nishikiori, S.; Takahashi, M.; Kitazawa, T. Spin-Crossover Behavior of Hofmann-Type-Like Complex Fe(4,4'-bipyridine)Ni(CN)4·nH2O Depending on Guest Species. *Magnetochemistry* **2016**, *2* (1), 8. DOI: 10.3390/magnetochemistry2010008.

(121) Kitase, K.; Kitazawa, T. A novel two-step Fe-Au type spin-crossover behavior in a Hofmann-type coordination complex {Fe(4-methylpyrimidine)2Au(CN)22}. *Dalton transactions (Cambridge, England : 2003)* **2020**, *49* (35), 12210–12214. DOI: 10.1039/D0DT01681K.

(122) Michalowicz, A.; Moscovici, J.; Charton, J.; Sandid, F.; Benamrane, F.; Garcia, Y. EXAFS and thermodynamics of Fe(II) spin transition polymeric compounds. *Journal of synchrotron radiation* **2001**, *8* (Pt 2), 701–703. DOI: 10.1107/S0909049500018057.

(123) Mohamed, A.; Lee, M.; Kitase, K.; Kitazawa, T.; Kim, J.-Y.; Cho, D.-Y. Soft X-ray Absorption Spectroscopy Study of Spin Crossover Fe-Compounds: Persistent High Spin Configurations under Soft X-ray Irradiation. *Crystals* **2018**, *8* (11), 433. DOI: 10.3390/cryst8110433.

(124) *Magnetic properties of some spin-crossover, high-spin, and low-spin cobalt (II) complexes with Schiff bases derived from 3-formylsalicylic acid*, 1984.

(125) Cantin, C.; Kliava, J.; Servant, Y.; Sommier, L.; Kahn, O. Variable temperature EPR study of Fe2+ spin transition in Cu2+ doped [Fe(trz)(Htrz)2](BF4). *Appl. Magn. Reson.* **1997**, *12* (1), 87–93. DOI: 10.1007/BF03161994.

(126) Timken, M. D.; Wilson, S. R.; Hendrickson, D. N. Dynamics of spin-state interconversion and cooperativity for ferric spin-crossover complexes in the solid state. 4. Pyruvic acid thiosemicarbazone complex. *Inorg. Chem.* **1985**, *24* (21), 3450–3457. DOI: 10.1021/ic00215a030.

(127) Grünsteudel, H.; Paulsen, H.; Meyer-Klaucke, W.; Winkler, H.; Trautwein, A. X.; Grünsteudel, H. F.; Baron, A.; Chumakov, A. I.; Rüffer, R.; Toftlund, H. *Hyperfine Interactions* **1998**, *113* (1/4), 311–317. DOI: 10.1023/A:1012641614937.

(128) Félix, G.; Mikolasek, M.; Peng, H.; Nicolazzi, W.; Molnár, G.; Chumakov, A. I.; Salmon, L.; Bousseksou, A. Lattice dynamics in spin-crossover nanoparticles through nuclear inelastic scattering. *Phys. Rev. B* **2015**, *91* (2). DOI: 10.1103/PhysRevB.91.024422.

(129) H. Grünsteudel, H. Paulsen, W. Meyer-Klaucke, H. Winkler, A. X. Trautwein, H. F. *Hyperfine Interact.*, Vol. 113, 1998.

(130) Nagai, Y.; Saito, H.; Hyodo, T.; Vértes, A.; Süvegh, K. Local structural deformation in [Zn(1–propyltetrazole)6](BF4)2 and [Fe(1–propyltetrazole)6](BF4)2 crystals observed by positron-annihilation spectroscopy. *Phys. Rev. B* **1998**, *57* (22), 14119–14122. DOI: 10.1103/PhysRevB.57.14119.

(131) Vértes, A.; Süvegh, K.; Hinek, R.; Gütlich, P. Positron annihilation study of spin-crossover in [FexZn1–x(ptz)6](BF4)2 single crystals. *Journal of Physics and Chemistry of Solids* **1994**, *55* (11), 1269–1275. DOI: 10.1016/0022-3697(94)90209-7.

(132) Blundell, S. J.; Pratt, F. L.; Lancaster, T.; Marshall, I. M.; Steer, C. A.; Heath, S. L.; Létard, J.-F.; Sugano, T.; Mihailovic, D.; Omerzu, A. μ SR studies of organic and molecular magnets. *Polyhedron* **2003**, *22* (14-17), 1973–1980. DOI: 10.1016/S0277-5387(03)00257-2.

(133) Campbell, S. J.; KSENOFONTOV, V.; Garcia, Y.; Lord, J. S.; Boland, Y.; Gütlich, P. Muon Spin Rotation and Mössbauer Investigations of the Spin Transition in [Fe(ptz) 6](ClO 4) 2⊥. *J. Phys. Chem. B* **2003**, *107* (51), 14289–14295. DOI: 10.1021/jp036078u.

(134) Roubeau, O.; Gubbens, P.; Visser, D.; Blaauw, M.; Dalmas de Réotier, P.; Yaouanc, A.; Haasnoot, J. G.; Reedijk, J.; Sakarya, S.; Jayasooriya, U. A.; Cottrell, S. P.; King, P. Observation of the spin-crossover in [Fe(btr)2(NCS)2]·H2O (btr=4,4'-bis-1,2,4-triazole) with μSR. *Chemical Physics Letters* **2004**, *395* (4-6), 177–181. DOI: 10.1016/j.cplett.2004.07.016.

(135) Murray, K. S.; Kepert, C. J. Cooperativity in Spin Crossover Systems: Memory, Magnetism and Microporosity. In *Spin crossover in transition metal compounds*; Gütlich, P., Garcia, Y., Eds.; Topics in current chemistry, Vol. 233; Springer, 2004; pp 195–228. DOI: 10.1007/b13536.

(136) Halcrow, M. A., Ed. *Spin-crossover materials*:*Properties and applications*; Wiley, 2013. DOI: 10.1002/9781118519301.

(137) Weber, B. Novel Mononuclear Spin-Crossover Complexes. In *Spin-crossover materials*:*Properties and applications*; Halcrow, M. A., Ed.; Wiley, 2013; pp 55–76. DOI: 10.1002/9781118519301.ch2.

(138) Baldé, C.; Bauer, W.; Kaps, E.; Neville, S.; Desplanches, C.; Chastanet, G.; Weber, B.; Létard, J. F. Light-Induced Excited Spin-State Properties in 1D Iron(II) Chain Compounds. *Eur. J. Inorg. Chem.* **2013**, *2013* (15), 2744–2750. DOI: 10.1002/ejic.201201422.

(139) Petrouleas, V.; Tuchagues, J.-P. Fe[5NO2-sal-N(1,4,7,10)]: a new iron(II) complex exhibiting an unusual two-step spin conversion afforded by a hexadentate ligand with a N4O2, donor set. *Chemical Physics Letters* **1987**, *137* (1), 21–25. DOI: 10.1016/0009-2614(87)80297-X.

(140) Salmon, L.; Bousseksou, A.; Donnadieu, B.; Tuchagues, J.-P. Two novel iron(II) materials based on dianionic N4O2 Schiff bases: structural properties and spin-crossover characteristics in the series Fe(3-X,5-NO2-sal-N(1,4,7,10) (X = H, 3-MeO, 3-EtO). *Inorg. Chem.* **2005**, *44* (6), 1763–1773. DOI: 10.1021/ic048387k.

(141) Weber, B. Spin crossover complexes with N4O2 coordination sphere—The influence of covalent linkers on cooperative interactions. *Coordination Chemistry Reviews* **2009**, *253* (19-20), 2432–2449. DOI: 10.1016/j.ccr.2008.10.002.

(142) Costa, J. S.; Balde, C.; Carbonera, C.; Denux, D.; Wattiaux, A.; Desplanches, C.; Ader, J.-P.; Gütlich, P.; Létard, J.-F. Photomagnetic properties of an iron(II) low-spin complex with an unusually long-lived metastable LIESST state. *Inorg. Chem.* **2007**, *46* (10), 4114–4119. DOI: 10.1021/ic062418p. Published Online: Apr. 11, 2007.

(143) Schönfeld, S.; Bauer, W.; Thallmair, S.; Hörner, G.; Weber, B. Running in the Family: Molecular Factors controlling Spin Crossover of Iron(II) Complexes with Schiff-base like Ligands. *Z. anorg. allg. Chem.* **2021**, *647* (8), 905–914. DOI: 10.1002/zaac.202000409.

(144) Ashley, D. C.; Jakubikova, E. Tuning the Redox Potentials and Ligand Field Strength of Fe(II) Polypyridines: The Dual π-Donor and π-Acceptor Character of Bipyridine. *Inorg. Chem.* **2018**, *57* (16), 9907–9917. DOI: 10.1021/acs.inorgchem.8b01002. Published Online: Aug. 8, 2018.

(145) van der Lubbe, S. C. C.; Vermeeren, P.; Fonseca Guerra, C.; Bickelhaupt, F. M. The Nature of Nonclassical Carbonyl Ligands Explained by Kohn-Sham Molecular Orbital Theory. *Chem. Eur. J.* **2020**, *26* (67), 15690–15699. DOI: 10.1002/chem.202003768. Published Online: Nov. 3, 2020.

(146) Kershaw Cook, L. J.; Kulmaczewski, R.; Mohammed, R.; Dudley, S.; Barrett, S. A.; Little, M. A.; Deeth, R. J.; Halcrow, M. A. A Unified Treatment of the Relationship Between Ligand Substituents and Spin State in a Family of Iron(II) Complexes. *Angew. Chem.* **2016**, *128* (13), 4399–4403. DOI: 10.1002/ange.201600165.

(147) Kulmaczewski, R.; Bamiduro, F.; Shahid, N.; Cespedes, O.; Halcrow, M. A. Structural Transformations and Spin-Crossover in FeL2 2+ Salts (L=4-{tert-Butylsulfanyl}-2,6-di{pyrazol-1-yl}pyridine): The Influence of Bulky Ligand Substituents. *Chem. Eur. J.* **2021**, *27* (6), 2082–2092. DOI: 10.1002/chem.202004072. Published Online: Dec. 23, 2020.

(148) Deeth, R. J.; Halcrow, M. A.; Kershaw Cook, L. J.; Raithby, P. R. Ab Initio Ligand Field Molecular Mechanics and the Nature of Metal-Ligand π-Bonding in Fe(II) 2,6-di(pyrazol-1-yl)pyridine Spin Crossover Complexes. *Chem. Eur. J.* **2018**, *24* (20), 5204–5212. DOI: 10.1002/chem.201704558. Published Online: Dec. 11, 2017.

(149) Hansch, C.; Leo, A.; Taft, R. W. A survey of Hammett substituent constants and resonance and field parameters. *Chem. Rev.* **1991**, *91* (2), 165–195. DOI: 10.1021/cr00002a004.

(150) Hogue, R. W.; Miller, R. G.; White, N. G.; Feltham, H. L. C.; Jameson, G. N. L.; Brooker, S. Hysteretic spin crossover in iron(II) complexes of a new pyridine-triazole-pyrazine ligand is tuned by choice of NCE co-ligand. *Chemical communications (Cambridge, England)* **2014**, *50* (12), 1435–1437. DOI: 10.1039/c3cc43922d.

(151) Klingele, J.; Kaase, D.; Klingele, M. H.; Lach, J. Synthesis and mononuclear complexes of the bis-bidentate ligand 2,5-di(2-pyridyl)-1,3,4-thiadiazole (dptd): spin crossover in Fe(II)(dptd)2(NCSe)2 and Fe(II)(dptd)2(NCBH3)2·H2O. *Dalton transactions (Cambridge, England : 2003)* **2012**, *41* (4), 1397–1406. DOI: 10.1039/c1dt11396h. Published Online: Nov. 29, 2011.

(152) Klingele, J.; Kaase, D.; Schmucker, M.; Lan, Y.; Chastanet, G.; Létard, J.-F. Thermal spin crossover and LIESST effect observed in complexes Fe(L(Ch))2(NCX)2 L(Ch) = 2,5-di(2-pyridyl)-1,3,4-chalcadiazole; Ch = O, S, Se; X = S, Se, BH3. *Inorg. Chem.* **2013**, *52* (10), 6000–6010. DOI: 10.1021/ic400342m. Published Online: Apr. 26, 2013.

(153) Moliner, N.; Gaspar, A. B.; Muñoz, M. C.; Niel, V.; Cano, J.; Real, J. A. Light- and thermal-induced spin crossover in Fe(abpt)2(N(CN)2)2. Synthesis, structure, magnetic properties, and high-spin<--low spin relaxation studies. *Inorg. Chem.* **2001**, *40* (16), 3986–3991. DOI: 10.1021/ic0100976.

(154) Moliner, N.; Muñoz, M.; Létard, S.; Létard, J.-F.; Solans, X.; Burriel, R.; Castro, M.; Kahn, O.; Real, J. A. Spin-crossover in the [Fe(abpt)2(NCX)2] (X=S, Se) system: structural, magnetic, calorimetric and photomagnetic studies. *Inorganica Chimica Acta* **1999**, *291* (1-2), 279–288. DOI: 10.1016/S0020-1693(99)00128-0.

(155) Scott, H. S.; Ross, T. M.; Chilton, N. F.; Gass, I. A.; Moubaraki, B.; Chastanet, G.; Paradis, N.; Lètard, J.-F.; Vignesh, K. R.; Rajaraman, G.; Batten, S. R.; Murray, K. S. Crown-linked dipyridylamino-triazine ligands and their spin-crossover iron(II) derivatives: magnetism, photomagnetism and cooperativity. *Dalton transactions (Cambridge, England : 2003)* **2013**, *42* (47), 16494–16509. DOI: 10.1039/c3dt51839f.

(156) Fürmeyer, F.; Münzberg, D.; Carrella, L. M.; Rentschler, E. First Cobalt(II) Spin Crossover Compound with N4S2-Donorset. *Molecules (Basel, Switzerland)* **2020**, *25* (4). DOI: 10.3390/molecules25040855. Published Online: Feb. 14, 2020.

(157) Rodríguez-Jiménez, S.; Barltrop, A. S.; White, N. G.; Feltham, H. L. C.; Brooker, S. Solvent Polarity Predictably Tunes Spin Crossover T1/2 in Isomeric Iron(II) Pyrimidine Triazoles. *Inorg. Chem.* **2018**, *57* (11), 6266–6282. DOI: 10.1021/acs.inorgchem.8b00128. Published Online: May. 16, 2018.

(158) Herold, C. F.; Carrella, L. M.; Rentschler, E. A Family of Dinuclear Iron(II) SCO Compounds Based on a 1,3,4-Thiadiazole Bridging Ligand. *Eur. J. Inorg. Chem.* **2015**, *2015* (22), 3632–3636. DOI: 10.1002/ejic.201500483.

(159) Real, J. A.; Gaspar, A. B.; Niel, V.; Muñoz, M. Communication between iron(II) building blocks in cooperative spin transition phenomena. *Coordination Chemistry Reviews* **2003**, *236* (1-2), 121–141. DOI: 10.1016/S0010-8545(02)00220-5.

(160) Paez-Espejo, M.; Sy, M.; Boukheddaden, K. Elastic Frustration Causing Two-Step and Multistep Transitions in Spin-Crossover Solids: Emergence of Complex Antiferroelastic Structures. *Journal of the American Chemical Society* **2016**, *138* (9), 3202–3210. DOI: 10.1021/jacs.6b00049. Published Online: Feb. 26, 2016.

(161) Chastanet, G.; Sciortino, N. F.; Neville, S. M.; Kepert, C. J. High Spin to Low Spin Relaxation Regime Change in a Multistep 3D Spin-Crossover Material. *Eur. J. Inorg. Chem.* **2018**, *2018* (3-4), 314–319. DOI: 10.1002/ejic.201701127.

(162) Ltard, J.-F.; Chastanet, G.; Nguyen, O.; Marcn, S.; Marchivie, M.; Guionneau, P.; Chasseau, D.; Gtlich, P. Spin Crossover Properties of the [Fe(PM - BiA) 2 (NCS) 2] Complex - Phases I and II. *Monatshefte fr Chemie / Chemical Monthly* **2003**, *134* (2), 165–182. DOI: 10.1007/s00706-002-0537-0.

(163) Stoleriu, L.; Chakraborty, P.; Hauser, A.; Stancu, A.; Enachescu, C. Thermal hysteresis in spin-crossover compounds studied within the mechanoelastic model and its potential application to nanoparticles. *Phys. Rev. B* **2011**, *84* (13). DOI: 10.1103/PhysRevB.84.134102.

(164) Hasegawa, Y.; Sakamoto, R.; Takahashi, K.; Nishihara, H. Bis(E)-2,6-bis(1H-pyrazol-1-yl)-4-styrylpyridineiron(II) complex: relationship between thermal spin crossover and crystal solvent. *Inorg. Chem.* **2013**, *52* (3), 1658–1665. DOI: 10.1021/ic302640m. Published Online: Jan. 24, 2013.

(165) Fürmeyer, F.; Carrella, L.; Rentschler, E. 2D Layer Arrangement of Solely [HS-HS] or [LS-LS] Molecules in the [HS-LS] State of a Dinuclear Fe(II) Spin Crossover Complex. *Crystals* **2020**, *10* (6), 448. DOI: 10.3390/cryst10060448.

(166) Kershaw Cook, L. J.; Shepherd, H. J.; Comyn, T. P.; Baldé, C.; Cespedes, O.; Chastanet, G.; Halcrow, M. A. Decoupled spin crossover and structural phase transition in a molecular iron(II) complex. *Chem. Eur. J.* **2015**, *21* (12), 4805–4816. DOI: 10.1002/chem.201406307. Published Online: Jan. 30, 2015.

(167) Li, J.-Y.; He, C.-T.; Chen, Y.-C.; Zhang, Z.-M.; Liu, W.; Ni, Z.-P.; Tong, M.-L. Tunable cooperativity in a spin-crossover Hoffman-like metal–organic framework material by aromatic guests. *J. Mater. Chem. C* **2015**, *3* (30), 7830–7835. DOI: 10.1039/C5TC00432B.

(168) Liu, W.; Wang, L.; Su, Y.-J.; Chen, Y.-C.; Tucek, J.; Zboril, R.; Ni, Z.-P.; Tong, M.-L. Hysteretic Spin Crossover in Two-Dimensional (2D) Hofmann-Type Coordination Polymers. *Inorg. Chem.* **2015**, *54* (17), 8711–8716. DOI: 10.1021/acs.inorgchem.5b01341. Published Online: Aug. 10, 2015.

(169) Ossinger, S.; Näther, C.; Buchholz, A.; Schmidtmann, M.; Mangelsen, S.; Beckhaus, R.; Plass, W.; Tuczek, F. Spin Transition of an Iron(II) Organoborate Complex in Different Polymorphs and in Vacuum-

Deposited Thin Films: Influence of Cooperativity. *Inorg. Chem.* **2020**, *59* (12), 7966–7979. DOI: 10.1021/acs.inorgchem.9b03354. Published Online: Feb. 9, 2020.

(170) Nassirinia, N.; Amani, S.; Teat, S. J.; Roubeau, O.; Gamez, P. Enhancement of spin-crossover cooperativity mediated by lone pair-π interactions and halogen bonding. *Chemical communications (Cambridge, England)* **2014**, *50* (8), 1003–1005. DOI: 10.1039/c3cc48334g.

(171) *Effect of metal dilution on the spin-crossover behavior in [FexM1-x (phen) 2 (NCS) 2](M= Mn, Co, Ni, Zn)*, 1982.

(172) *Solid state effects on spin transitions: magnetic, calorimetric, and moessbauer-effect properties of [FexCo1-x (4, 4'-bis-1, 2, 4-triazole) 2 (NCS) 2]. cntdot. H2O …*, 1994.

(173) Balde, C.; Desplanches, C.; Nguyen, O.; Létard, J.-F.; Freysz, E. Complete temperature study of the relaxation from HS to LS state in the mixed [Fe x Zn 1-x (Phen) 2 (NCS) 2] systems (with x = 1, 0.73, 0.5, 0.32, 0.19 and 0.04). *J. Phys.: Conf. Ser.* **2009**, *148*, 12026. DOI: 10.1088/1742-6596/148/1/012026.

(174) *Solid-state effects in spin transitions: influence of iron (II) dilution on the magnetic and calorimetric properties of the series [FexNi1-x (4, 4'-bis (1, 2, 4-triazole)) 2 …*, 1994.

(175) Sylla, M. S.; Baldé, C.; Daro, N.; Desplanches, C.; Marchivie, M.; Chastanet, G. On the Effect of the Internal Pressure on the Photoinduced Spin-Crossover Behavior of [Fe x M 1- x (1,10-phenanthroline) 2 (NCS) 2] Solid Solutions (M = Ni II , Zn II , and Cd II). *Eur. J. Inorg. Chem.* **2018**, *2018* (3-4), 297–304. DOI: 10.1002/ejic.201700350.

(176) Sugiyarto, K. H.; Craig, D. C.; Rae, A. D.; Goodwin, H. A. Structural, Magnetic and Mössbauer Spectral Studies of Salts of Bis[2,6-bis(pyrazol-3-yl)pyridine]iron(II)—a Spin Crossover System. *Aust. J. Chem.* **1994**, *47* (5), 869. DOI: 10.1071/CH9940869.

(177) *A MODEL OF 2-STAGE SPIN TRANSITIONS*, 1986.

(178) Schneider, C. J.; Cashion, J. D.; Moubaraki, B.; Neville, S. M.; Batten, S. R.; Turner, D. R.; Murray, K. S. The magnetic and structural elucidation of 3,5-bis(2-pyridyl)-1,2,4-triazolate-bridged dinuclear iron(II) spin crossover compounds. *Polyhedron* **2007**, *26* (9-11), 1764–1772. DOI: 10.1016/j.poly.2006.09.003.

(179) Schneider, C. J.; Cashion, J. D.; Chilton, N. F.; Etrillard, C.; Fuentealba, M.; Howard, J. A. K.; Létard, J.-F.; Milsmann, C.; Moubaraki, B.; Sparkes, H. A.; Batten, S. R.; Murray, K. S. Spin Crossover in a 3,5-Bis(2-pyridyl)-1,2,4-triazolate-Bridged Dinuclear Iron(II) Complex [{Fe(NCBH 3)(py)} 2 (μ-L 1) 2] - Powder versus Single Crystal Study. *Eur. J. Inorg. Chem.* **2013**, *2013* (5-6), 850–864. DOI: 10.1002/ejic.201201075.

(180) Zhong, Z. J.; Tao, J.-Q.; Yu, Z.; Dun, C.-Y.; Liu, Y.-J.; You, X.-Z. A stacking spin-crossover iron(II) compound with a large hysteresis †. *J. Chem. Soc., Dalton Trans.* **1998** (3), 327–328. DOI: 10.1039/A706841G.

(181) Chen, J.-T.; Zhao, X.-H.; Zhang, Y.-Z. Manipulating the spin crossover behavior in a series of {FeFeII} complexes. *Dalton transactions (Cambridge, England : 2003)* **2020**, *49* (18), 5949–5956. DOI: 10.1039/D0DT00016G. Published Online: Apr. 21, 2020.

(182) Tsukiashi, A.; Nakaya, M.; Kobayashi, F.; Ohtani, R.; Nakamura, M.; Harrowfield, J. M.; Kim, Y.; Hayami, S. Intermolecular Interaction Tuning of Spin-Crossover Iron(III) Complexes with Aromatic Counteranions. *Inorg. Chem.* **2018**, *57* (5), 2834–2842. DOI: 10.1021/acs.inorgchem.7b03126. Published Online: Feb. 20, 2018.

(183) Jonathan Kiehl, Tim Hochdörffer, Luca Carrella, Volker Schünemann, Mathilde H. Nygaard, Jacob Overgaard, Eva Rentschler. Strongly cooperative mononuclear [Fe(L1)2(NCX)2] complexes exhibit highly versatile magnetic bistability:Manuscript in preparation.

(184) Youinou, M.-T.; Rahmouni, N.; Fischer, J.; Osborn, J. A. Self-Assembly of a Cu4 Complex with Coplanar Copper(I) Ions: Synthesis, Structure, and Electrochemical Properties. *Angew. Chem. Int. Ed. Engl.* **1992**, *31* (6), 733–735. DOI: 10.1002/anie.199207331.

(185) Avila, C. M.; Lopes, A. B.; Gonçalves, A. S.; da Silva, L. L.; Romeiro, N. C.; Miranda, A. L. P.; Sant'Anna, C. M. R.; Barreiro, E. J.; Fraga, C. A. M. Structure-based design and biological profile of (E)-N-(4-Nitrobenzylidene)-2-naphthohydrazide, a novel small molecule inhibitor of IκB kinase-β. *European journal of medicinal chemistry* **2011**, *46* (4), 1245–1253. DOI: 10.1016/j.ejmech.2011.01.045. Published Online: Feb. 3, 2011.

(186) Beckert, R.; Fanghänel, E.; Habicher, W. D.; Knölker, H.-J.; Metz, P.; Schwetlick, K. *Organikum*:*Organisch-chemisches Grundpraktikum*, 24., vollständig überarbeitete und aktualisierte Auflage; Wiley-VCH Verlag, 2015.

(187) Tao, J.-Q.; Gu, Z.-G.; Wang, T.-W.; Yang, Q.-F.; Zuo, J.-L.; You, X.-Z. Spin-crossover iron(II) complexes [Fe(Medpq)(py)2(NCS)2] and [Fe(Medpq)(py)2(NCSe)2]: syntheses, characterization and magnetic properties. *Inorganica Chimica Acta* **2007**, *360* (15), 4125–4132. DOI: 10.1016/j.ica.2007.06.006.

(188) Erickson, N. E.; Sutin, N. The So-Called cis-trans Isomerism of Bis(isothiocyanato) tetra(pyridine) iron(II). *Inorg. Chem.* **1966**, *5* (10), 1834–1835. DOI: 10.1021/ic50044a050.

(189) Kitchen, J. A.; Jameson, G. N. L.; Tallon, J. L.; Brooker, S. Spin crossover in co-crystallised 2 ratio 1 cisratiotrans Fe(II)(pldpt)(2)(NCS)(2) occurs only in (1/3) of the iron centres. *Chemical communications (Cambridge, England)* **2010**, *46* (18), 3200–3202. DOI: 10.1039/b927036a. Published Online: Mar. 18, 2010.

(190) Zhu, D.; Xu, Y.; Yu, Z.; Guo, Z.; Sang, H.; Liu, T.; You, X. A Novel Bis(trans -thiocyanate)iron(II) Spin-Transition Molecular Material with Bidentate Triaryltriazole Ligands and Its Bis(cis-thiocyanate)iron(II) High-Spin Isomer. *Chem. Mater.* **2002**, *14* (2), 838–843. DOI: 10.1021/cm010688u.

(191) Real, A.; Zarembowitch, J.; Kahn, O.; Solans, X. Magnetic interaction and spin transition in iron(II) dinuclear compounds. Crystal structure of (.mu.-2,2'-bipyrimidine)bis[(2,2'-bipyrimidine)bis(thiocyanato)iron(II)]. *Inorg. Chem.* **1987**, *26* (18), 2939–2943. DOI: 10.1021/ic00265a005.

(192) Kitchen, J. A.; White, N. G.; Gandolfi, C.; Albrecht, M.; Jameson, G. N. L.; Tallon, J. L.; Brooker, S. Room-temperature spin crossover and Langmuir-Blodgett film formation of an iron(II) triazole complex featuring a long alkyl chain substituent: the tail that wags the dog. *Chemical communications (Cambridge, England)* **2010**, *46* (35), 6464–6466. DOI: 10.1039/C0CC01008A. Published Online: Jul. 7, 2010.

(193) Gobeze, W. A.; Milway, V. A.; Olguín, J.; Jameson, G. N. L.; Brooker, S. Nine diiron(II) complexes of three bis-tetradentate pyrimidine based ligands with NCE (E = S, Se, BH3) coligands. *Inorg. Chem.* **2012**, *51* (16), 9056–9065. DOI: 10.1021/ic3012052. Published Online: Jul. 27, 2012.

(194) Nakamoto, K. *Infrared and Raman Spectra of inorganic and coordination compounds*, 3. ed.; Wiley, 1978.

(195) Youngme, S.; Phatchimkun, J.; Suksangpanya, U.; Pakawatchai, C.; van Albada, G. A.; Quesada, M.; Reedijk, J. A new unique tetranuclear Cu(II) compound with double bridging thiocyanate anions: Synthesis, X-ray structure and magnetism of [Cu4(μ1,3-NCS)6(dpyam)4(O2CH)2(H2O)2] (dpyam=di-2-pyridylamine). *Inorganic Chemistry Communications* **2006**, *9* (2), 242–247. DOI: 10.1016/j.inoche.2005.11.017.

(196) Galding, M. R.; Virovets, A. V.; Kazakov, I. V.; Scheer, M.; Smirnov, S. N.; Timoshkin, A. Y. Diminished electron density in the Vaska-type rhodium(I) complex trans-Rh(NCBH3)(CO)(PPh3)2. *Acta crystallographica. Section C, Structural chemistry* **2016**, *72* (Pt 7), 514–517. DOI: 10.1107/S2053229616008536. Published Online: Jun. 3, 2016.

(197) Hedelt, R.; Schulzke, C.; Rehder, D. A cyanohydridoborato–vanadium(II) complex, trans-[V(NCBH3)2(thf)4]. *Inorganic Chemistry Communications* **2000**, *3* (6), 300–302. DOI: 10.1016/S1387-7003(00)00069-1.

(198) Baba, H.; Nakano, M. Magnetostructural examination of Mn(III) complexes [Mn(cyclam)X2]+ with strong axial ligands. *Polyhedron* **2009**, *28* (9-10), 2087–2091. DOI: 10.1016/j.poly.2009.02.013.

(199) Liu, F.-C.; Yang, P.-S.; Chen, C.-Y.; Lee, G.-H.; Peng, S.-M. Syntheses, structures, and dynamic properties of M(CO)2(η3-C3H5)(L–L)(NCBH3) (M=Mo, W; L–L=dppe, bipy, en). *Journal of Organometallic Chemistry* **2008**, *693* (3), 537–545. DOI: 10.1016/j.jorganchem.2007.11.039.

(200) Barrios, L. A.; Peyrecave-Lleixà, E.; Craig, G. A.; Roubeau, O.; Teat, S. J.; Aromí, G. Unusual Crystal Packing in a Family of [Fe{2,6-bis(pyrazol-3-yl)pyridine} 2] 2+ Compounds and the Effect on the Occurrence of Spin Crossover and Its Cooperative Character. *Eur. J. Inorg. Chem.* **2014**, *2014* (35), 6013–6021. DOI: 10.1002/ejic.201403009.

(201) Janiak, C. A critical account on π–π stacking in metal complexes with aromatic nitrogen-containing ligands †. *J. Chem. Soc., Dalton Trans.* **2000** (21), 3885–3896. DOI: 10.1039/B003010O.

(202) Brooker, S. Spin crossover with thermal hysteresis: practicalities and lessons learnt. *Chem. Soc. Rev.* **2015**, *44* (10), 2880–2892. DOI: 10.1039/C4CS00376D. Published Online: Apr. 24, 2015.

(203) Miller, R. G.; Narayanaswamy, S.; Tallon, J. L.; Brooker, S. Spin crossover with thermal hysteresis in cobalt(ii) complexes and the importance of scan rate. *New J. Chem.* **2014**, *38* (5), 1932. DOI: 10.1039/C3NJ01451G.

(204) Muñoz Lara, F. J.; Gaspar, A. B.; Aravena, D.; Ruiz, E.; Muñoz, M. C.; Ohba, M.; Ohtani, R.; Kitagawa, S.; Real, J. A. Enhanced bistability by guest inclusion in Fe(II) spin crossover porous coordination polymers. *Chemical communications (Cambridge, England)* **2012**, *48* (39), 4686–4688. DOI: 10.1039/C2CC31048A. Published Online: Apr. 5, 2012.

(205) Gómez, V.; Sáenz de Pipaón, C.; Maldonado-Illescas, P.; Waerenborgh, J. C.; Martin, E.; Benet-Buchholz, J.; Galán-Mascarós, J. R. Easy Excited-State Trapping and Record High TTIESST in a Spin-Crossover Polyanionic Fe(II) Trimer. *Journal of the American Chemical Society* **2015**, *137* (37), 11924–11927. DOI: 10.1021/jacs.5b07879. Published Online: Sep. 11, 2015.

(206) Létard, J.-F.; Chastanet, G.; Tokoro, H.; Ohkoshi, S. Rubidium Manganese Hexacyanoferrate Solid Solutions: Towards Hidden Phases. *CIC* **2016**, *6* (1), 34–39. DOI: 10.2174/1877944105666150910200534.

(207) Sheu, C.-F.; Pillet, S.; Lin, Y.-C.; Chen, S.-M.; Hsu, I.-J.; Lecomte, C.; Wang, Y. Magnetostructural relationship in the spin-crossover complex t-{Fe(abpt)2N(CN)22}: polymorphism and disorder phenomenon. *Inorg. Chem.* **2008**, *47* (23), 10866–10874. DOI: 10.1021/ic800879c.

(208) Paradis, N.; Chastanet, G.; Palamarciuc, T.; Rosa, P.; Varret, F.; Boukheddaden, K.; Létard, J.-F. Detailed Investigation of the Interplay Between the Thermal Decay of the Low Temperature Metastable HS State and the Thermal Hysteresis of Spin-Crossover Solids. *J. Phys. Chem. C* **2015**, *119* (34), 20039–20050. DOI: 10.1021/acs.jpcc.5b03680.

(209) Hauser, A.; Guetlich, P.; Spiering, H. High-spin .fwdarw. low-spin relaxation kinetics and cooperative effects in the hexakis(1-propyltetrazole)iron bis(tetrafluoroborate) and [Zn1-xFex(ptz)6](BF4)2(ptz = 1-propyltetrazole) spin-crossover systems. *Inorg. Chem.* **1986**, *25* (23), 4245–4248. DOI: 10.1021/ic00243a036.

(210) Hauser, A.; Jeftić, J.; Romstedt, H.; Hinek, R.; Spiering, H. Cooperative phenomena and light-induced bistability in iron(II) spin-crossover compounds. *Coordination Chemistry Reviews* **1999**, *190-192*, 471–491. DOI: 10.1016/S0010-8545(99)00111-3.

(211) Verat, A. Y.; Ould-Moussa, N.; Jeanneau, E.; Le Guennic, B.; Bousseksou, A.; Borshch, S. A.; Matouzenko, G. S. Ligand strain and the nature of spin crossover in binuclear complexes: two-step spin crossover in a 4,4'-bipyridine-bridged iron(II) complex {Fe(dpia)(NCS)(2)}(2)(4,4'-bpy) (dpia = di(2-picolyl)amine; 4,4'-bpy = 4,4'-bipyridine). *Chem. Eur. J.* **2009**, *15* (39), 10070–10082. DOI: 10.1002/chem.200900921.

(212) Amoore, J. J. M.; Kepert, C. J.; Cashion, J. D.; Moubaraki, B.; Neville, S. M.; Murray, K. S. Structural and magnetic resolution of a two-step full spin-crossover transition in a dinuclear iron(II) pyridyl-bridged compound. *Chem. Eur. J.* **2006**, *12* (32), 8220–8227. DOI: 10.1002/chem.200601069.

(213) Gütlich, Philipp, Bill, Eckhard, Trautwein, Alfred. *Mossbauer spectroscopy and transition metal chemistry*:*Fundamentals and Applications*.

(214) Köhler, C.; Rentschler, E. The First 1,3,4-Oxadiazole Based Dinuclear Iron(II) Complexes Showing Spin Crossover Behavior with Hysteresis. *Eur. J. Inorg. Chem.* **2016**, *2016* (13-14), 1955–1960. DOI: 10.1002/ejic.201501278.

(215) Matouzenko, G. S.; Jeanneau, E.; Verat, A. Y.; Bousseksou, A. Spin crossover and polymorphism in a family of 1,2-bis(4-pyridyl)ethene-bridged binuclear iron(II) complexes. A key role of structural distortions. *Dalton transactions (Cambridge, England : 2003)* **2011**, *40* (37), 9608–9618. DOI: 10.1039/c1dt10312a. Published Online: Aug. 22, 2011.

(216) Real, J. A.; Castro, I.; Bousseksou, A.; Verdaguer, M.; Burriel, R.; Castro, M.; Linares, J.; Varret, F. Spin Crossover in the 2,2'-Bipyrimidine- (bpym-) Bridged Iron(II) Complexes [Fe(L)(NCX) 2] 2 (bpym) (L = 2, 2'-Bithiazoline (bt) and bpym; X = S, Se). X-ray Absorption Spectroscopy, Magnetic Susceptibility, Calorimetric, and Mössbauer Spectroscopy Studies. *Inorg. Chem.* **1997**, *36* (3), 455–464. DOI: 10.1021/ic960509o.

(217) Syassen, K. Ruby under pressure. *High Pressure Research* **2008**, *28* (2), 75–126. DOI: 10.1080/08957950802235640.

(218) McMahon, M. I. High-pressure crystallography. *Topics in current chemistry* **2012**, *315*, 69–109. DOI: 10.1007/128_2011_132.

(219) Mathilde Holm Nygaard. High-pressure Crystallography and Spin Crossover in Molecular Magnets. Master's thesis, Aarhus University, Aarhus, Denmark, 2021.

(220) Macrae, C. F.; Sovago, I.; Cottrell, S. J.; Galek, P. T. A.; McCabe, P.; Pidcock, E.; Platings, M.; Shields, G. P.; Stevens, J. S.; Towler, M.; Wood, P. A. Mercury 4.0: from visualization to analysis, design and prediction. *J Appl Crystallogr* **2020**, *53* (Pt 1), 226–235. DOI: 10.1107/S1600576719014092. Published Online: Feb. 1, 2020.

(221) Kitchen, J. A.; Brooker, S. Spin crossover in iron(II) complexes of 3,5-di(2-pyridyl)-1,2,4-triazoles and 3,5-di(2-pyridyl)-1,2,4-triazolates. *Coordination Chemistry Reviews* **2008**, *252* (18-20), 2072–2092. DOI: 10.1016/j.ccr.2007.11.010.

(222) Bousseksou, A.; Nasser, J.; Linares, J.; Boukheddaden, K.; Varret, F. Ising-like model for the two-step spin-crossover. *J. Phys. I France* **1992**, *2* (7), 1381–1403. DOI: 10.1051/jp1:1992217.

(223) Boinnard, D.; Bousseksou, A.; Dworkin, A.; Savariault, J. M.; Varret, F.; Tuchagues, J. P. Two-step spin conversion of [FeII(5-NO2-sal-N(1,4,7,10))]: 292, 153, and 103 K x-ray crystal and molecular structure, infrared, magnetic, Moessbauer, calorimetric, and theoretical studies. *Inorg. Chem.* **1994**, *33* (2), 271–281. DOI: 10.1021/ic00080a015.

(224) Klingele, M. H.; Moubaraki, B.; Cashion, J. D.; Murray, K. S.; Brooker, S. The first X-ray crystal structure determination of a dinuclear complex trapped in the low spin-high spin state: Fe(II)2(PMAT)2(BF4)4.DMF. *Chemical communications (Cambridge, England)* **2005** (8), 987–989. DOI: 10.1039/b415891a. Published Online: Jan. 4, 2005.

(225) Matouzenko, G. S.; Luneau, D.; Molnár, G.; Ould-Moussa, N.; Zein, S.; Borshch, S. A.; Bousseksou, A.; Averseng, F. A Two-Step Spin Transition and Order–Disorder Phenomena in the Mononuclear Compound [Fe(Hpy-DAPP)](BF4)2. *Eur. J. Inorg. Chem.* **2006**, *2006* (13), 2671–2682. DOI: 10.1002/ejic.200600068.

(226) Bartual-Murgui, C.; Codina, C.; Roubeau, O.; Aromí, G. A Sequential Method to Prepare Polymorphs and Solvatomorphs of Fe(1,3-bpp)2 (ClO4)2 ·nH2 O (n=0, 1, 2) with Varying Spin-Crossover Behaviour. *Chem. Eur. J.* **2016**, *22* (36), 12767–12776. DOI: 10.1002/chem.201601843. Published Online: Aug. 2, 2016.

(227) Zhang, W.; Zhao, F.; Liu, T.; Yuan, M.; Wang, Z.-M.; Gao, S. Spin crossover in a series of iron(II) complexes of 2-(2-Alkyl-2H-tetrazol-5-yl)-1,10-phenanthroline: effects of alkyl side chain, solvent, and anion. *Inorg. Chem.* **2007**, *46* (7), 2541–2555. DOI: 10.1021/ic062062h. Published Online: Mar. 1, 2007.

(228) Hagiwara, H.; Masuda, T.; Ohno, T.; Suzuki, M.; Udagawa, T.; Murai, K. Neutral Molecular Iron(II) Complexes Showing Tunable Bistability at Above, Below, and Just Room Temperature by a Crystal Engineering Approach: Ligand Mobility into a Three-Dimensional Flexible Supramolecular Network. *Crystal Growth & Design* **2017**, *17* (11), 6006–6019. DOI: 10.1021/acs.cgd.7b01141.

(229) Moliner, N.; Muñoz, M.; Létard, S.; Létard, J.-F.; Solans, X.; Burriel, R.; Castro, M.; Kahn, O.; Real, J. A. Spin-crossover in the [Fe(abpt)2(NCX)2] (X=S, Se) system:Structural, magnetic, calorimetric and photomagnetic studies. *Inorganica Chimica Acta* **1999**, *291* (1-2), 279–288. DOI: 10.1016/S0020-1693(99)00128-0.

(230) Harding, D. J.; Phonsri, W.; Harding, P.; Gass, I. A.; Murray, K. S.; Moubaraki, B.; Cashion, J. D.; Liu, L.; Telfer, S. G. Abrupt spin crossover in an iron(III) quinolylsalicylaldimine complex: structural

insights and solvent effects. *Chemical communications (Cambridge, England)* **2013**, *49* (56), 6340–6342. DOI: 10.1039/c3cc42125b.

(231) Berdiell, I. C.; Kulmaczewski, R.; Shahid, N.; Cespedes, O.; Halcrow, M. A. The number and shape of lattice solvent molecules controls spin-crossover in an isomorphous series of crystalline solvate salts. *Chemical communications (Cambridge, England)* **2021**, *57* (53), 6566–6569. DOI: 10.1039/d1cc02624k.

(232) Zhou, J.; Zhu, B.-W.; Luan, J.; Liu, Z.; Fang, J.-K.; Bao, X.; Peng, G.; Tucek, J.; Bao, S.-S.; Zheng, L.-M. In air a spin crossover active iron(II) complex of amine/NCBH3(-) ligands is converted to a low spin complex of imine/CN(-) ligands. *Dalton transactions (Cambridge, England : 2003)* **2015**, *44* (47), 20551–20561. DOI: 10.1039/C5DT03464G. Published Online: Nov. 9, 2015.

(233) Huang, L.; Nakajo, K.; Ozawa, S.; Matsuda, H. Decomposition of dichloromethane in a wire-in-tube pulsed corona reactor. *Environ. Sci. Technol.* **2001**, *35* (6), 1276–1281. DOI: 10.1021/es0011414.

(234) Halcrow, M. A. Spin-crossover Compounds with Wide Thermal Hysteresis. *Chem. Lett.* **2014**, *43* (8), 1178–1188. DOI: 10.1246/cl.140464.

(235) Weber, B.; Bauer, W.; Obel, J. An iron(II) spin-crossover complex with a 70 K wide thermal hysteresis loop. *Angew. Chem. Int. Ed. Engl.* **2008**, *47* (52), 10098–10101. DOI: 10.1002/anie.200802806.

(236) Lochenie, C.; Bauer, W.; Railliet, A. P.; Schlamp, S.; Garcia, Y.; Weber, B. Large thermal hysteresis for iron(II) spin crossover complexes with N-(pyrid-4-yl)isonicotinamide. *Inorg. Chem.* **2014**, *53* (21), 11563–11572. DOI: 10.1021/ic501624b. Published Online: Oct. 14, 2014.

(237) Létard, J.-F.; Guionneau, P.; Codjovi, E.; Lavastre, O.; Bravic, G.; Chasseau, D.; Kahn, O. Wide Thermal Hysteresis for the Mononuclear Spin-Crossover Compound cis -Bis(thiocyanato)bis[N -(2'-pyridylmethylene)-4-(phenylethynyl)anilino]iron(II). *Journal of the American Chemical Society* **1997**, *119* (44), 10861–10862. DOI: 10.1021/ja972441x.

(238) Pillet, S. Spin-crossover materials: Getting the most from x-ray crystallography. *Journal of Applied Physics* **2021**, *129* (18), 181101. DOI: 10.1063/5.0047681.

(239) Forestier, T.; Mornet, S.; Daro, N.; Nishihara, T.; Mouri, S.; Tanaka, K.; Fouché, O.; Freysz, E.; Létard, J.-F. Nanoparticles of iron(II) spin-crossover. *Chemical communications (Cambridge, England)* **2008** (36), 4327–4329. DOI: 10.1039/b806347h. Published Online: Jul. 16, 2008.

(240) Bartual-Murgui, C.; Natividad, E.; Roubeau, O. Critical assessment of the nature and properties of Fe(ii) triazole-based spin-crossover nanoparticles. *J. Mater. Chem. C* **2015**, *3* (30), 7916–7924. DOI: 10.1039/c5tc01174d.

(241) Valverde-Muñoz, F. J.; Kazan, R.; Boukheddaden, K.; Ohba, M.; Real, J. A.; Delgado, T. Downsizing of Nanocrystals While Retaining Bistable Spin Crossover Properties in Three-Dimensional Hofmann-Type {Fe(pz)Pt(CN)4}-Iodine Adducts. *Inorg. Chem.* **2021**, *60* (12), 8851–8860. DOI: 10.1021/acs.inorgchem.1c00765. Published Online: Jun. 3, 2021.

(242) Hünig, S. *Arbeitsmethoden in der organischen Chemie*:*(mit Einführungspraktikum)*; Lehmanns Media LOB.de, 2006.

(243) Gunnlaugsson, H. P. Spreadsheet based analysis of Mössbauer spectra. *Hyperfine Interactions* **2016**, *237* (1). DOI: 10.1007/s10751-016-1271-z.

(244) Gottlieb, H. E.; Kotlyar, V.; Nudelman, A. NMR Chemical Shifts of Common Laboratory Solvents as Trace Impurities. *J. Org. Chem.* **1997**, *62* (21), 7512–7515. DOI: 10.1021/jo971176v.

(245) Sheldrick, G. M. SHELXT - integrated space-group and crystal-structure determination. *Acta Crystallogr A Found Adv* **2015**, *71* (Pt 1), 3–8. DOI: 10.1107/S2053273314026370. Published Online: Jan. 1, 2015.

(246) Sheldrick, G. M. Crystal structure refinement with SHELXL. *Acta crystallographica. Section C, Structural chemistry* **2015**, *71* (Pt 1), 3–8. DOI: 10.1107/S2053229614024218. Published Online: Jan. 1, 2015.

(247) Dolomanov, O. V.; Bourhis, L. J.; Gildea, R. J.; Howard, J. A. K.; Puschmann, H. OLEX2 : a complete structure solution, refinement and analysis program. *J Appl Crystallogr* **2009**, *42* (2), 339–341. DOI: 10.1107/S0021889808042726.

(248) Bain, G. A.; Berry, J. F. Diamagnetic Corrections and Pascal's Constants. *J. Chem. Educ.* **2008**, *85* (4), 532. DOI: 10.1021/ed085p532.

(249) Su, D.; Liu, Y.; Li, S.; Ding, S.; Jin, Y.; Wang, Z.; Hu, X.; Zhang, L. Selective Extraction of Americium(III) over Europium(III) Ions with Pyridylpyrazole Ligands: Structure-Property Relationships. *Eur. J. Inorg. Chem.* **2017**, *2017* (3), 651–658. DOI: 10.1002/ejic.201601011.

(250) Winterstein, A.; Schön, K. IV. Mitteilung: Polycyclische aromatische Kohlenwasserstoffe. *Hoppe-Seyler´s Zeitschrift für physiologische Chemie* **1934**, *230* (1-6), 146–158. DOI: 10.1515/bchm2.1934.230.1-6.146.

(251) Berglund, M.; Dalence-Guzmán, M. F.; Skogvall, S.; Sterner, O. SAR studies of capsazepinoid bronchodilators 3: The thiourea part (coupling region) and the 2-(4-chlorophenyl)ethyl moiety (C-region). *Bioorganic & medicinal chemistry* **2008**, *16* (5), 2529–2540. DOI: 10.1016/j.bmc.2007.11.056. Published Online: Nov. 28, 2007.

(252) Narayana, B.; Vijaya Raj, K. K.; Ashalatha, B. V.; Kumari, N. S. Synthesis of some new 2-(6-methoxy-2-naphthyl)- 5-aryl-1,3,4-oxadiazoles as possible non-steroidal anti-inflammatory and analgesic agents. *Archiv der Pharmazie* **2005**, *338* (8), 373–377. DOI: 10.1002/ardp.200500974.

11. Appendix

11.1. NMR-Spectroscopy
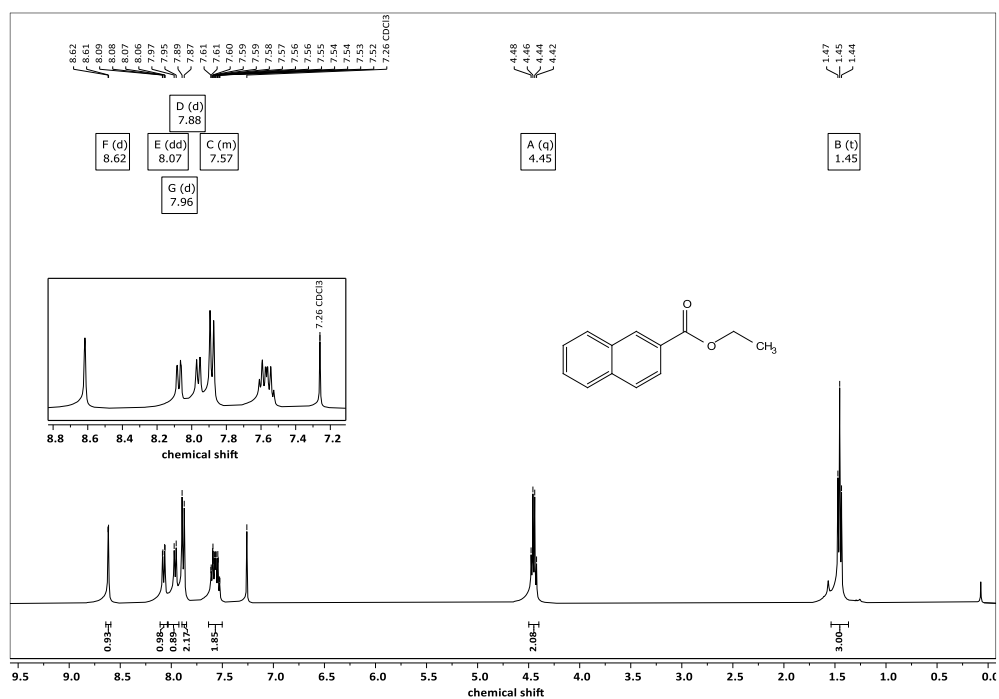
Figure 70: ^{1}H-NMR spectra of Ethyl-2-naphthoate.
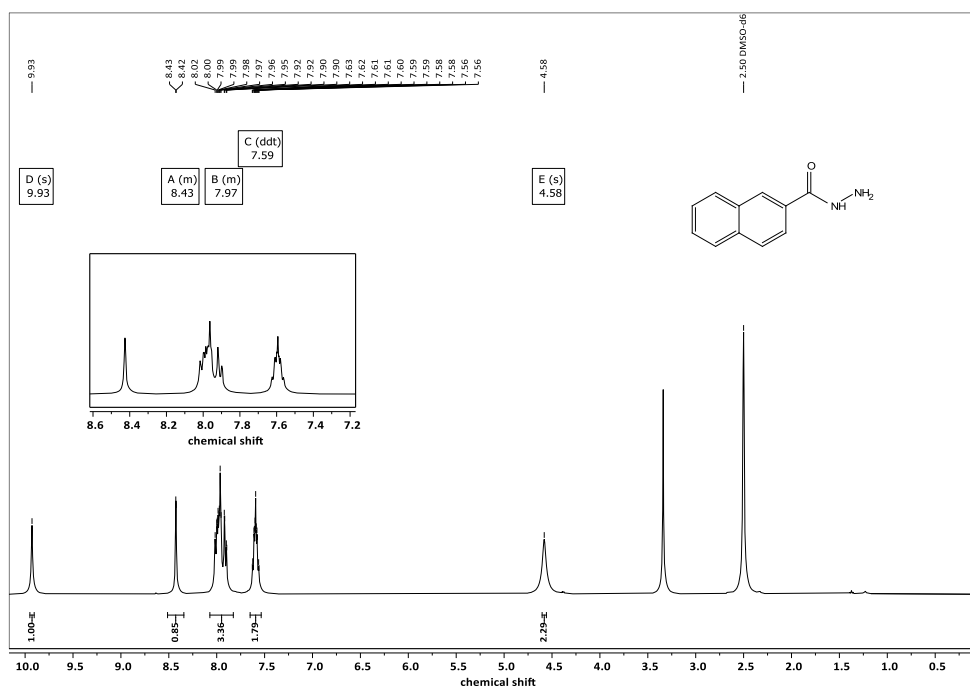
Figure 71: ^{1}H-NMR spectra of 2-Naphthohydrazide.
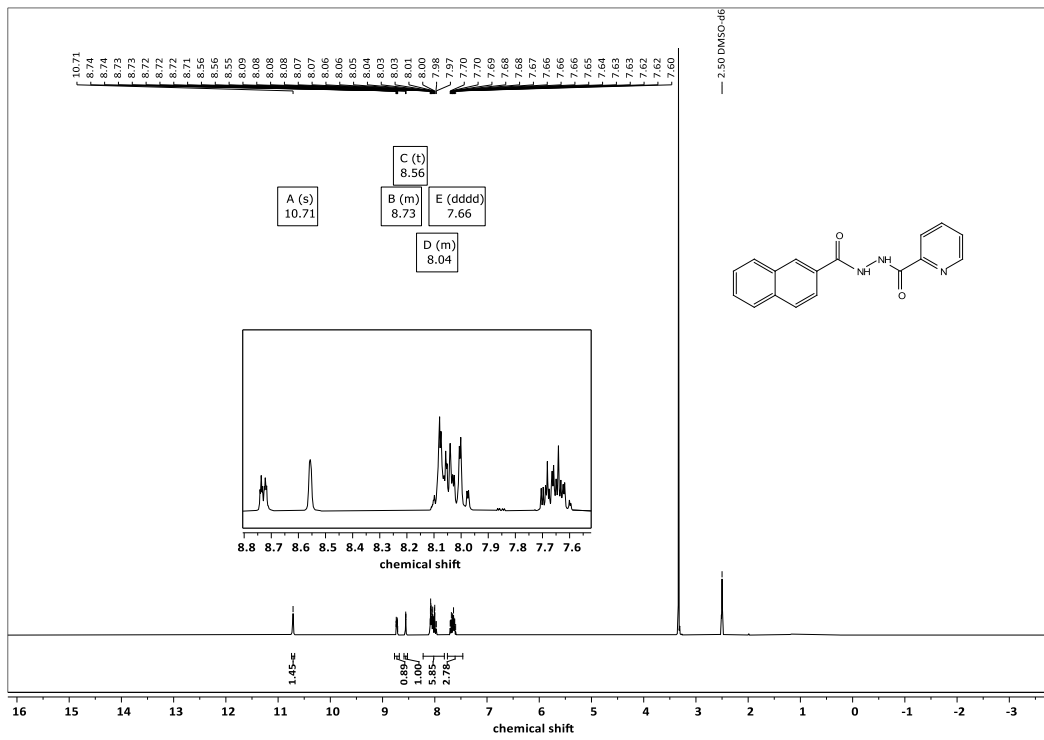
Figure 72: ¹H-NMR spectra of N'-(2-naphthoyl)-picolinohydrazid.
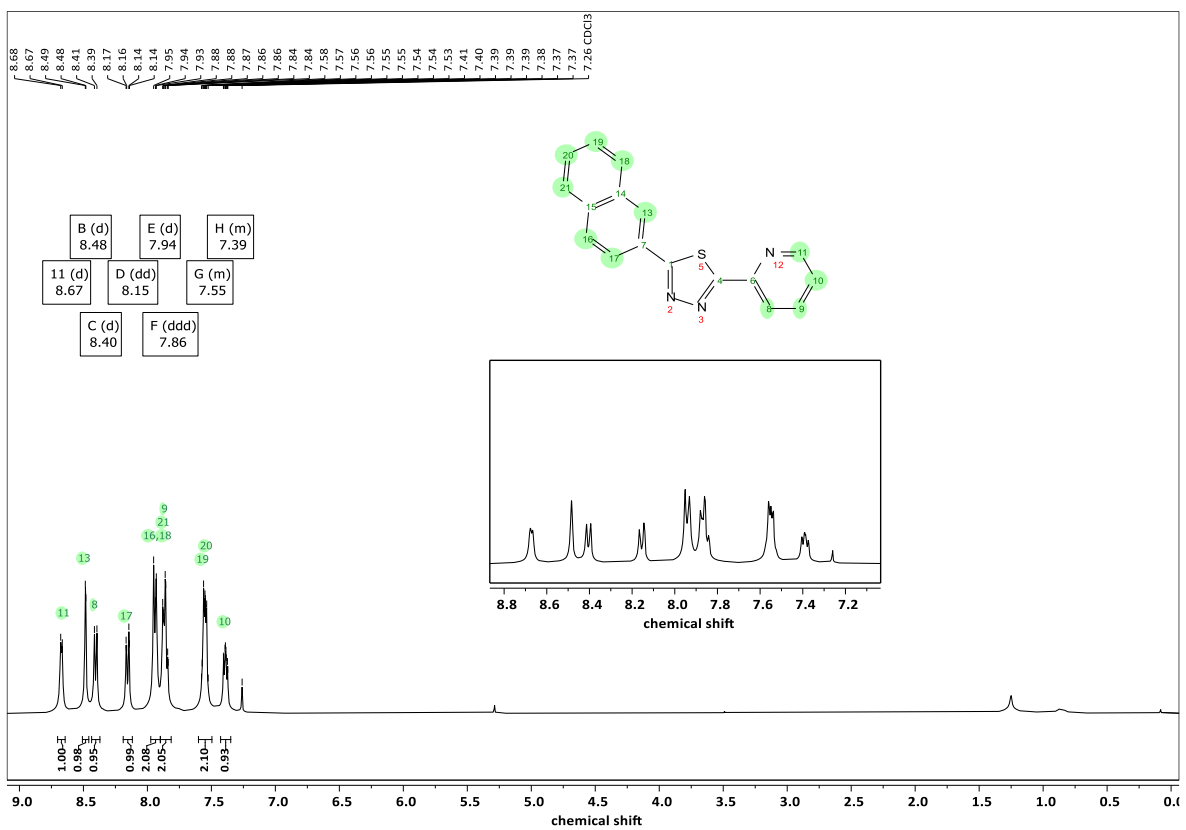
*Figure 73: ¹H-NMR spectra of 2-(naphthalen-2-yl)-5-(pyridin-2-yl)-1,3,4-thiadiazole **L¹**.*
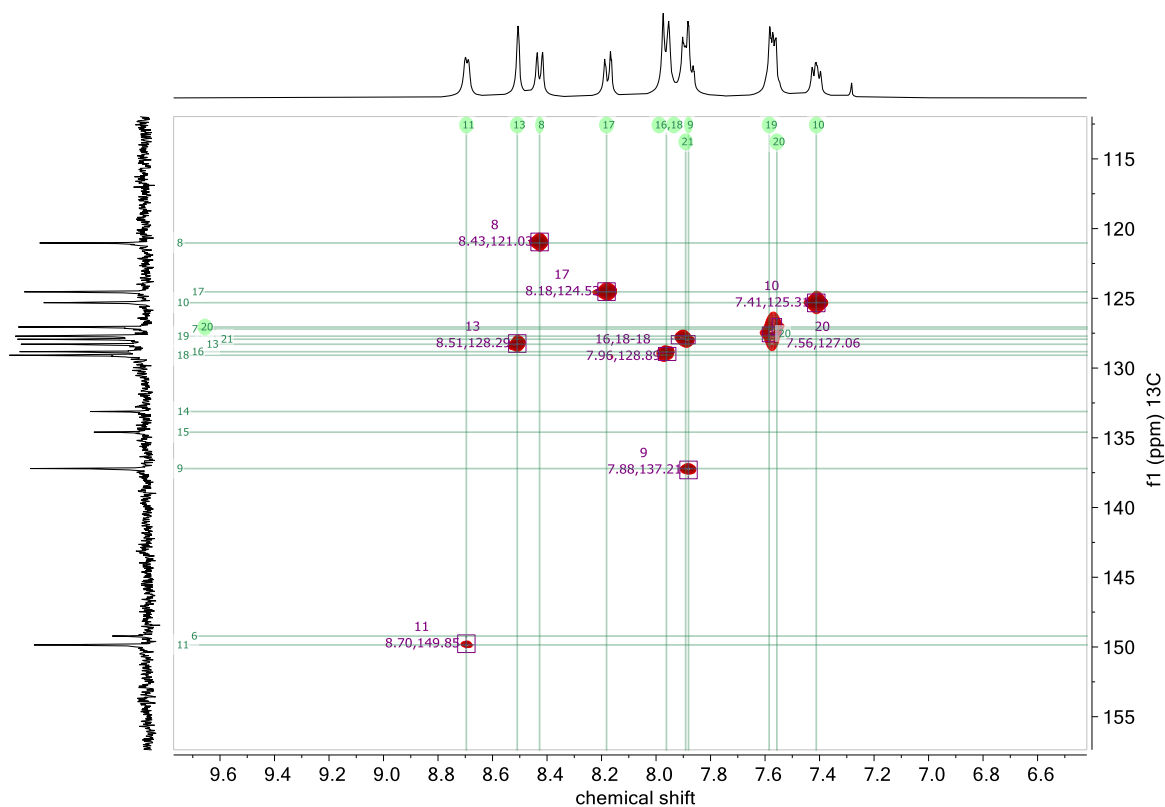
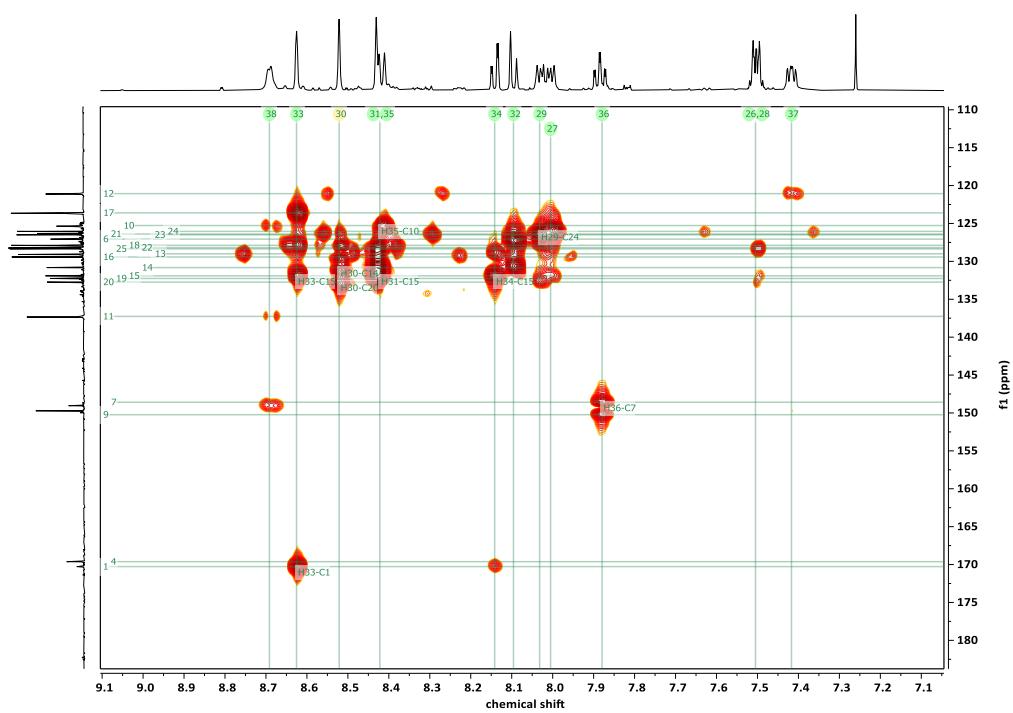*Figure 74: HSQC NMR-spectra of 2-(naphthalen-2-yl)-5-(pyridin-2-yl)-1,3,4-thiadiazole L¹.*
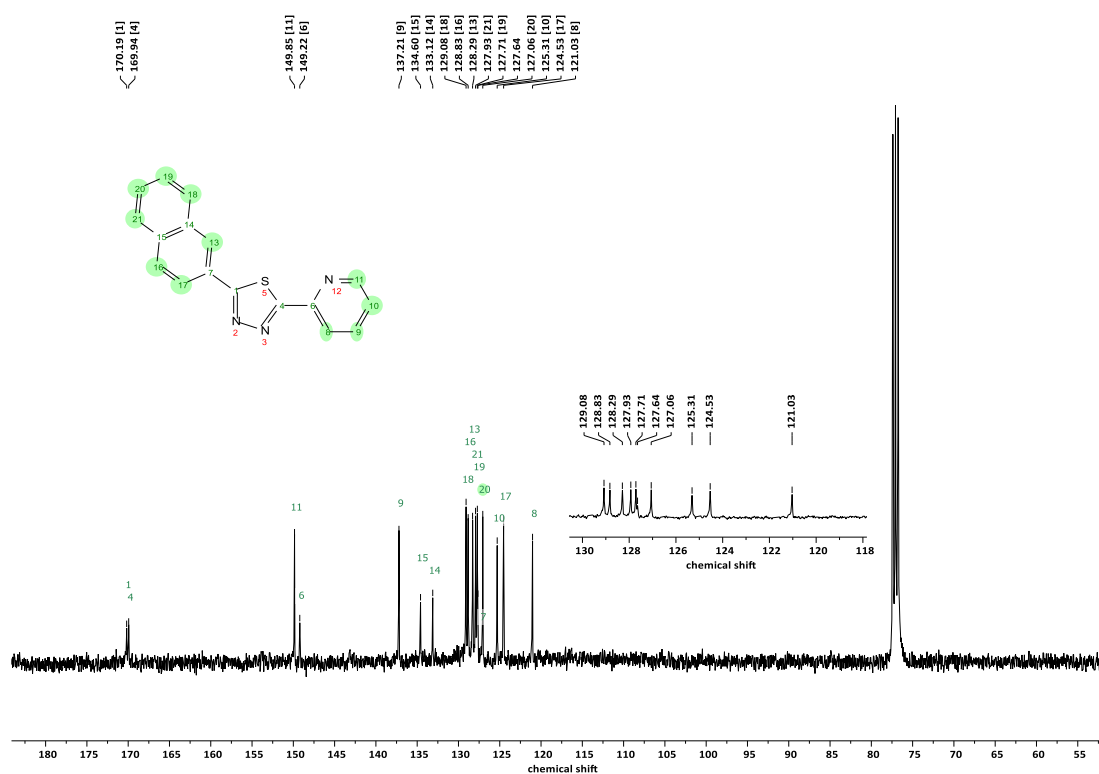
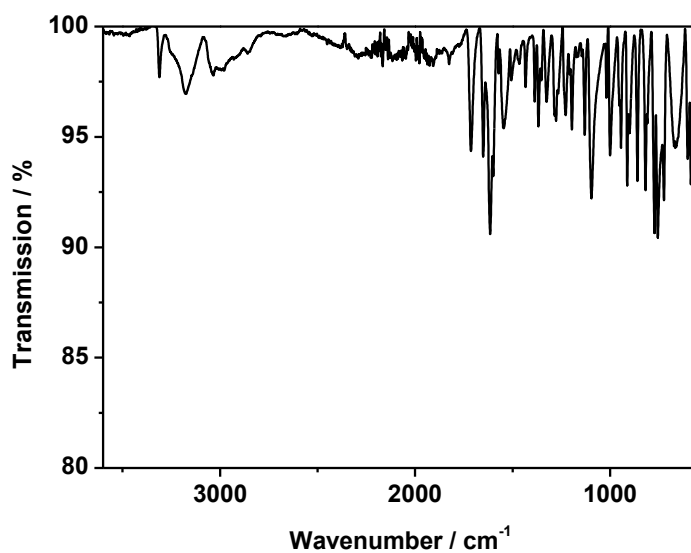*Figure 75: C¹³ NMR spectra of 2-(naphthalen-2-yl)-5-(pyridin-2-yl)-1,3,4-thiadiazole L¹.*
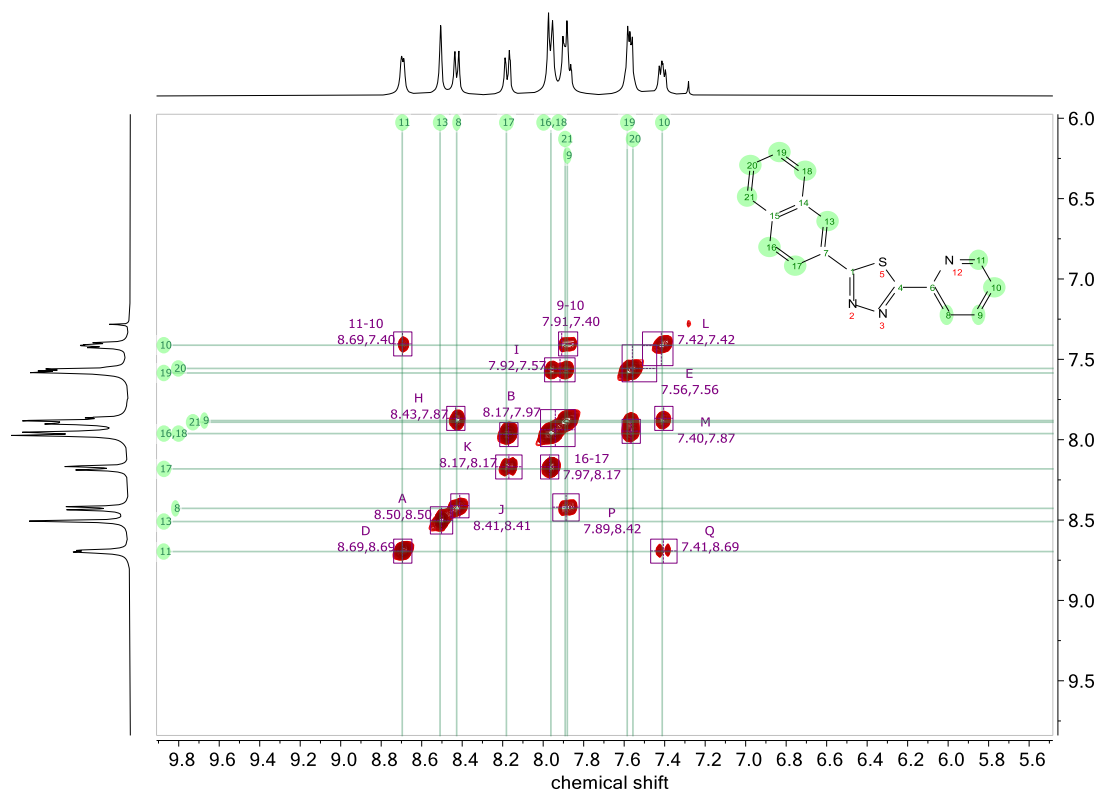
*Figure 76: COSY NMR-spectra of 2-(naphthalen-2-yl)-5-(pyridin-2-yl)-1,3,4-thiadiazole **L¹**.*
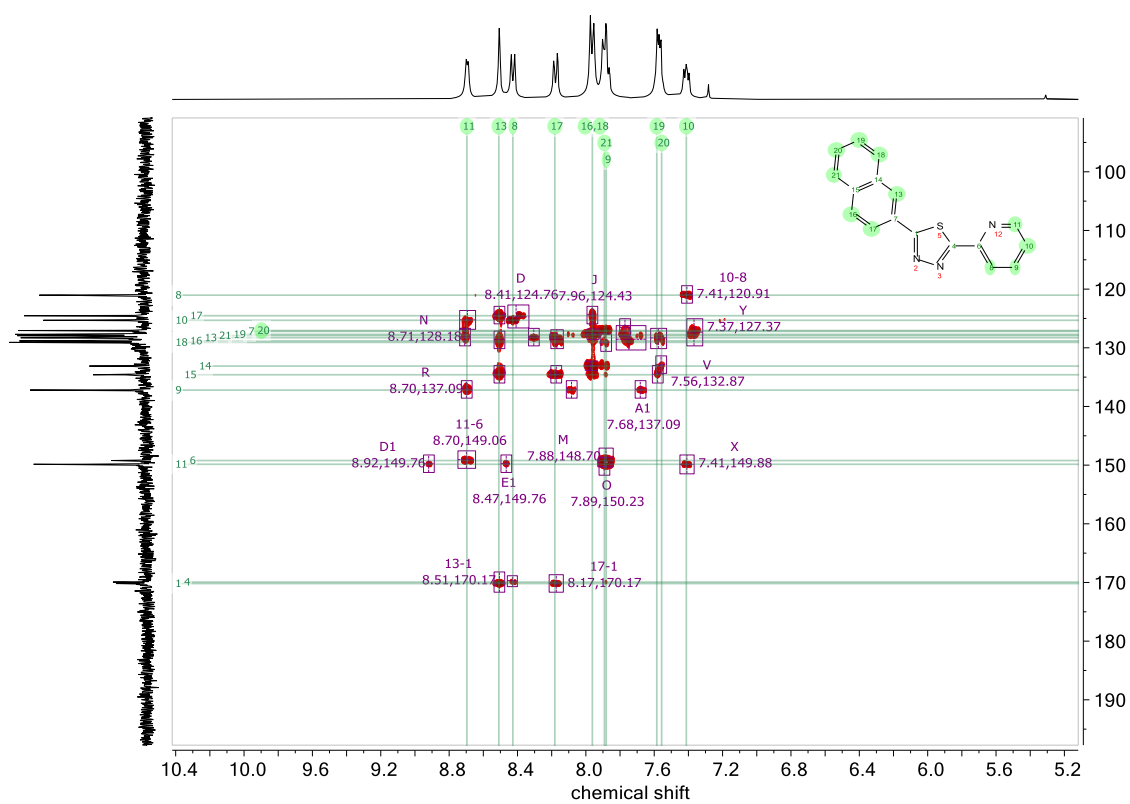
*Figure 77: HMBC NMR spectra of 2-(naphthalen-2-yl)-5-(pyridin-2-yl)-1,3,4-thiadiazole **L¹**.*
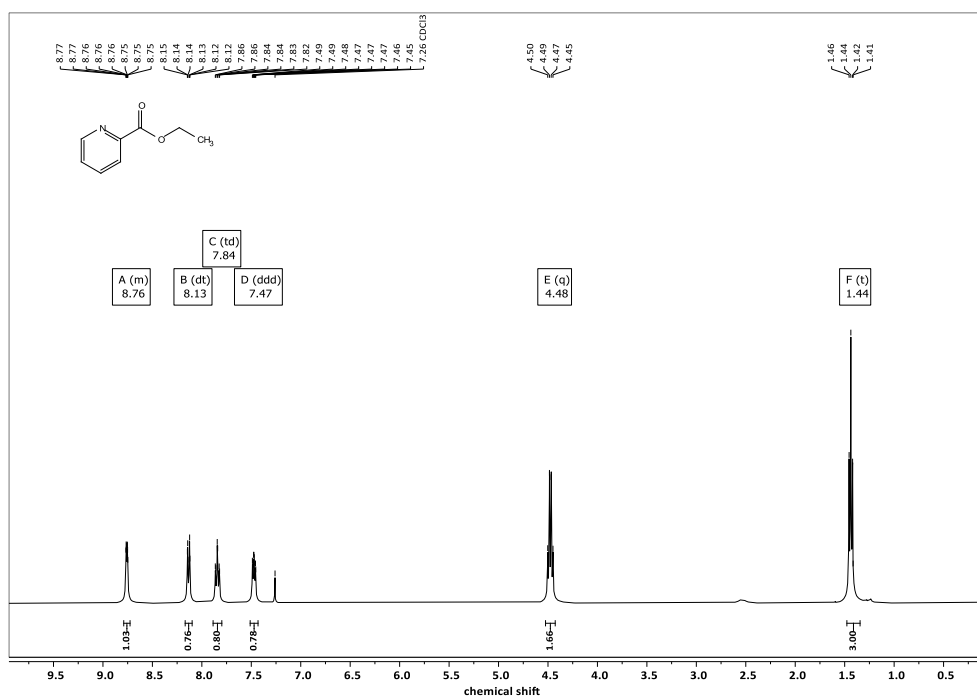
Figure 78: ^{1}H-NMR spectra of ethyl pyridine-2-carboxylate measured at 400 MHz.
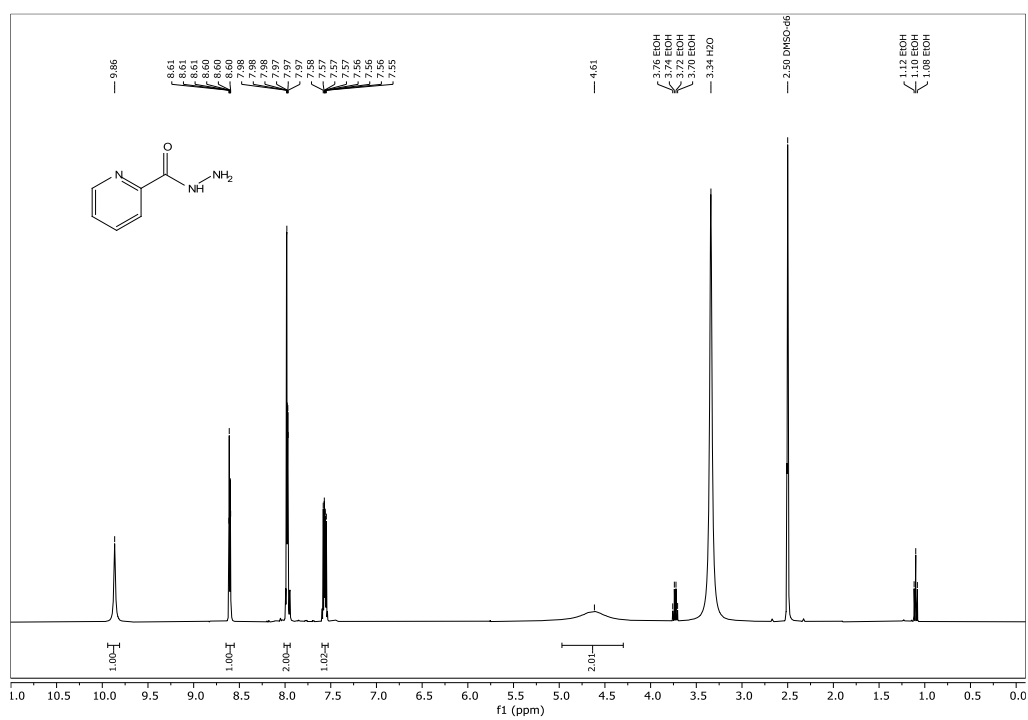
Figure 79: ^{1}H-NMR spectra of ethyl pyridine-2-carboxylic acid hydrazide measured at 400 MHz.
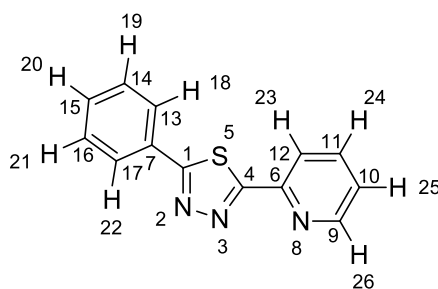
*Figure 80: representation of 2-(pyridin-2-yl)-5-phenyl-1,3,4-thiadiazole **L²** including consecutive atom numbers.*
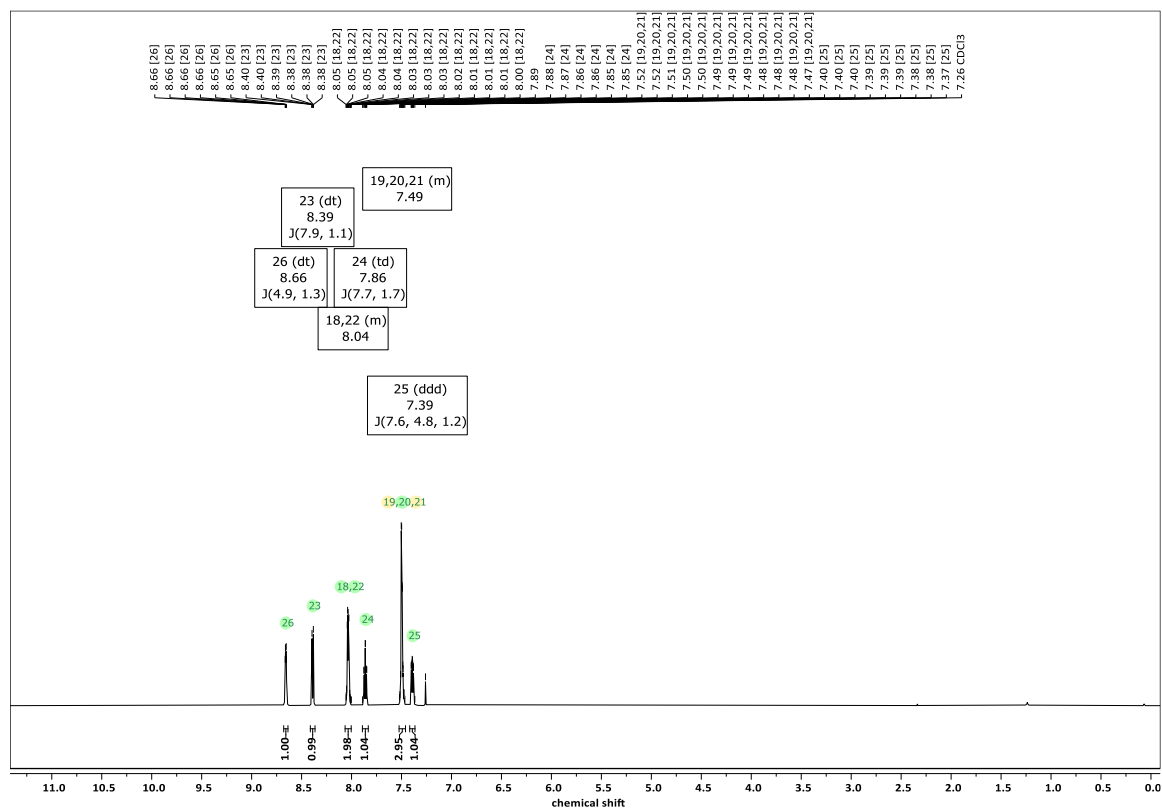
*Figure 81: ¹H-NMR spectra of 2-(pyridin-2-yl)-5-phenyl-1,3,4-thiadiazole **L²** measured at 600 MHz.*

*Figure 82: 13C- NMR spectra of 2-(pyridin-2-yl)-5-phenyl-1,3,4-thiadiazole **L²** measured at 151 MHz.*

*Figure 83: COSY spectra of 2-(pyridin-2-yl)-5-phenyl-1,3,4-thiadiazole **L²**.*

*Figure 84: HSQC spectra of 2-(pyridin-2-yl)-5-phenyl-1,3,4-thiadiazole **L²**.*

*Figure 85: HMQC spectra of 2-(pyridin-2-yl)-5-phenyl-1,3,4-thiadiazole **L²**.*
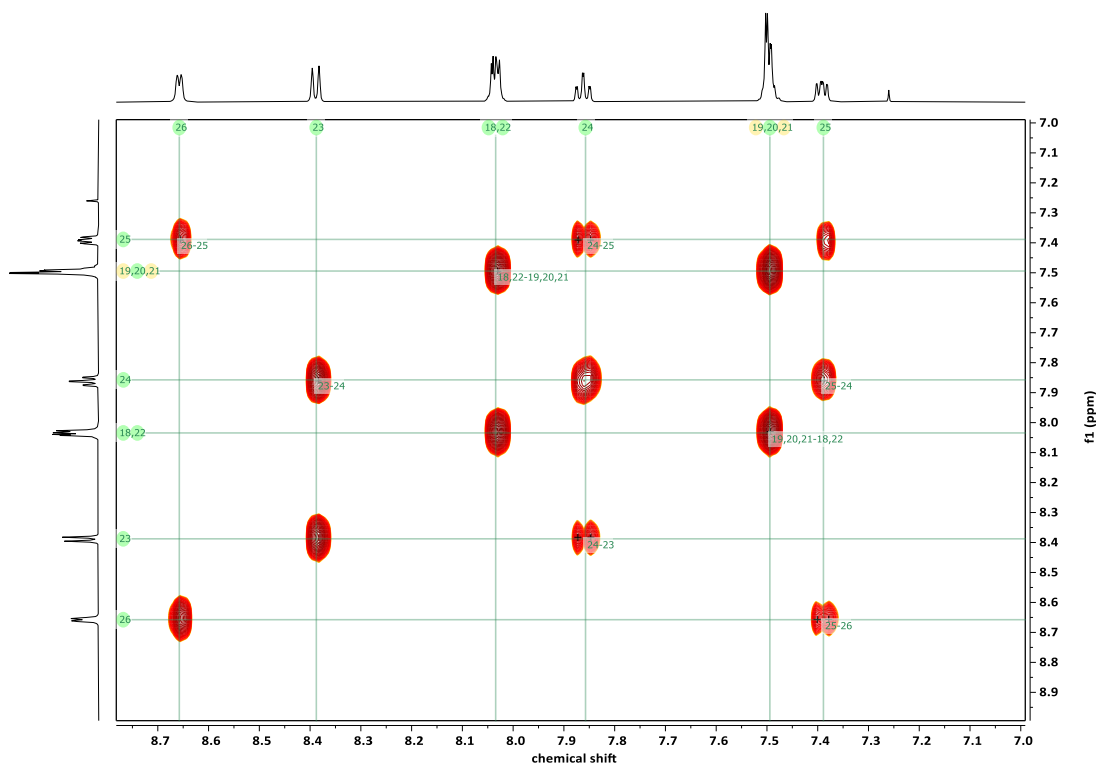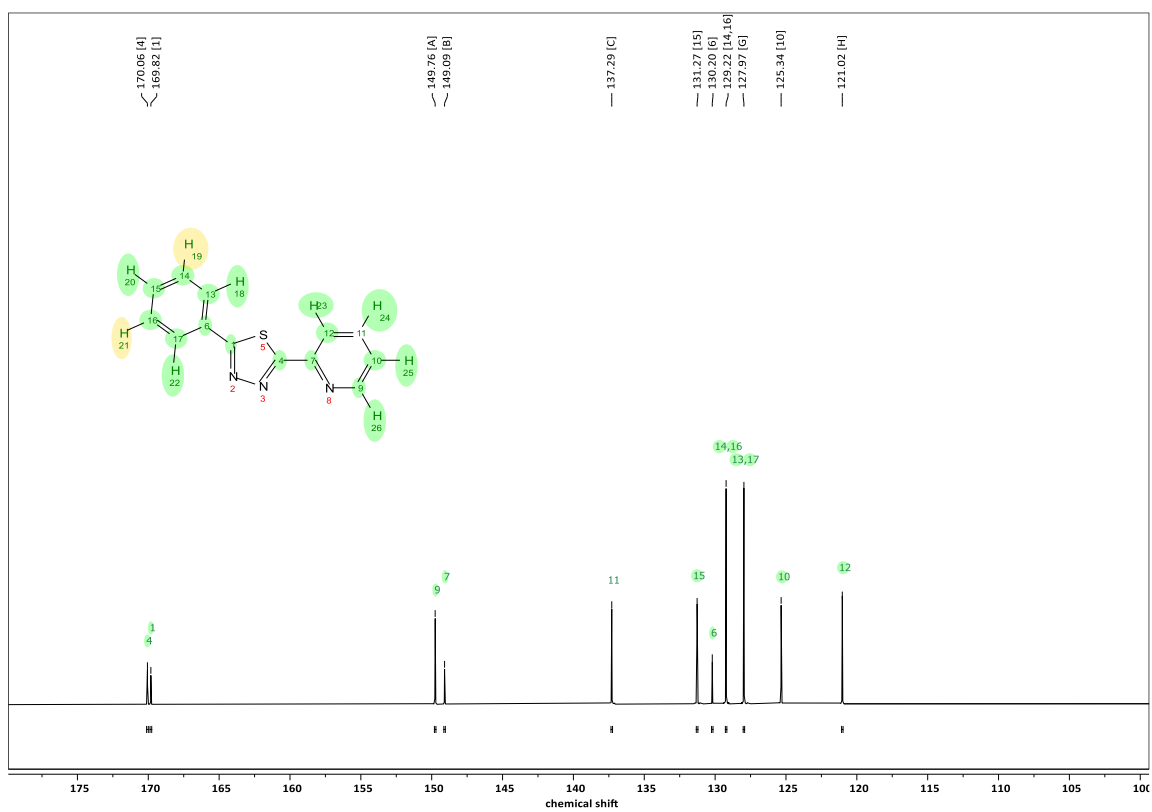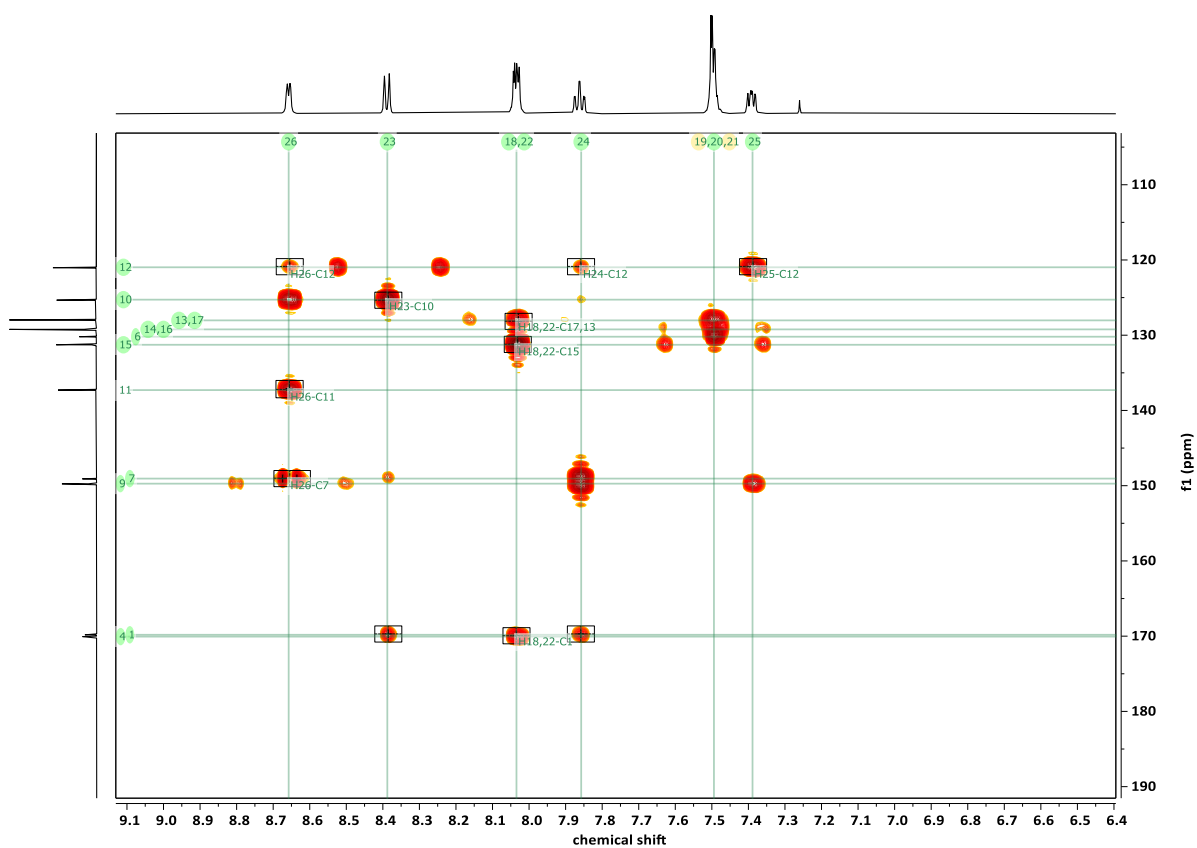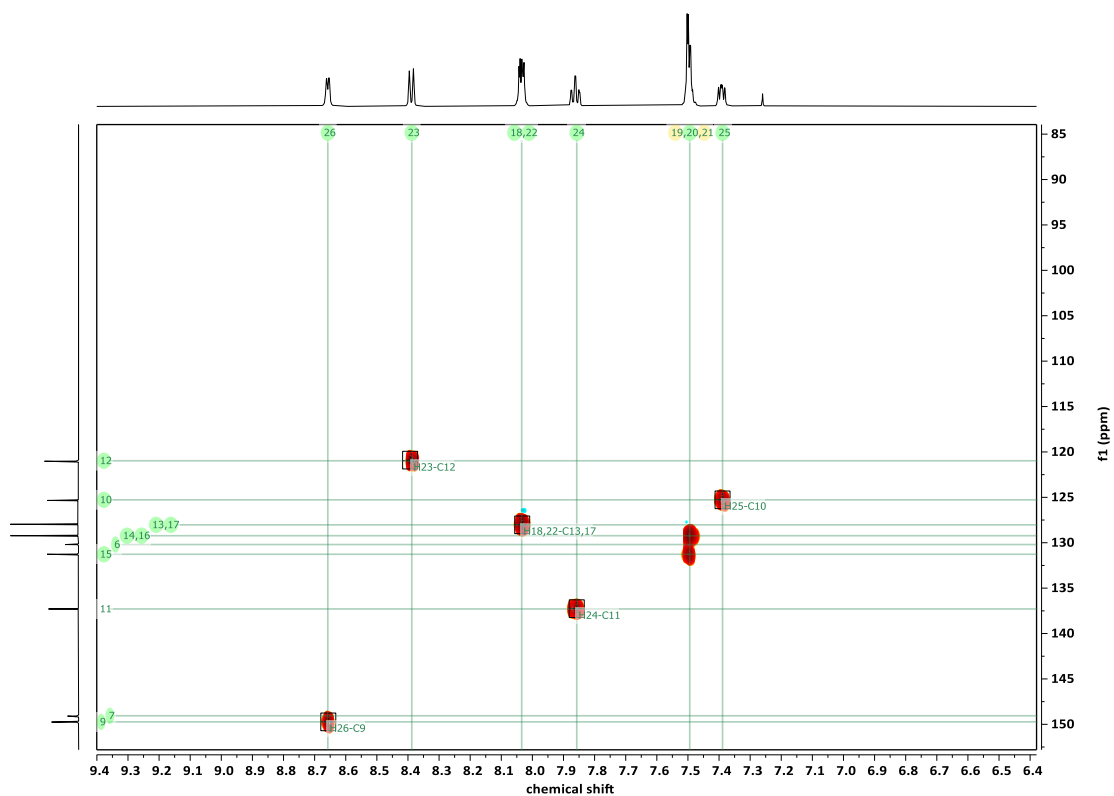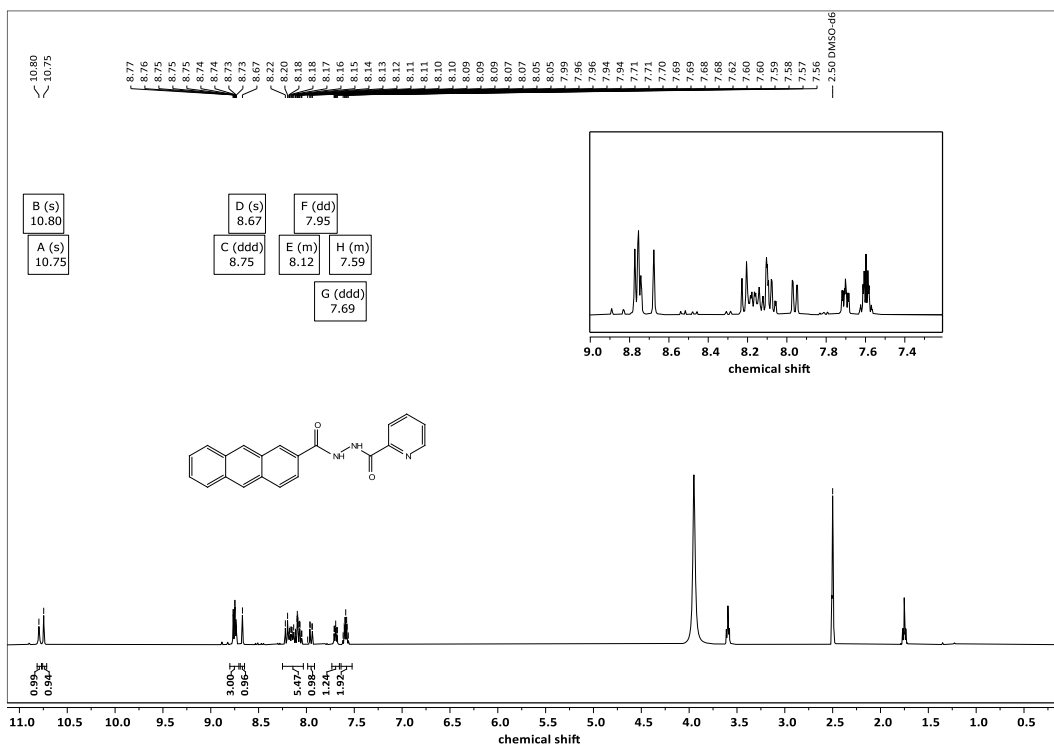
Figure 86: ¹H-NMR spectra of N'-(2-anthracenyl) pyridine-2-carboxylic acid hydrazide.
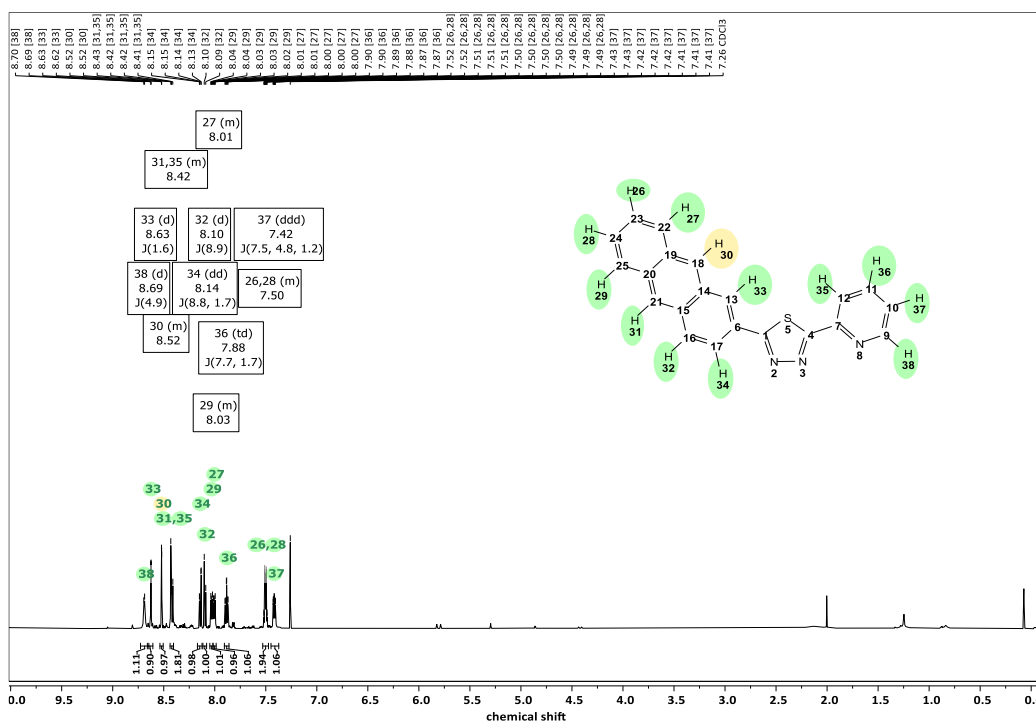
Figure 87: ¹H-NMR spectra of 2-(anthracen-2-yl)-5-(pyridin-2-yl)-1,3,4-thiadiazole (L³) measured at 600 MHz.
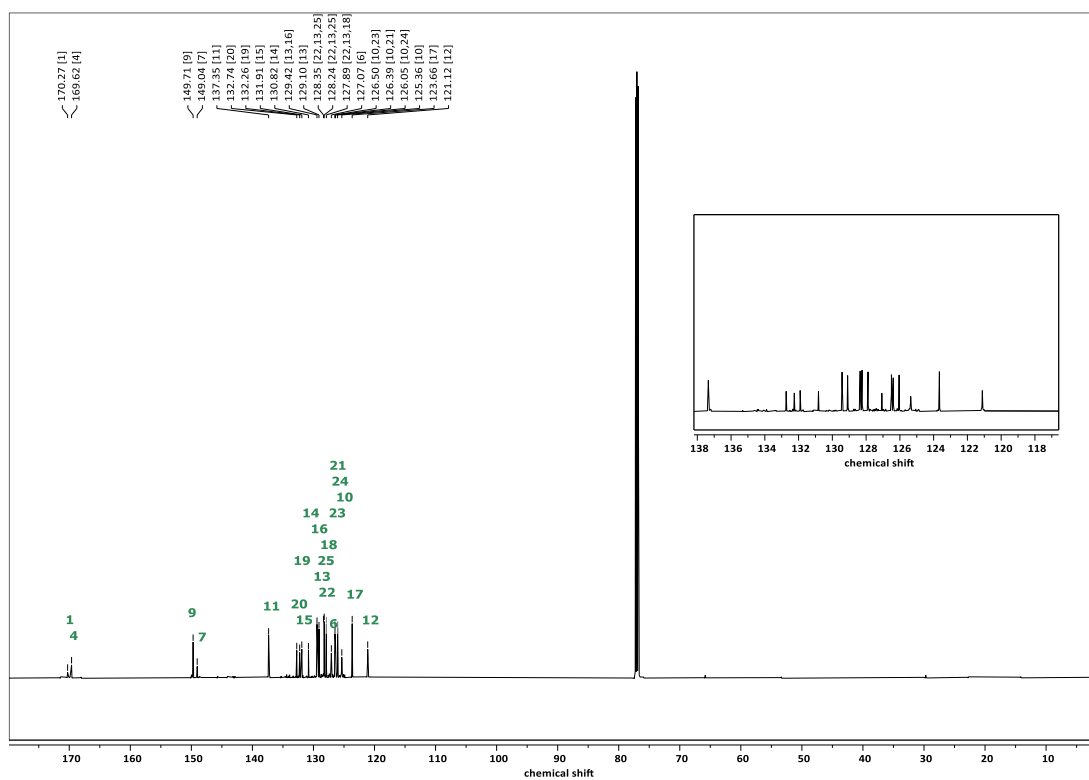
Figure 88: ^{13}H-NMR spectra of 2-(anthracen-2-yl)-5-(pyridin-2-yl)-1,3,4-thiadiazole (L^3) measured at 151 MHz.
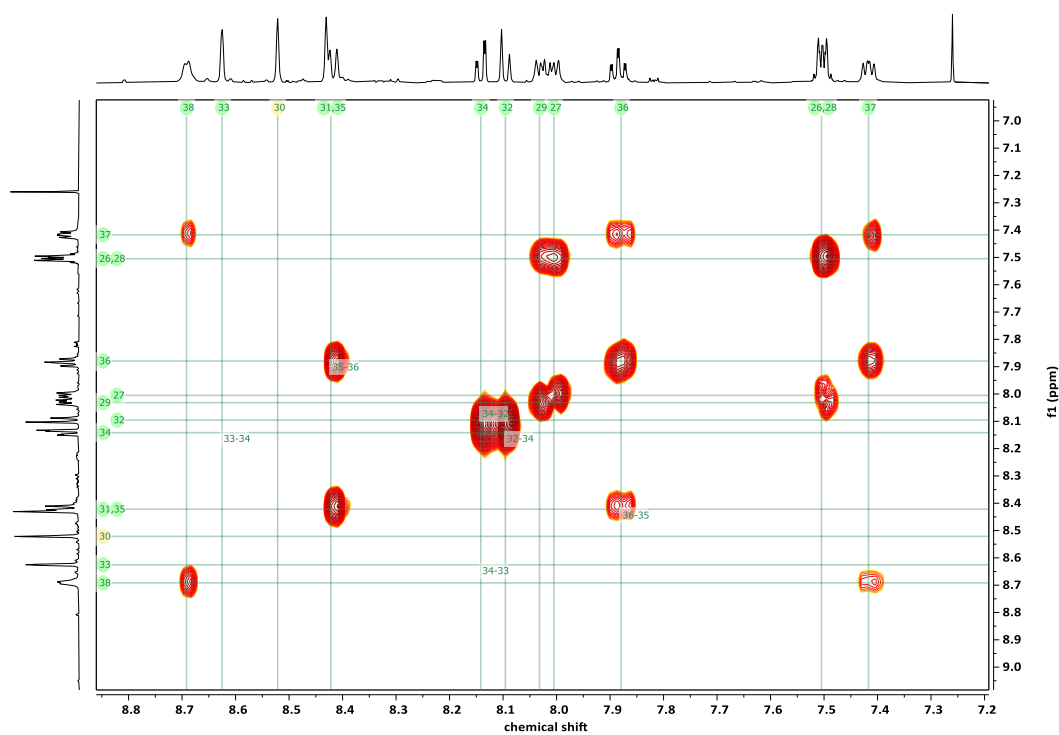
Figure 89: COSY spectra of 2-(anthracen-2-yl)-5-(pyridin-2-yl)-1,3,4-thiadiazole (L^3)
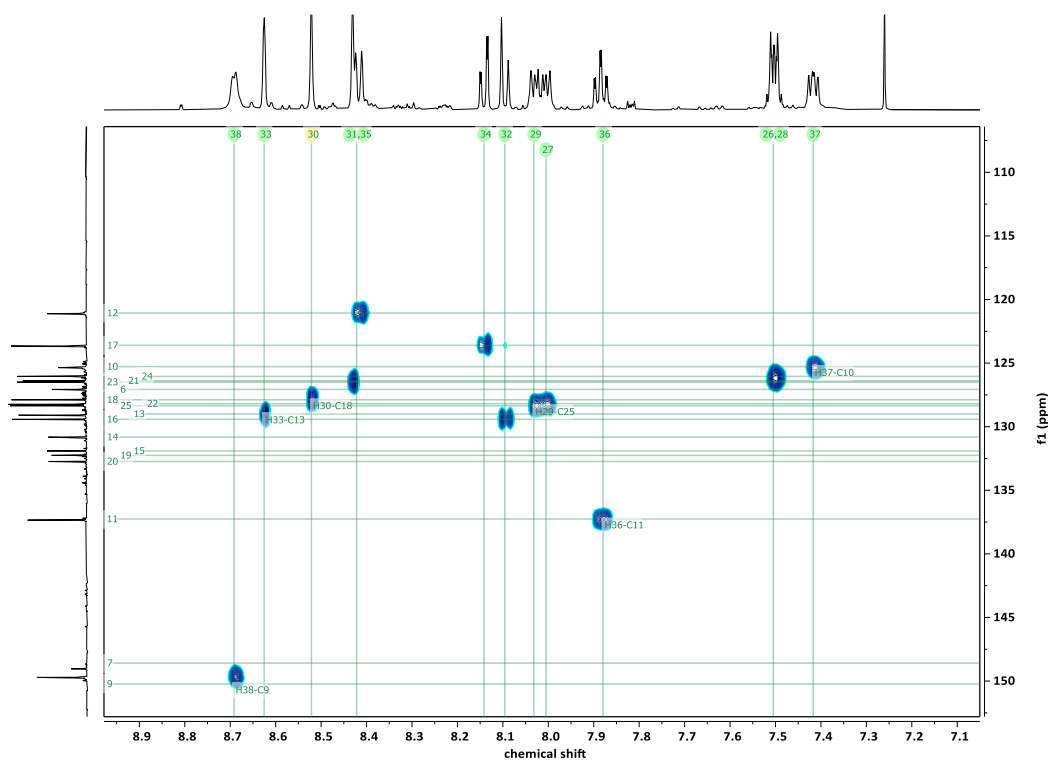
Figure 90: HSQC spectra of 2-(anthracen-2-yl)-5-(pyridin-2-yl)-1,3,4-thiadiazole (L³).

Figure 91: HMBC spectra of 2-(anthracen-2-yl)-5-(pyridin-2-yl)-1,3,4-thiadiazole (L³).
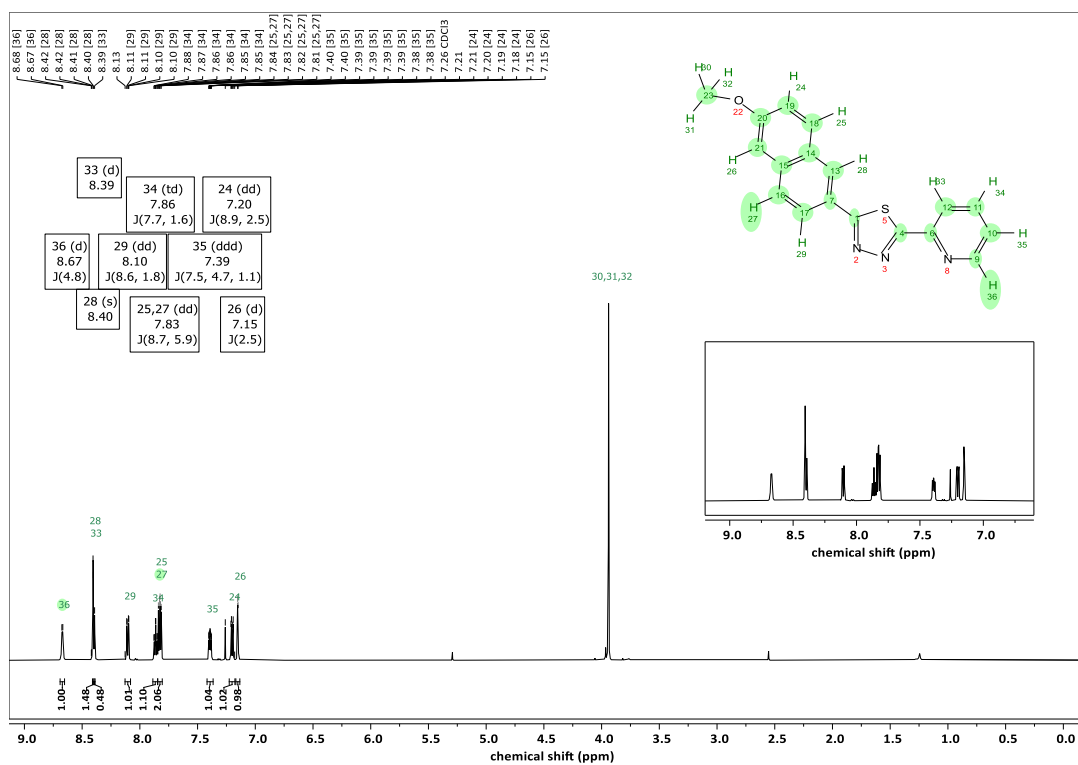
*Figure 92: ¹H-NMR spectra of 2-(6-methoxynaphthalen-2-yl)-5-(pyridin-2-yl)-1,3,4-thiadiazole **L⁴** measured at 600 MHz in CDCl₃.*
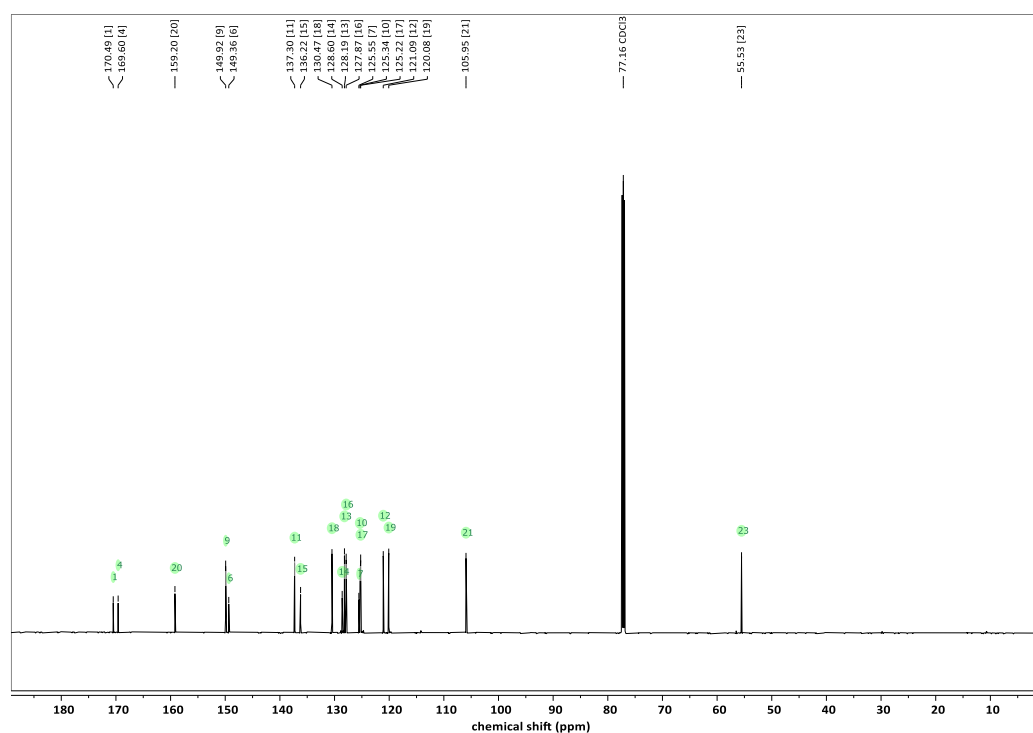
*Figure 93: ¹³C-NMR spectra of 2-(6-methoxynaphthalen-2-yl)-5-(pyridin-2-yl)-1,3,4-thiadiazole **L⁴** measured at 151 MHz in CDCl₃.*
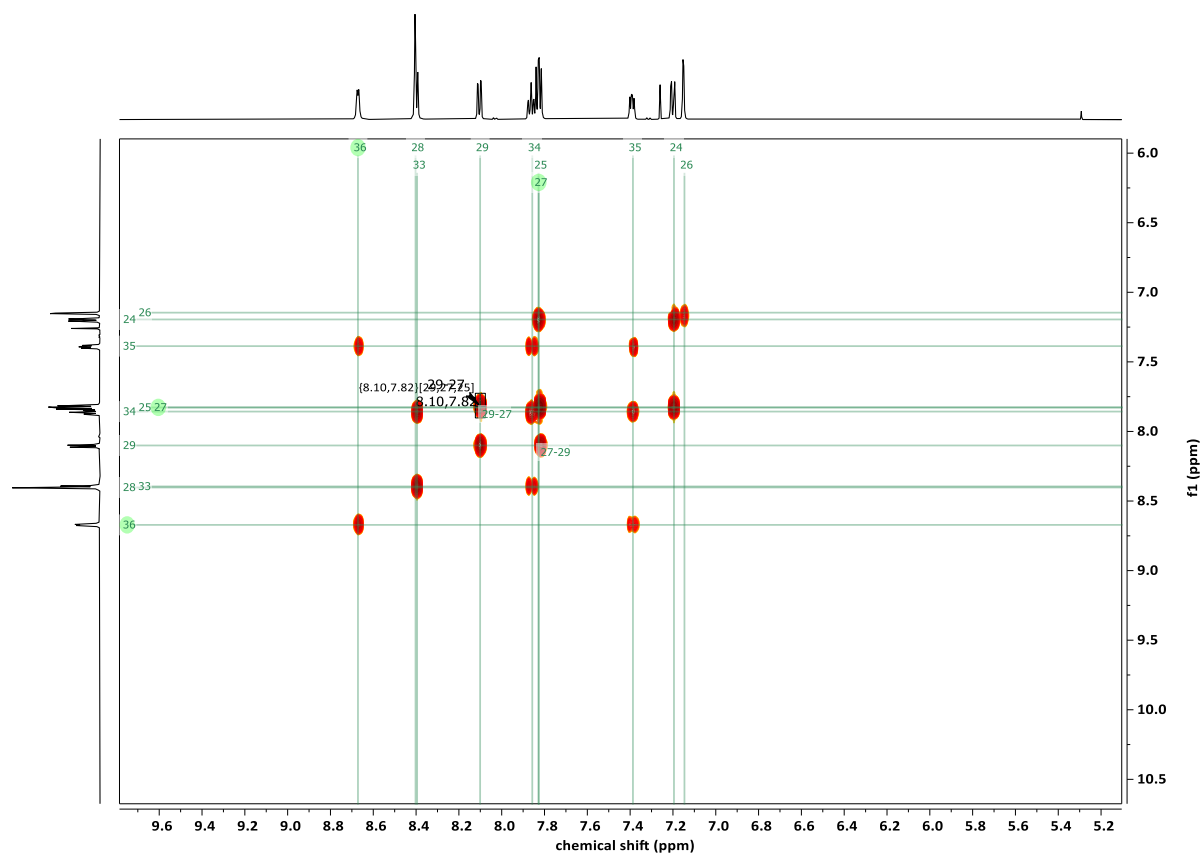
Figure 94: COSY-spectra of 2-(6-methoxynaphthalen-2-yl)-5-(pyridin-2-yl)-1,3,4-thiadiazole **L⁴** in CDCl₃.
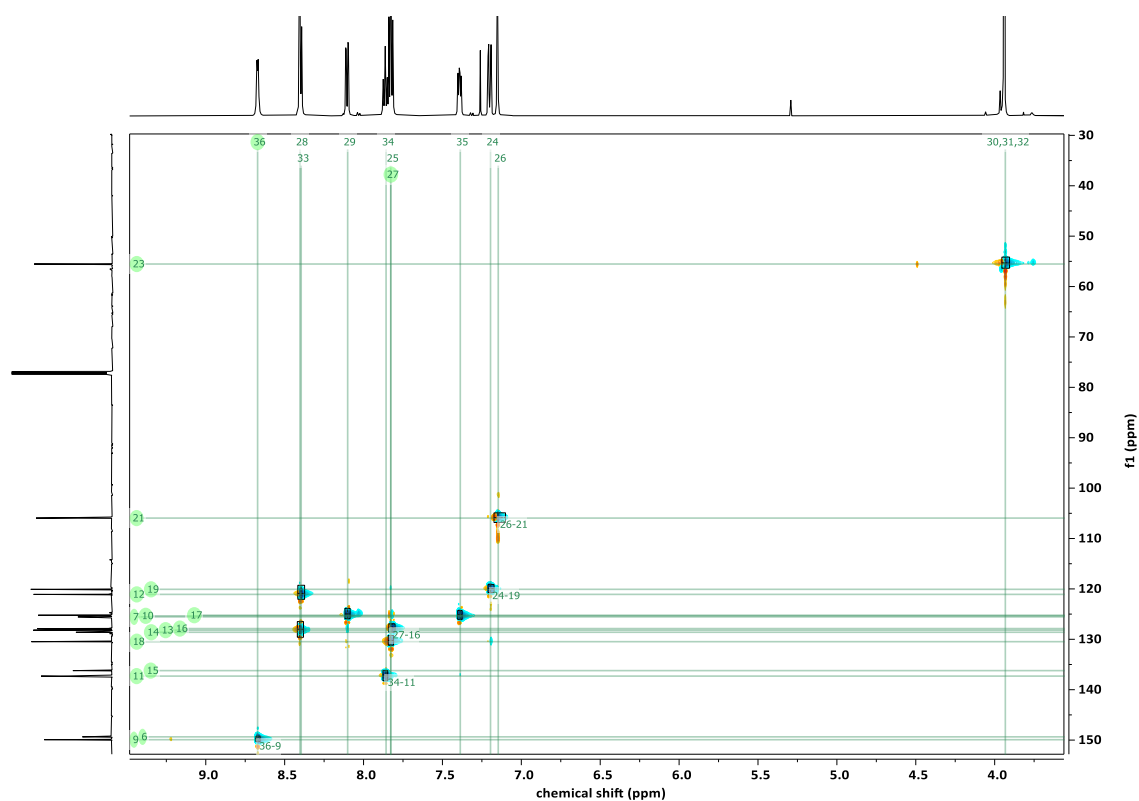
Figure 95: ¹H-¹³C-HSQC-spectra of 2-(6-methoxynaphthalen-2-yl)-5-(pyridin-2-yl)-1,3,4-thiadiazole **L⁴** in CDCl₃.
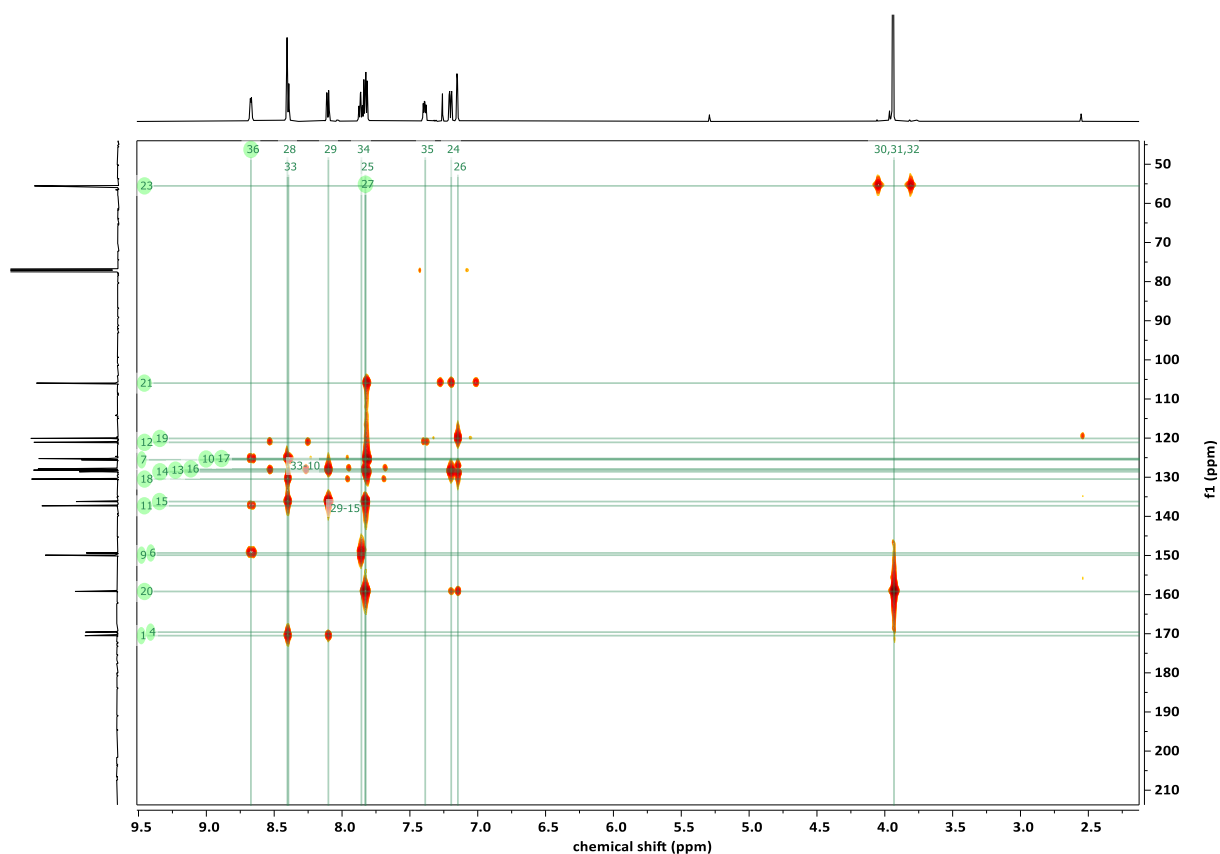
*Figure 96: ^{1}H-^{13}C- HMBC-spectra of 2-(6-methoxynaphthalen-2-yl)-5-(pyridin-2-yl)-1,3,4-thiadiazole **L⁴** in CDCl₃.*

11.2.   IR-Spectroscopy

Figure 97: IR-spectra of 2-Naphthohydrazide.
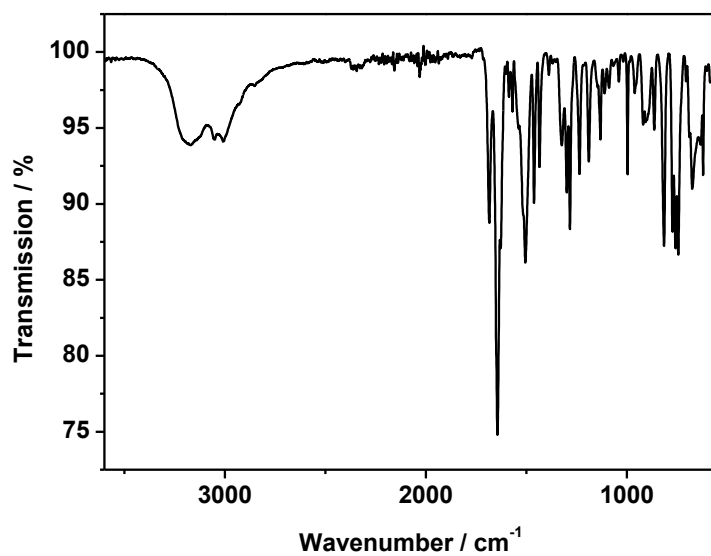
Figure 98: IR-spectra of N'-(2-naphthoyl)-picolinohydrazide.
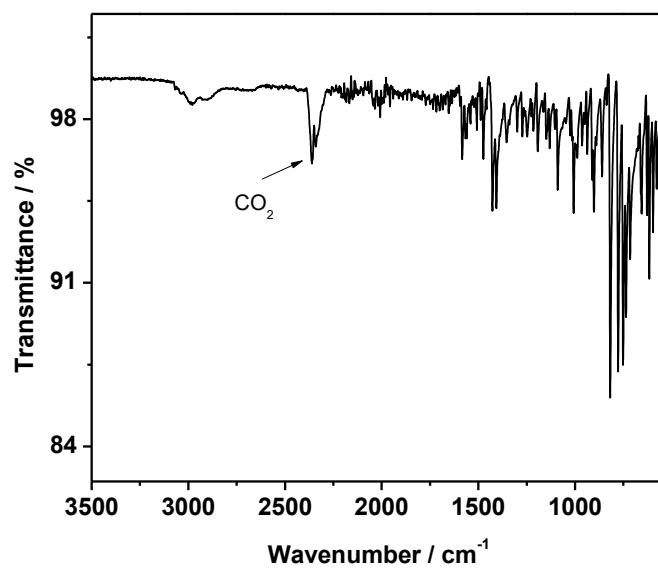
*Figure 99:IR-spectra of 2-(naphthalen-2-yl)-5-(pyridin-2-yl)-1,3,4-thiadiazole **L¹**.*
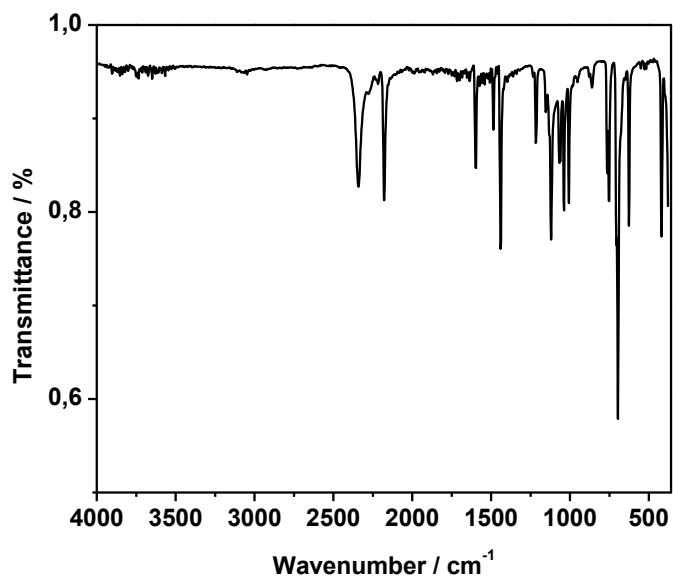
Figure 100: IR-spectra of Fe^{II}(py)$_4$(NCBH$_3$)$_2$.
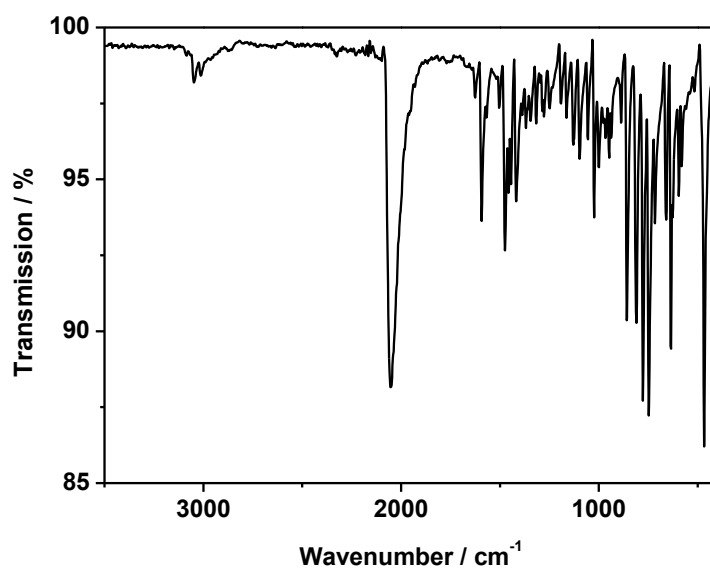
*Figure 101:IR-spectra of [Fe(L1)$_2$(NCS)$_2$] **C1**.*
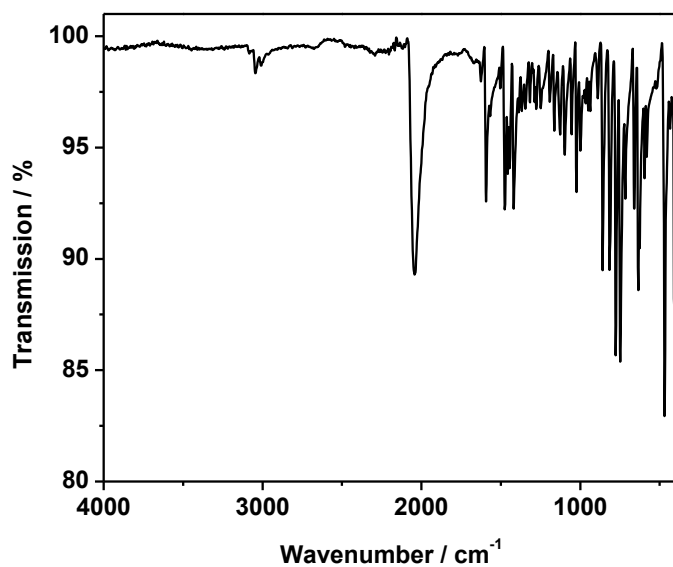
*Figure 102: IR-spectra of [Fe(L1)$_2$(NCSe)$_2$] **C2**.*
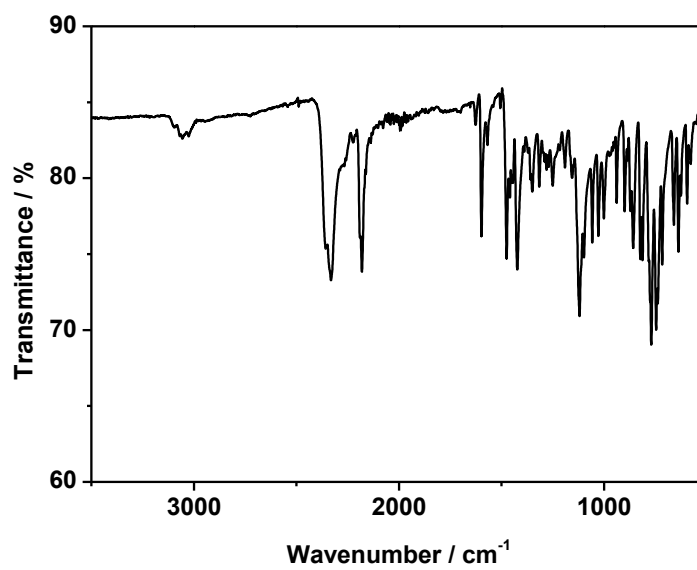
*Figure 103: IR-spectra of [Fe(L1)$_2$(NCBH$_3$)$_2$] · C$_7$H$_8$ **C3**.*
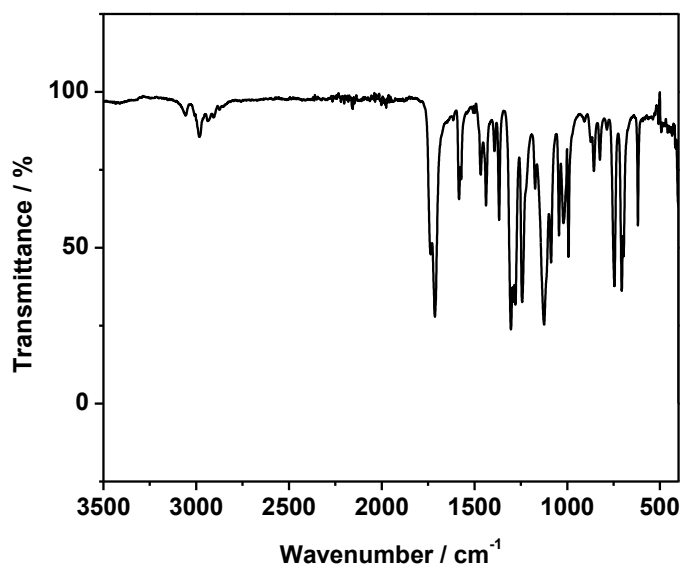
Figure 104: IR-spectra of ethyl picolinate.
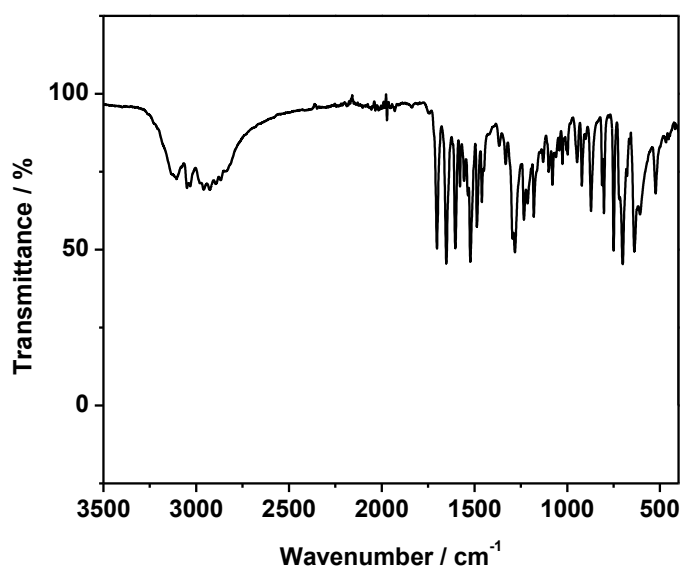
Figure 105: IR-spectra of N'-(2-benzoyl) pyridine-2-carboxylic acid hydrazide.
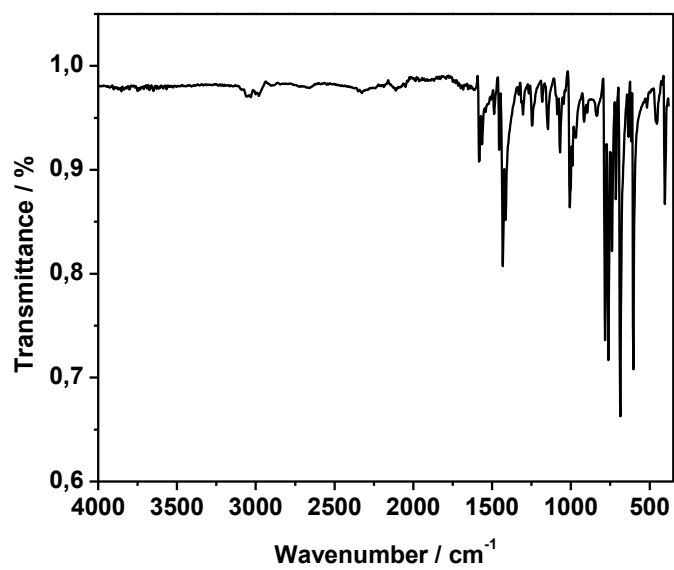
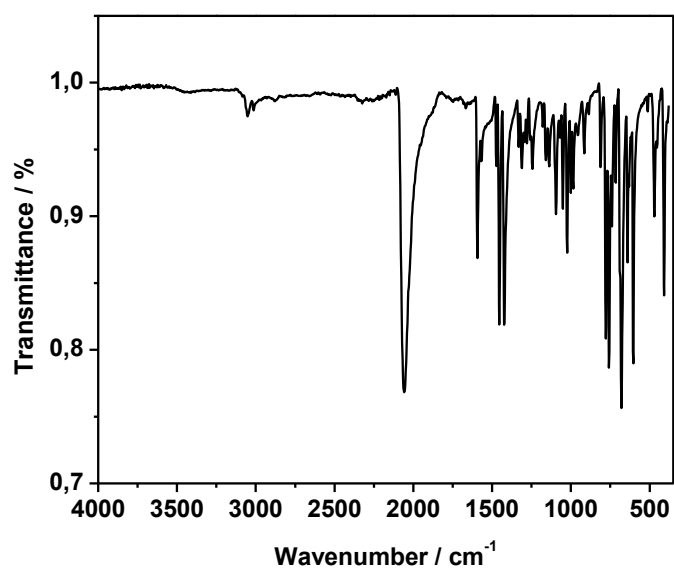*Figure 106: IR-spectra of 2-(pyridin-2-yl)-5-phenyl-1,3,4-thiadiazole **L²**.*

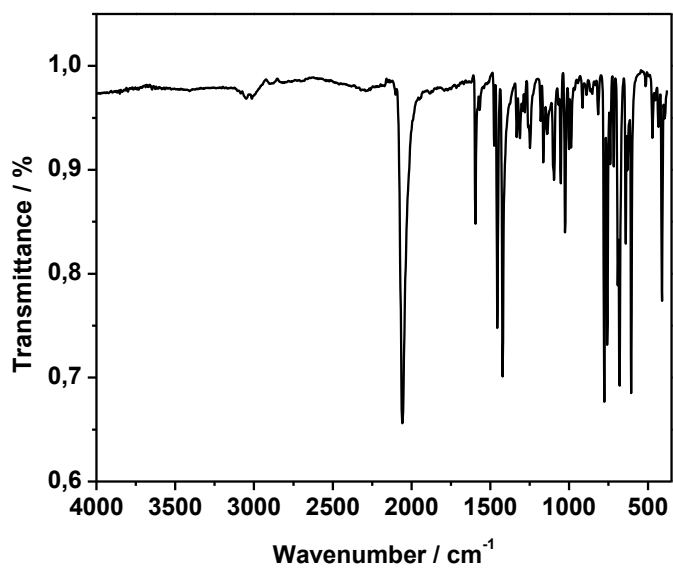*Figure 107: IR-spectra of [Fe(L²)₂(NCS)₂] · 2 CH₂Cl₂ **C4**.*

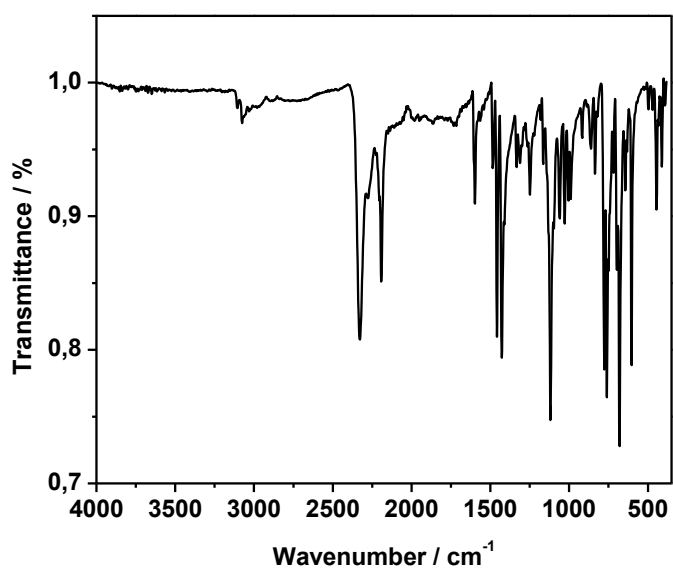*Figure 108: IR-spectra of [Fe(L²)₂(NCSe)₂] · MeOH **C5**.*

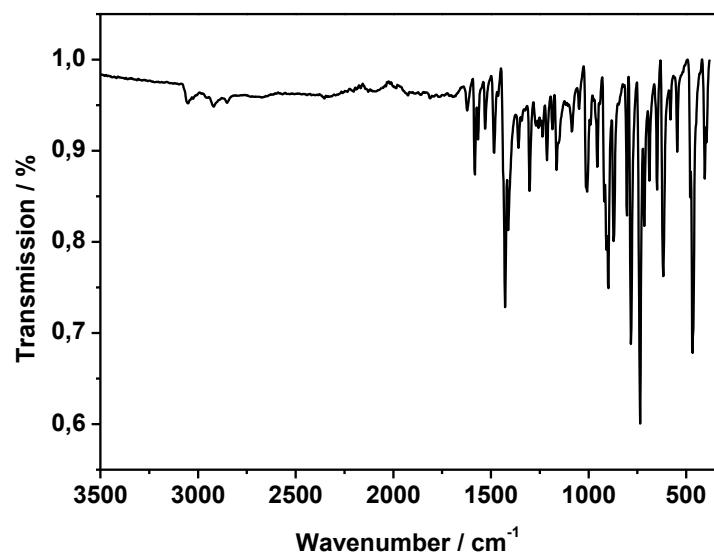*Figure 109: IR-spectra of [Fe(L²)₂(NCBH₃)₂] **C6**.*

*Figure 110: IR-spectra of 2-(anthracen-2-yl)-5-(pyridin-2-yl)-1,3,4-thiadiazole **L³**.*
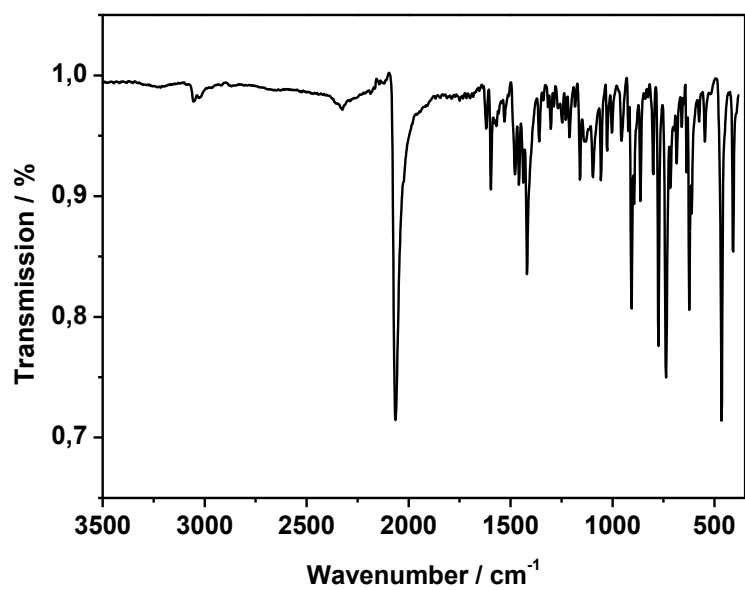

*Figure 111: IR-spectra of [Fe(L³)₂(NCS)₂] **C7**.*
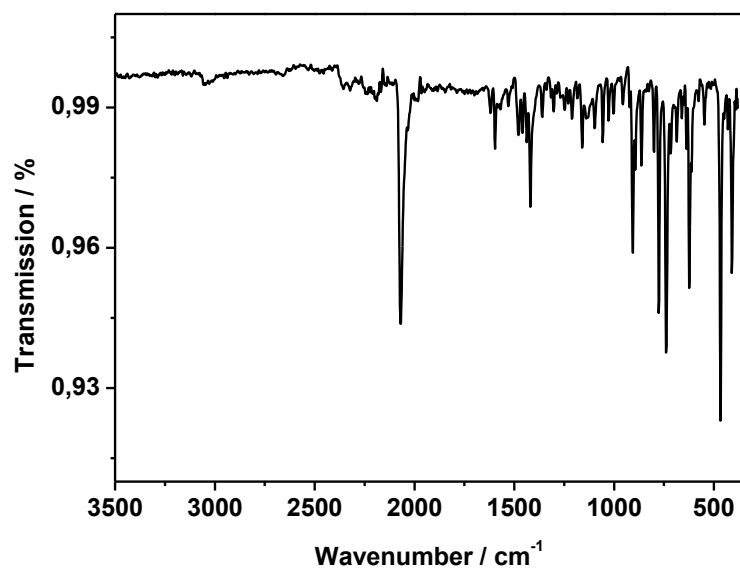
Figure 112: IR-spectra of [Fe(L^3)$_2$(NCSe)$_2$] **C8.**

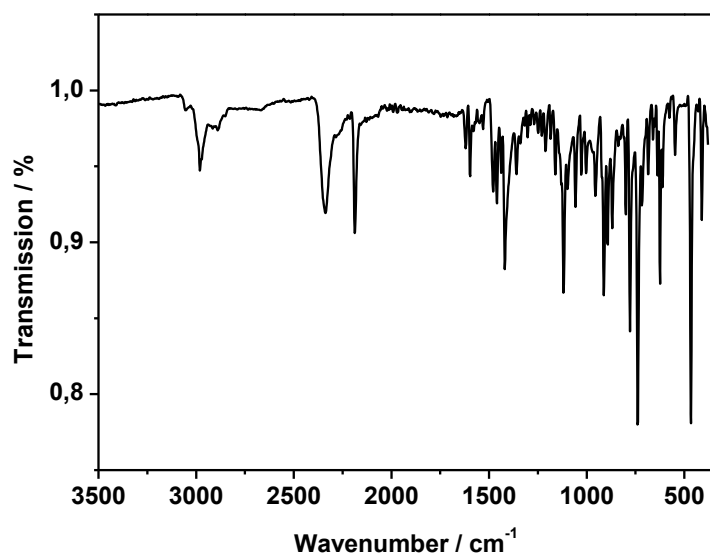*Figure 113: IR-spectra of [Fe(L^3)$_2$(NCBH$_3$)$_2$]* **C9.**
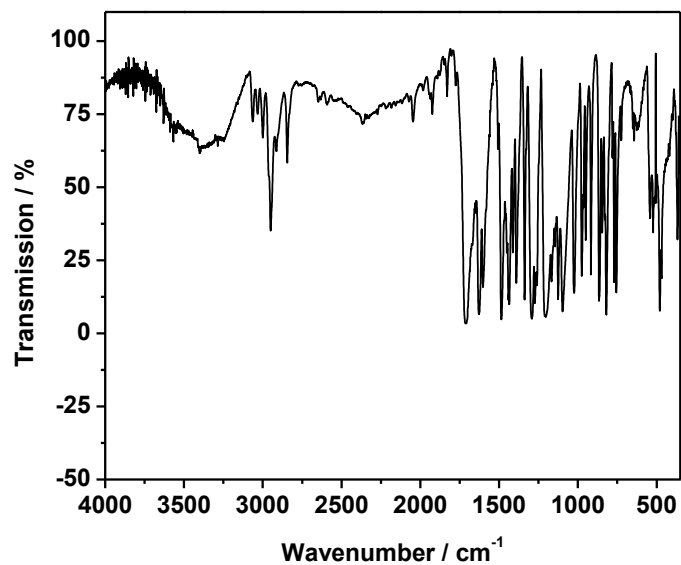
Figure 114: IR-spectra of 6-methoxy naphthoate.
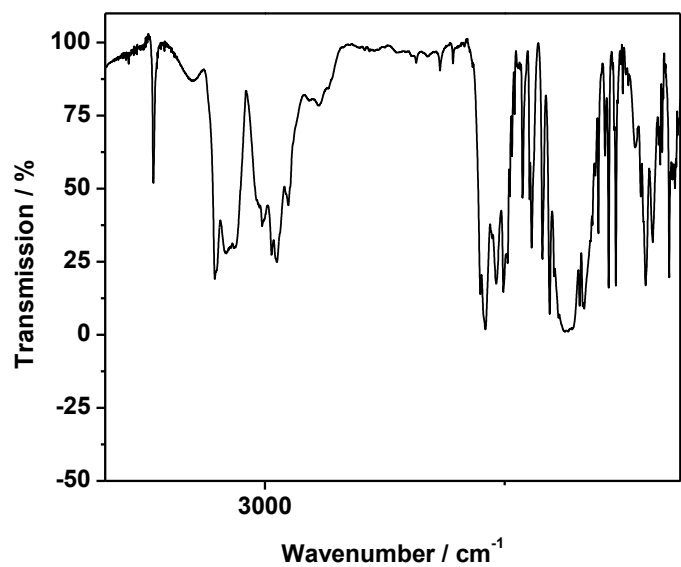
Figure 115: IR-spectra of 6-methoxy-2-naphthohydrazide.

Figure 116: IR-spectra of N'-(6-methoxy-2-naphthoyl) pyridine-2-carboxylic acid hydrazide.
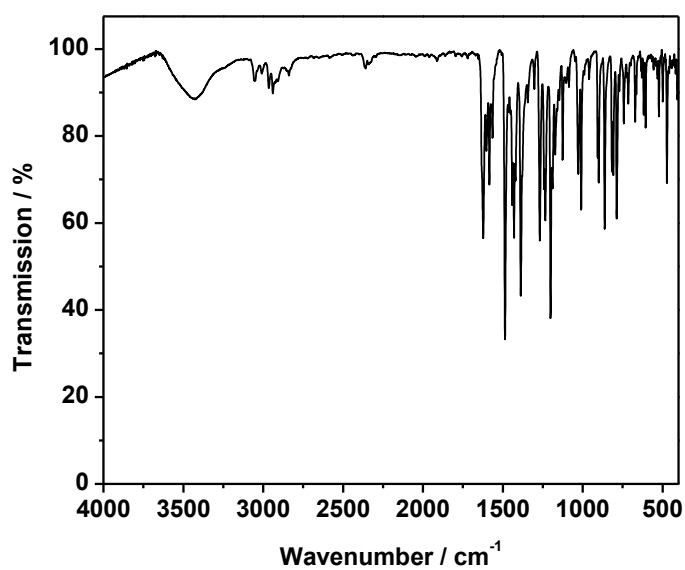
*Figure 117: IR-spectra of 2-(6-methoxynaphthalen-2-yl)-5-(pyridin-2-yl)-1,3,4-thiadiazole **L⁴**.*
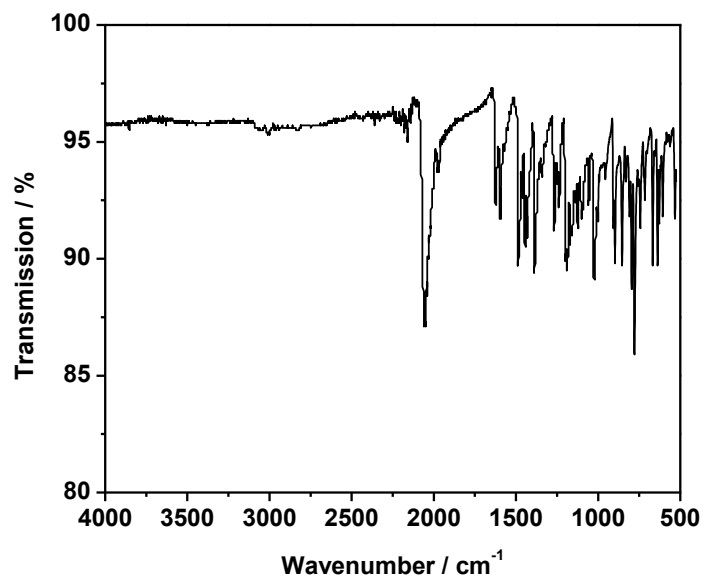
Figure 118: IR-spectra of [Fe^{II}(L^4)$_2$(NCS)$_2$] · 2 CH$_2$Cl$_2$ **C10.**
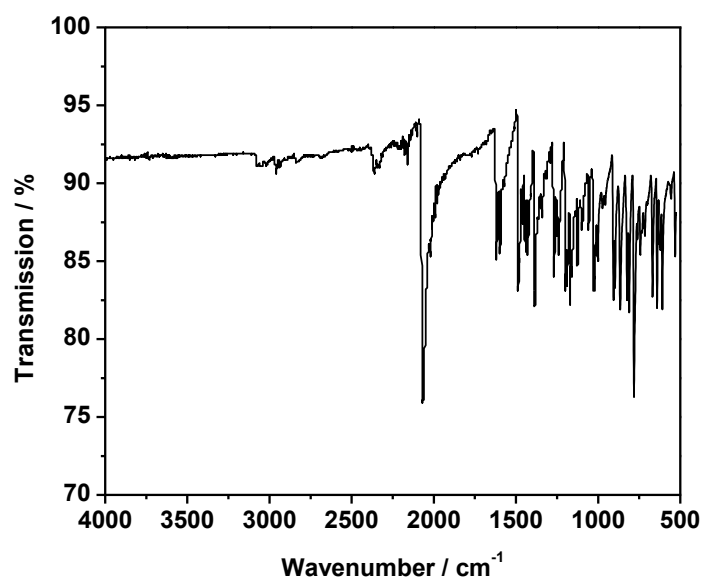
Figure 119: IR-spectra of [Fe^{II}(L^4)$_2$(NCSe)$_2$] · 2 CH$_2$Cl$_2$ **C11.**
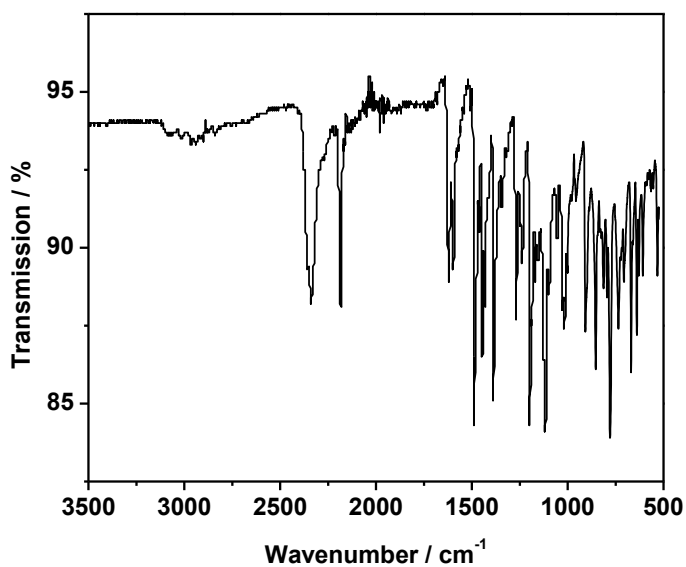
*Figure 120: IR-spectra of [Fe^{II}(L^4)$_2$(NCBH$_3$)$_2$] · 2 CH$_2$Cl$_2$ **C12**.*

11.3.   Mass Spectrometry
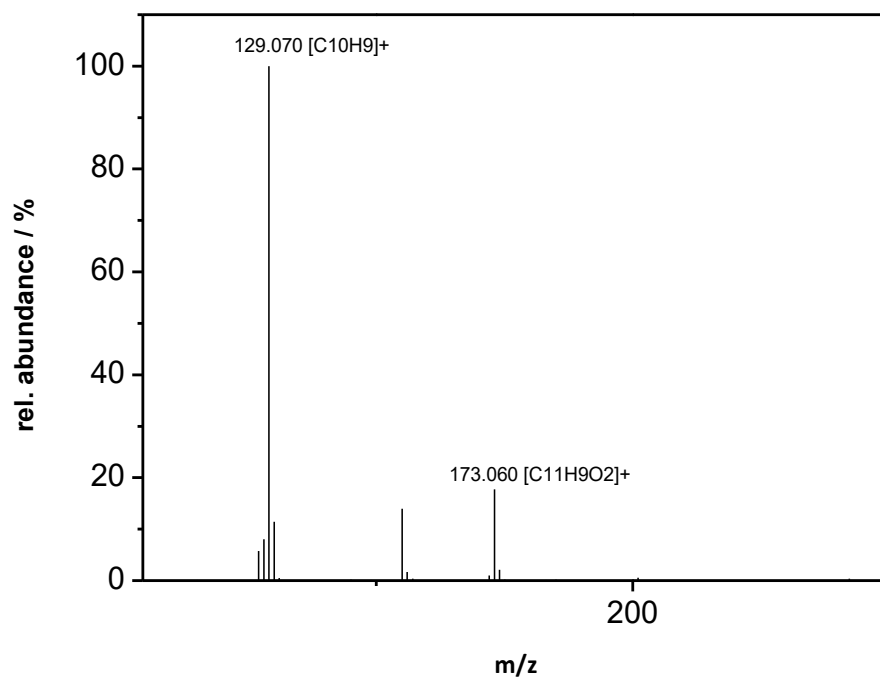
Figure 121: APCI-MS of Ethyl-2-naphthoate.
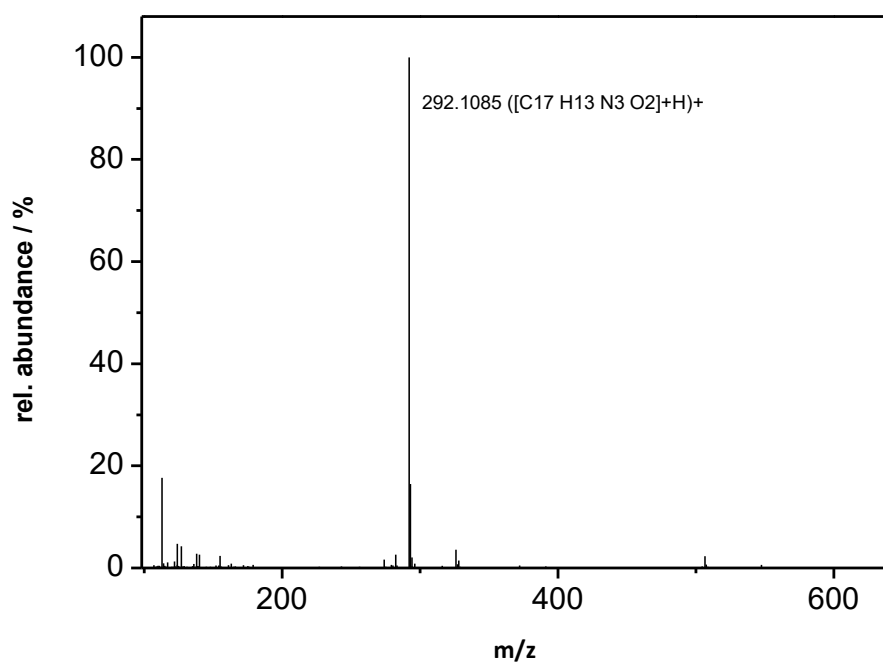
Figure 122: APCI-MS spectra of N'-(2-naphthoyl)-picolinohydrazide.
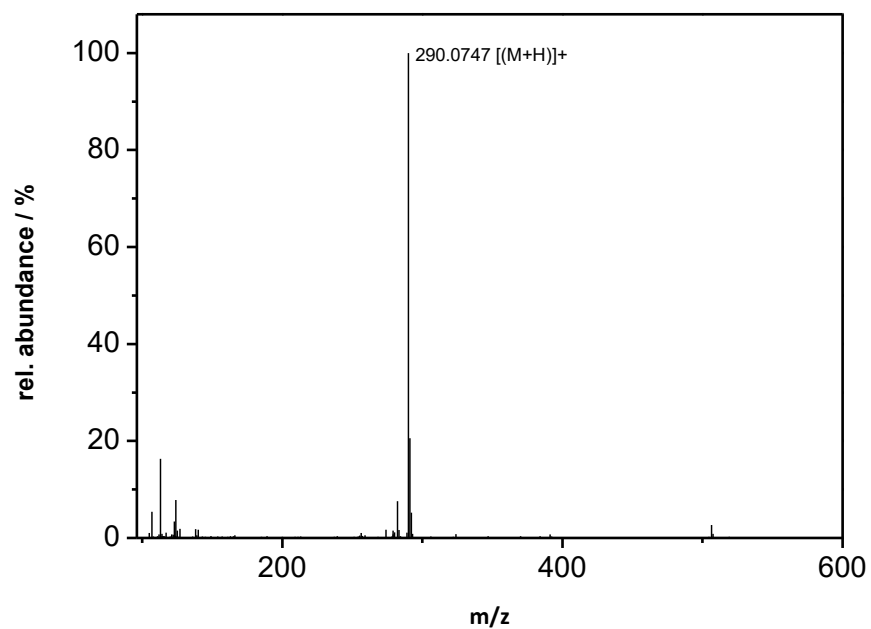
Figure 123: APCI-MS spectra of 2-(naphthalen-2-yl)-5-(pyridin-2-yl)-1,3,4-thiadiazole L¹.
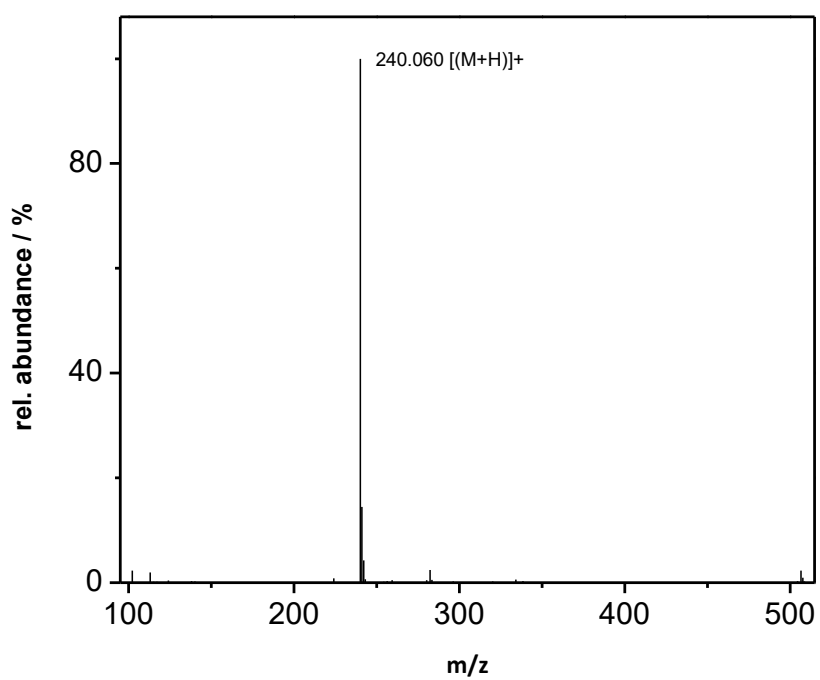
*Figure 124: APCI-MS spectra of 2-(pyridin-2-yl)-5-phenyl-1,3,4-thiadiazole **L²**.*
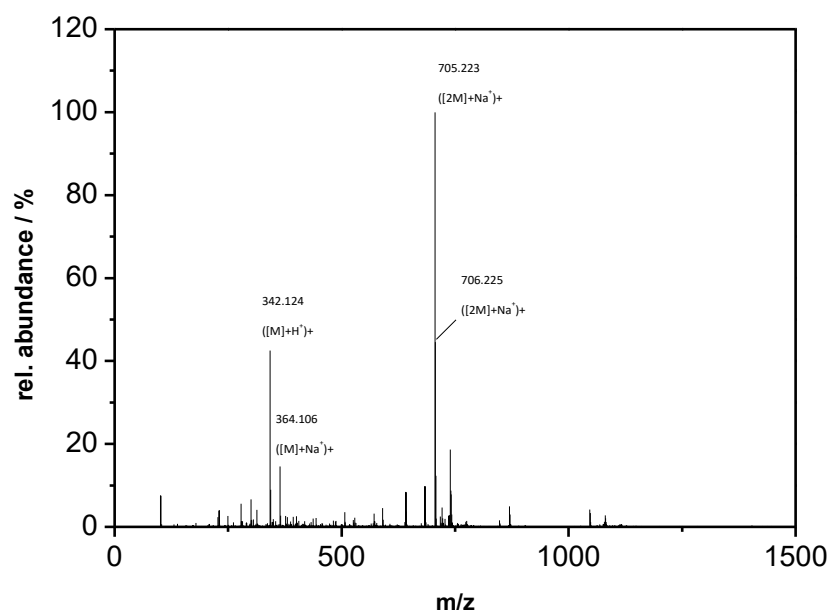
Figure 125: APCI-MS spectra N'-(2-anthracenyl) pyridine-2-carboxylic acid hydrazide.
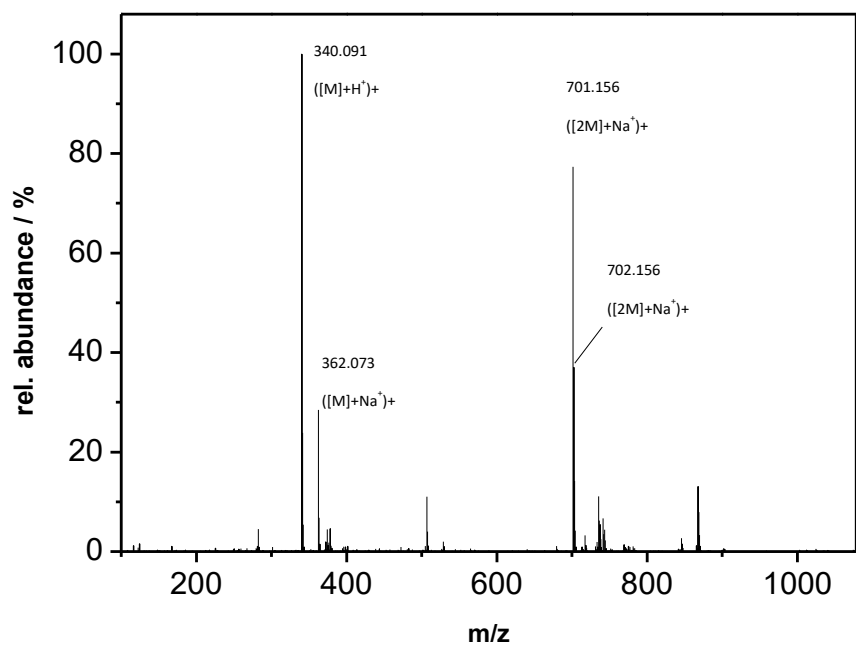
*Figure 126: APCI-MS spectra of 2-(anthracen-2-yl)-5-(pyridin-2-yl)-1,3,4-thiadiazole **L³**.*
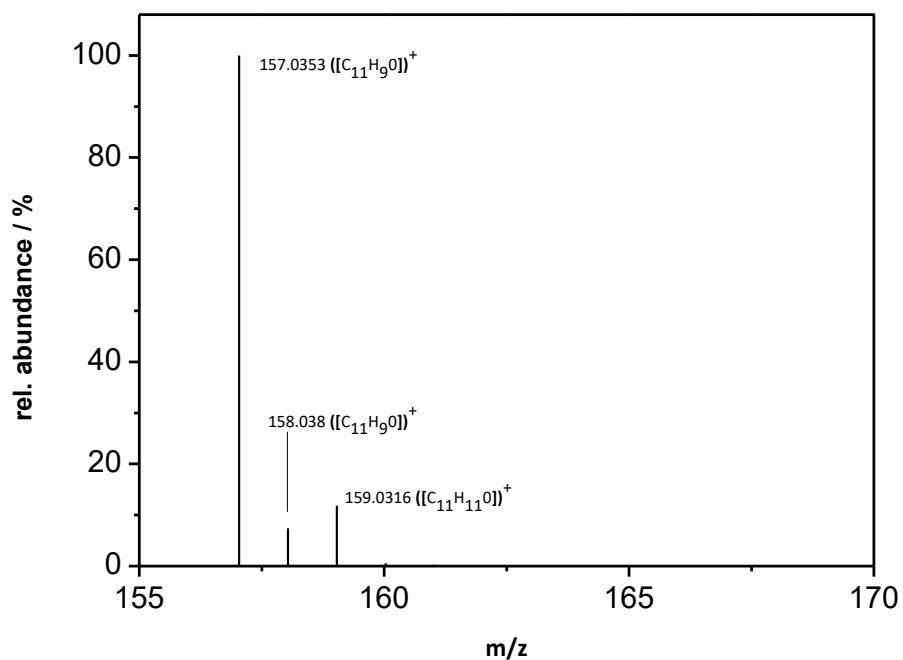
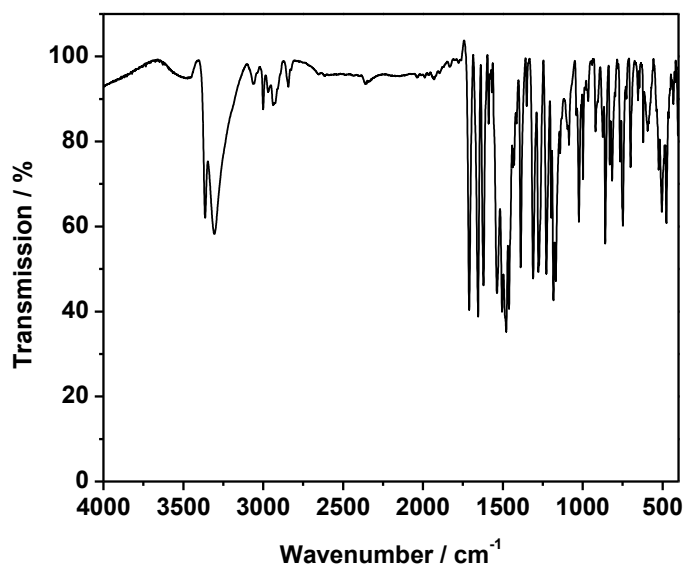*Figure 127: APCI-MS spectra of methyl 6-methoxy-2-naphthoate.*
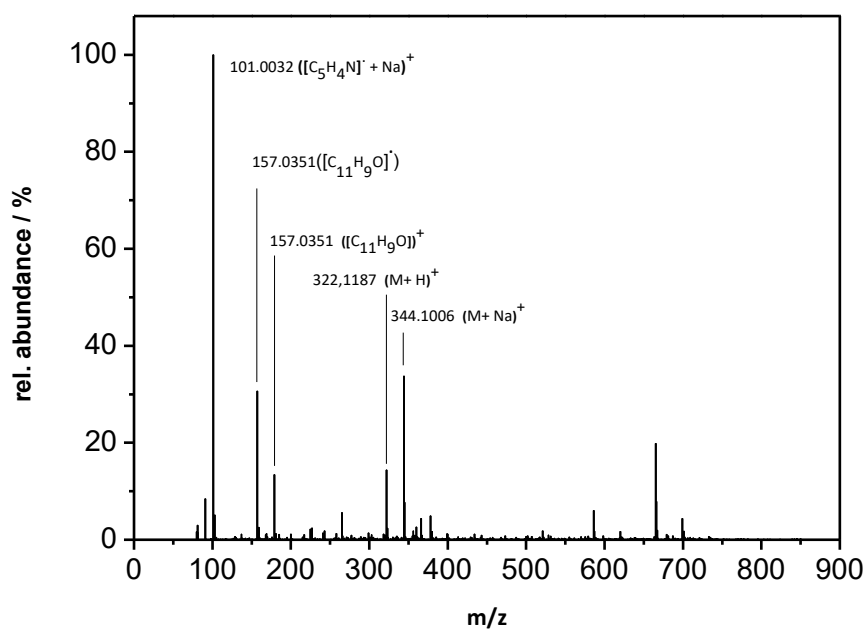
Figure 128: APCI-MS spectra of N'-(6-methoxy-2-naphthoyl) pyridine-2-carboxylic acid hydrazide.
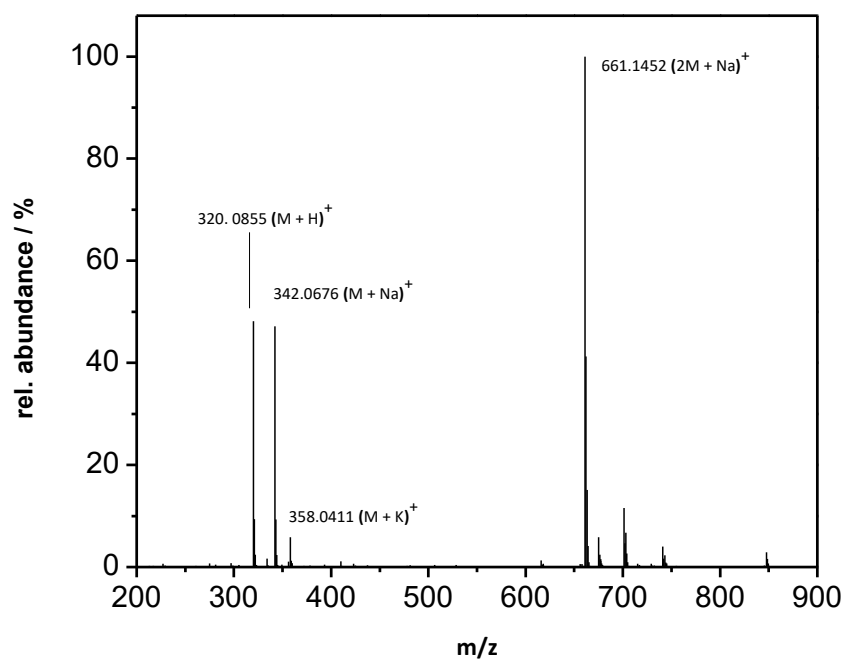
Figure 129: APCI-MS spectra of 2-(6-methoxynaphthalen-2-yl)-5-(pyridin-2-yl)-1,3,4-thiadiazole L⁴.

11.4. Additional Crystallographic Data and Figures

11.4.1. [Fe^{II}(**L^1**)$_2$(NCX)$_2$] · n(Solv) (**C1**, **C2**, **C3**)

| Compound	C1 at 20 K	C1 at 70 K
Empirical formula	C36H22FeN8S4	C36H22FeN8S4
Formula weight / g mol^{-1}	750.70	750.70
Crystal size / mm	0.1 x 0.1 x 0.1	0.1 x 0.1 x 0.1
Crystal system	triclinic	triclinic
Space group	P-1	P-1
Unit cell dimensions		
a / Å	7.817(2)	7.6757(5)
b / Å	9.050(3)	8.9164(6)
c / Å	11.954(4)	12.1868(8)
α / °	96.655(7)	95.5853(11)
β / °	90.513(15)	92.7802(11)
γ / °	110.806(12)	111.7974(11)
V /Å^3	783.9(5)	767.51(9)
Z	1	1
$\rho_{calc.}$ / g cm^{-3}	1.590	1.624
μ / mm^{-1}	0.032	0.063
F(000)	384	384
T / K	20.01	70
Diffractometer	Pilatus3 X CdTe	Pilatus3 X CdTe
Radiation	synchrotron	synchrotron
θ-range for data collection/°	0.963 < θ < 9.419	0.856 < θ < 10.893
Index ranges	-9 < h < 9	-11 < h < 11
	-12 < h < 11	-13 < h < 13
	-15 < h < 15	-18 < h < 18
Collected reflections	5635	38571
Independent reflections	3014	5798
Completeness	0.775	0.986
Max. and min. transmission	0.9705 and 0.8485	0.9955 and 9146
R_{Int}	0.0436	0.0471
R_{Sigma}	0.0640	0.0272
Data / restraints / parameters	3014 / 0 / 223	5798 / 0 / 223
Goodness-of-fit on F^2	0.971	1.059
R$_1$ [I > 2 σ (I)]	0.0493	0.0388
Final wR$_2$ [I ≥ 2σ(I)]	0.1229	0.0987
Final R$_1$ [alldata]	0.0693	0.0503
Final wR$_2$ [alldata]	0.1330	0.1053
Ø M-N-Bindung	2.14	1.956
∑ / °	65.20	43.96

Table 2: Crystallographic data of C1 measured with Pilatus3 X CdTe device at 20 K and 70 K.

Compound	C1 at 90 K	C1 at 173 K
Empirical formula	C36H22FeN8S4	C36H22FeN8S4
Formula weight / g mol^{-1}	750.70	750.70
Crystal size / mm	0.04 x 0.023 x 0.013	0.04 x 0.023 x 0.013
Crystal system	triclinic	triclinic
Space group	P-1	P-1
Unit cell dimensions		
a / Å	7.7806(8)	7.9572(7)
b / Å	9.0356(9)	9.2700(8)
c / Å	12.3660(13)	12.0921(11)
α / °	95.582(8)	96.372(7)
β / °	92.641(8)	89.899(7)
γ / °	111.716(7)	110.583(7)
V /Å^3	800.66(15)	829.06(13)
Z	1	1
$\rho_{calc.}$ / g cm^{-3}	1.557	1.504
μ / mm^{-1}	0.775	0.748
F(000)	384	384
T / K	90(2)	173(2)
Diffractometer	STOE STADIVARI	STOE STADIVARI
Radiation	Mo-Kα	Mo-Kα
θ-range for data collection/∘	2.445 < θ < 25.994	2.364 < θ < 25.990
Index ranges	-9 < h < 9 -11 < h < 11 -15 < h < 15	-9 < h < 9 -11 < h < 11 -14 < h < 14
Collected reflections	10196	10719
Independent reflections	3141	3252
Completeness	0.999	0.999
Max. and min. transmission	0.9847 and 0.6193	0.9850 and 0.6082
R_{Int}	0.0626	0.0630
R_{Sigma}	0.0706	0.0703
Data / restraints / parameters	3141 / 0 / 223	3252 / 0 / 223
Goodness-of-fit on F^2	1.069	1.126
R$_1$ [I > 2 σ (I)]	0.0675	0.0679
Final wR$_2$ [I ≥ 2σ(I)]	0.1386	0.1304
Final R$_1$ [alldata]	0.1169	0.1193
Final wR$_2$ [alldata]	0.1613	0.1524
Ø M-N-Bindung	1.99	2.16
∑ / °	45.00	67.04

Table 3: Crystallographic data of C1 measured with a Stoe Stadivari device at 90 K and 173 K.

Compound	C2 at 200 K	C3 at 160 K
Empirical formula	C36H22FeN8S2Se2	C43H36B2FeN8S2
Formula weight / g mol^{-1}	844.50	806.39
Crystal size / mm	0.05 x 0.033 x 0.014	0.1 x 0.047 x 0.01
Crystal system	triclinic	triclinic
Space group	P-1	P-1
Unit cell dimensions		
a / Å	8.2475(5)	9.0457(6)
b / Å	10.4557(7)	10.0567(7)
c / Å	10.6955(7)	10.8219(9)
α / °	81.572(5)	84.951(6)
β / °	84.194(5)	83.165(6)
γ / °	67.985(4)	89.633(6)
V /Å^3	844.75(10)	973.67(12)
Z	1	1
$\rho_{calc.}$ / g cm^{-3}	1.660	1.375
μ / mm^{-1}	2.765	4.447
F(000)	42	418
T / K	200	160
Diffractometer	STOE STADIVARI	STOE IPDS 2T
Radiation	Mo-Kα	Cu- Kα
θ-range for data collection/°	2.116 < θ < 30.581	4.130 < θ < 59.979
Index ranges	-11 < h < 10	-10 < h < 10
	-14 < h < 12	-11 < k < 11
	-15 < h < 15	-12 < l < 11
Collected reflections	13722	8334
Independent reflections	4586	3369
Completeness	0.885	0.984
Max. and min. transmission	0.9277 and 0.4778	0.9565 and 0.6370
R_{Int}	0.0289	0.0636
R_{Sigma}	0.0370	0.0845
Data / restraints / parameters	4586 / 0 / 223	2844 / 42 / 276
Goodness-of-fit on F^2	1.005	1.084
R$_1$ [I > 2 σ (I)]	0.0479	0.1035
Final wR$_2$ [I ≥ 2σ(I)]	0.1338	0.1925
Final R$_1$ [alldata]	0.0865	0.1802
Final wR$_2$ [alldata]	0.1537	0.2433
Ø M-N-Bindung	2.167	2.08
$\sum$ / °	72.88	59.48

Table 4: Crystallographic data of C2 measured with a Stoe Stadivari device at 200K and data of C3 measured with a STOE IPDS 2T device at 160 K.
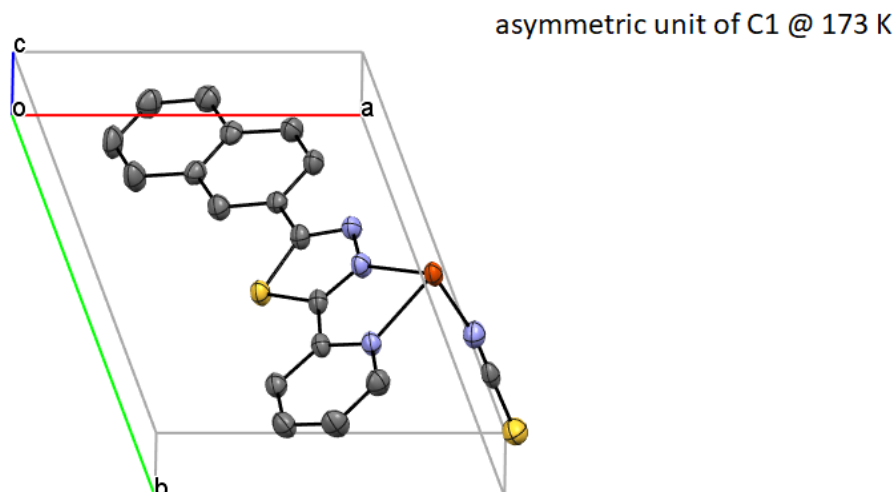
Figure 130: Asymmetric Unit of [Fe(L¹)₂(NCS)₂] C1 @ 173 K. View down reciprocal cell axis c*. Color Code: grey-C, yellow-sulfur, blue-N, orange-Fe, white-H. ORTEP representation with atomic displacement parameters at 50% level of probability. Hydrogen atoms are omitted for clarity.

Distance / Å		Angle / °	
N2-Fe1	2.20(1)	N2-Fe1-N1	104.3(1)
N4-Fe1	2.09(1)	N2-Fe1-N1	75.6(9)
N1-Fe1	2.19(9)	N1-Fe1-N2	104.3(1)
N2-Fe1	2.20(1)	N2-Fe1-N1	75.6(9)
N1-Fe1	2.19(9)	N4-Fe1-N2	90.5(2)
N4-Fe1	2.09(1)	N4-Fe1-N1	91.9(3)
		N4-Fe1-N2	89.4(8)
		N4-Fe1-N1	88.0(7)
		N4-Fe1-N1	91.9(3)
		N4-Fe1-N2	90.5(2)
		N4-Fe1-N1	88.0(7)
		N4-Fe1-N2	89.4(8)
Ø M-N-distance	2.16(4)	∑ / °	67.0(4)

Table 5: Selected bond lengths and angles including the calculated values of the average F-N-distances and the octahedral distortion parameter ∑ of [Fe(L¹)₂(NCS)₂] C1 at 173 K.

Distance / Å		Angle / °	
N2-Fe1	2.17(7)	N2-Fe1-N1	75.7(8)
N10-Fe1	2.16(5)	N1-Fe1-N2	104.2(2)
N1-Fe1	2.17(7)	N1-Fe1-N2	75.7(8)
N10-Fe1	2.16(5)	N1-Fe1-N2	104.2(2)
N1-Fe1	2.07(9)	N10-Fe1-N2	89.4(8)
N2-Fe1	2.07(9)	N10-Fe1-N1	88.4(6)
		N10-Fe1-N2	90.5(2)
		N10-Fe1-N1	91.5(4)
		N10-Fe1-N1	88.4(6)
		N10-Fe1-N2	89.4(8)

		N10-Fe1-N1	91.5(4)
		N10-Fe1-N2	90.5(2)
Ø M-N-distance	2.140(3)	∑ / °	65.1(2)

Table 6: Selected bond lengths and angles including the calculated values of the average F-N-distances and the octahedral distortion parameter ∑ of [Fe(L¹)₂(NCS)₂] C1 at 20 K.

Distance / Å		Angle / °	
N2-Fe1	1.96(7)	N2-Fe1-N1	80.4(0)
N1-Fe1	1.98(6)	N1-Fe1-N2	99.6(0)
N2-Fe1	1.96(7)	N1-Fe1-N2	80.4(09
N10-Fe1	1.91(5)	N1-Fe1-N2	99.6(0)
N1-Fe1	1.98(6)	N10-Fe1-N2	89.8(2)
N10-Fe1	1.91(5)	N10-Fe1-N1	88.8(0)
		N10-Fe1-N2	90.1(8)
		N10-Fe1-N1	91.1(8)
		N10-Fe1-N1	88.8(0)
		N10-Fe1-N2	89.8(2)
		N10-Fe1-N1	91.2(0)
		N10-Fe1-N2	90.2(0)
Ø M-N-distance	1.95(6)	∑ / °	43.9(2)

Table 7: Selected bond lengths and angles including the calculated values of the average F-N-distances and the octahedral distortion parameter ∑ of [Fe(L¹)₂(NCS)₂] C1 at 70 K.
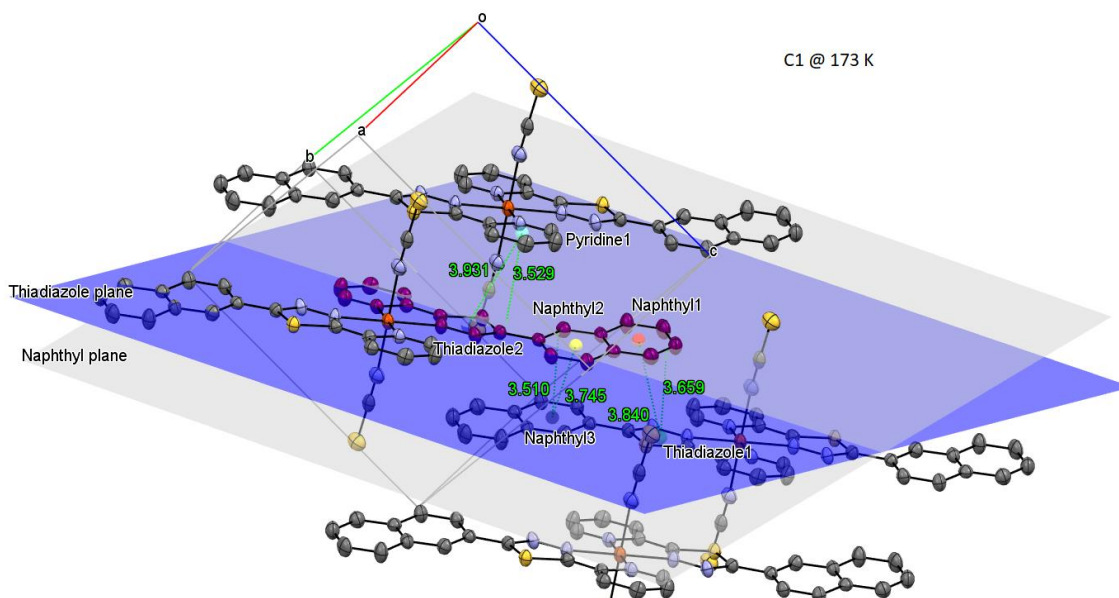
*Figure 131: Representation of all proceeding π-π-interactions of one coordinating ligand L1 (marked in purple) with anti-parallel aligned ligand molecules of neighbouring **C1** complex molecules at 173 K. The planes named "naphthyl plane" and "thiadiazole plane" are those located in the respective molecular groups of the purple-coloured molecule. The points nemd "thiadiazole1-2", "naphthyl 1-3" and "pyridine1" are the respective centroids of the respective interacting π-systems. The average distance of the π-π-interactions is represented by the respective solder that falls on the respective plane of the interacting partner. Calculation of the Offset of the pipi interacting partners was done using the Pythagorean theorem. Color*

Code: grey-C, yellow-sulfur, blue-N, orange-Fe, white-H. ORTEP representation with atomic displacement parameters at 50% level of probability.

	Object1	Object2	Length / Å	Offset of π-π-interacting centroids / Å
Centroid distance perpendicular to respective object plane (average π-π-interaction distance)	Thiadiazole1	Naphthyl plane	3.65(9)	
	Naphthyl3	Naphthyl plane	3.51(1)	
	Pyridine1	Thiadiazole plane	3.52(9)	
Centroid to Centroid distance	Naphthyl1	Thiadiazole1	3.84(1)	1.16(5)
	Naphthyl2	Naphthyl3	3.74(5)	1.30(6)
	Thiadiazole2	Pyridine1	3.93(1)	1.73(2)

*Table 8: Overview of all π-π-interactions proceeding from one molecule of L1 with anti-parallel aligned ligand molecules of neighbouring **C1** complex molecules at 173 K. Calculation of the Ofset of the pipi interacting partners was done using the Pythagorean theorem.*
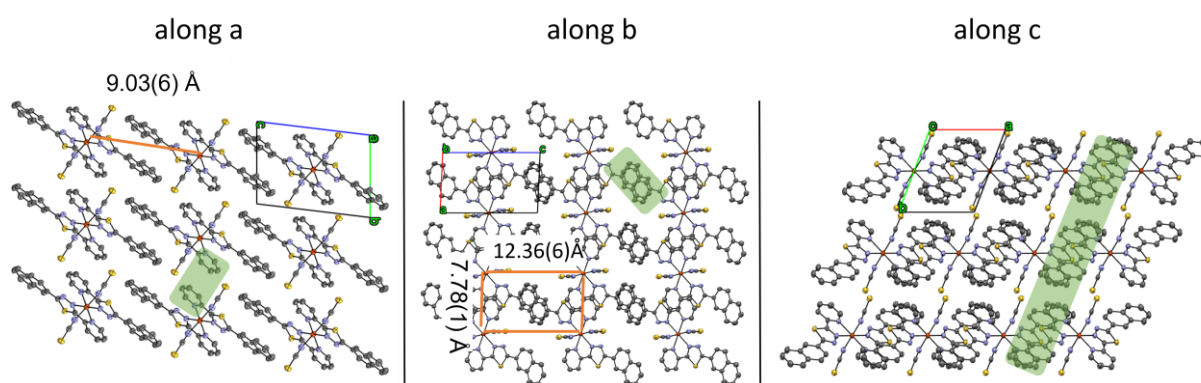
*Figure 132: **along a**: Selected part of the crystal structure of **C1** at 173 K along the a-axis. **along b**: Selected part of the crystal structure of **C1** at 173 K along the b-axis. **along c**: Selected part of the crystal structure of **C1** at 173 K along the c-axis. Color Code: grey-C, yellow-sulphur, blue-N, orange-Fe, white-H. ORTEP representation with atomic displacement parameters at 50% level of probability. Highlighted are the π-π-interacting anti-parallel aligned ligands of neighbouring complex molecules, respectively and the Fe-Fe distances (orange lines) along the different axis.*

asymmetric unit of C1 @ 90 K
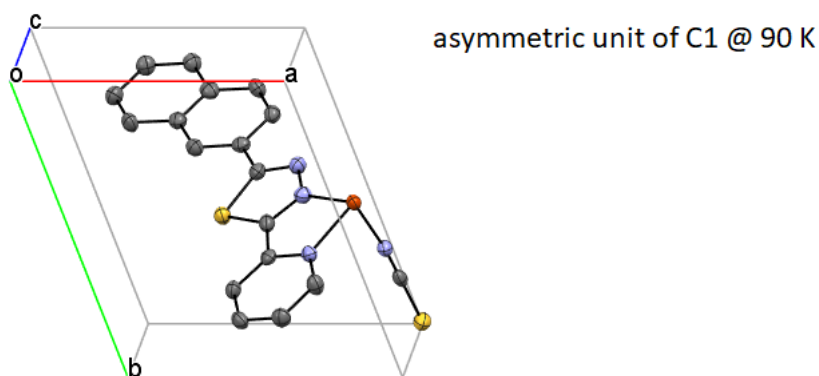
Figure 133: Asymmetric Unit of [Fe(L^1)$_2$(NCS)$_2$] C1 @ 90 K. View down reciprocal cell axis c*. Color Code: grey-C, yellow-sulfur, blue-N, orange-Fe, white-H. ORTEP representation with atomic displacement parameters at 50% level of probability.

Distance / Å		Angle / °	
N2-Fe1	2.00(1)	N2-Fe1-N1	80.3(7)
N4-Fe1	1.94(3)	N1-Fe1-N2	99.6(3)
N1-Fe1	2.02(3)	N1-Fe1-N2	80.3(7)
N4-Fe1	1.94(3)	N1-Fe1-N2	99.6(3)
N1-Fe1	2.02(3)	N4-Fe1-N2	90.2(6)
N2-Fe1	2.00(1)	N4-Fe1-N1	88.6(4)
		N4-Fe1-N2	89.7(4)
		N4-Fe1-N1	91.3(6)
		N4-Fe1-N1	88.6(4)
		N4-Fe1-N2	90.2(6)
		N4-Fe1-N1	91.3(6)
		N4-Fe1-N2	89.7(4)
Ø M-N-distance	1.98(9)	$\sum$ / °	45.0(0)

Table 9: Selected bond lengths and angles including the calculated values of the average F-N-distances and the octahedral distortion parameter $\sum$ of [Fe(L^1)$_2$(NCS)$_2$] C1 at 90 K.

*Figure 134: Representation of all proceeding π-π-interactions of one coordinating ligand L1 (marked in purple) with anti-parallel aligned ligand molecules of neighbouring **C1** complex molecules at 90 K. The planes named "naphthyl plane" and "thiadiazole plane" are those located in the respective molecular groups of the purple coloured molecule. The points nemd "thiadiazole1-2", "naphthyl 1-3" and "pyridine1" are the respective centroids of the respective interacting π-systems. The average distance of the π-π-interactions is repre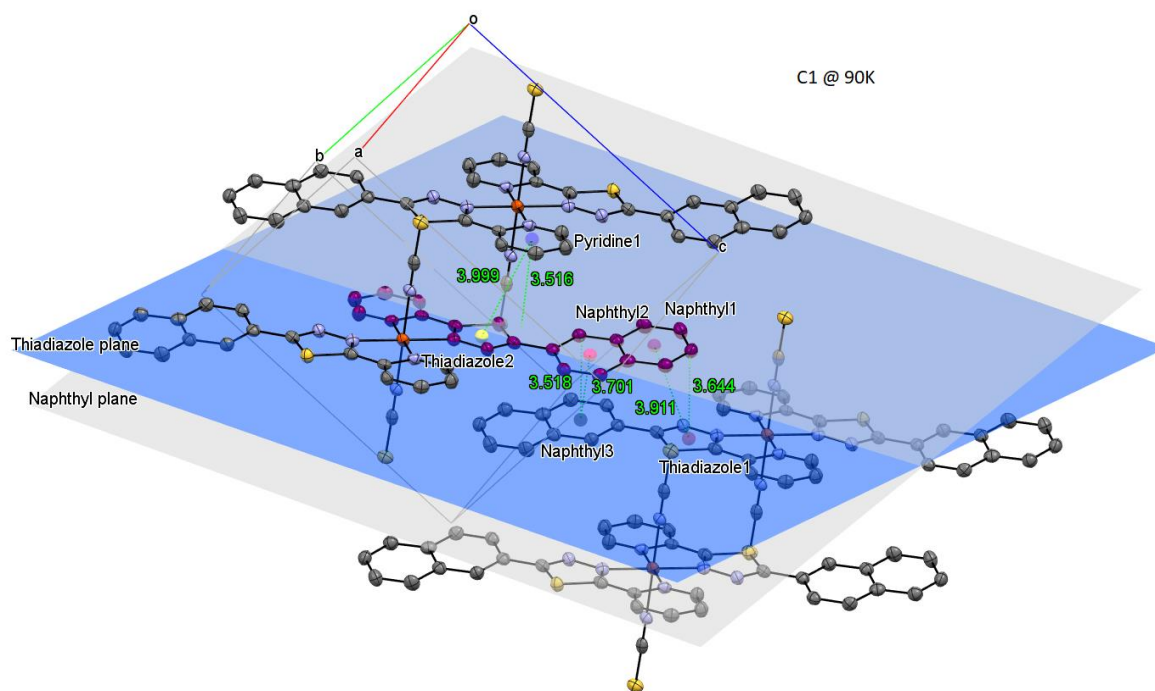sented by the respective solder that falls on the respective plane of the interacting partner. Calculation of the Offset of the pipi interacting partners was done using the Pythagorean theorem. Color Code: grey-C, yellow-sulfur, blue-N, orange-Fe, white-H. ORTEP representation with atomic displacement parameters at 50% level of probability.*

	Object1	Object2	Length / Å	Offset of π-π-interacting centroids / Å
Centroid distance perpendicular to respective object plane (average π-π-interaction distance)	Thiadiazole1	Naphthyl plane	3.64(4)	
	Naphthyl3	Naphthyl plane	3.51(8)	
	Pyridine1	Thiadiazole plane	3.51(6)	
Centroid to Centroid distance	Naphthyl1	Thiadiazole1	3.91(1)	1.42(0)
	Naphthyl3	Naphthyl2	3.70(1)	1.49(4)
	Pyridine1	Thiadiazole2	3.99(9)	1.90(5)

*Table 10: Overview of all π-π-interactions proceeding from one molecule of L1 with anti-parallel aligned ligand molecules of neighbouring **C1** complex molecules at 90 K. Calculation of the Ofset of the pipi interacting partners was done using the Pythagorean theorem.*

along a   along b   along c

*Figure 135: **along a**: Selected part of the crystal structure of **C1** at 90 K along the a-axis. **along b:** Selected part of the crystal structure of **C1** at 90 K along the b-axis. **along c:** Selected part of the crystal structure of **C1** at 90 K along the c-axis. Color Code: grey-C, yellow-sulphur, blue-N, orange-Fe, white-H. ORTEP representation with atomic displacement parameters at 50% level of probability. Highlighted are the π-π-interacting anti-parallel aligned ligands of neighbouring complex molecules, respectively and the Fe-Fe distances (orange lines) along the different axis.*

asymmetric unit of C2 @ 200 K

Figure 136: Asymmetric Unit of C2 @ 200 K. View down reciprocal cell axis c*. Color Code: grey-C, yellow-sulfur, blue-N, orange-Fe, white-H. ORTEP representation with atomic displacement parameters at 50% level of probability. Hydrogen atoms are omitted for clarity.
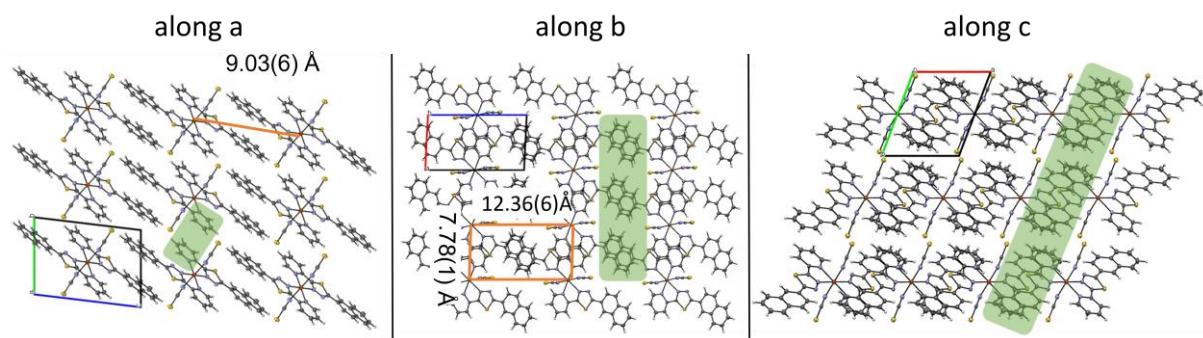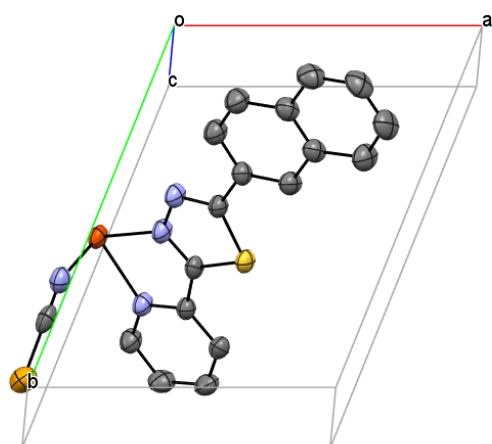
C2 @ 200K

| along a | along b | along c |
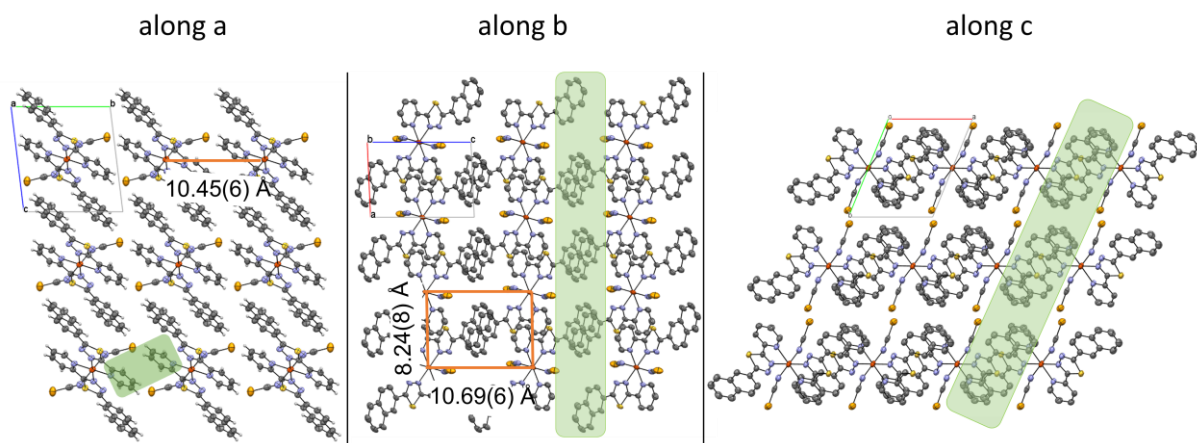
*Figure 137: **along a**: Selected part of the crystal structure of **C2** at 200 K along the a-axis. **along b:** Selected part of the crystal structure of **C2** at 200 K along the b-axis. **along c:** Selected part of the crystal structure of **C2** at 200 K along the c-axis. Color Code: grey-C, yellow-sulphur, blue-N, orange-Fe, light-orange Se, white-H. ORTEP representation with atomic displacement parameters at 50% level of probability. Highlighted are the π-π-interacting anti-parallel aligned ligands of neighbouring complex molecules, respectively and the Fe-Fe distances (orange lines) along the different axis.*
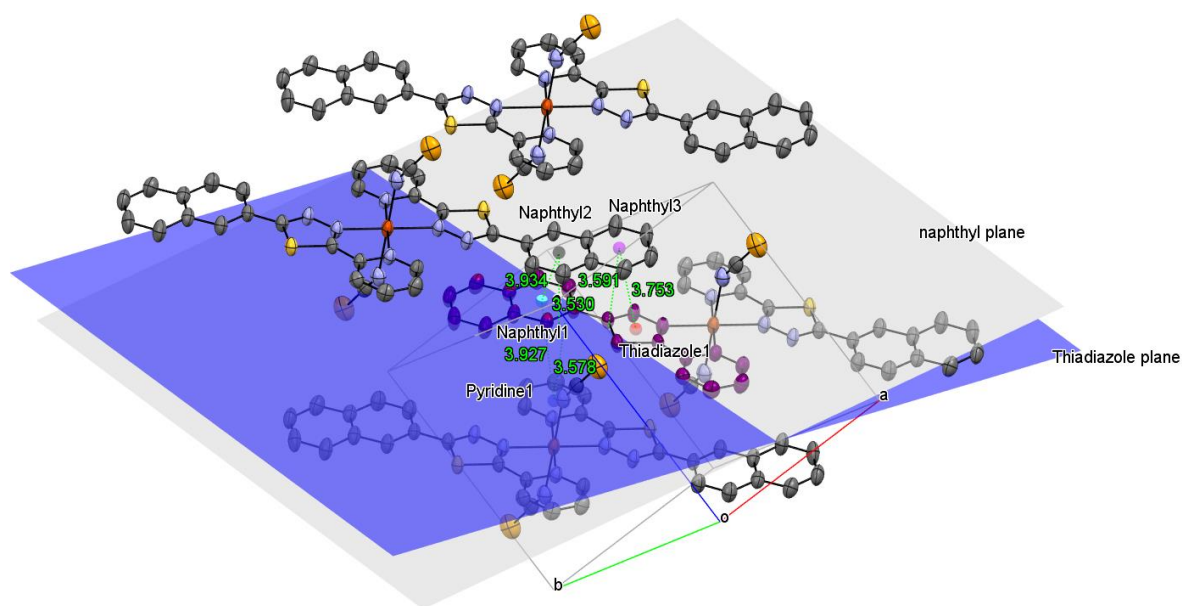
*Figure 138: Representation of all proceeding π-π-interactions of one coordinating ligand L1 (marked in purple) with anti-parallel aligned ligand molecules of neighbouring **C2** complex molecules at 200 K. The planes named "naphthyl plane" and "thiadiazole plane" are those located in the respective molecular groups of the purple coloured molecule. The points named "thiadiazole1", "naphthyl 1-3" and "pyridine1" are the respective centroids of the respective interacting π-systems. The average distance of the π-π-interactions is represented by the respective solder that falls on the respective plane of the interacting partner. Calculation of the Offset of the pipi interacting partners was done using the Pythagorean theorem. Colour Code: grey-C, yellow-sulphur, blue-N, orange-Fe, white-H. ORTEP representation with atomic displacement parameters at 50% level of probability.*

	Object1	Object2	Length / Å	Offset of π-π-interacting centroids / Å
Centroid distance perpendicular to respective object plane (average π-π-interaction distance)	Pyridine1	Thiadiazole plane	3.57(8)	
	Naphthyl2	naphthyl plane	3.53(1)	
	Naphthyl3	Thiadiazole plane	3.59(1)	
Centroid to Centroid distance	Naphthyl1	Pyridine1	3.92(7)	1.61(8)
	Thiadiazole1	Naphthyl3	3.75(3)	1.30(6)
	Naphthyl2	Naphthyl1	3.93(4)	1.73(6)

*Table 11: Overview of all π-π-interactions proceeding from one molecule of L1 with anti-parallel aligned ligand molecules of neighbouring **C2** complex molecules at 200 K. Calculation of the Offset of the π-π-interacting partners was done using the Pythagorean theorem.*

Distance / Å		Angle / °	
N4-Fe1	2.16(6)	N2-Fe1-N1	76.6(9)
N4-Fe1	2.16(6)	N1-Fe1-N2	103.3(1)
N2-Fe1	2.07(8)	N2-Fe1-N1	76.6(9)
N1-Fe1	2.24(7)	N1-Fe1-N2	103.3(1)
N2-Fe1	2.07(8)	N4-Fe1-N2	91.8(1)
N1-Fe1	2.24(7)	N4-Fe1-N1	89.9(4)
		N4-Fe1-N2	88.1(9)
		N4-Fe1-N1	90.0(6)
		N4-Fe1-N1	89.9(4)
		N4-Fe1-N2	91.8(1)
		N4-Fe1-N1	90.0(6)
		N4-Fe1-N2	88.1(9)
Ø M-N-distance	2.16(7)	∑ / °	72.8(8)

*Table 12: Selected bond lengths and angles including the calculated values of the average F-N-distances and the octahedral distortion parameter ∑ of **C2** at 200 K.*
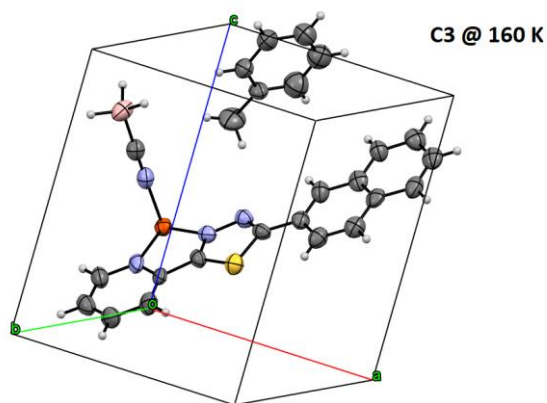
*Figure 139: Asymmetric Unit of **C3** @ 160 K. Color Code: light pink-B, grey-C, yellow-sulfur, blue-N, orange-Fe, green-Cl white-H. ORTEP representation with atomic displacement parameters at 50% level of probability.*

Distance / Å		Angle / °	
N2-Fe1	2.09(3)	N2-Fe1-N1	77.9(5)
N4-Fe1	2.03(7)	N1-Fe1-N2	102.0(5)
N1-Fe1	2.11(2)	N1-Fe1-N2	77.9(5)
N4-Fe1	2.03(7)	N1-Fe1-N2	102.0(5)
N1-Fe1	2.11(2)	N4-Fe1-N2	90.1(2)
N2-Fe1	2.09(3)	N4-Fe1-N1	87.3(1)
		N4-Fe1-N2	89.8(8)
		N4-Fe1-N1	92.7(0)
		N4-Fe1-N1	87.3(1)
		N4-Fe1-N2	90.1(2)
		N4-Fe1-N1	92.7(0)
		N4-Fe1-N2	77.9(5)
c	2.08(1)	$\sum$ / °	59.4(8)

*Table 13: Selected bond lengths and angles including the calculated values of the average F-N-distances and the octahedral distortion parameter $\sum$ of **C3** at 160 K.*
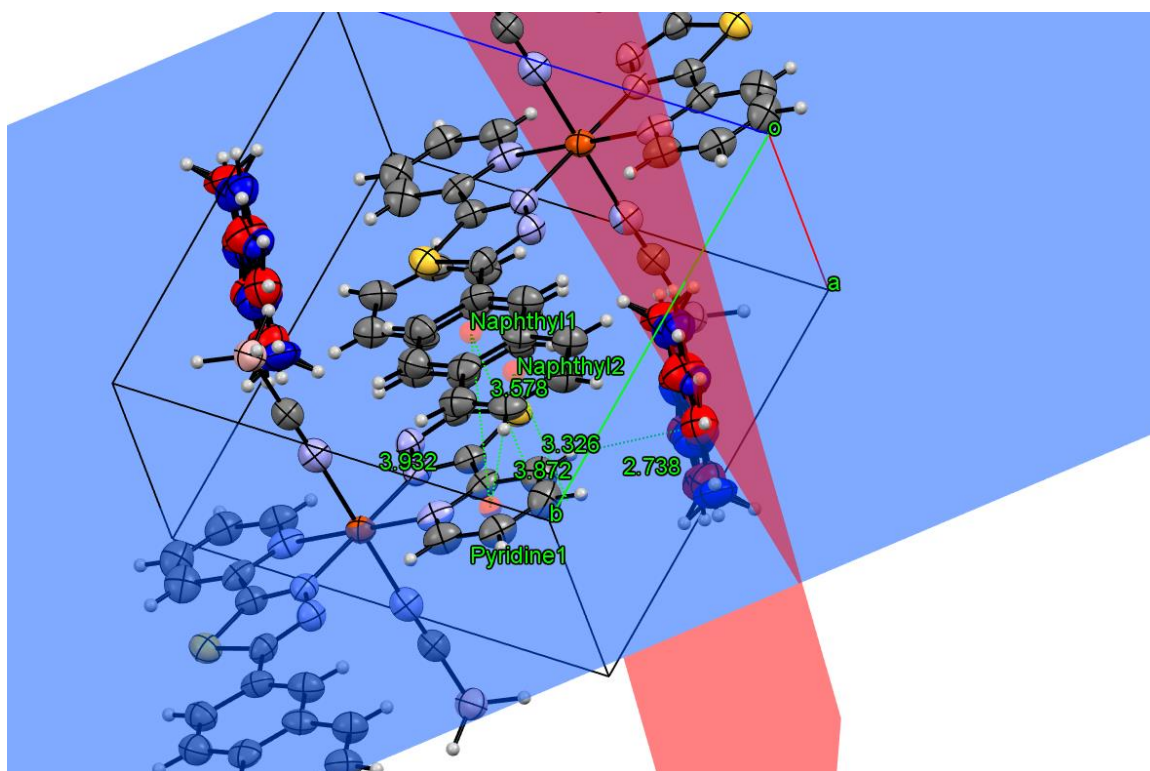
*Figure 140: Representation of all proceeding π-π-interactions of one coordinating ligand L1 with anti-parallel aligned ligand molecules of neighbouring **C3** complex molecules at 163 K. The planes named "pyridine plane" and "toluene plane" are those located in the respective molecular groups of the respective molecule. The points named "pyridine1" and "naphthyl 1 and 2" are the respective centroids of the respective interacting π-systems. The average distance of the π-π-interactions is represented by the respective solder that falls on the respective plane of the interacting partner. Calculation of the Offset of the π-π-interacting partners was done using the Pythagorean theorem. Additionally, the incorporated disordered toluene molecules are building T-shape C-H···π-interactions with the neighbouring ligand molecules of the complexes. Colour Code: light pink-B, grey-C, yellow-sulphur, blue-N, orange-Fe, white-H. The disordered toluene solvent molecules are marked in dark blue and red, respectively, depending on their symmetry operation. ORTEP representation with atomic displacement parameters at 50% level of probability*

	Object1	Object2	Length / Å	Offset of π-π-interacting centroids / Å
Centroid distance perpendicular to respective object plane (average π-π-interaction distance)	Naphthyl1	pyridineplane	3.57(8)	
	Naphthyl2	pyridine plane	3.32(6)	
Centroid to Centroid distance	Naphthyl1	Pyridine1	3.93(2)	1.63(1)
	Naphthyl2	Pyridine1	3.87(2)	1.98(2)

*Table 14: Overview of all π-π-interactions proceeding from one molecule of L1 with anti-parallel aligned ligand molecules of neighbouring **C3** complex molecules at 160 K. Calculation of the Offset of the π-π-interacting partners was done using the Pythagorean theorem.*

11.4.2. $[Fe^{II}(L^2)_2(NCX)_2] \cdot n(Solv)$ (**C4**, **C5**, **C6**)

Compound	[Fe(L2)₂(NCS)₂] C4 at 173 K	[Fe(L2)₂(NCSe)₂] C5 at 90 K	[Fe(L2)₂(NCSe)₂] C5 at 240 K
Empirical formula	C30H22Cl4FeN8S4	C29H22FeN8OS2Se2	C29H22FeN8OS2Se2
Formula weight / g mol⁻¹	820.44	776.43	776.43
Crystal size / mm	0.42 x 0.203 x 0.07	0.09 x 0.067 x 0.05	0.09 x 0.067 x 0.05
Crystal system	triclinic	monoclinic	monoclinic
Space group	P-1	$P12_1/c1$	$P12_1/c1$
Unit cell dimensions			
a / Å	7.6780(4)	15.9027(3)	16.1339(14)
b / Å	9.4991(5)	13.3775(2)	13.6784(8)
c / Å	12.8340(7)	14.0680(4)	14.1908(13)
α / °	91.848(4)	90	90
β / °	106.239(4)	104.263(2)	103.296(7)
γ / °	103.277(4)	90	90
V /Å³	870.00(8)	2900.55(11)	3047.8(4)
Z	1	4	4
$\rho_{calc.}$ / g cm⁻³	1.566	1.778	1.692
μ / mm⁻¹	1.017	3.215	3.059
F(000)	416	1544	1544
T / K	173	100	240
Diffractometer	STOE STADIVARI	STOE STADIVARI	STOE STADIVARI
Radiation	Mo-Kα	Mo-Kα	Mo-Kα
θ-range for data collection/°	2.215 < θ < 30.673	2.016 < θ < 30.981	1.975 < θ < 30.879
Index ranges	-10 < h < 10 -13 < k < 13 -18 < l < 18	-22 < h < 22 -19 < k < 18 -20 < l < 20	-23 < h < 23 -19 < k < 19 -20 < l < 20
Collected reflections	14168	55015	52405
Independent reflections	4781	56287	53524
Completeness	0.886	0.916	0.913
Max. and min. transmission	0.9010 and 0.1182	0.9913 and 0.4829	0.9540 and 0.1087
R_{Int}	0.0255	0.0309	0.1313
R_{Sigma}	0.0258	0.0310	0.0994
Data / restraints / parameters	4781 / 18 / 233	8440 / 0 / 390	8787 / 0 / 389
Goodness-of-fit on F^2	1.099	1.058	0.941
R₁ [I > 2 σ (I)]	0.0541	0.0288	0.1002
Final wR₂ [I ≥ 2σ(I)]	0.1562	0.0783	0.2481
Final R₁ [alldata]	0.0617	0.0453	0.1622
Final wR₂ [alldata]	0.1633	0.0809	0.2722
Ø M-N-Bindung	2.16(7)	1.98(3)	
Σ / °	67.94	41.24	

Table 15: Crystallographic data of [Fe(L²)₂(NCS)₂] C4 and [Fe(L²)₂(NCSe)₂] C5 measured with a Stoe Stadivari device at 173 K, and 90 K.
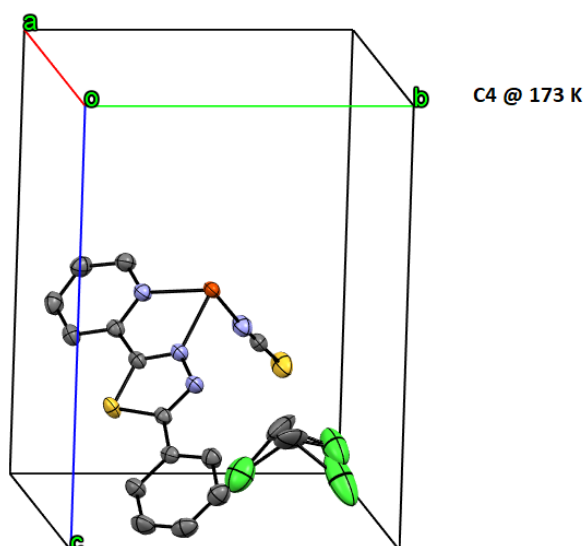
Figure 141: Asymmetric Unit of C4 @ 173 K. View down reciprocal cell axis a*. Color Code: grey-C, yellow-sulfur, blue-N, orange-Fe, green-Cl white-H. ORTEP representation with atomic displacement parameters at 50% level of probability. Hydrogen atoms are omitted for clarity.

Distance / Å		Angle / °	
Distance		Angle	
N4-Fe1	2.09(3)	N2-Fe1-N1	75.36
N4-Fe1	2.09(3)	N1-Fe1-N2	104.64
N2-Fe1	2.18(7)	N2-Fe1-N1	75.36
N1-Fe1	2.23(1)	N1-Fe1-N2	104.64
N2-Fe1	2.18(7)	N4-Fe1-N1	88.78
N1-Fe1	2.23(1)	N4-Fe1-N2	87.96
		N4-Fe1-N1	91.22
		N4-Fe1-N2	92.04
		N4-Fe1-N1	87.96
		N4-Fe1-N2	88.78
		N4-Fe1-N1	92.04
Ø M-N-distance	2.21(6)	$\sum$ / °	67.94

*Table 16: Selected bond lengths and angles including the calculated values of the average F-N-distances and the octahedral distortion parameter $\sum$ of **C4** at 173 K.*

along a

along b

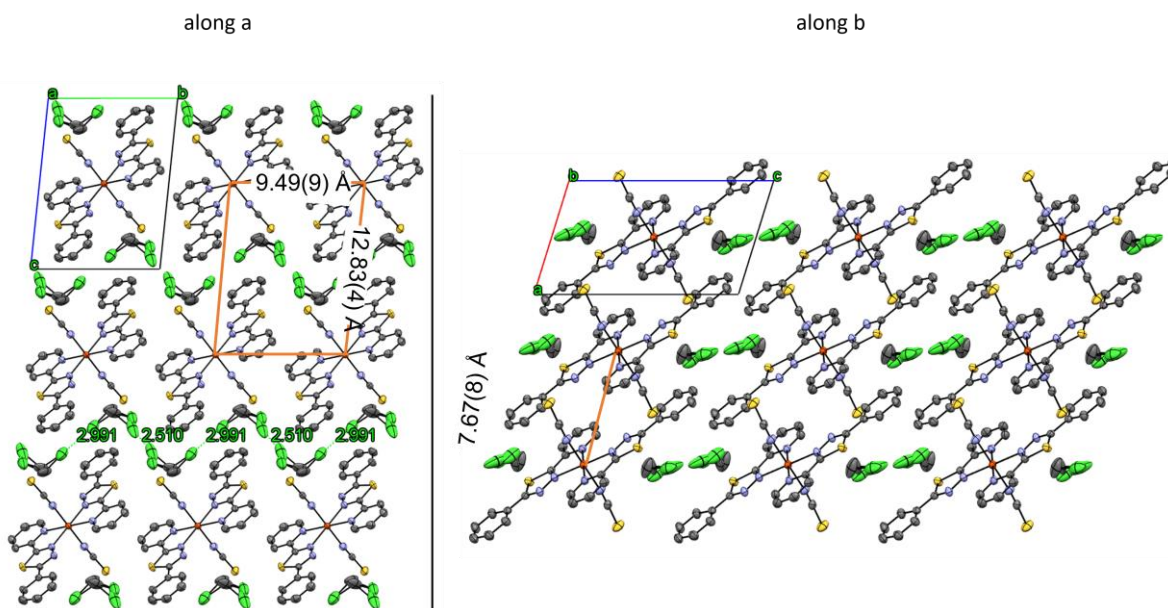*Figure 142: **C4** @ 173 K. View down crystallographic a-axis. Highlighted are alternating distances of dichloromethane solvent molecules along b-axis and the Fe-Fe-distances along the different spatial directions Color Code: grey-C, yellow-sulfur, blue-N, orange-Fe, green-Cl white-H. ORTEP representation with atomic displacement parameters at 50% level of probability. Hydrogen atoms are omitted for clarity.*
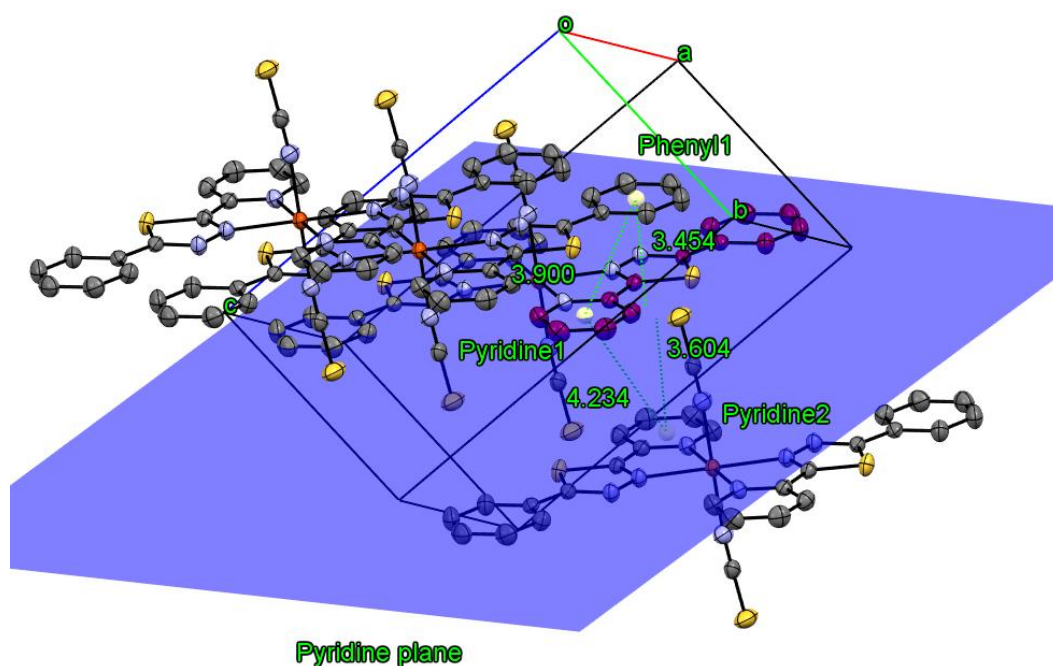
*Figure 143: Representation of all proceeding π-π-interactions of one coordinating ligand **L²** (marked in purple) with anti-parallel aligned ligand molecules of neighbouring **C4** complex molecules at 173 K. The plane named "phenyl plane" and is located in the respective molecular groups of the purple coloured molecule. The points named "Phenyl1", "Pyridin 1 and 2" are the respective centroids of the respective interacting π-systems. The average distance of the π-π-interactions is represented by the respective solder that falls on the plane of the interacting partner. Calculation of the Offset of the π-π-interacting partners was done using the Pythagorean theorem. Color Code: grey-C, yellow-sulfur, blue-N, orange-Fe, white-H. ORTEP representation with atomic displacement parameters at 50% level of probability. Hydrogens and solvent molecules are omitted for clarity.*

	Object1	Object2	Length / Å	Offset of π-π-interacting centroids / Å
Centroid distance perpendicular to respective object plane (average π-π-interaction distance)	Phenyl 1	Pyridine plane	3.45(4)	
	Pyridine 2	Pyridine plane	3.60(4)	
Centroid to Centroid distance	Pyridine 1	Phenyl 1	3.90(0)	1.81(1)
	Pyridine 1	Pyridine 2	4.23(4)	2.22(2)

*Table 17: Overview of all π-π-interactions proceeding from one molecule of **L²** with anti-parallel aligned ligand molecules of neighbouring **C4** complex molecules at 173 K. Calculation of the Offset of the π-π-interacting partners was done using the Pythagorean theorem.*

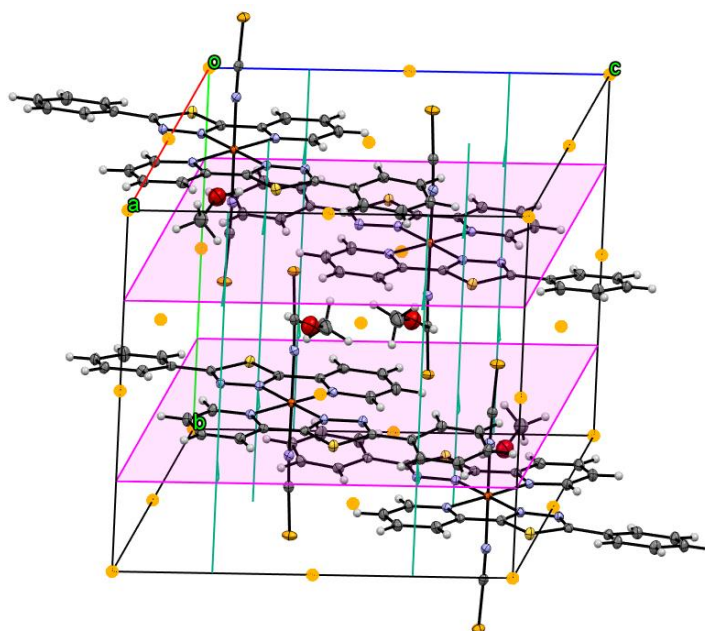*Figure 144: Unit Cell of [Fe(L2)2(NCSe)2] · MeOH (C5) at 90 K. Color Code: grey-C, yellow-sulfur, blue-N, orange-Fe, re-Ol white-H. Centres of inversion are represented by yellow dots, glides are shown in magenta while 2-fold screw axis are shown in cyan. ORTEP representation with atomic displacement parameters at 50% level of probability. Hydrogen atoms are omitted for clarity.*

along a　　　　　　　　　along b　　　　　　　　　along c
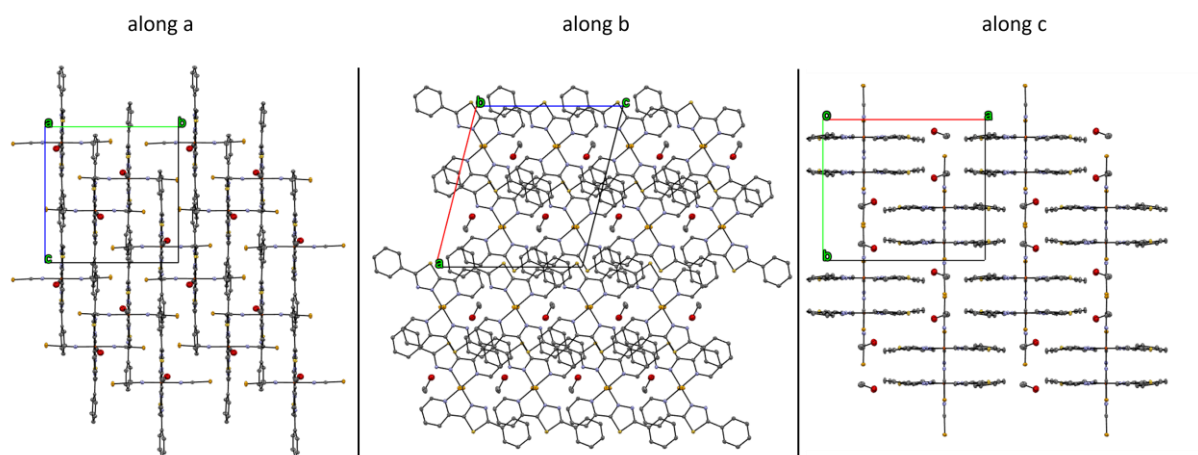
*Figure 145: **along a**: Selected part of the crystal structure of **C5** along the a-axis. **along b:** Selected part of the crystal structure of C5 along the b-axis.; **along c:** Selected part of the crystal structure of C5 along the c-axis. Color Code: grey-C, yellow-S, blue-N, orange-Fe, red-O, white-H. ORTEP representation with atomic displacement parameters at 50% level of probability.*

Distance / Å		Angle / °	
Fe1-N4	2.02(3)	N5-Fe1-N4	80.1(5)
Fe1-N5	1.98(3)	N4-Fe1-N2	99.7(4)
Fe1-N1	2.01(9)	N2-Fe1-N1	80.3(3)
Fe1-N2	1.98(5)	N2-Fe1-N4	99.7(4)
Fe1-N8	1.94(5)	N4-Fe1-N5	80.1(5)
Fe1-N7	1.94(2)	N5-Fe1-N1	99.8(0)
		N1-Fe1-N2	80.3(3)
		N7-Fe1-N2	89.8(4)
		N7-Fe1-N4	90.9(6)
		N7-Fe1-N5	89.6(5)
		N7-Fe1-N1	89.8(9)
		N8-Fe1-N1	89.6(2)
Ø M-N-distance	1.98(3)	∑ / °	41.2(4)

*Table 18: Selected bond lengths and angles including the calculated values of the average F-N-distances and the octahedral distortion parameter ∑ of **C5** at 90 K.*
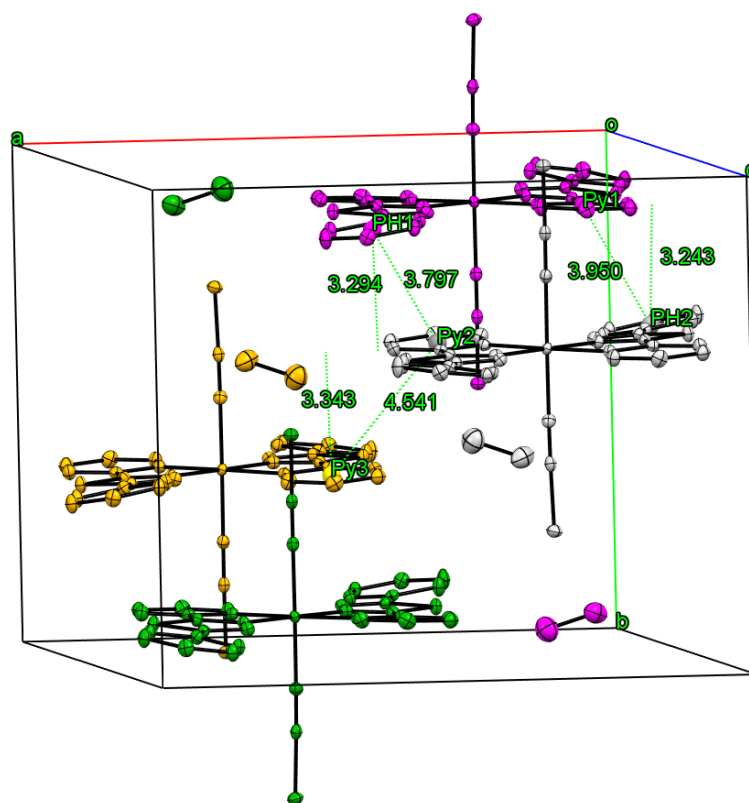
*Figure 146: Representation of all proceeding π-π-interactions of one coordinating ligand **L²** with anti-parallel aligned ligand molecules of neighbouring **C5** complex molecules at 90 K. The points named Py1, PH1, Py2, PH2 and Py3 are the respective centroids of the respective interacting π-systems. The average distance of the π-π-interactions is represented by the respective solder that falls on the plane of the interacting partner. Calculation of the Offset of the π-π-interacting partners was done using the Pythagorean theorem. Color code represent the respective symmetry operation. ORTEP representation with atomic displacement parameters at 50% level of probability. Hydrogens and solvent molecules are omitted for clarity.*

	Object1	Object2	Length / Å	Offset of π-π-interacting centroids / Å
Centroid distance perpendicular to respective object plane (average π-π-interaction distance)	PH 2	Py1 plane	3.24(3)	
	PH1	Py2 plane	3.29(4)	
	Py3	Py2 plane	3.34(3)	
Centroid to Centroid distance	Py1	PH2	3.95(0)	
	PH1	Py2	3.79(7)	
	Py2	Py3	4.54(1)	

*Table 19: Overview of all π-π-interactions proceeding from one molecule of **L²** with anti-parallel aligned ligand molecules of neighbouring **C4** complex molecules at 173 K. Calculation of the Offset of the π-π-interacting partners was done using the Pythagorean theorem.*

Distance / Å		Angle / °	
Fe1-N4	2.18(8)	N5-Fe1-N4	75.5(9)
Fe1-N5	2.15(2)	N5-Fe1-N1	103.8(2)
Fe1-N7	2.07(7)	N1-Fe1-N2	75.6(6)
Fe1-N1	2.17(6)	N2-Fe1-N4	104.9(3)
Fe1-N8	2.09(7)	N7-Fe1-N4	90.2(4)
Fe1-N2	2.16(3)	N7-Fe1-N5	89.8(2)
		N7-Fe1-N1	90.4(8)
		N7-Fe1-N2	90.0(8)
		N8-Fe1-N2	88.6(9)
		N8-Fe1-N1	90.0(5)
		N8-Fe1-N5	92.0(1)
		N8-Fe1-N4	89.2(5)
Ø M-N-distance	2.14(2)	$\sum$ / °	62.6(0)

*Table 20: Selected bond lengths and angles including the calculated values of the average F-N-distances and the octahedral distortion parameter $\sum$ of **C5** at 240 K.*

11.4.3.   [Fe^{II}(L^1)$_2$(NCX)$_2$] · n(Solv) (**C7**, **C8**, **C9**)

Compound	[Fe(L^3)$_2$(NCS)$_2$] C7	[Fe(L^3)$_2$(NCSe)$_2$] C8
Empirical formula	C44H26FeN8S4	C44H26FeN8S2Se2
Formula weight / g mol^{-1}	850.82	944.62
Crystal size / mm	0.09 x 0.049 x 0.008	0.07 x 0.052 x 0.02
Crystal system	triclinic	triclinic
Space group	P-1	P-1
Unit cell dimensions		
a / Å	8.2156(11)	8.2718(15)
b / Å	10.5031(16)	10.5941(19)
c / Å	11.0020(18)	11.1235(19)
α / °	86.480(13)	85.850(14)
β / °	86.568(12)	87.421(15)
γ / °	84.625(11)	83.080(15)
V /Å^3	942.0(2)	964.5(3)
Z	1	1
$\rho_{calc.}$ / g cm^{-3}	1.500	1.626
μ / mm^{-1}	0.668	2.432
F(000)	436	472
T / K	120	173
Diffractometer	STOE STADIVARI	STOE STADIVARI
Radiation	Mo-Kα	Mo-Kα
θ-range for data collection/°	2.494 < θ < 30.903	1.941 < θ < 25.999
Index ranges	-11 < h < 11 -15 < h < 14 -15 < h < 13	-9 < h < 10 -12 < h < 13 -13 < h < 13
Collected reflections	12936	13785
Independent reflections	12936	17467
Completeness	0.857	0.999
Max. and min. transmission	0.9795 and 0.1177	0.9033 and 0.1064
R_{Int}	0.1403	0.0729
R_{Sigma}	0.2573	0.0870
Data / restraints / parameters	5104 / 0 / 259	3796 / 0 / 259
Goodness-of-fit on F^2	0.765	0.903
R$_1$ [I > 2 σ (I)]	0.0669	0.0535
Final wR$_2$ [I ≥ 2σ(I)]	0.1325	0.1263
Final R$_1$ [alldata]	0.1983	0.0862
Final wR$_2$ [alldata]	0.1635	0.1376
Ø M-N-Bindung	2.16(7)	2.16(9)
Σ / °	77.7(2)	79.5(2)

*Table 21: crystallographic data of [Fe(L^3)$_2$(NCS)$_2$] **C7** and [Fe(L^3)$_2$(NCSe)$_2$] **C8**.*

Compound	$[Fe(L^3)_2(CN)_2]\cdot 1.15\ CH_2Cl_2\cdot 2.85\ MeOH$ C9 at 120 K	$[Fe(L^3)_2(CN)_2]\cdot 1.15\ CH_2Cl_2\cdot 2.85\ MeOH$ C9 at 240 K
Empirical formula	C48H39.70Cl2.30FeN8O2.85S2	C48H36Cl2FeN8O3S2
Formula weight / g mol^{-1}	975.68	963.73
Crystal size / mm	0.13 x 0.098 x 0.035	0.130 x 0.098 x 0.035
Crystal system	monoclinic	
Space group	P121/c1	
Unit cell dimensions		
a / Å	20.8725(5)	10.9236(10)
b / Å	19.8431(4)	20.1041(14)
c / Å	10.8507(3)	20.8394(23)
α / °	90.00	90.00
β / °	93.564(2)	92.913(8)
γ / °	90.00	90.00
V /Å^3	4485.40(19)	4570.6(7)
Z	4	1
$\rho_{calc.}$ / g cm^{-3}	1.445	0.350
μ / mm^{-1}	0.619	0.15
F(000)	2014	496
T / K	120	240
Diffractometer	STOE STADIVARI	STOE STADIVARI
Radiation	Mo-Kα	Mo-Kα
θ-range for data collection/°	1.955 < θ < 30.919	1.87 < θ < 21.25
Index ranges	-30 < h < 29 -28 < h < 22 -15 < h < 15	-10 < h < 10 -20 < h < 15 -10 < h < 19
Collected reflections	42630	6563
Independent reflections	42633	3193
Completeness	0.893	
Max. and min. transmission	0.9421 and 0.8409	and
R_{Int}	0.0319	0.1147
R_{Sigma}	0.0537	0.0452
Data / restraints / parameters	12683 / 56 / 649	- / - / -
Goodness-of-fit on F^2	0.944	/
R$_1$ [I > 2 σ (I)]	0.0419	/
Final wR$_2$ [I ≥ 2σ(I)]	0.1107	/
Final R$_1$ [alldata]	0.0698	/
Final wR$_2$ [alldata]	0.1193	/
Ø M-N-Bindung	/	/
Σ / °	/	/

*Table 22: crystallographic data of $[Fe(L^3)_2(CN)_2]\cdot 1.15\ CH_2Cl_2\cdot 2.85\ MeOH$ **C9** at 120 K and 240 K.*
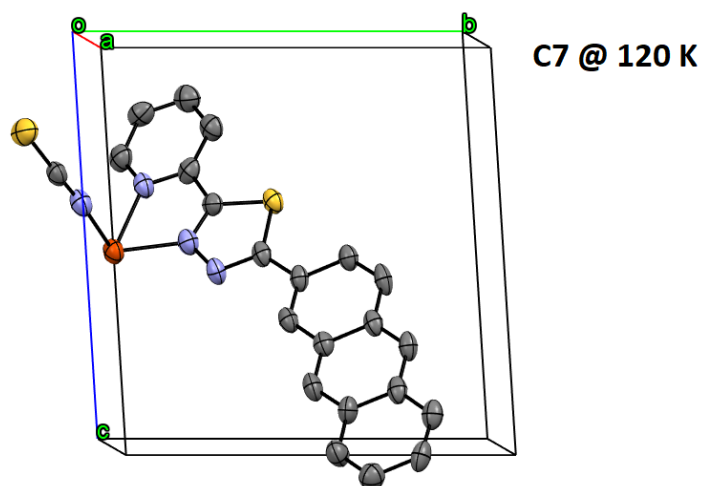
*Figure 147: Asymmetric Unit of **C7** @ 120 K. View down reciprocal cell axis a*, i.e. perpendicular to bc-plane. Color Code: grey-C, yellow-sulfur, blue-N, orange-Fe, white-H. ORTEP representation with atomic displacement parameters at 50% level of probability.*

Distance / Å		Angle / °	
Distance		Angle	
N2-Fe1	2.19(6)	N2-Fe1-N1	75.7(1)
N1-Fe1	2.21(5)	N1-Fe1-N2	104.2(9)
N4-Fe1	2.10(0)	N2-Fe1-N1	75.7(1)
N2-Fe1	2.19(6)	N1-Fe1-N2	104.2(9)
N4-Fe1	2.10(0)	N4-Fe1-N2	86.8(5)
N1-Fe1	2.21(5)	N4-Fe1-N1	91.9(9)
		N4-Fe1-N2	93.1(5)
		N4-Fe1-N1	88.0(1)
		N4-Fe1-N1	91.9(9)
		N4-Fe1-N2	86.8(5)
		N4-Fe1-N1	88.0(1)
		N4-Fe1-N2	93.1(5)
Ø M-N-distance	2.16(7)	$\sum$ / °	77.7(2)

*Table 23: Selected bond lengths and angles including the calculated values of the average F-N-distances and the octahedral distortion parameter $\sum$ of **C7** at 120 K.*
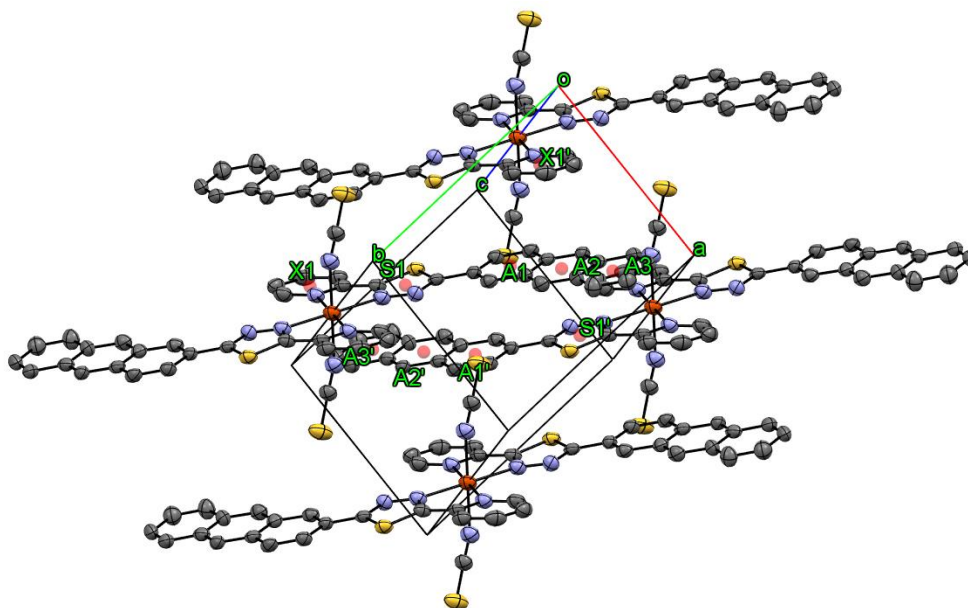
*Figure 148: Packing of **C7** complex molecules at 120 K. The points named X1, X1', S1, S1', A1, A2, A3, A1', A2' and A3' are the respective centroids of the respective interacting π-systems. Color Code: grey-C, yellow-sulfur, blue-N, orange-Fe, white-H. ORTEP representation with atomic displacement parameters at 50% level of probability. Hydrogens and solvent molecules are omitted for clarity.*
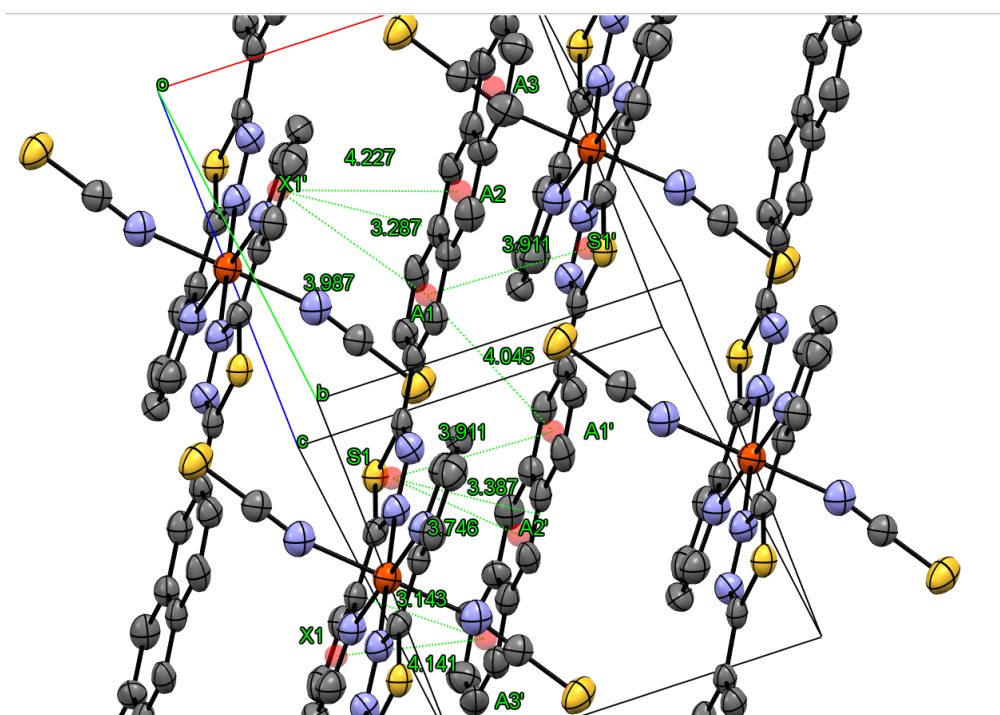
*Figure 149: Representation of all proceeding π-π-interactions of one coordinating ligand L3 with anti-parallel aligned ligand molecules of neighbouring **C7** complex molecules at 120 K. The points named X1, X1', S1, S1', A1, A2, A3, A1', A2' and A3' are the respective centroids of the respective interacting π-systems. The average distance of the π-π-interactions is represented by the respective solder that falls on the plane of the interacting partner. Calculation of the Offset of the π-π-interacting partners was done using the Pythagorean theorem. Color Code: grey-C, yellow-sulfur, blue-N, orange-Fe, white-H. ORTEP*

representation with atomic displacement parameters at 50% level of probability. Hydrogens and solvent molecules are omitted for clarity.

	Object1	Object2	Length / Å	Offset of π-π-interacting centroids / Å
Centroid distance perpendicular to respective object plane (average π-π-interaction distance)	X1'	Anthracene plane	3.28(7)	
	A3'	Pyridine plane	3.14(3)	
	S1	Anthracene plane	3.38(7)	
	A1'	Anthracene plane	3.40(0)	
Centroid to Centroid distance	X1'	A1	3.98(7)	2.25(6)
	X1'	A2	4.22(7)	2.65(7)
	A3'	X1	4.14(1)	1.73(6)
	A1	A1'	4.04(5)	2.19(1)
	A1	S1'	3.91(1)	1.95(5)
	S1	A2'	3.74(6)	1.60(0)
	S1	A1'	3.91(1)	1.95(5)

*Table 24: Overview of all π-π-interactions proceeding from one molecule of **L3** with anti-parallel aligned ligand molecules of neighbouring **C7** complex molecules at 120 K. Calculation of the Offset of the π-π-interacting partners was done using the Pythagorean theorem.*
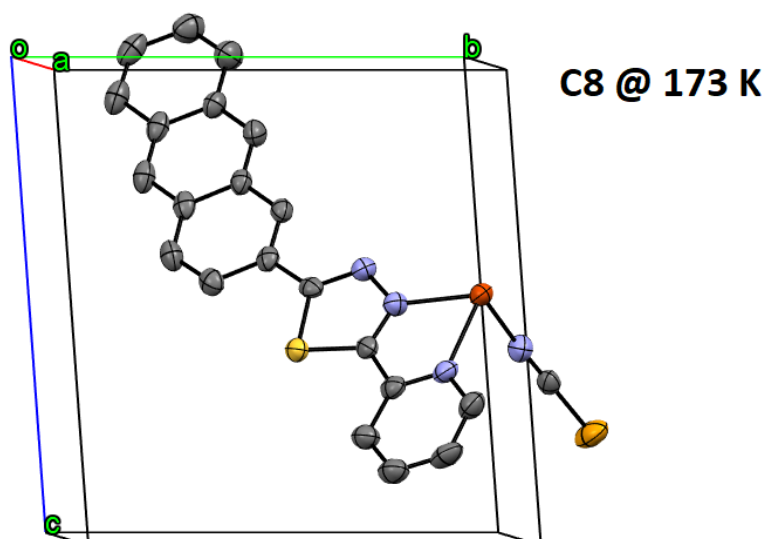

*Figure 150: Asymmetric Unit of **C8** @ 173 K. View down reciprocal cell axis a*, i.e. perpendicular to bc-plane. Color Code: grey-C, yellow-sulfur, blue-N, orange-Fe, light orange-Se, white-H. ORTEP representation with atomic displacement parameters at 50% level of probability.*

Distance / Å		Angle / °	
N1-Fe1	2.20(7)	N2-Fe1-N1	75.4(9)
N2-Fe1	2.20(1)	N1-Fe1-N2	104.5(1)
N4-Fe1	2.10(1)	N2-Fe1-N1	75.4(9)
N1-Fe1	2.20(7)	N1-Fe1-N2	104.5(1)
N2-Fe1	2.20(1)	N4-Fe1-N1	91.4(2)
N4-Fe1	2.10(1)	N4-Fe1-N2	86.0(5)
		N4-Fe1-N1	88.5(8)
		N4-Fe1-N2	93.9(5)
		N4-Fe1-N2	86.0(5)
		N4-Fe1-N1	91.4(2)
		N4-Fe1-N2	93.9(5)
		N4-Fe1-N1	88.5(8)
Ø M-N-distance	2.16(9)	$\sum$ / °	79.5(2)

*Table 25: Selected bond lengths and angles including the calculated values of the average F-N-distances and the octahedral distortion parameter $\sum$ of **C8** at 173 K.*
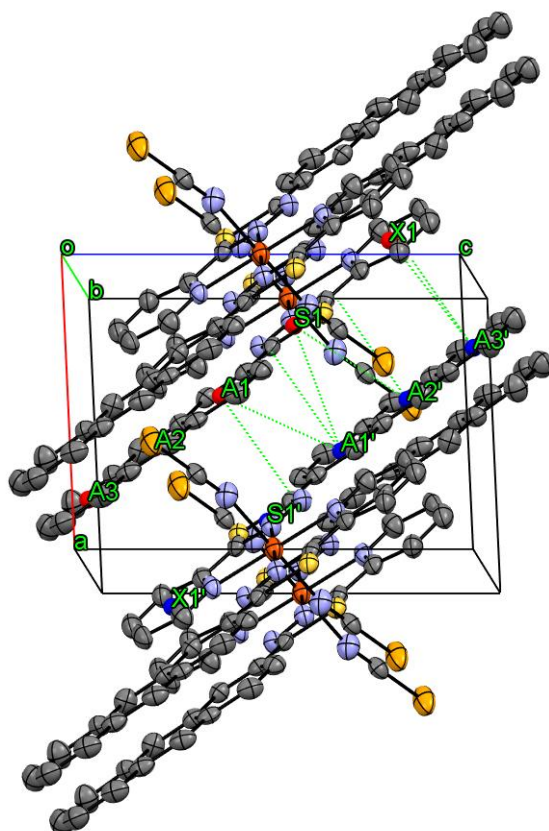

*Figure 151: Packing of **C8** complex molecules at 173 K. The points named X1, X1', S1, S1', A1, A2, A3, A1', A2' and A3' are the respective centroids of the respective interacting π-systems. View down reciprocal cell axis b*, i.e. perpendicular to ac-plane. Color Code: grey-C, yellow-sulfur, blue-N, orange-Fe, light orange-Se, white-H. ORTEP representation with atomic displacement parameters at 50% level of probability. Hydrogens and solvent molecules are omitted for clarity.*
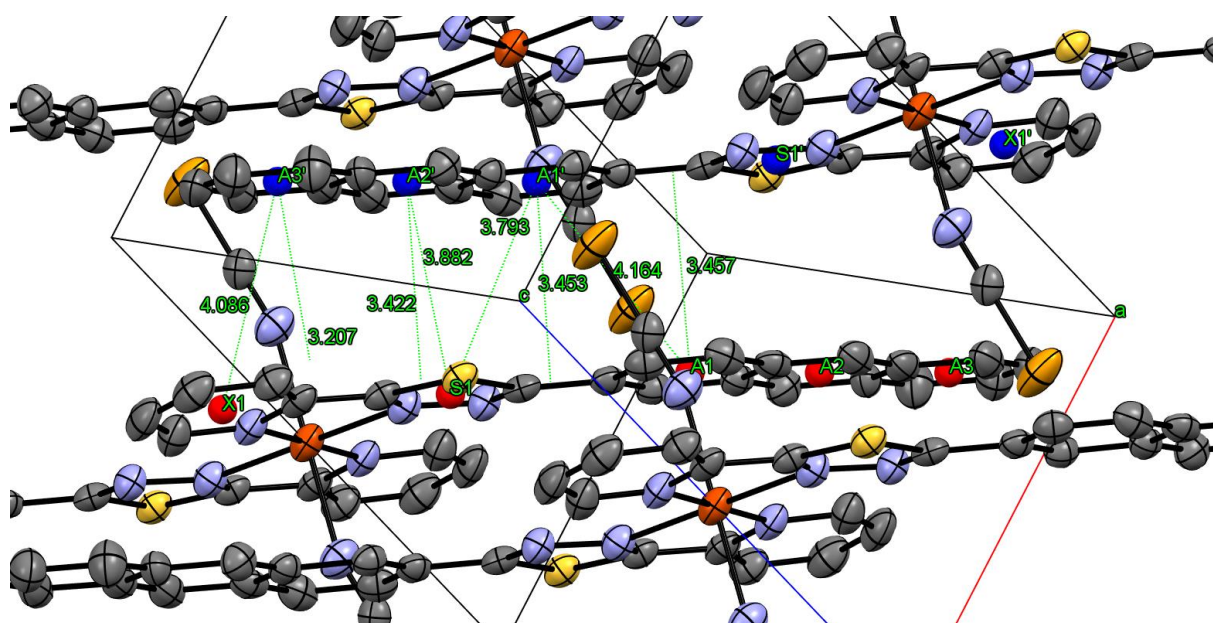
*Figure 152: Representation of all proceeding π-π-interactions of one coordinating ligand L3 with anti-parallel aligned ligand molecules of neighbouring **C8** complex molecules at 173 K. The points named X1, X1', S1, S1', A1, A2, A3, A1', A2' and A3' are the respective centroids of the respective interacting π-systems. The average distance of the π-π-interactions is represented by the respective solder that falls on the plane of the interacting partner. Calculation of the Offset of the π-π-interacting partners was done using the Pythagorean theorem. Color Code: grey-C, yellow-sulfur, blue-N, orange-Fe, light orange-Se, white-H. ORTEP representation with atomic displacement parameters at 50% level of probability. Hydrogens and solvent molecules are omitted for clarity.*

	Object1	Object2	Length / Å	Offset of π-π-interacting centroids / Å
Centroid distance perpendicular to respective object plane (average π-π-interaction distance)	A1'	Thiadiazole plane	3.45(3)	
	A3'	Pyridine plane	3.20(7)	
	A2'	Anthracene plane	3.42(2)	
	A1	Anthracene plane	3.45(7)	
Centroid to Centroid distance	X1	A3'	4.08(6)	2.53(2)
	A2'	S1	3.79(3)	1.83(3)
	A1'	S1	3.88(2)	1.56(9)
	A1'	A1	4.16(4)	3.32(1)

*Table 26: Overview of all π-π-interactions proceeding from one molecule of **L3** with anti-parallel aligned ligand molecules of neighbouring **C8** complex molecules at 173 K. Calculation of the Offset of the π-π-interacting partners was done using the Pythagorean theorem.*
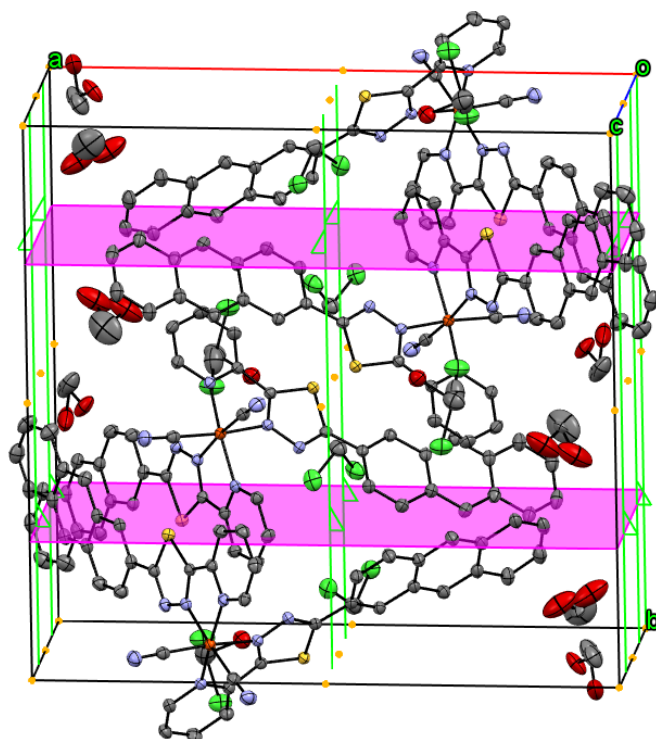
*Figure 153: Unit Cell of **[Fe^{II}(L^3)$_2$(CN)$_2$] · 1.15 CH$_2$Cl$_2$ · 2.85 MeOH (C9)** at 120 K. Color Code: grey-C, yellow-sulfur, blue-N, orange-Fe, red-O, green-Cl, white-H. Centres of inversion are represented by yellow dots, glides are shown in magenta while 2-fold screw axis are shown in green. ORTEP representation with atomic displacement parameters at 50% level of probability. Hydrogen atoms are omitted for clarity.*
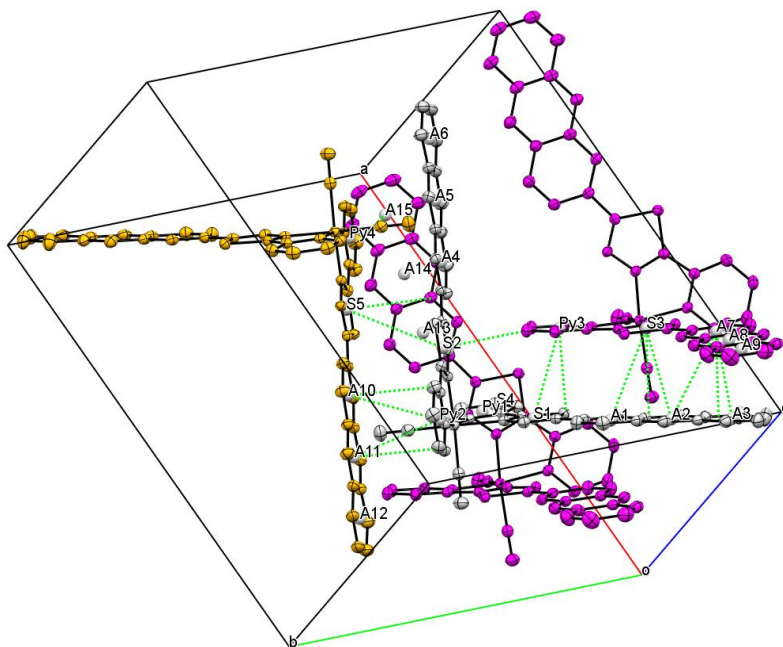

*Figure 154: Packing of **[Fe^{II}(L^3)$_2$(CN)$_2$] · 1.15 CH$_2$Cl$_2$ · 2.85 MeOH (C9)** complex molecules at 120 K. The points named A1-16, Py1-5 and S1-5 are the respective centroids of the respective interacting π-systems. Color code represent the respective symmetry operation. ORTEP representation with atomic displacement parameters at 50% level of probability. Green dotted lines represent the distances from centroid to centroid and the actual π-π-interactions. Hydrogens and solvent molecules are omitted for clarity.*
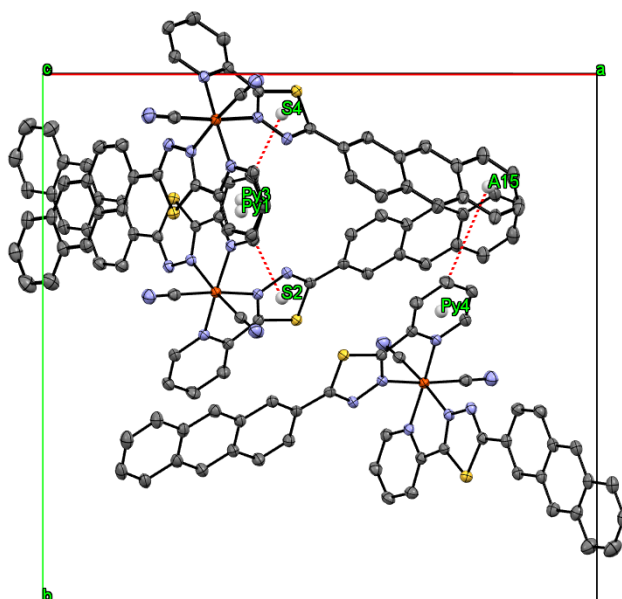
Figure 155: Packing of [Fe^{II}(L^3)$_2$(CN)$_2$] · 1.15 CH$_2$Cl$_2$ · 2.85 MeOH (C9) complex molecules at 120 K. View down along crystallographic c-axis The points named A15, Py1-4 and S2 and S4 are the respective centroids of the CH··· π respective interacting systems. Color Code: grey-C, yellow-sulfur, blue-N, orange-Fe, light, green-Cl, white-H. ORTEP representation with atomic displacement parameters at 50% level of probability. Red dotted lines represent the distances T-shaped CH···π-interactions. Hydrogens and solvent molecules are omitted for clarity.

Distance / Å		Angle / °	
N4-Fe1	1.98(1)	N1-Fe1-N2	80.30
N5-Fe1	1.98(5)	N2-Fe1-N4	91.47
N1-Fe1	1.98(3)	N4-Fe1-C44	93.58
N2-Fe1	1.94(8)	N1-Fe1-C44	94.85
C43-Fe1	1.91(4)	N5-Fe1-N1	92.32
C44-Fe1	1.91(4)	N5-Fe1-N2	91.66
		N5-Fe1-N4	81.06
		N5-Fe1-C44	90.50
		C43-Fe1-C44	88.12
		C43-Fe1-N4	91.90
		C43-Fe1-N2	90.32
		C43-Fe1-N1	94.91
		Fe-C44-N8	179.22
		Fe-C43-N7	176.23

Table 27: Selected bond lengths and of C9 at 120 K.

Centroid to Centroid distance	Object1	Object2	Length / Å	Offset of π-π-interacting centroids / Å
	A7	A3	3.63(5)	0.94(1)
	A7	A2	4.15(2)	2.21(6)
	S3	A2	3.99(4)	1.96(2)
	S3	A1	4.01(6)	2.00(6)

	Py3	S1	3.68(1)	1.45(3)
	Py2	A11	3.70(1)	1.49(8)
	Py2	A10	3.70(2)	1.44(1)
	S5	S2	4.16(5)	2.36(4)
Centroid distance perpendicular to respective object plane (average π-π-interaction distance)	S3	Anthracene A1, A2, A3	3.47(9)	
	A7	Anthracene A1, A2, A3	3.51(1)	
	Py3	Thiadiazole S1	3.38(2)	
	A11	Pyridine P2	3.38(1)	
	A10	Pyridine P2	3.4(10)	
	S5	Thiadiazole S2	3.42(9)	
T-shape CH···π distances	C24	S4	3.37(9)	
	S2	C24	3.37(9)	
	C3	A15	4.08(9)	

*Table 28: Overview of all π-π-interactions proceeding from one molecule of **L³** with anti-parallel aligned ligand molecules of neighbouring **C9** complex molecules at 120 K. Calculation of the Offset of the π-π-interacting partners was done using the Pythagorean theorem.*

11.4.4. $[Fe^{II}(L^1)_2(NCX)_2] \cdot n(Solv)$ (**C10**, **C11**, **C12**)

Compound	$[Fe^{II}(L^4)_2(NCS)_2] \cdot 2$ CH$_2$Cl$_2$ C10	$[Fe^{II}(L^4)_2(NCSe)_2] \cdot 2$ CH$_2$Cl$_2$ C11	$[Fe^{II}(L^4)_2(NCBH_3)_2] \cdot 2$ CH$_2$Cl$_2$ C12
Empirical formula	C39H28Cl2FeN8O2S4	C39H28Cl2FeN8O2S2Se2	C39H34B2Cl2FeN8O2S2
Formula weight / g mol^{-1}	895.68	989.48	859.23
Crystal size / mm	0.1 x 0.063 x 0.04	0.06 x 0.045 x 0.02	0.05 x 0.027 x 0.01
Crystal system	triclinic	triclinic	triclinic
Space group	P-1	P-1	P-1
Unit cell dimensions			
a / Å	9.1486(7)	9.2058(5)	9.1476(7)
b / Å	9.3149(7)	9.3650(6)	9.3286(7)
c / Å	12.3427(9)	12.3209(8)	12.1172(9)
α / °	81.118(6)	81.398(5)	80.435(6)
β / °	73.150(6)	73.040(5)	74.135(6)
γ / °	87.799(7)	87.022(5)	87.554(6)
V /Å^3	994.57(13)	1004.55(11)	980.79(13)
Z	1	1	1
$\rho_{calc.}$ / g cm^{-3}	1.495	1.636	1.455
μ / mm^{-1}	0.770	2.471	0.674
F(000)	458	494	442
T / K	173(2)	173(2)	100(2)
Diffractometer	STOE STADIVARI	STOE STADIVARI	STOE STADIVARI
Radiation	Mo-Kα	Mo-Kα	Mo-Kα
θ-range for data collection/°	2.213 < θ < 30.891	2.200 < θ < 30.744	2.214 < θ < 30.374
Index ranges	-12 < h < 12 −13 < k < 12 −15 < l < 17	-12 < h < 13 −13 < k < 12 −17 < l < 13	-12 < h < 13 −13 < k < 13 −17 < l < 16
Collected reflections	16314	12859	12319
Independent reflections	5541	5511	5223
Completeness	0.883	0.879	0.885
Max. and min. transmission	0.9714 and 0.3743	1.0000 and 0.4154	0.9984 and 0.5593
R_{Int}	0.0469	0.0415	0.0861
R_{Sigma}	0.0680	0.0542	0.1485
Data / restraints / parameters	5541 / 0 / 269	5511 / 0 / 269	5223 / 0 / 270
Goodness-of-fit on F^2	1.009	1.009	1.084
R_1 [I > 2 σ (I)]	0.0587	0.0589	0.0968
Final wR$_2$ [I ≥	0.1215	0.1392	0.1723

2σ(I)]			
Final R_1 [alldata]	0.1226	0.1004	0.2104
Final wR_2 [alldata]	0.1461	0.1622	0.2176
Ø M-N-Bindung	2.16(4)	2.12(7)	1.99(2)
∑ / °	66.8(8)	64.8(8)	48.4(0)

Table 29: Crystallographic datat of [Fe^II(L^4)_2(NCS)_2] · 2 CH_2Cl_2 C10, [Fe^II(L^4)_2(NCSe)_2] · 2 CH_2Cl_2 C11 and [Fe^II(L^4)_2(NCBH_3)_2] · 2 CH_2Cl_2 C12.

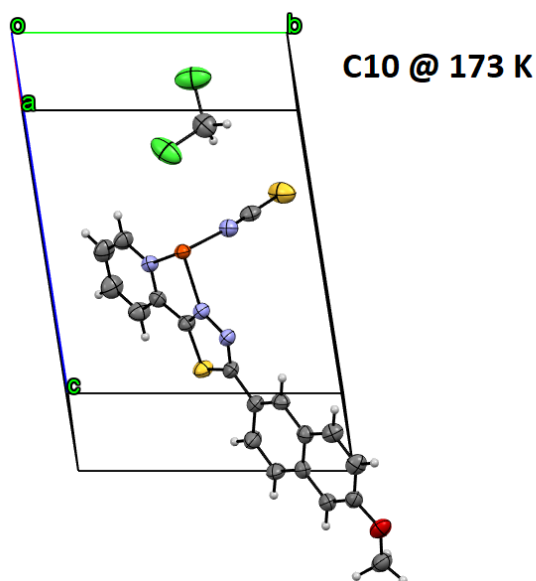*Figure 156: Asymmetric Unit of **C10** at 173 K. View down reciprocal cell axis a*, i.e. perpendicular to bc-plane. Color Code: grey C, yellow-sulfur, blue-N, orange-Fe, red-O, green-Cl, white-H. ORTEP representation with atomic displacement parameters at 50% level of propability.*

Distance / Å		Angle / °	
N3-Fe1	2.20(4)	N3-Fe1-N1	75.5(5)
N1-Fe1	2.18(8)	N1-Fe1-N3	104.4(5)
N4-Fe1	2.10(1)	N3-Fe1-N1	75.5(5)
N3-Fe1	2.20(4)	N1-Fe1-N3	104.4(5)
N1-Fe1	2.18(8)	N4-Fe1-N3	91.4(2)
N4-Fe1	2.10(1)	N4-Fe1-N1	90.8(5)
		N4-Fe1-N3	88.5(8)
		N4-Fe1-N1	89.1(5)
		N4-Fe1-N1	90.8(5)
		N4-Fe1-N3	91.4(2)
		N4-Fe1-N1	89.1(5)
		N4-Fe1-N3	88.5(8)
Ø M-N-distance	2.16(4)	∑ / °	66.8(8)

*Table 30: Selected bond lengths and angles including the calculated values of the average F-N-distances and the octahedral distortion parameter ∑ of **C10** at 173 K.*
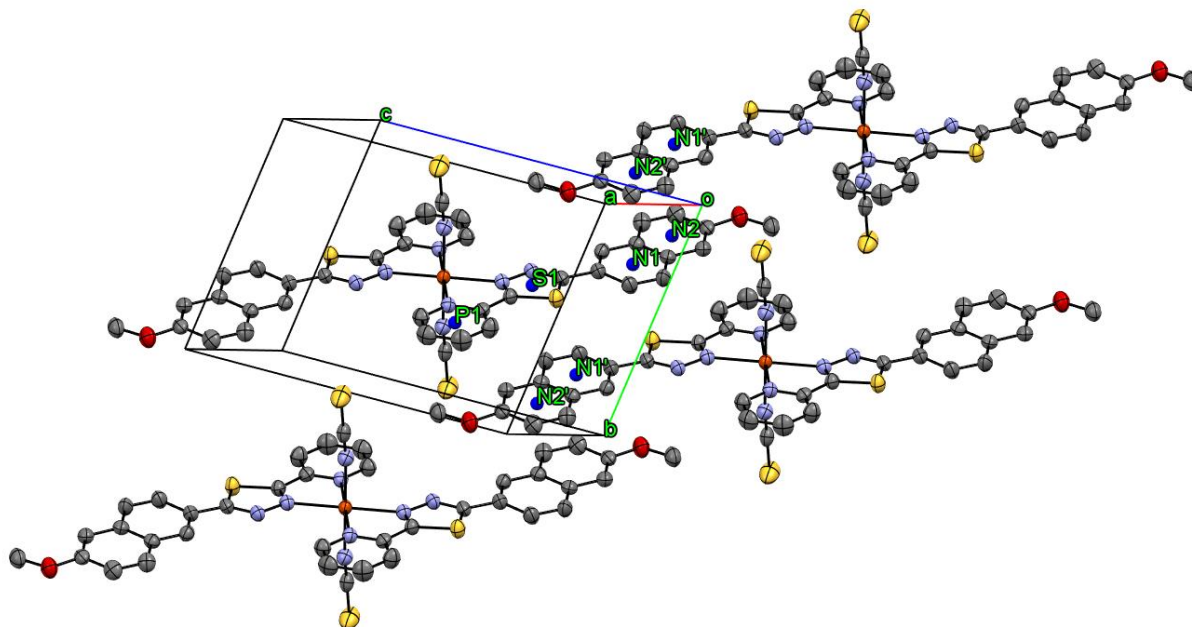
*Figure 157: Expended contacts of **C10** complex molecules at 173 K. The points named P1, S1, N1, N2, N1'adnd N2' are the respective centroids of the respective interacting π-systems. Color Code: grey-C, yellow-sulfur, blue-N, orange-Fe, light green-Cl, red-O, white-H. ORTEP representation with atomic displacement parameters at 50% level of probability. Hydrogens and solvent molecules are omitted for clarity.*
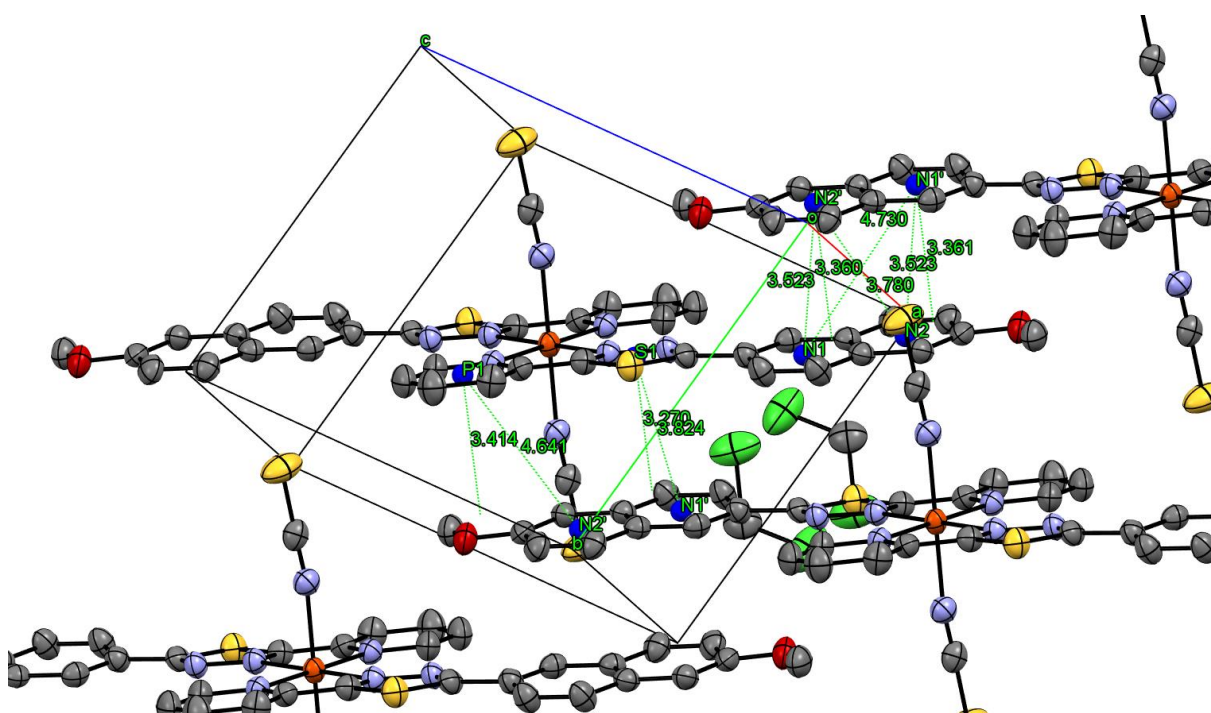

*Figure 158: Representation of all proceeding π-π-interactions of one coordinating ligand **L⁴** with anti-parallel aligned ligand molecules of neighbouring **C10** complex molecules at 173 K. The points named P1, S1, N1, N2, N1'adnd N2' are the respective centroids of the respective interacting π-systems. The average distance of the π-π-interactions is represented by the respective solder that falls on the plane of the interacting partner. Calculation of the Offset of the π-π-interacting partners was done using the Pythagorean theorem. Color Code: grey-C, yellow-sulfur, blue-N, orange-Fe, green-Cl, red-O, white-H. ORTEP representation with atomic displacement parameters at 50% level of probability. Hydrogens are omitted for clarity.*

	Object1	Object2	Length / Å	Offset of π-π-interacting centroids / Å
Centroid distance perpendicular to respective object plane (average π-π-interaction distance)	P1	Naphthyl plane (N1',N2')	3.41(4)	
	S1	Naphthyl plane (N1',N2')	3.27(0)	
	N2'	Napthyl plane (N1, N2)	3.36(0)	
	N1'	Napthyl plane (N1, N2)	3.36(1)	
Centroid to Centroid distance	N2'	N1	3.52(3)	1.05(9)
	N2	N1'	3.52(3)	1.05(6)
	N2'	N2	3.7(8)	3.30(6)
	P1	N2'	4.64(1)	3.14(4)
	S1	N1'	3.82(4)	1.98(2)

*Table 31: Overview of all π-π-interactions proceeding from one molecule of **L⁴** with anti-parallel aligned ligand molecules of neighbouring **C10** complex molecules at 173 K. Calculation of the Offset of the π-π-interacting partners was done using the Pythagorean theorem.*
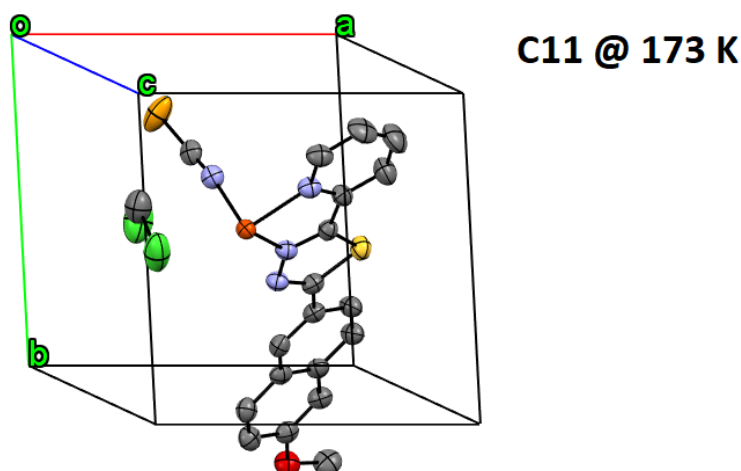

*Figure 159: Asymmetric Unit of **C11** at 173 K. View down reciprocal cell axis c*, i.e. perpendicular to ab-plane. Color Code: grey C, yellow-sulfur, blue-N, orange-Fe, red-O, green-Cl, light-orange-Se, white-H. ORTEP representation with atomic displacement parameters at 50% level of propability.*

Distance / Å		Angle / °	
N3-Fe1	2.15(9)	N3-Fe1-N1	76.6(1)
N1-Fe1	2.14(8)	N1-Fe1-N3	103.3(9)
N3-Fe1	2.15(9)	N3-Fe1-N1	76.6(1)
N1-Fe1	2.14(8)	N1-Fe1-N3	103.3(9)
N4-Fe1	2.07(5)	N4-Fe1-N3	88.1(3)
N4-Fe1	2.07(5)	N4-Fe1-N1	89.0(4)
		N4-Fe1-N3	91.8(7)
		N4-Fe1-N1	90.9(6)
		N4-Fe1-N1	89.0(4)
		N4-Fe1-N3	88.1(3)
		N4-Fe1-N1	90.9(6)
		N4-Fe1-N3	91.8(7)
		Fe1-N4-C19	171.4(4)
		N4-C19-Se1	179.2(4)
Ø M-N-distance	2.12(7)	$\sum$ / °	64.8(8)

*Table 32: Selected bond lengths and angles including the calculated values of the average F-N-distances and the octahedral distortion parameter ∑ of **C11** at 173 K.*
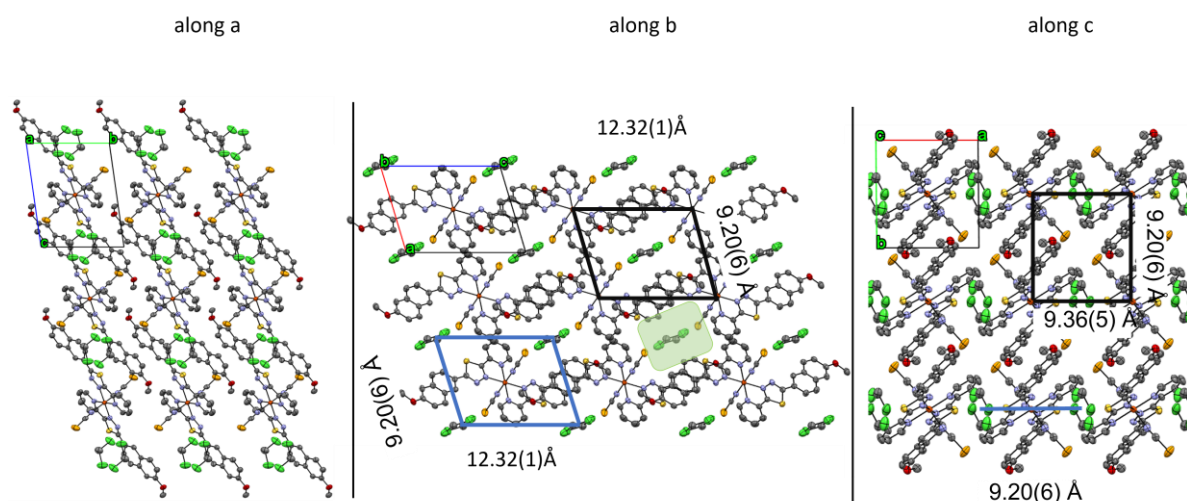

*Figure 160: **along a**: Selected part of the crystal structure of **C11** at 173 K along the a-axis. **along b:** Selected part of the crystal structure of **C11** at 173 K along the b-axis. **along c:** Selected part of the crystal structure of **C11** at 173 K along the c-axis. Color Code: grey-C, yellow-sulphur, blue-N, orange-Fe, green-Cl, light orange-Se, white-H. ORTEP representation with atomic displacement parameters at 50% level of probability. Highlighted are the π-π-interacting anti-parallel aligned ligands of neighbouring complex molecules, respectively. Highlighted are the Fe-Fe distances (black boxes) along the different axis and the distances of the centre of the cavities (blue box).*
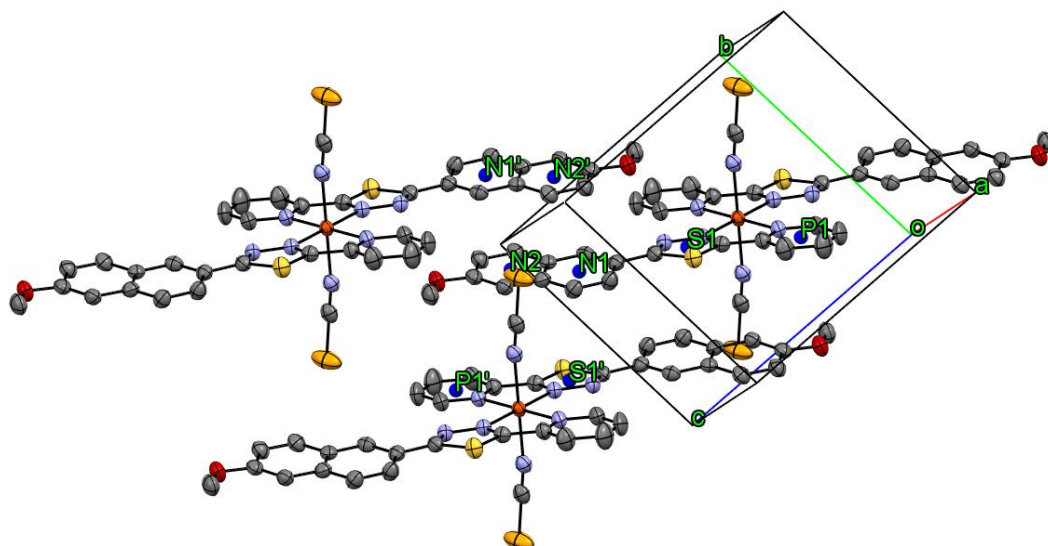
*Figure 161: Expended contacts of **C11** complex molecules at 173 K. The points named P1, P1', S1, N1, N2, N1'adnd N2' are the respective centroids of the respective interacting π-systems. Color Code: grey-C, yellow-sulfur, blue-N, orange-Fe, light green-Cl, red-O, light-orange Se, white-H. ORTEP representation with atomic displacement parameters at 50% level of probability. Hydrogens and solvent molecules are omitted for clarity.*
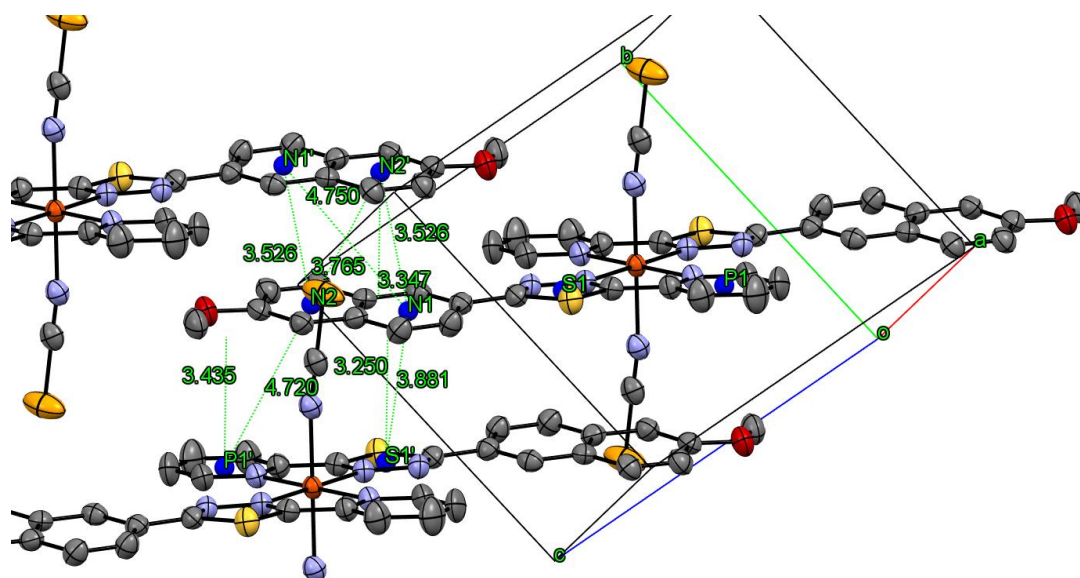

*Figure 162: Representation of all proceeding π-π-interactions of one coordinating ligand **L⁴** with anti-parallel aligned ligand molecules of neighbouring **C11** complex molecules at 173 K. The points named P1, P1', S1, N1, N2, N1'adnd N2' are the respective centroids of the respective interacting π-systems. The average distance of the π-π-interactions is represented by the respective solder that falls on the plane of the interacting partner. Calculation of the Offset of the π-π-interacting partners was done using the Pythagorean theorem. Color Code: grey-C, yellow-sulfur, blue-N, orange-Fe, green-Cl, red-O, light-orange Se, white-H. ORTEP representation with atomic displacement parameters at 50% level of probability. Hydrogens are omitted for clarity.*

	Object1	Object2	Length / Å	Offset of π-π-interacting centroids / Å
Centroid distance perpendicular to respective object plane (average π-π-interaction distance)	N2'	Naphthyl plane (N1,´N2)	3.34(7)	
	S1'	Naphthyl plane (N1, N2)	3.25(0)	
	P1'	Napthyl plane (N1, N2)	3.43(5)	
Centroid to Centroid distance	N2	P1'	4.72(0)	3.23(7)
	S1'	N1	3.88(1)	2.12(1)
	N2'	N1	3.52(6)	1.32(0)
	N2'	N2	3.76(5)	1.72(4)
	N1'	N1	4.75(0)	3.18(3)

*Table 33: Overview of all π-π-interactions proceeding from one molecule of **L⁴** with anti-parallel aligned ligand molecules of neighbouring **C11** complex molecules at 173 K. Calculation of the Offset of the π-π-interacting partners was done using the Pythagorean theorem.*
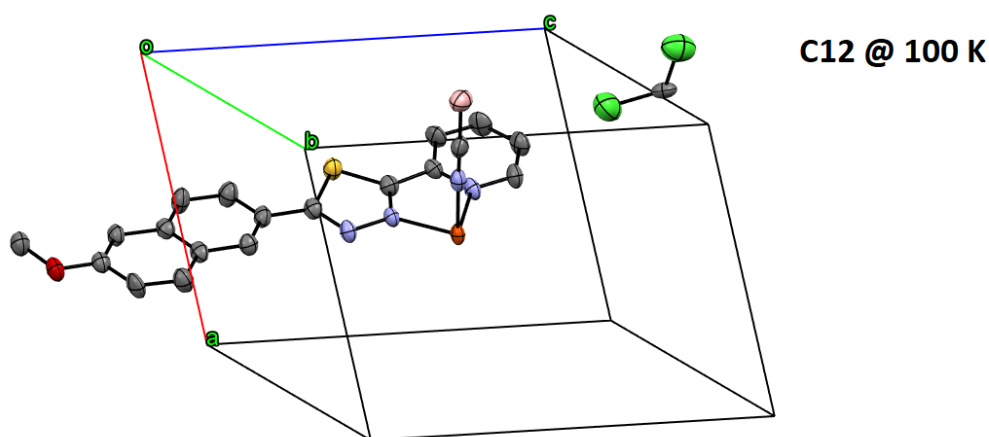

*Figure 163: Asymmetric Unit of **C12** at 100 K. Color Code: grey C, yellow-sulfur, blue-N, orange-Fe, red-O, green-Cl, light red-B, white-H. ORTEP representation with atomic displacement parameters at 50% level of propability.*

Distance / Å		Angle / °	
N2-Fe1	1.99(6)	N2-Fe1-N1	80.1(9)
N2-Fe1	1.99(6)	N1-Fe1-N2	99.8(1)
N1-Fe1	2.03(4)	N2-Fe1-N1	80.1(9)
N1-Fe1	2.03(4)	N1-Fe1-N2	99.8(1)
N4-Fe1	1.94(6)	N4-Fe1-N2	89.2(9)
N4-Fe1	1.94(6)	N4-Fe1-N1	88.4(2)
		N4-Fe1-N2	90.7(1)
		N4-Fe1-N1	91.5(8)
		N4-Fe1-N1	88.4(2)
		N4-Fe1-N2	89.2(9)

		N4-Fe1-N1	91.5(8)
		N4-Fe1-N2	80.1(9)
		Fe1-N4-C19	175.6(7)
		N4-C19-B1	178.2(8)
Ø M-N-distance	1.99(2)	∑ / °	48.4(0)

Table 34: Selected bond lengths and angles including the calculated values of the average F-N-distances and the octahedral distortion parameter ∑ of C12 at 100 K.

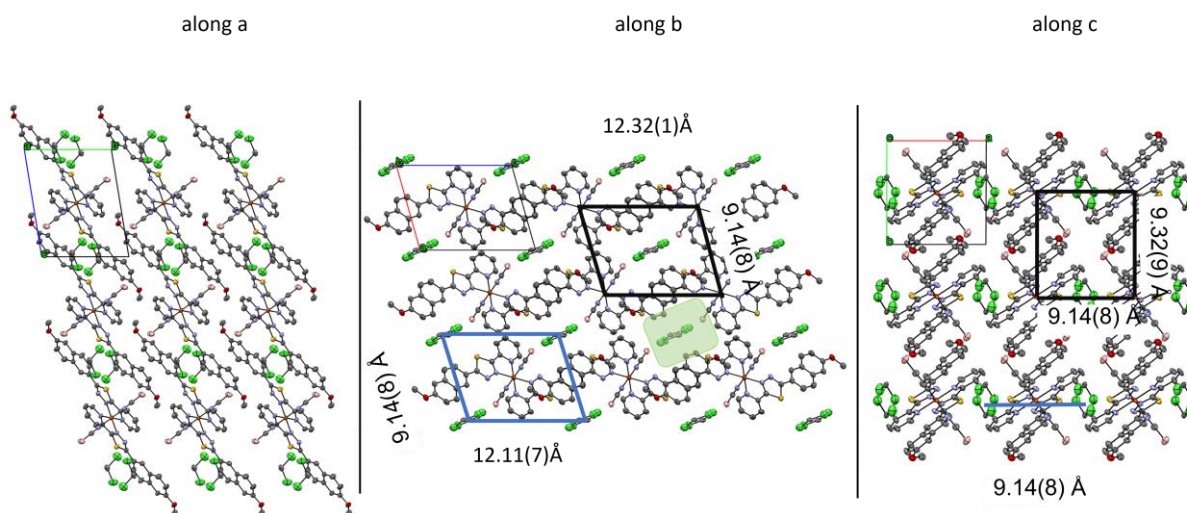along a   along b   along c

*Figure 164: **along a**: Selected part of the crystal structure of **C12** at 100 K along the a-axis. **along b:** Selected part of the crystal structure of **C12** at 100 K along the b-axis. **along c:** Selected part of the crystal structure of **C12** at 100 K along the c-axis. Color Code: grey-C, yellow-sulphur, blue-N, orange-Fe, green-Cl, light orange-Se, white-H. ORTEP representation with atomic displacement parameters at 50% level of probability. Highlighted are the π-π-interacting anti-parallel aligned ligands of neighbouring complex molecules, respectively. Highlighted are the Fe-Fe distances (black boxes) along the different axis and the distances of the centre of the cavities (blue box).*
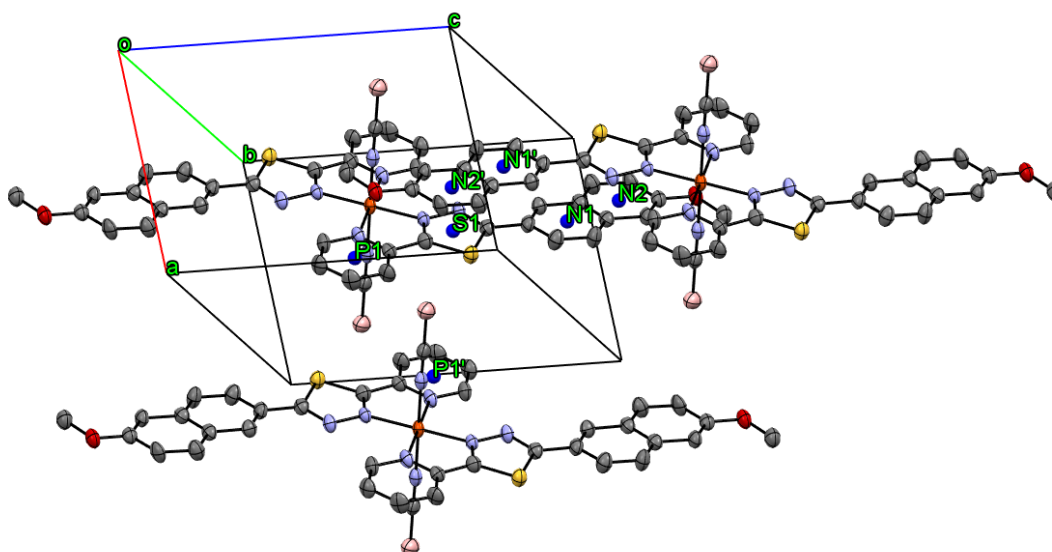

*Figure 165: Expended contacts of **C12** complex molecules at 100 K. The points named P1, P1', S1, N1, N2, N1'adnd N2' are the respective centroids of the respective interacting π-systems. Color Code: grey-C, yellow-sulfur, blue-N, orange-Fe, light red-O,*

light-red B, white-H. ORTEP representation with atomic displacement parameters at 50% level of probability. Hydrogens and solvent molecules are omitted for clarity.
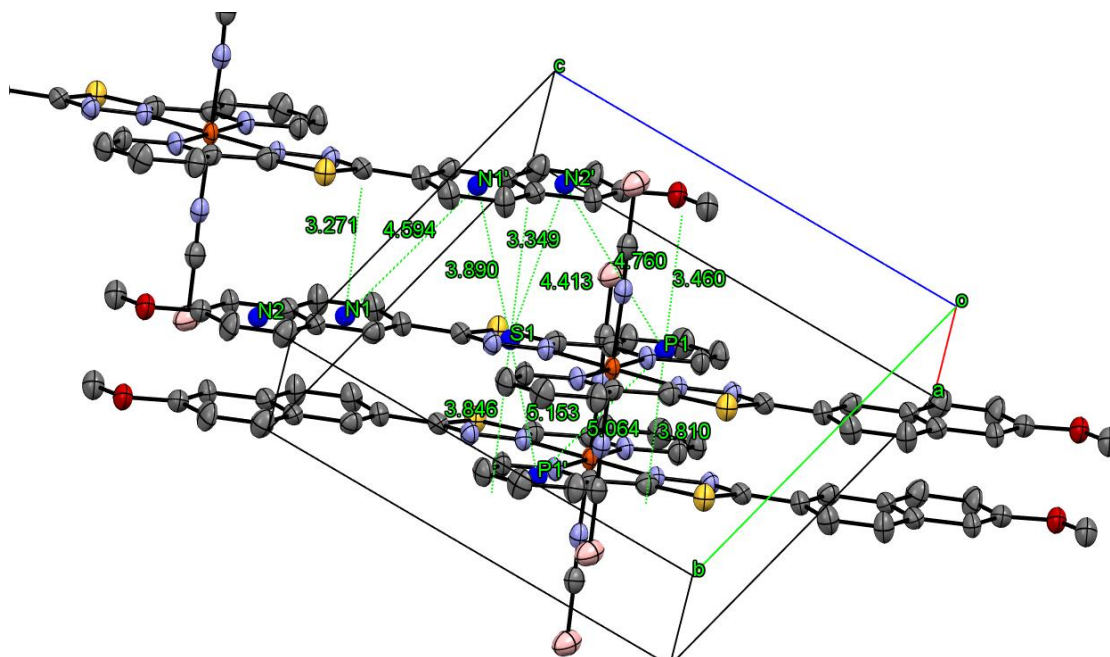

*Figure 166: Representation of all proceeding π-π-interactions of one coordinating ligand **L⁴** with anti-parallel aligned ligand molecules of neighbouring **C12** complex molecules at 100 K. The points named P1, P1', S1, N1, N2, N1'and N2' are the respective centroids of the respective interacting π-systems. The average distance of the π-π-interactions is represented by the respective solder that falls on the plane of the interacting partner. Calculation of the Offset of the π-π-interacting partners was done using the Pythagorean theorem. Color Code: grey-C, yellow-sulfur, blue-N, orange-Fe, red-O, light-red B, white-H. ORTEP representation with atomic displacement parameters at 50% level of probability. Hydrogens and solvent molecules are omitted for clarity.*

	Object1	Object2	Length / Å	Offset of π-π-interacting centroids / Å
Centroid distance perpendicular to respective object plane (average π-π-interaction distance)	N1'	Naphthyl plane (N1,´N2')	3.27(1)	
	S1	Naphthyl plane (N1', N2')	3.34(9)	
	P1	Napthyl plane (N1', N2')	3.46(0)	
	S1	Pyridine plane P1'	3.84(6)	
	P1	Pyridine plane P1'	3.81(0)	
Centroid to Centroid distance	N1'	N1	4.59(4)	3.22(6)
	S1	N1'	3.89(0)	1.97(9)
	S1	N2'	4.41(3)	2.87(4)
	S1	P1'	5.15(3)	3.26(9)
	P1	P1'	5.06(4)	3.42(9)
	P1	N2'	4.76(0)	3.33(6)

*Table 35: Overview of all π-π-interactions proceeding from one molecule of **L⁴** with anti-parallel aligned ligand molecules of neighbouring **C12** complex molecules at 100 K. Calculation of the Offset of the π-π-interacting partners was done using the Pythagorean theorem.*

11.5. Mössbauer Spectroscopy

11.5.1. Mössbauer data of [Fe^{II}(**L^1**)$_2$(NCS)$_2$] **C1**
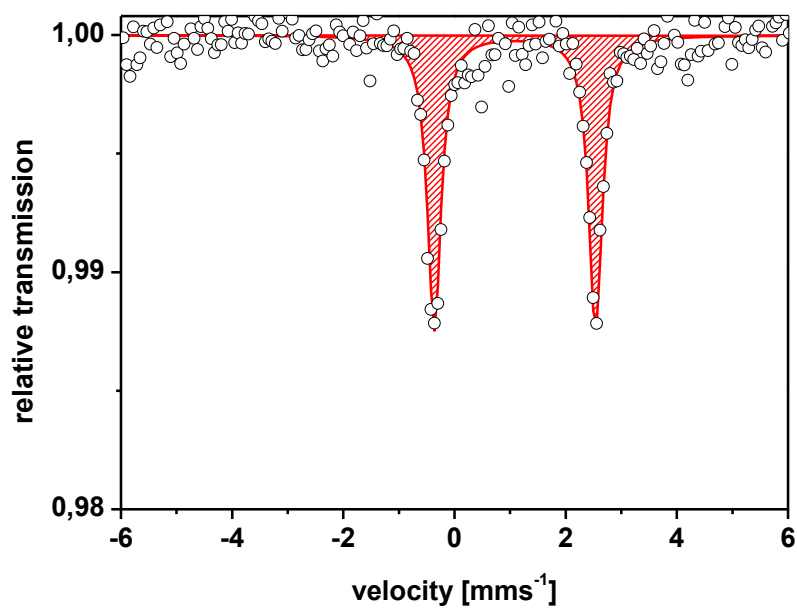

*Figure 167: Mössbauer spectra of slow cooled **C1** measured at 230 K: **Colour code**: HS-states are depicted in red; LS-states are depicted in blue, the overall fits are depicted in black, while the black cycrles represent the actual measurement values. Solid lines are fits with parameters given in Table 36.*
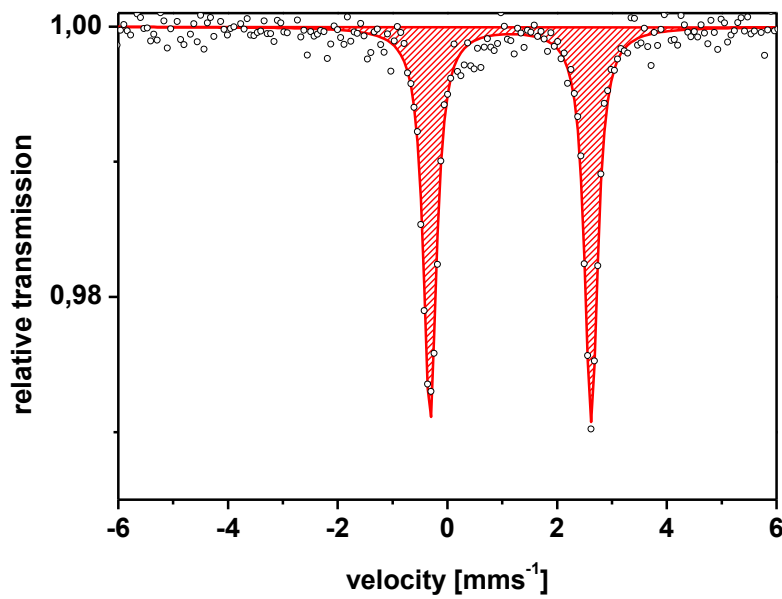
*Figure 168: Mössbauer spectra of slow cooled **C1** measured at 120 K: **Colour code**: HS-states are depicted in red; LS-states are depicted in blue, the overall fits are depicted in black, while the black cycrles represent the actual measurement values. Solid lines are fits with parameters given in Table 36.*
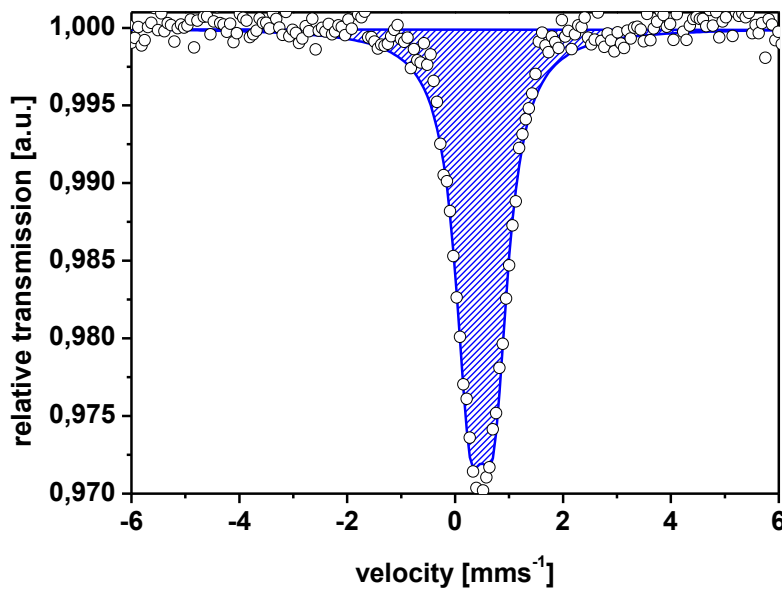

*Figure 169: Mössbauer spectra of quenched and subsequent heated **C1** measured at 100 K: **Colour code**: HS-states are depicted in red; LS-states are depicted in blue, the overall fits are depicted in black, while the black cycrles represent the actual measurement values. Solid lines are fits with parameters given in Table 36.*
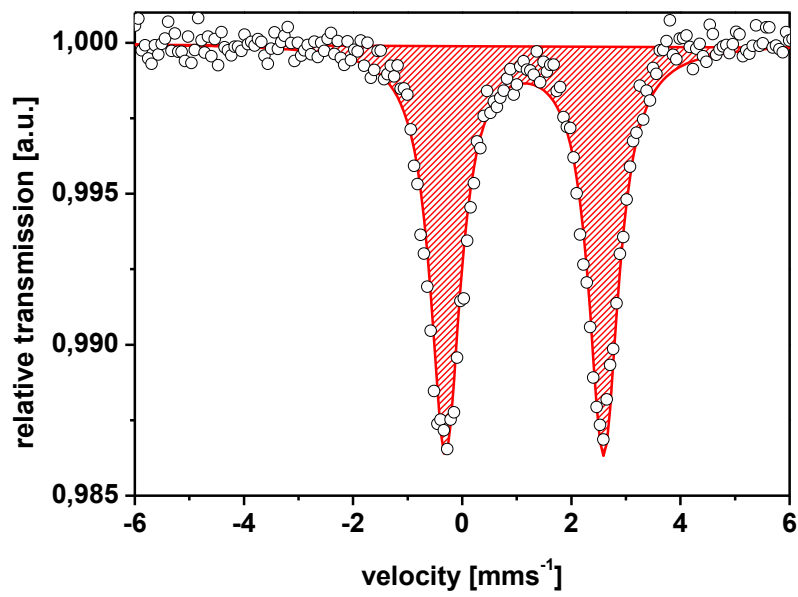
*Figure 170: Mössbauer spectra of quenched and subsequent heated **C1** and measured at 150 K: **Colour code**: HS-states are depicted in red; LS-states are depicted in blue, the overall fits are depicted in black, while the black cycrles represent the actual measurement values. Solid lines are fits with parameters given Table 36.*

*Figure 171: Mössbauer spectra of quenched and subsequent heated **C1** and measured at 230 K: **Colour code**: HS-states are depicted in red; LS-states are depicted in blue, the overall fits are depicted in black, while the black cycrles represent the actual measurement values. Solid lines are fits with parameters given in Table 36.*
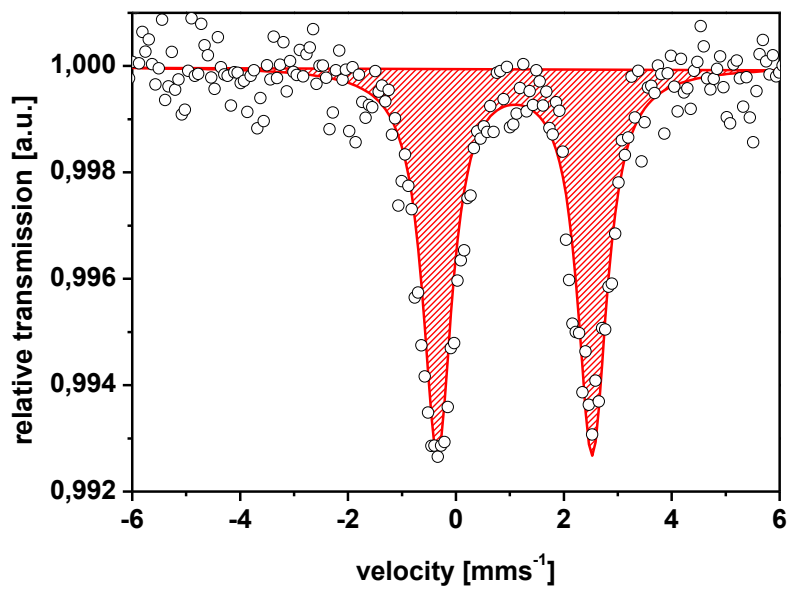
T (K)	component	δ (mms^{-1})	ΔE_Q (mms^{-1})	Γ (mms^{-1})	Area (%)
Slow cooling of C1 down from 298 K to 77 K					
298	HS	1.05(2)	2.83(2)	0.35(2)	100
230	HS	1.09(2)	2.90(2)	0.30(2)	100
120	HS	1.15(2)	2.94(2)	0.29(2)	100
110	HS	1.16(2)	2.95(1)	0.35(1)	84
	LS	0.50(1)	0.42(1)	0.30(1)	16
100	HS	1.17(1)	2.95(1)	0.3(1)	32
	LS	0.50(1)	0.42(1)	0.3(1)	68
77	HS	1.17(1)	2.95(1)	0.35(1)	14
	LS	0.50(1)	0.42(1)	0.30(1)	86
Fast cooling of C1 and Subsequent heating from 15 K to 298 K					
15	HS	1.19(3)	2.97(3)	0.78(4)	33
	LS	0.50(3)	0.45(3)	0.85(4)	67
25	HS	1.19(3)	2.95(3)	0.69(4)	37
	LS	0.5(3)	0.44(3)	0.69(4)	63
77	HS	1.19(3)	2.94(3)	0.70(4)	7
	LS	0.49(3)	0.44(3)	0.70(4)	93
85					
95	LS	0.49(3)	0.44(3)	0.66(4)	100
100					
110					
120	HS	1.15(3)	2.94(3)	0.70(4)	100
150	HS	1.14(3)	2.90(3)	0.66(4)	100
230	HS	1.09(3)	2.87(3)	0.66(4)	100
298	HS	1.05(3)	2.80(3)	0.45(4)	100

*Table 36: Isomer shifts (δ), quadrupole splittings (Δ), linewidths (Γ) and site populations (relative area in %) for all measured Mössbauer spectra of slow cooled (1 K/min) **C1** and heated (1.25 K/min) **C1** from low temperatures. The line width at half maximum is given as Γ. Errors are given in brackets, whereas the error of the area is 2 %.*
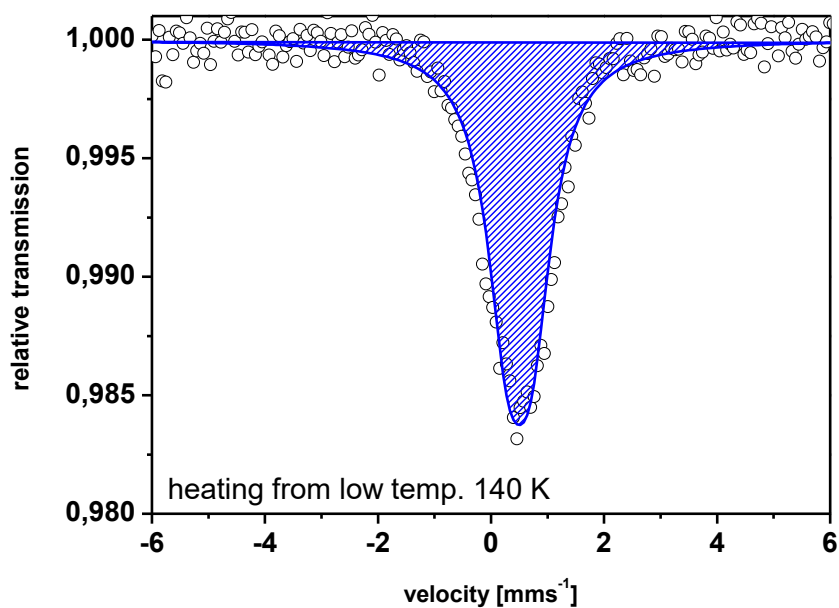
11.5.2.   Mössbauer data of [Fe^{II}(**L^1**)$_2$(NCSe)$_2$] **C2**

*Figure 172: Mössbauer spectra of quenched and subsequent heated from low temperature of **C2** and measured at 140 K: **Colour code**: HS-states are depicted in red; LS-states are depicted in blue, the overall fits are depicted in black, while the black cycrles represent the actual measurement values. Solid lines are fits with parameters given in Table 37.*
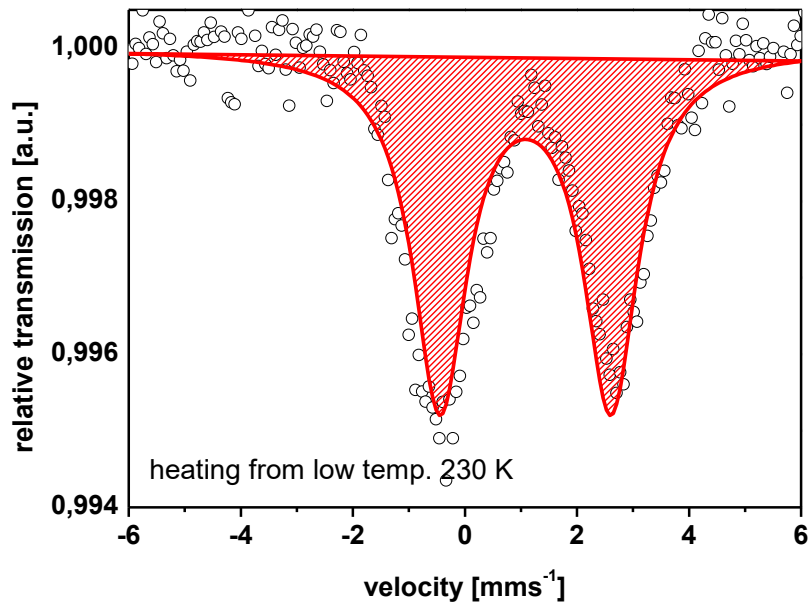

*Figure 173: Mössbauer spectra of quenched and subsequent heated from low temperature of **C2** and measured at 230 K: **Colour code**: HS-states are depicted in red; LS-states are depicted in blue, the overall fits are depicted in black, while the black cycrles represent the actual measurement values. Solid lines are fits with parameters given Table 37.*

T (K)	component	δ (mms^{-1})	ΔE_Q (mms^{-1})	Γ (mms^{-1})	Area (%)

Slow cooling of C2 down from 298 K to 77 K

180	HS	1.09(2)	3.10(2)	0.42(2)	100
154	HS	1.13(2)	3.19(2)	0.41(2)	100
140	HS	1.13(2)	3.23(2)	0.35(2)	100
96	HS	1.14(2)	3.27(2)	0.38(2)	24
	LS	0.51(2)	0.42(2)	0.33(2)	76
77	LS	0.53(2)	0.43(2)	0.35(2)	100

Subsequent slow heating of C2 from 77 K to 298 K

77	LS	0.52(2)	0.43(2)	0.32(2)	100
140	HS	1.10(2)	3.16(2)	0.30(2)	23
	LS	0.50(2)	0.41(2)	0.35(2)	77
154	HS	1.10(2)	3.16(2)	0.30(2)	77
	LS	0.50(2)	0.41(2)	0.35(2)	23
180	HS	1.09(2)	3.10(2)	0.42(2)	100
298	HS	1.04(2)	2.95(2)	0.38(2)	100

Fast cooling of C2 and subsequent heating from 15 K to 298 K

15 K	HS	1.14(3)	3.10(3)	0.70(4)	15
	LS	0.50(3)	0.40(3)	0.75(4)	85
77 K	LS	0.53(3)	0.43(3)	0.73(4)	100
140 K	LS	0.50(3)	0.42(3)	0.80(4)	100
180 K	HS	1.09(3)	3.10(3)	1.06(4)	97
	LS	0.48(3)	0.43(3)	0.80(4)	3
230 K	HS	1.08(3)	2.85(3)	0.70(4)	100
298 K	HS	1.04(3)	3.05(3)	1.03(4)	100

*Table 37: Isomer shifts (δ), quadrupole splittings (Δ), linewidths (Γ) and site populations (relative area in %) for all measured Mössbauer spectra of slow cooled and heated **C2** with a heating and cooling rate of 1 K/min each and of subsequent heated (1.25 K/min) **C2** from low temperatures. Errors are given in brackets, whereas the error of the area is 2 %.*
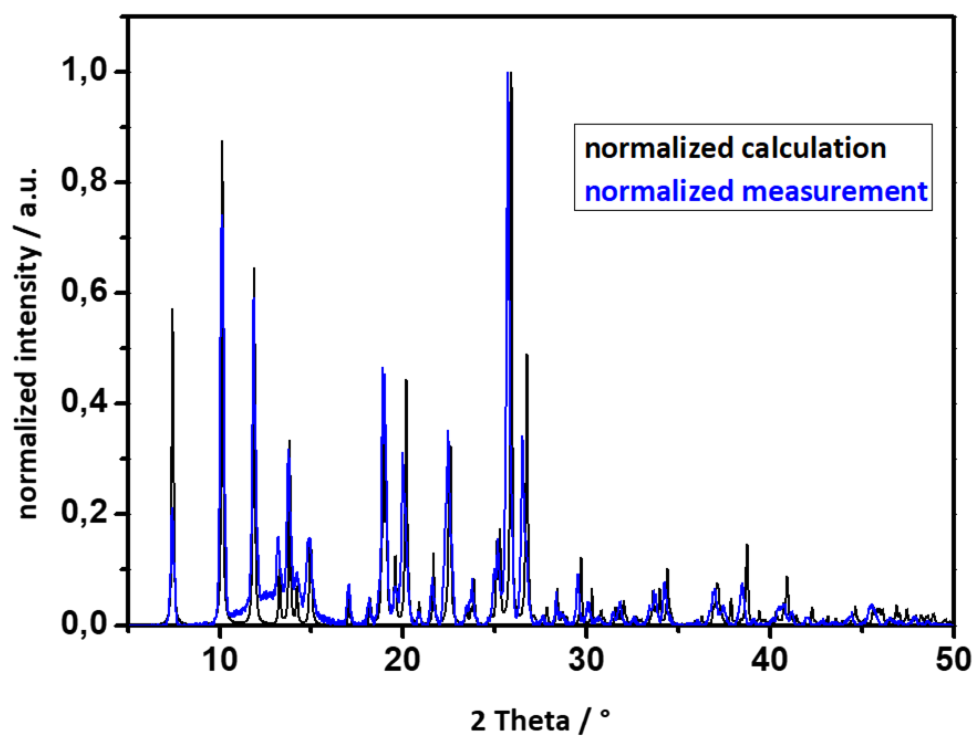
11.6. Powder XRD-Data

Figure 174: normalized calculated (black) and measured (blue) Powder-XRD of C1.

11.7. Pressure induced SCO of C1

Structure at given Pressure point	P0	P1	P2	P3	P5	P6
Pressure (GPa)	0	0.24(2)	0.40(2)	0.52(5)	0.8(3)	1.02(6)
Temperature (K)	295	295	295	295	295	295
Space group	P-1	P-1	P-1	P-1	P-1	P-1
a (Å)	7.9902(7)	7.935(3)	7.916(2)	7.895(3)	7.665(4)	7.7257(7)
b (Å)	9.3878(8)	9.249(4)	9.201(4)	9.172(6)	7.703(4)	8.9868(9)
c (Å)	12.028(1)	11.901(2)	11.811(2)	11.770(2)	13.6855(14)	11.794(4)
α (°)	83.902(7)	83.20(3)	82.86(3)	82.47(3)	88.84(2)	82.631(19)
β (°)	89.685(7)	89.56(2)	89.44(2)	89.43(2)	88.22(2)	88.591(19)
γ (°)	69.419(8)	69.05(4)	68.64(3)	68.58(5)	72.00(5)	67.169(9)
Volume (Å^3)	839.39(13)	809.4(5)	794.3(4)	786.0(7)	768.1(6)	746.0(3)
R_1	0.0502	0.0945	0.0933	0.0849	0.1213	0.0818
wR_2	0.1714	0.2711	0.2862	0.2809	0.2993	0.2345
R_{int}	0.0411	0.2188	0.1569	0.1757	0.411	0.1209
GooF	0.889	1.554	1.155	1.098	1.487	1.71
Fe-N1 (Å)	2.200(3)	2.17(3)	2.19(3)	2.19(3)	2.17(4)	1.989(18)
Fe-N2 (Å)	2.199(3)	2.168(13)	2.166(15)	2.152(15)	2.164(15)	2.01(3)
Fe-N4 (Å)	2.091(4)	2.05(4)	2.10(4)	2.03(4)	2.05(5)	1.95(2)
Ø M-N-distance	2.163(6)	2.131(7)	2.154(4)	2.125(4)	2.131(0)	1.984(7)

Structure at given Pressure point	P7	P8	P9	P10
Pressure (GPa)	1.14(3)	1.74(2)	2.7(1)	3.22(4)
Temperature (K)	295	295	295	295
Space group	P-1	P-1	P-1	P-1
a (Å)	7.713(4)	7.689(3)	7.692(7)	7.7048(8)
b (Å)	8.957(8)	8.966(6)	8.989(17)	9.0341(11)
c (Å)	11.772(3)	11.5094(19)	11.132(7)	11.122(3)
α (°)	82.41(5)	81.46(3)	79.6(2)	80.12(2)
β (°)	88.53(3)	89.03(2)	89.70(12)	89.885(19)
γ (°)	66.98(7)	66.24(5)	65.3(3)	65.315(11)
Volume (Å^3)	739.3(9)	715.6(6)	684.4(1.7)	690.6(3)
R1	0.0845	0.0743	-	0.0883
wR2	0.2402	0.21	-	0.2126
Rint	0.1965	0.1062	-	0.2213
GooF	1.479	1.316	-	1.185
Fe-N1 (Å)	1.95(4)	1.97(3)	-	1.98(2)
Fe-N2 (Å)	1.98(2)	1.955(14)	-	1.99(3)
Fe-N4 (Å)	1.96(4)	1.95(4)	-	1.91(3)
Ø M-N-distance	1.96(6)	1.96(1)		1.96(3)

Table 38: Unit cell and refinement parameters of C1 at different pressure points measured by Mathilde H. Nygaard and Dr. Jacob Overgaard. "-" indicate that data is not available. The table was reproduced with permission.[219]

	Fe-N1 bond	Fe-N2 bond	Fe-N4 bond
P0 bond length (Å)	2.200(3)	2.200(3)	2.091(4)
P5 bond length (Å)	2.17(3)	2.16(2)	2.05(5)
P6 bond length (Å)	1.99(1)	2.01(3)	1.95(2)
Difference P5-P6 (Å)	0.18(5)	0.16(4)	0.10(7)
Difference P5-P6 (%)	8.2	7.2	5.1
Difference P0-P6 (Å)	0.21(2)	0.19(3)	0.15(3)
Difference P0-P6 (%)	9.5	8.6	7.2
Difference P0-P5 (Å)	0.03(4)	0.04(2)	0.04(5)
Difference P0-P5 (%)	1.4	1.8	1.9

Table 39: Comparison of Fe-N bond lengths for the P0, P5 and P6 structures. The Fe-N bond length differences between the structures at different pressure point are included in (Å) and percentage, respectively. The table is reproduced with permission.[219]

11.8. Temperature variable magnetic Susceptibility data
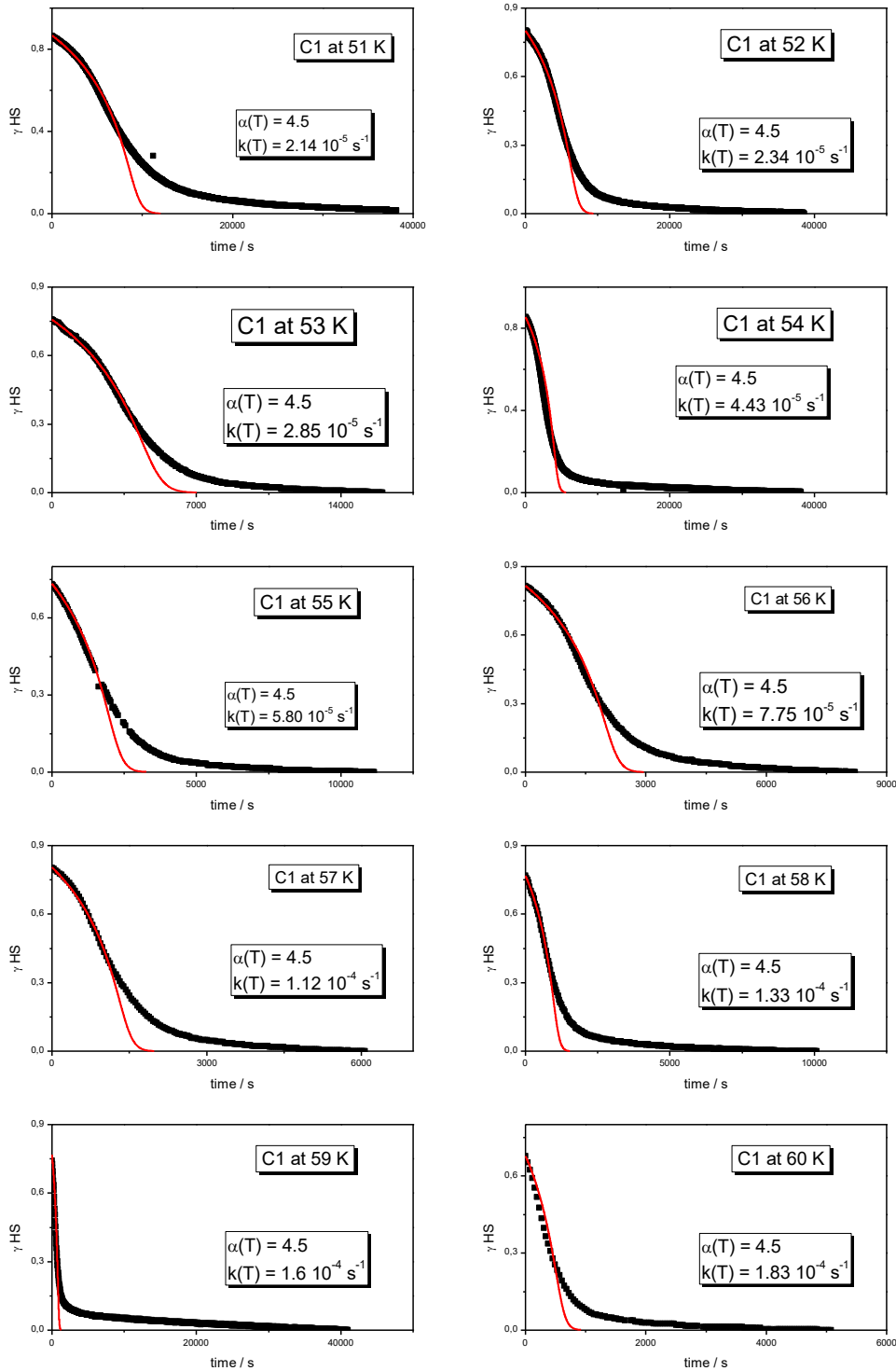
Figure 175: All relaxation measurements of the magnetic susceptibility of C1, presented as the HS-fraction vs. time in seconds. The black curves are the experimental data, whereas the red curve represents the sigmoidal simulation at the respective temperatures.
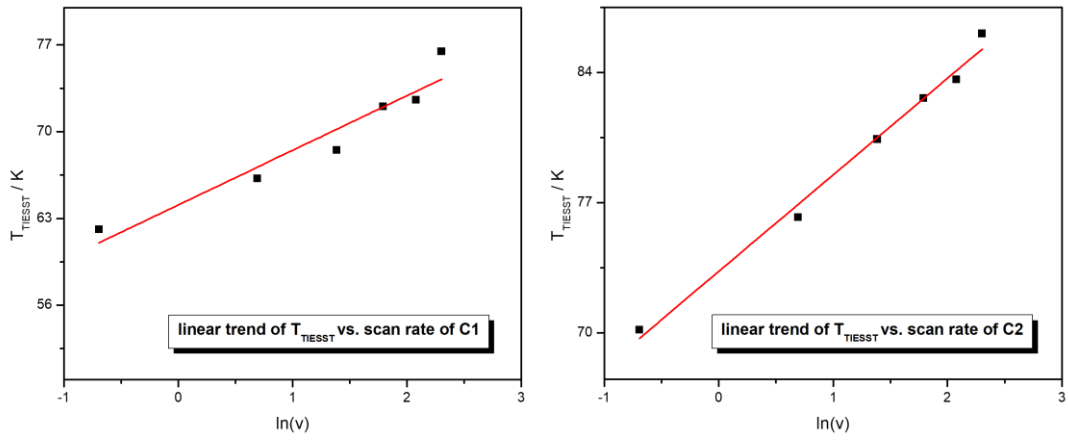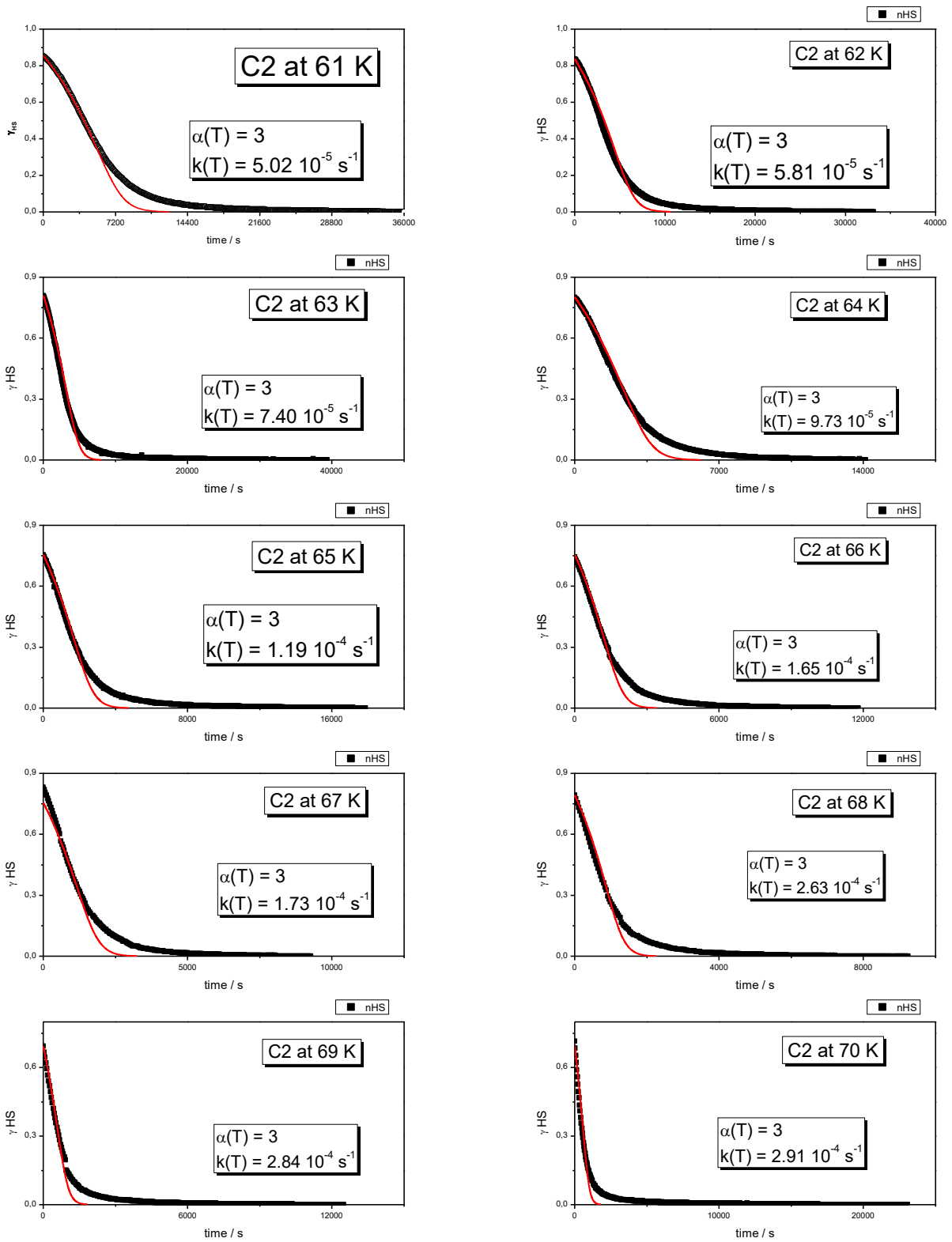
Figure 176: Plot of T_{TIESST} values of C1 and C2 as a function of the logarithm of the scan rate, with tentative linear regression.

Figure 177: All relaxation measurements of the magnetic susceptibility of C2, presented as the HS-fraction vs. time in seconds. The black curves are the experimental data, whereas the red curve represents the sigmoidal simulation at the respective temperatures.
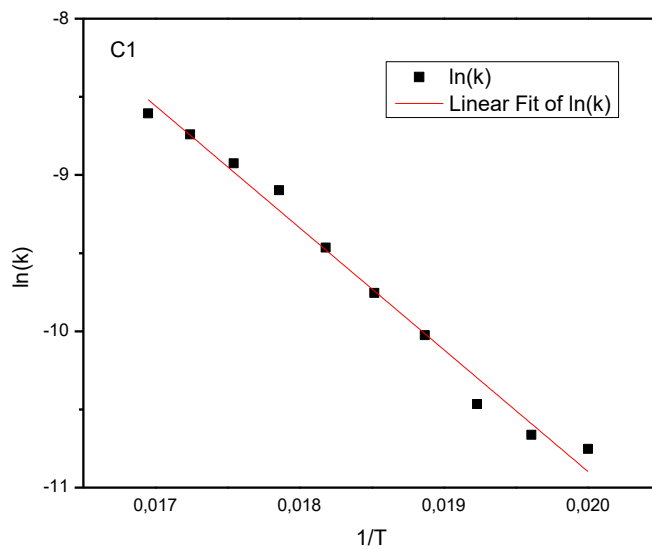
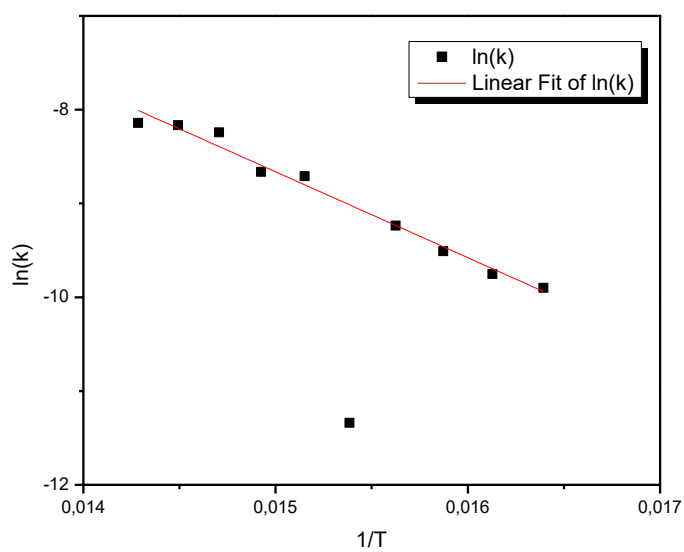*Figure 178: ln(k) of C1 as function of 1/T, giving an activation barrier of 538,138 cm^{-1}.*

Figure 179: ln(k) of C2 as function of 1/T, giving an activation barrier of 631,833 cm^{-1}. The erroneous point was ignored in the linear regression.
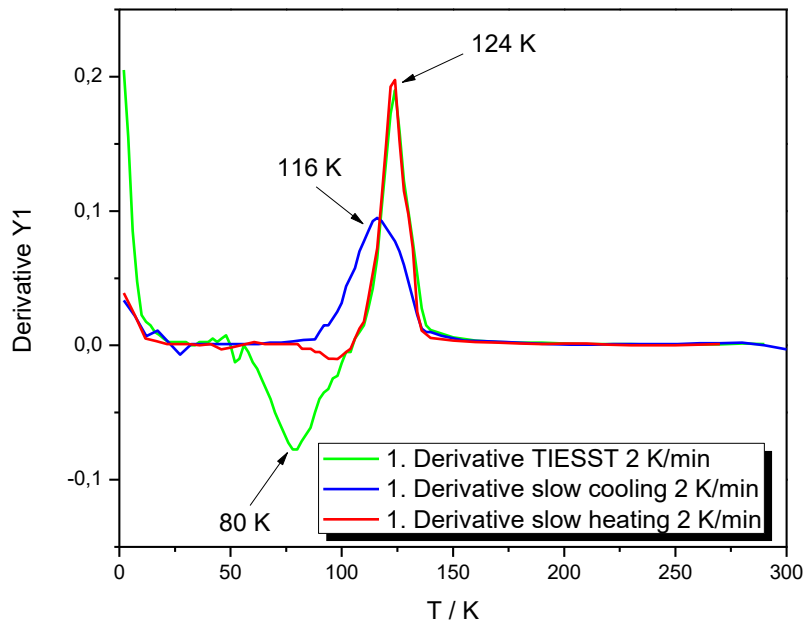
*Figure 180: First Derivative of the variable temperature magnetic susceptibility measurement of a dried sample of **C5** showing the spin transition temperatures during the different cooling and heating processes.*
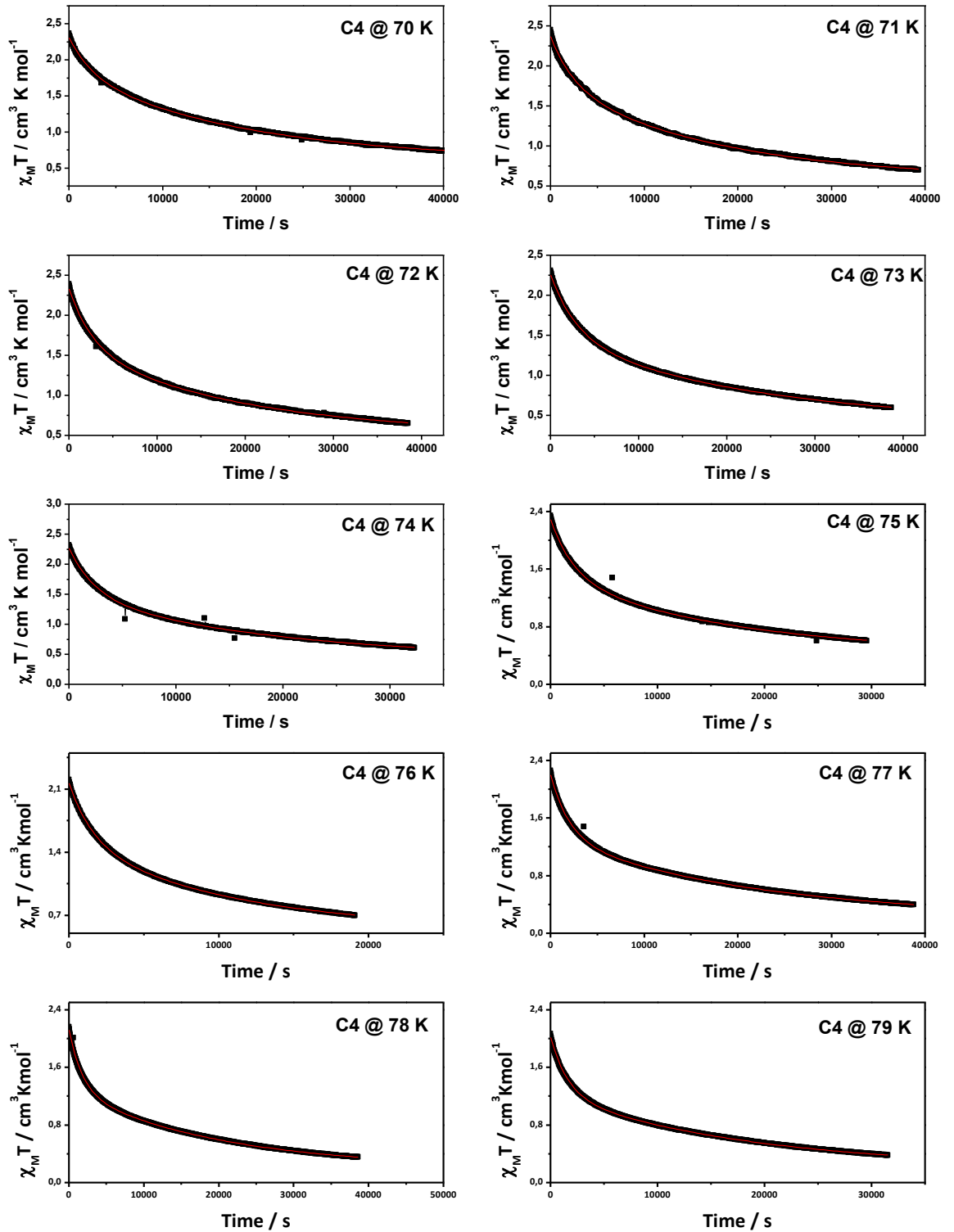
Figure 181: All relaxation measurements of the magnetic susceptibility of C4, presented as $X_M T$ vs. time in seconds. The black curves are the experimental data, whereas the red curve represents the double exponential law at the respective temperatures.
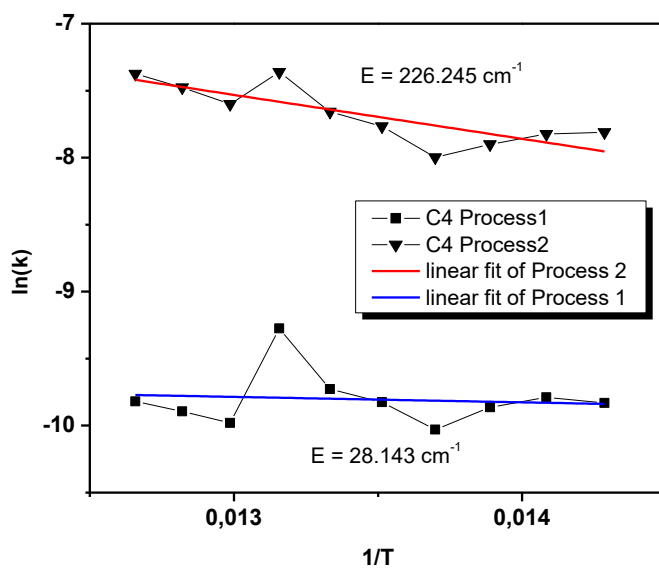
Figure 182: Calculated values of ln(k) vs 1/T, inclusive linear fits of the respective processes: process 1 (triangles) and process 2 (squares).

Process 1			Process 2		
T / K	(1/T) / K^{-1}	k(T) / s^{-1}	ln(k(T))	k(T) / s^{-1}	ln(k(T))
70	0.01429	$5.37632 \cdot 10^{-5}$	-9.83092	$4,05374 \cdot 10^{-4}$	-7,8107
71	0.01408	$5.60496 \cdot 10^{-5}$	-9.78927	$4,0038 \cdot 10^{-4}$	-7,8231
72	0.01389	$5.2007E \cdot 10^{-5}$	-9.86413	$3,70696 \cdot 10^{-4}$	-7,90013
73	0.0137	$4.40826 \cdot 10^{-5}$	-10.02945	$3,36271 \cdot 10^{-4}$	-7,99759
74	0.01351	$5,40717 \cdot 10^{-5}$	-9,8252	$4.23477 \cdot 10^{-5}$	-7.76701
75	0.01333	$4.72749 \cdot 10^{-5}$	-9,72762	$5,96141 \cdot 10^{-5}$	-7.65695
76	0.01316	$9.37087 \cdot 10^{-5}$	-9.27532	$6.35144 \cdot 10^{-4}$	-7,36166
77	0.01299	$4.63547 \cdot 10^{-5}$	-9.97919	$5,00645 \cdot 10^{-4}$	-7,59961
78	0.01282	$5,04363 \cdot 10^{-5}$	-9,8948	$5.65996 \cdot 10^{-5}$	-7,47692
79	0.01266	$5.43962 \cdot 10^{-5}$	-9.81922	$6.27274 \cdot 10^{-5}$	-7.37413

Table 40: extracted values of the fits of the time-dependend relaxation measurements of C4.
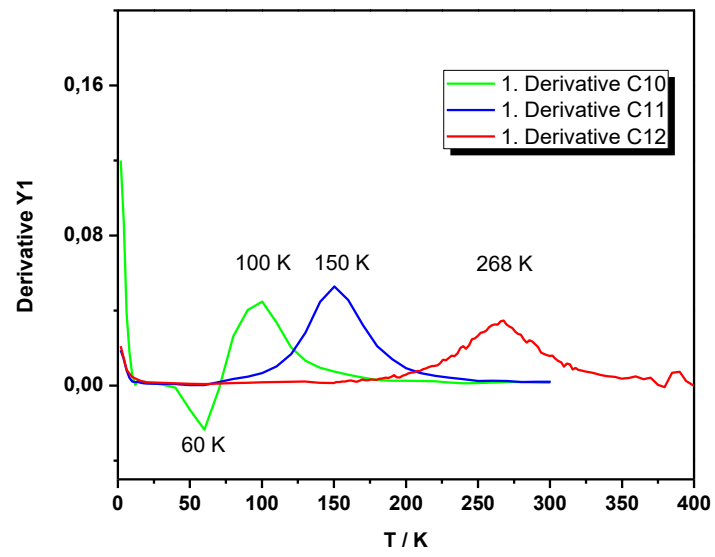
*Figure 183: First Derivative of the variable temperature magnetic susceptibility measurement of a dried sample of **C5** showing the spin transition temperatures during the different cooling and heating processes*